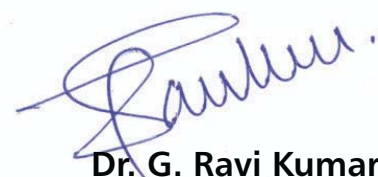BARC NEWSLETTER

Founder's Day special issue 2017

From the Editor's Desk...

The Founder's day Special issue of the BARC Newsletter published on the eve of Founder's day celebration, carries award winning works of our Scientists and Engineers. Articles by the 2015 DAE awardees are being published in this issue.

This year a total of twenty four papers are being published in this issue. The CD contains articles from the recipients of the following awards:

1. Homi Bhabha Science & Technology Award
2. Scientific & Technical Excellence Award
3. Young Applied Scientist/Technologist Award
4. Young Scientist Award
5. Young Engineer Award

Individual papers can be accessed from the Contents as well as from the Author Index by clicking on the hyperlinks.

Dr. G. Ravi Kumar
On behalf of the Editorial Committee

BARC NEWSLETTER

Founder's Day Special Issue October 2017

C O N T E N T S

DAE AWARDS 2015

DAE Homi Bhabha Science & Technology Awards

DAE Scientific & Technical Excellence Awards

* Recipient of the award

* Recipient of the award

* Recipient of the award

DAE Young Scientist Awards

DAE Young Engineer Awards

* Recipient of the award

Trichoderma - Genes, Genomes and Applications

Prasun K. Mukherjee
Nuclear Agriculture and Biotechnology Division

Abstract

Trichoderma species are a group of filamentous fungi with immense applications in agriculture and biotechnology. These fungi are the most commonly used biofungicides and plant growth promoters, and are widely used in industry as source of hydrolytic enzymes. An urge to understand the mechanisms underlying these beneficial properties led to studying the genetics of *Trichoderma* spp. Before the genome era, several genes were cloned and functions studied using molecular approaches. With the advent of the genome era, whole genome sequences of as many as 12 different species are available in the database and there has been a huge information flow leading to better understanding of the biology at the genome scale. We have obtained several mutants of *Trichoderma*, some very useful in basic research, while others having improved biocontrol properties. We have isolated a novel strain of *Trichoderma* that has proved effective in decomposition of dry plant biomass. The technology has been transferred to two companies. In addition, we have developed a novel mass multiplication method that has been transferred to several companies, some having launched commercial production.

Introduction

The filamentous fungi *Trichoderma* spp. (Fig. 1) are of immense economical importance, being the most widely used biofungicides in today's agriculture, and as source of industrially important enzymes (1, 2). These fungi are mycoparasites (fungi parasitic on other fungi) on many plant pathogenic fungi (Fig. 2) and produce copious amounts of secondary metabolites, many being antimicrobial (3, 4). These fungi colonize roots and induce systemic resistance in plants against invading pathogens, thus improving plant immunity. Many strains are reported to promote plant growth through mobilization of nutrients and production of phytohormones, and impart tolerance to several abiotic stresses like drought and salinity stress (1). These fungi are omnipresent in soil, tree bark, marine environment as well as endophytes (living inside plants and imparting beneficial effects) (5). Several hundred species comprise the genus *Trichoderma*, and more than 200 species are well defined (6). *Trichoderma* spp. produce profuse conidia, the active propagules in most of the commercial products. There are more than 300 commercial formulations that are available in the Indian market alone, and due to a ban or limited usage of chemical fungicides, many multinational companies have also started marketing *Trichoderma*-based biofungicides all over the world.

Even though *Trichoderma*-based formulations are easily available, quality control is a big issue and there is a need for genetic improvement of existing strains and formulations for farmers' benefits. *Trichoderma* spp. are good decomposers of plant biomass too, and hence can play an important role in environmental clean-up and recycling of residues. Systematic research on these economically important fungi were initiated in BARC in 1993, and our work for over two decades have added to the knowledgebase as well as the development of several commercially viable technologies.
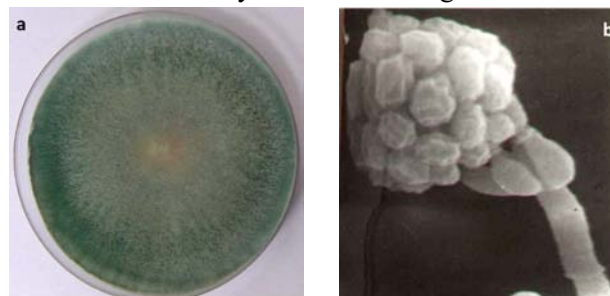
Fig. 1: Culture of *Trichoderma virens* cultivated on potato dextrose agar for three days, with profuse green pigmented conidia (a) and typical conidia (spores) borne on conidiophores (b).

Fig. 2: Mycoparasitism (a) and antibiosis (b) of *Trichoderma* on plant pathogens. During a mycoparasitic interaction, *Trichoderma* (thinner hyphae) coils around and lyse the pathogen hyphae (a). *Trichoderma* spp. also produce antimicrobial compounds that inhibit growth of plant pathogens (b).

Identification of genes involved in biocontrol and conidiation

Before the advent of the genome era, we were looking for genes that are involved in biocontrol and conidiation by gene knockout using homologous recombination strategy. Mutants were obtained with deletion in a target gene, and compared with the wild type for phenotypes. Using this strategy, we have identified two mitogen activated protein kinases (MAPK) to be involved in repression of conidiation, and in parasitism of the plant pathogen *Sclerotium rolfsii* (Fig. 3)(7). Similarly, deletion of an adenylate cyclase gene *tac1* resulted in extremely slow growing colonies, indicating vital role of this gene in colony growth of *Trichoderma* (Fig. 4)(8). One of the MAP kinases is also involved in induction of systemic immunity in plants (9).
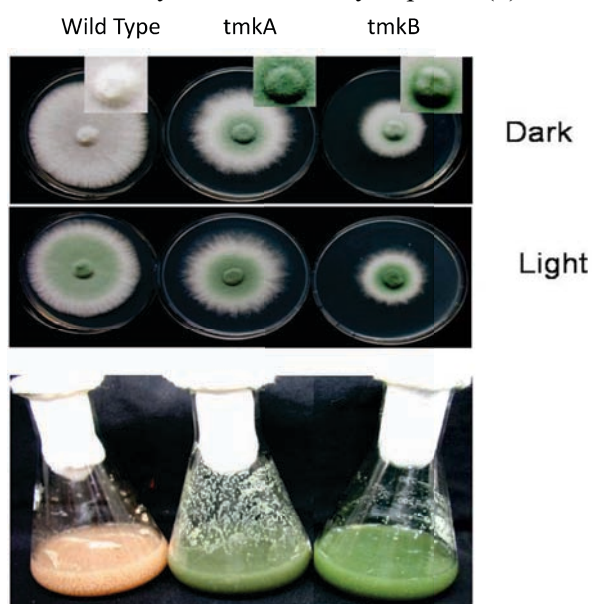
Fig. 3: Deletion of the mitogen activated protein kinase genes *tmkA* and *tmkB* de-represses conidiation in *Trichoderma virens*.
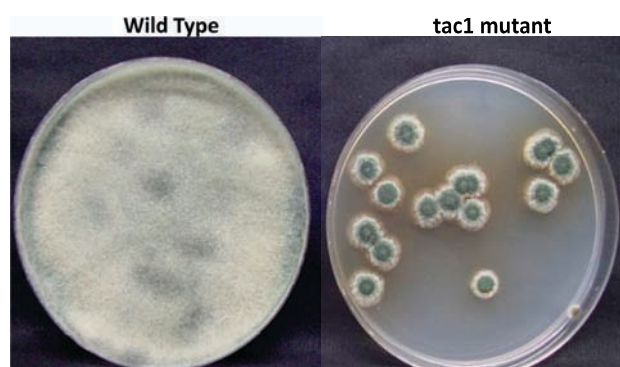
Fig. 4: Deletion of adenylate cyclase -encoding gene *tac1* impairs vegetative growth in *Trichoderma virens*.

***Trichoderma* genomics**

Trichoderma genomics era began with the publication of the whole genome sequence of the industrial workhorse *Trichoderma reesei* (10). The genome sequence analysis identified several novel genes involved in biomass degradation and helped in understanding the complex regulation underlying the ability of this fungus to produce plant biomass degrading enzymes. Interestingly, whole genome sequencing of a mutant strain revealed the genetic secret (deletion of the carbon catabolite repressor Cre1) behind the hyperproduction of cellulases in the commercially used mutant strain (11). The genomics of biocontrol began with the publication of the whole genome sequence of two biocontrol species -*Trichoderma virens* and *T. atroviride*. Our's has been the only institute from India to have participated in this international effort (12). A comparative analysis of the non-mycoparasitic *T. reesei* with strongly mycoparasitic *T. virens* and *T. atroviride* revealed that the genomes of mycoparasites are enriched in genes for mycoparasitism, namely chitinolytic and gluconolytic enzymes and genes for secondary metabolism. Based on this study, it was concluded that mycoparasitism is an ancestral trait of *Trichoderma* (5).

Apart from these three species, whole genome sequence of *T. harzianum* and *T. asperellum*, *T. citrinoviride*, *T. longibrachiatum, T. parareesei, T. koningii*, *T. guizhouense*, *T. gamsii*, *T. pleuroti* and *T. hamatum* are now available in the database.

Mining of *Trichoderma* genomes for genes involved in secondary metabolism

Trichoderma species are prolific producers of secondary metabolites which have been implicated

in biocontrol, induced resistance as well as growth promotion (3, 4). Even though a few genes for secondary metabolism were studied earlier, with the genome sequencing, it became clear that most of the genes related to a secondary metabolite biosynthesis are grouped together as gene clusters. Using genome mining, we have identified several novel gene clusters involved in the biosynthesis of secondary metabolites, both volatile and non-volatile. Part of the "vir" cluster was discovered by us using a radiation-induced mutant (Fig. 5) that does not produce the antimicrobial and anti-cancer compound viridin (13). This was the first gene cluster to have been discovered in any *Trichoderma* spp. With the help of the genome sequence, we could un-earth the entire gene cluster comprising 8 genes (Fig. 6). This gene cluster is similar to a gene cluster that we discovered in the genome of an unrelated fungus *Aspergillus oryzae*. Gene deletion experiment confirmed the role of this gene cluster in biosynthesis of several volatile sesquiterepenes including some compounds known to be involved in interaction of insects with plants (14). *Trichoderma virens* has been known to produce gliotoxin (a strong antimicrobial) for more than 80 years and the biosynthesis gene cluster was identified by us (3, 15, 16). *Trichoderma virens* "P" strains do not produce gliotoxin, instead it produces gliovirin, another antimicrobial and anticancer agent of microbial origin. Since the genome of the "P" strain was not available, we closed this gap by sequencing the genome of an Indian strain of *Trichoderma virens* "P" strain (deposited in GenBank under the accession No. LQCH00000000, this is the first genome sequence of any *Trichoderma* from India). A detailed analysis of the genome revealed the presence of a gene cluster comprising of 22 genes (Fig. 7). This gene cluster has high similarity with a gene cluster from *Aspergillus udagawae*. The role of this gene cluster in biosynthesis of gliovirin was confirmed by gene knockout followed by LC-MS/MS analysis (17). Using genome mining, we have also identified the viridin biosynthesis gene cluster in *Trichoderma virens* genome (unpublished). Viridin is a strong antimicrobial and an anti-cancer compound and discovery of this gene cluster would help in over-producing this compound and also to stop the conversion of antimicrobial viridin to phytotoxic viridiol. We have also discovered several new gene clusters with unknown products, thus opening the path for metabolic engineering to discover novel secondary metabolites

for applications in agriculture and health sector (18, 19).
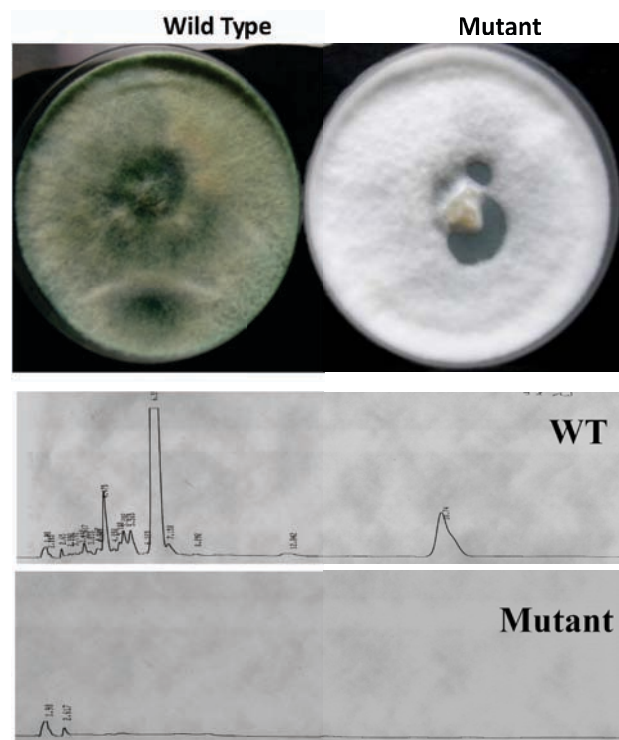
Fig. 5: A non-conidiating and non-viridin producing mutant of *Trichoderma virens*, induced by gamma radiation.
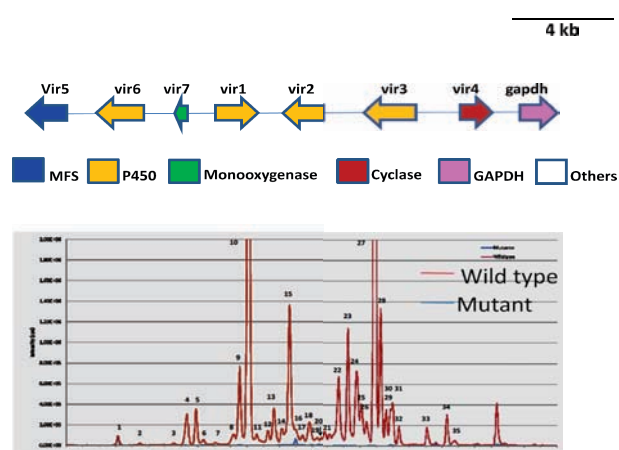
Fig. 6: The *vir* gene cluster is involved in the biosynthesis of volatile sesquiterpenes as revealed by comparison of volatome of wild type and *vir4* knockout mutant by GC-MS.
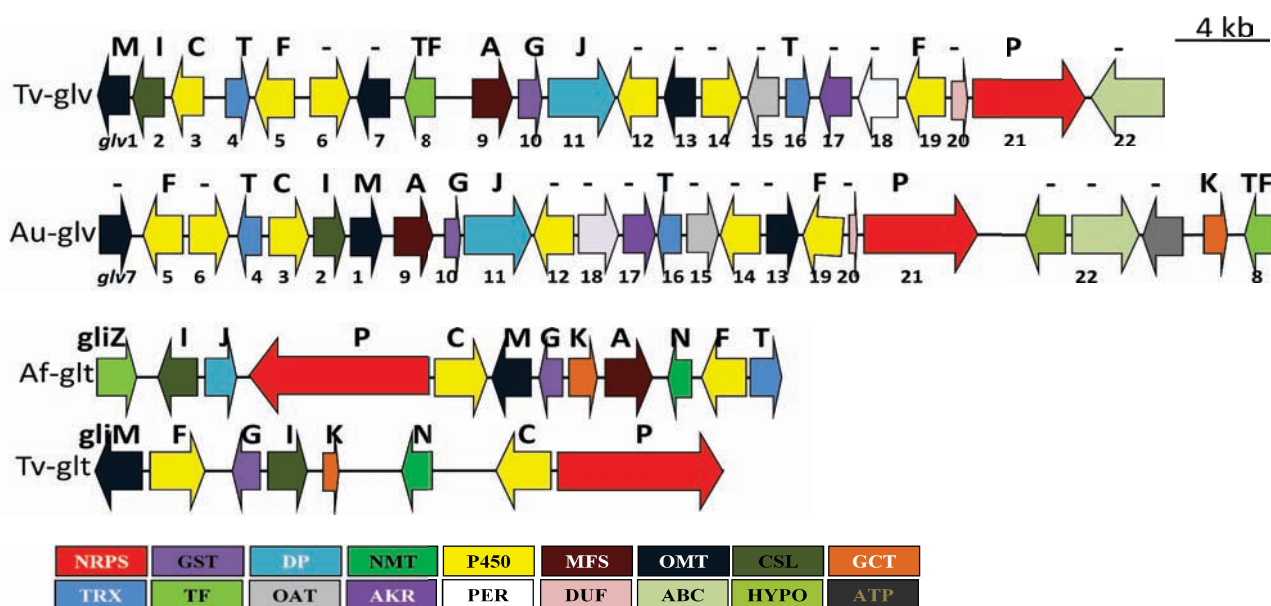
Fig. 7: The gliovirin gene cluster of *Trichoderma virens* and it's orthologous cluster in *Aspergillus udagawae.* The gliotoxin gene cluster present in "Q" strains of *Trichoderma virens* and also, in *Aspergillus fumigatus* are included.

Trichoderma genomes as source of transgenes

Once identified, certain genes for biotic and abiotic stress tolerance can be transferred to crop plants for improving yield potential. *Trichoderma* genomes are rich in such candidate genes and several such genes have been successfully transferred to plants (20). We have been able to improve disease tolerance in plants by transferring an endochitinase gene (21, 22). Similarly, transgenic expression of a gene for glutathione S-transferase improved tolerance to anthracine, heavy metal and salt (23, 24) (Fig. 8). Anthracene also got degraded to naphthalenes in plants expressing this gene (23), opening up the possibility of phytoremediation of anthracene (and possibly other PAHs) contaminated soils.
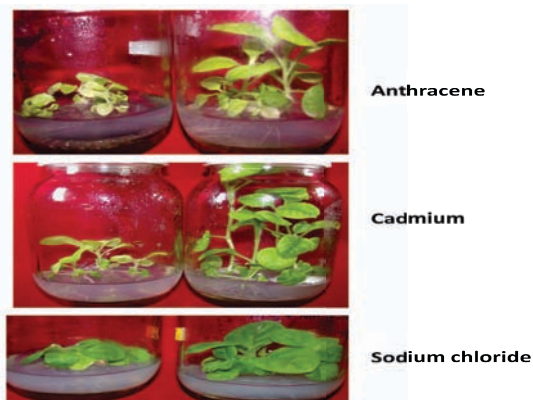
Fig. 8: Enhanced abiotic stress tolerance of transgenic tobacco plants expressing *Trichoderma virens* GST gene.

Development of a novel mass multiplication technology

As mentioned earlier, more than 300 *Trichoderma*-based commercial formulations are available in Indian market. Most of these companies use sorghum grains or potato-based media for cultivating these fungi, which are not only expensive but also results in wastage of food. These formulations are also amended with some chemicals like carboxymethyl-cellulose and detergents (as spreaders/ stickers), and hence in strict sense cannot be applied in organic agriculture, defeating the basic purpose of biological control. We have developed a simple mass multiplication technology using tamarind seeds as a cheap substrate. Tamarind seeds not only support profuse growth and conidiation of *Trichoderma*, the formulation based on tamarind seeds are also having intrinsic stickiness, and thus, are purely organic in nature (Fig. 9). A patent (1236/MUM/2012) has been filed and this technology has been transferred to five biotech companies, two of them having launched products already.

Strain improvement using induced mutagenesis

Using gamma-radiation, we have been able to mutagenize *T. virens* for enhancing biocontrol potential. Wild type culture was exposed to 1250 Gy gamma-radiation and several stable mutants differing in conidial pigmentation were isolated.

Fig 9: A novel mass multiplication strategy for *Trichoderma* (a) and development of a granular seed dressing formulation (b). Chickpea seeds treated with the formulation (c). Please note uniform coating on treated seeds.

One such mutant (designated as G2), with brown colour conidia was isolated which produced more pigments in culture and was also a hyper-producer of the antimicrobial compound viridin (Fig. 10). In a series of experiments under controlled conditions, this mutant was found to be superior to the wild type in plant disease control potential. In a transcriptome analysis, several genes for secondary metabolism and mycoparasitism were found to be upregulated in this mutant. Using the tamarind-based mass cultivation technology developed by us, we have formulated this mutant under the name TrichoBARC (a seed dressing formulation). The bioefficacy of this formulation has been demonstrated in large scale field trials and found to be effective in controlling plant diseases and promoting plant growth (Fig. 11). This technology has already been transferred to a biotech company.

Isolation of a strain of *Trichoderma* for degradation of plant biomass

Trichoderma spp. are champions of biomass degradation and found naturally on tree bark and dead wood. We have isolated such a strain from bark of a mango tree located in Anushaktinagar and identified it to be *Trichoderma koningiopsis*. This
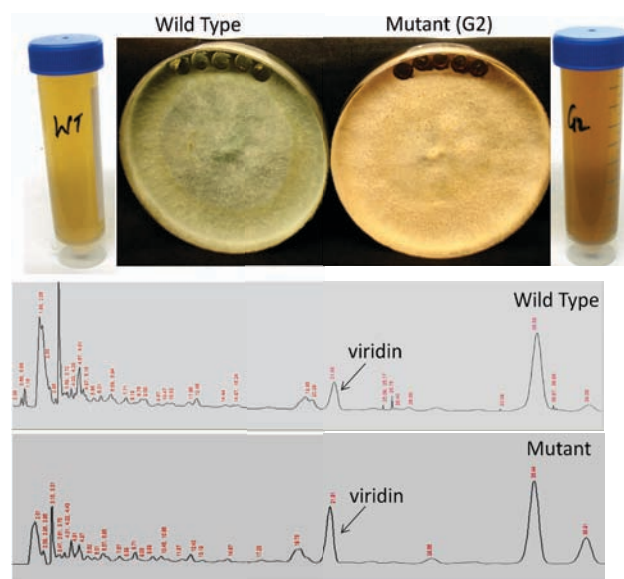
Fig. 10: Brown pigmented mutant (G2) of *Trichoderma virens* producing more viridin in culture.
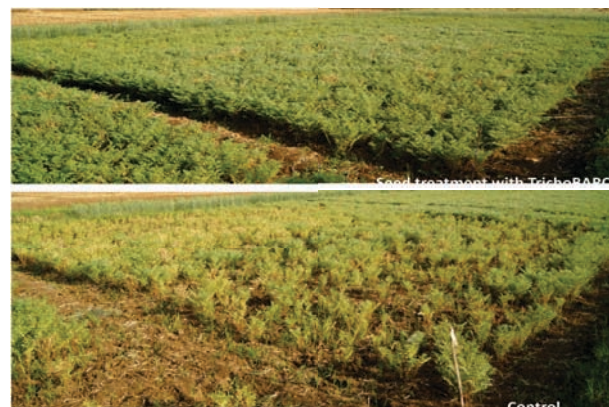
Fig. 11: Field trial at Raipur on biological control of collar rot of chickpea using the TrichoBARC seed dressing formulation developed at BARC. The formulation contains spores of a mutant strain of Trichoderma virens

Fig. 12. Accelerated decomposition of dry leaf biomass using TriComp, a formulation developed based on a novel strain of *Trichoderma koningiopsis* isolated from mango tree bark. A. Before treatment with TriComp; B. One month after treatment. Note complete decomposition of dry leaf biomass due to *Trichoderma* treatment.

strain has high cellulytic activities and degraded plant biomass (dry leaves/ garden wastes) efficiently, in 4-6 weeks' time (Fig. 12). A formulation (named as TriComp) based on this strain has been developed that is suitable for rapid composting of garden wastes. The efficacy of this composting technology has been demonstrated on site in a large housing society and an educational institute. The technology has been transferred to two companies.

Conclusions

Trichoderma spp. are fungi of immense economic significance, being widely used in agriculture and industry. We have developed several technologies related to agricultural and environmental applications of these fungi. In addition, we have also made fundamental contributions towards understanding the basic biology of these fungi at the genetics and genomics levels. The major focus of our research is to enhance the bioefficacy of these fungi through improvement of strains and formulations. The basic knowledge acquired are being applied towards the discovery of novel secondary metabolites and pathways for applications in agriculture and healthcare.

Acknowledgements

About the author

Dr. Prasun K. Mukherjee, Scientific Officer G, Bhabha Atomic Research Centre, Mumbai, is a Ph.D. (Plant Pathology) from G.B. Pant University of Agriculture and Technology, Pantnagar, which he earned as a Dr. K.S. Krishnan DAE Research Fellow. He has been working on *Trichoderma* for nearly three decades. He has made outstanding contributions in the field of practical application as well as high-end basic research on these beneficial fungi. He received the Homi Bhabha Science and Technology Award for his contribution in agricultural research. He is also a recipient of DAE Group Achievement Award (as a Group Leader) and VASVIK award. He has edited two books and is an Editor of two international journals. He is an elected fellow of the National Academy of Sciences, India (NASI) and the National Academy of Agricultural Sciences (NAAS). Currently Dr. Mukherjee is visiting Texas A&M University, USAL, as a Fulbright Scholar.

References

1. Mukherjee PK, Horwitz BA, Herrera-Estrella A, Schmoll M and Kenerley CM. 2013. *Trichoderma* research in the genome era. *Annu Rev Phytopathol* 51: 105-129.

2. Mukherjee PK, Horwitz, BA, Singh US, Mukherjee M, Schmoll M, Eds. 2013. *Trichoderma*- Biology and Applications. Commonwealth Agricultural Bureau International, UK.

3. Mukherjee PK, Horwitz BA and Kenerley CM. 2012. Secondary metabolism in *Trichoderma*- a genomic perspective. *Microbiology* 158: 35-45

4. Zeilinger, S. Gruber, S., Bansal, R. and Mukherjee P.K. 2016. Secondary metabolism in *Trichoderma* – Chemistry meets genomics. Fungal Biology Reviews 30: 74–90.

5. Druzhinina IS, Seidl-Seiboth V, Herrera-Estrella A, Horwitz BA, Kenerley CM, Monte E, Mukherjee PK, Zeilinger S, Grigoriev IV and Kubicek CP. 2011. *Trichoderma*: the genomics of opportunistic success. *Nature Reviews Microbiology* 9: 749-759.

6. Atanasova L., Druzhinina IS and Jaklitsch WM. 2013. Two hundred *Trichoderma* species recognized on the basis of molecular phylogeny. In: PK Mukherjee, BA Horwitz, US Singh, M Mukherjee, and M Schmoll Eds. *Trichoderma*: Biology and Applications, CABI, UK.

7. Kumar A, Scher K, Mukherjee M, Pardovitz-Kedmi E, Sible GV, Singh US, Kale SP, Mukherjee PK and Horwitz BA. 2010. Overlapping and distinct functions of two *Trichoderma virens* MAP kinases in cell-wall integrity, antagonistic properties and repression of conidiation. *Biochem Biophys Res Commun* 398:765-770.

8. Mukherjee M, Mukherjee PK and Kale SP. 2007. cAMP signalling is involved in growth, germination, mycoparasitism and secondary metabolism in *Trichoderma virens*. *Microbiology* 153:1734-1742.

9. Viterbo A, Harel M, Horwitz BA, Chet I and Mukherjee PK. 2005. *Trichoderma* mitogen-activated protein kinase signaling is involved in induction of plant systemic resistance. *Applied and Environmental Microbiology* 71: 6241-6246.

10. Martinez, D, Berka, RM, Henrissat, B, Saloheimo, M, Arvas, M, Baker, SE, Chapman J, Chertkov, O, et al. 2008. Genome sequencing and analysis of the biomass-degrading fungus *Trichoderma* reesei (syn. Hypocrea jecorina). Nature biotechnology, 26, p.553.

11. Le Crom, S., Schackwitz, W., Pennacchio, L., Magnuson, J.K., Culley, D.E., Collett, J.R., et al. 2009. Tracking the roots of cellulase hyperproduction by the fungus *Trichoderma reesei* using massively parallel DNA sequencing. Proceedings of the National Academy of Sciences, 106, 16151-16156.

12. Kubicek CP, Herrera-Estrella A, Seidl-Seiboth V, Martinez DA, Druzhinina IS, Thon M, Zeilinger S, Mukherjee PK, Mukherjee M et al. (2011). Comparative genome sequence analysis underscores mycoparasitism as the ancestral life style of *Trichoderma*. *Genome Biol* 12, no. 4: R40.

13. Mukherjee M, Horwitz BA, Sherkhane PD, Hadar R and Mukherjee PK (2006). A secondary metabolite biosynthesis cluster in *Trichoderma virens*: evidence from analysis of genes underexpressed in a mutant defective in morphogenesis and antibiotic production. *Curr Genet* 50:193-202.

14. Crutcher FK, Parich A, Schuhmacher R, Mukherjee PK, Zeilinger S, and Kenerley CM (2013). A putative terpene cyclase, vir4, is responsible for the biosynthesis of volatile terpene compounds in the biocontrol fungus *Trichoderma virens*. *Fungal Genet Biol* 56: 67-77.

15. Vargas WA, Mukherjee PK, Laughlin D, Wiest W, Moran-Diez ME and Kenerley CM (2014). Role of gliotoxin in the symbiotic and pathogenic interactions of *Trichoderma virens*. *Microbiol* 160: 2319-2330.

16. Schraf D., Brakhage AA and Mukherjee PK. 2016. Gliotoxin-bane or boon? Environmental Microbiology 18: 1096–1011.

17. Sherkhane PD, Bansal, R., Banerjee, K, Chatterjee, S., Oulkar, D., Jain P, Rosenfelder, L., Elgavish, S., Horwitz BA and Mukherjee PK. 2017. Genomics-driven discovery of the gliovirin biosynthesis gene cluster in the plant beneficial fungus *Trichoderma virens*. ChemistrySelect 2: 3347-3352.

18. Bansal R, Mukherjee PK. 2016. Identification of novel gene clusters for secondary metabolism in *Trichoderma* genomes. Microbiology 85: 185-190

19. Bansal R, Mukherjee PK. 2016. The terpenoid biosynthesis toolkit of *Trichoderma*. Natural Product Communications 11: 431-434.

20. Nicolás, C., Hermosa, R., Rubio, B., Mukherjee, P.K. and Monte, E. 2014. *Trichoderma* genes in plants for stress tolerance- status and prospects. Plant Science 228: 71-78.

21. Shah M, Mukherjee PK and Eapen S. 2010. Expression of a fungal endochitinase gene in transgenic tomato and tobacco results in enhanced tolerance to fungal pathogens. Physiology and Molecular Biology of Plants 16: 39-51 (Springer).

22. Kamble S, Mukherjee PK, Eapen S. 2016. Expression of an endochitinase gene from *Trichoderma virens* confers enhanced tolerance to *Alternaria* blight in transgenic *Brassica juncea* (L.) Czern and Coss lines. Physiology and Molecular Biology of Plants 22: 69-76.

23. Dixit P, Mukherjee PK, Sherkhane P, Kale SP, Eapen S. 2011. Enhanced tolerance and remediation of anthracene by transgenic tobacco plants expressing a fungal glutathione transferase gene. J Hazardous Materials 192: 270-276.

24. Dixit P, Mukherjee PK, Ramachandran V and Eapen S. 2011. Glutathione transferase from *Trichoderma virens* enhances cadmium tolerance without enhancing its accumulation in transgenic *Nicotiana tabacum*. PLoS One: 6(1): e16360. doi: 10.1371/journal.pone.0016360.

Technology Developments in Reprocessing Facilities

Kailash Agarwal
Associate Director, Nuclear Recycle Group

Nuclear technologies are used for generation of electricity and for production of a wide range of radionuclides for use in research & development, healthcare and industry. One of the special features of nuclear industry is that it uses nuclear fission as source of energy. As a result, a large amount of energy is available from relatively small amount of fuel. At the end of energy extraction of fuel, the spent fuel also contains many valuable fissile as well as radio-isotopes which have many applications as fuel for energy and other societal benefits. While most of the countries in the world perceive this spent fuel as 'waste', in India, this is treated as a value resource. India has adopted 'closed fuel cycle', where spent fuel is reprocessed for extracting and recycling back the nuclear materials. Reprocessing of spent fuel plays a key role in sustaining the three stage Indian Nuclear Power Programme for optimal utilization of Uranium as well as Thorium resources. Reprocessing operation yields Plutonium, whose utilization forms a vital bridge between our transitions from relatively scarce uranium resource to the use of abundantly available thorium in our nuclear power programme. Since five decades, the development and advancement in reprocessing flow sheet have been done to standardize the flow sheet and to attain the larger capacity reprocessing facilities. However, the developments in head end systems of reprocessing plants have always been the thrust area to attain automation and remote handling operation of head end systems, to minimize the manual intervention to reduce the personnel radiation exposure associated with operation as well as maintenance, to improve processing capacity etc. This paper highlights various developments and innovations carried out in reprocessing plant in last 7 to 8 years.

Direct Fuel Transfer System (DTFS):
The present existing conventional system employed for fuel handling and charging system will not be sufficient to meet the high through put reprocessing plant. Hence the necessity for development of underwater Direct Fuel Transfer System is essential to achieve the plant throughput capacity for a new reprocessing plant (INRP). A new concept of transfer of spent fuel from pool to spent fuel chopper directly has been designed and developed involving remote transfer of the spent fuel bundles from fuel pool to dissolver cell in an inclined trolley using automated system. This will have advantages in eliminating manual operations, saving man hours, eliminating dependency on skilled man power and minimizing man-rem consumption. The system is designed with built-in safety margin giving high service life, better redundancy, higher liability and modular construction with ease of operation and maintenance. This system is being employed for first time in reprocessing plant (INRP-1) to avoid handling of heavy cask and reduces cycle time resulting in improvement in the plant capacity. One such unit has been manufactured, installed at CTF Tarapur and tested for more than 15000 cycles with water and dummy fuel bundles including conducting remote maintenance trials. The system is ready for installation at INRP.
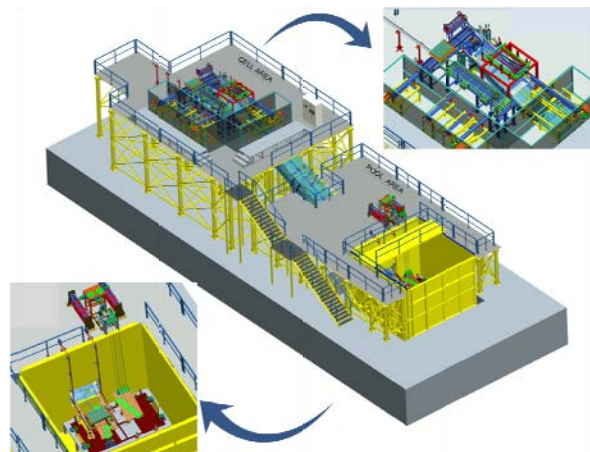
Fig.1: 3D model of DTFS
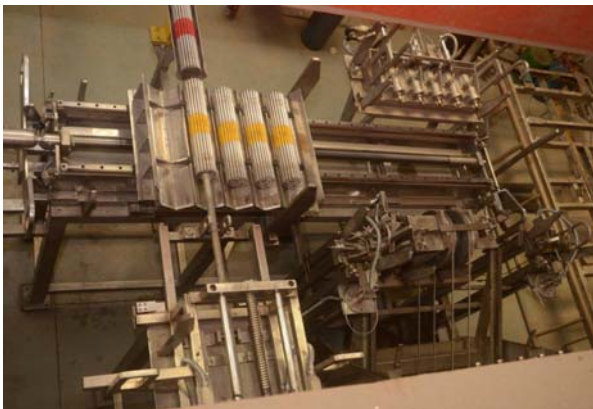
Fig. 2 Demonstration of DTFS

Fig 3A: Automated Charging Facility at P3A

Fig 3B: Automated Charging Facility at ROP

Development and Deployment of "Automated Spent Fuel Charging System for Reprocessing Plants":

In fuel reprocessing plants, fuel charging process involving pushing of fuel bundle into spent fuel chopper was manual operation and labour intensive. Introduction of automation in this step of fuel handling was required for reducing the operator fatigue, reducing the man-rem consumption and improving the productivity. The system integrates and automates all the operations of transfer port, charging dolly, charging cask door, automatic coupling and de-coupling of pusher rods, pushing of fuel bundles and retracement of all pushers. This system is first of it's kind in a reprocessing plant and required a multi-disciplinary work. The introduction of this system at KARP,PREFRE-2 and PREFRE-3A has improved the performance of the plants, has reduced dependence on skilled operators required for spent fuel charging and reduced the man-rem exposure. This machine has optimized the requirement of operators from six to just one and reduced man-rem exposure being a non-contact automatic operation. This system has successfully completed more than 6 to 8 years of operations at KARP and PREFRE-2. **The similar system has been designed for PP, Trombay and is under installation. This development is a major achievement for the head-end operations of a reprocessing plant which has benefitted the plant availabilityfor Head End operations.**

Innovations and improvements in Spent fuel chopper:

Spent Fuel Chopper (SFC) is the most critical equipment for a fuel reprocessing plant. The SFC, for TRP-2, Tarapur onwards, has been designed based on a novel concept of"Gang Chopping" which cuts 19 pins spent fuel bundle into multiple pieces in a single stroke. The SFC at existing reprocessing facilities PREFRE-1 and KARP has progressive type cutting features which is slow and time consuming. At initial stage, various teething problems surfaced and resulted in multiple shutdowns of plant. These problems were analyzed promptly and followed by providing feasible solutions in a time bound manner. The solutions were swiftly implemented without much affecting the plant operations. The major areas covered are as follows:

i. Design and implementation of a modified cutting tool assembly which induces lower peak stresses at critical locations to avoid premature failures during cutting operation. The modified shear tools are supported by advance features to discourage the accumulation of cut pieces into the inter-tool spaces, which was found to be the main reason for tool breakdowns in SFC of TRP-2, Tarapur. (Fig.4A)

ii. Improvements in shear module's design were also carried out. The modified shear module is maintenance friendly during assembly with SFC as well as during the manual contact maintenance. It comprises several features facilitating easy & remote dismantling and enabling saving of men-Rem expenditure during maintenance. (Fig. 4B)

iii. Design and implementation for a modified Component Transfer assembly (CTA) to ensure the positive transfer of spent fuel bundle from Fuel Feed Channel (FFC) to CTA tube.

iv. Implementations of removable type shear cavity cover and isolation gate for FFC to enable ease supervision & intervention in shear zone and avoidance of unwanted ingress of cut pieces respectively.
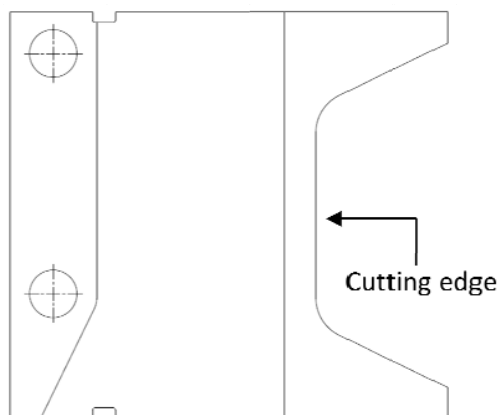
Fig: 4A
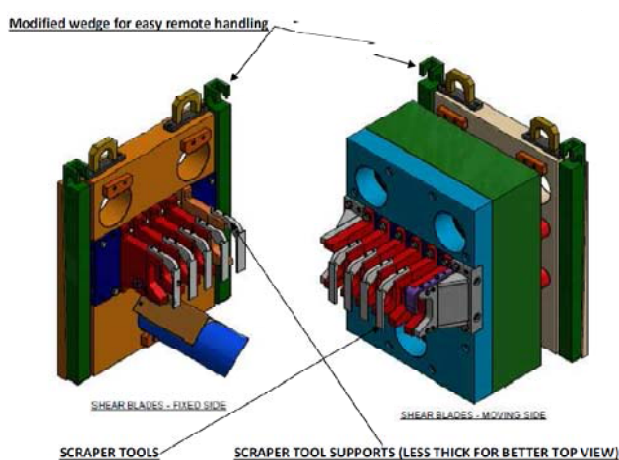
Fig: 4B

Development of Laser assisted fuel bundle dismantling and single pin chopping system:

The design & development of a S.F. chopping system assisted by laser dismantling was necessitated due to small size of hot cell which could not accommodate standard spent fuel chopper. The technology of the Laser dismantling of multi-pin bundle has been established to ensure segregation of even different fuel materials pins for future requirement. It includes customized equipment such as miniature power arm, CNC based positioning system for Nd-YAG laser head, trolley

for segregation of pins and the single pin chopping machine to chop the fuel pins. First time in reprocessing plant, Laser assisted fuel bundle dismantling and single pin chopping system has been successfully installed and operated at PRTRF, Trombay for reprocessing of irradiated thoria bundle at PHWR. The teething problems faced during commissioning phase were solved successfully.
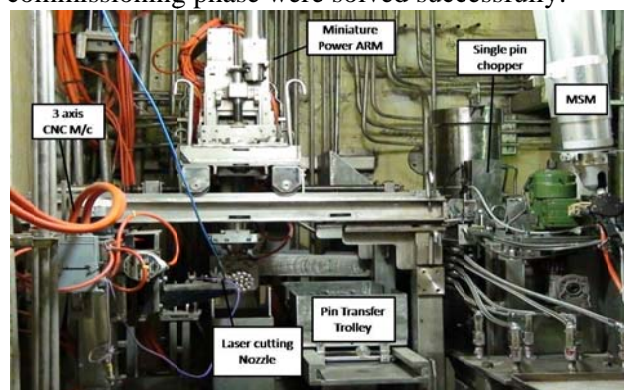
Fig. 5: Hot cell view of 'Laser assisted fuel bundle dismantling and single pin chopping system' at PRTRF, Trombay

Hull monitoring system:

The Special Nuclear Material Accounting (SNMA) is an important and necessary element of Quality Assurance in operations of a nuclear Recycle Plant. The total inventory of fissile materials present in hull waste is needed to assure criticality safety in the hulls during subsequent treatment& storage and also provides process control data on leach efficiency etc. The Hull monitoring is a key element for fissile material accountancy for the plant underinternational safeguard.Two techniques are available for Non Destructive Analysis(NDA) of fissile material in Hulls i.e passive technique and active interrogative technique. A technique, based on passive neutron counting of spontaneous neutrons from Pu 240 has been developed and deployed at PREFRE-2 for determining the fissile material quantity and is successfully being operated since last 4 years.The system has also been adopted in KARP and P3A, reprocessing plants of Kalpakkam for Hull monitoring.

The **Differential Die Away Technique** (DDA) based on active interrogation techniques has the advantage that it can detect very small quantities of fissile materials directly even in the presence of high neutron and gamma background and is much more sensitive compared to passive techniques which are
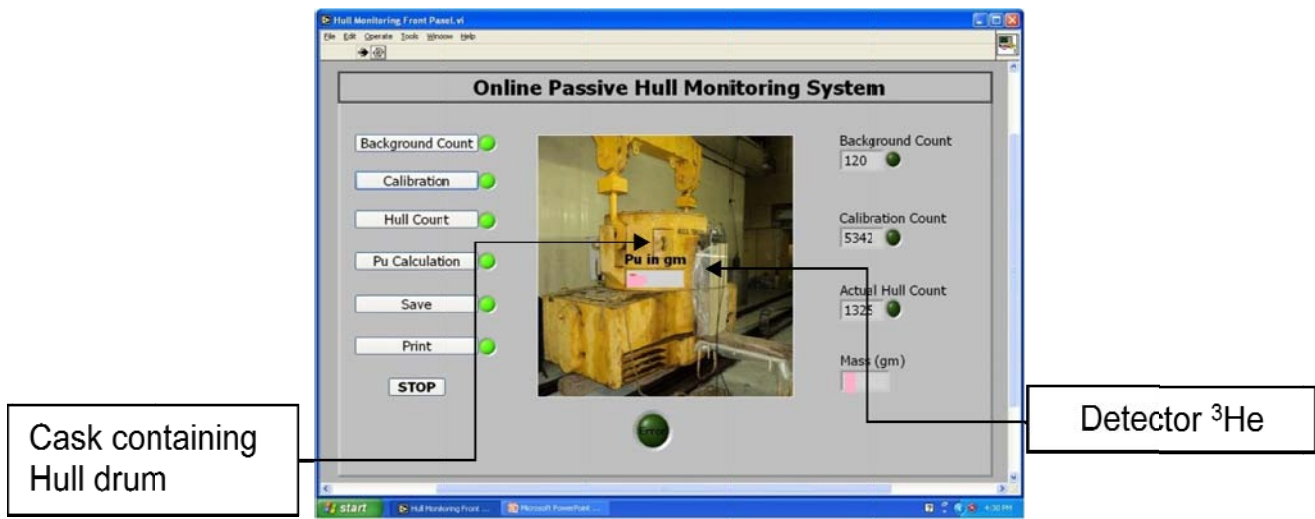
Fig 6 Hull Monitoring System, PREFRE 2, Tarapur

indirect measurement of fissile material with large error margins. Active neutron interrogation determines the total fissile content of the waste to be measured (comprising the fissile nuclides 235U, 239Pu and 241Pu) along with separate contribution of fissile material using delayed neutron analysis. For the DDA measurement 14MeV neutron pulses, generated by neutron generator are injected into a neutron moderating collar as the dissolver basket is rotated and lowered through the collar. After each pulse of neutrons, the fast neutron flux within the measurement cavity quickly dies away as the neutrons are thermalised, absorbed or escape. Any fissile material in the cavity slows the decay of the fast neutron flux as a result of neutron production from induced fissions. This allows a measure of fissile mass by counting the integrated fast neutron flux in the die away period. The major challenge was to design the mechanism for remote placement and movement of high active hull containing basket inside the DDA system. The mechanized device for hull monitoring system has been designed and developed for carrying out the measurement and verification of residual fissile material indissolver basket containing hull waste using DDA technique. Some of the trial experiments using spontaneous fission neutron from Pu^{240} have given encouraging results. This will be the first step towards achieving the goal for measurement of fissile material in the hull waste by setting up a demonstration facility of dissolver basket.

The new developed systems will be very useful for précised accountability of fissile material. The DDA techniques will be adopted in new plants like INRP1.
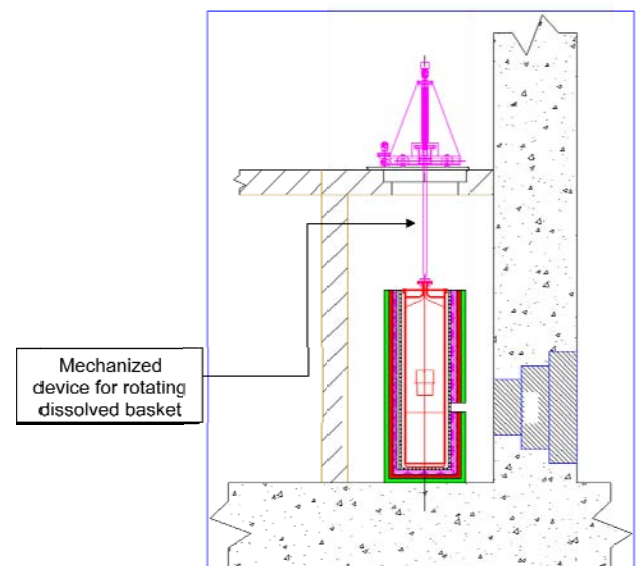
Fig .7: Mechanized device for rotating hull basket for monitoring using DDA techniques

Hull Compaction system:
After dissolution of spent fuel, the remaining hull contains some fraction of fission products and fissile material and needs to be managed as high level waste. First kind in India, a process of compaction of hull waste generated in reprocessing plants has been developed resulting in reduction of the solid High level waste volume.After completion of designs of 2000 Te Super Compactor with remote operation & maintenance features, fabrication and assembly of compactor system have been completed and the compactor system has been installed at CTF, Tarapur. Dummy trials are being carried out.

Operational feedback and improvements based on these trials would be made before usage in INRP. A volume reduction factor of about 5 can be achieved by this method.

Fig 8A: Hull Compactor at Tarapur
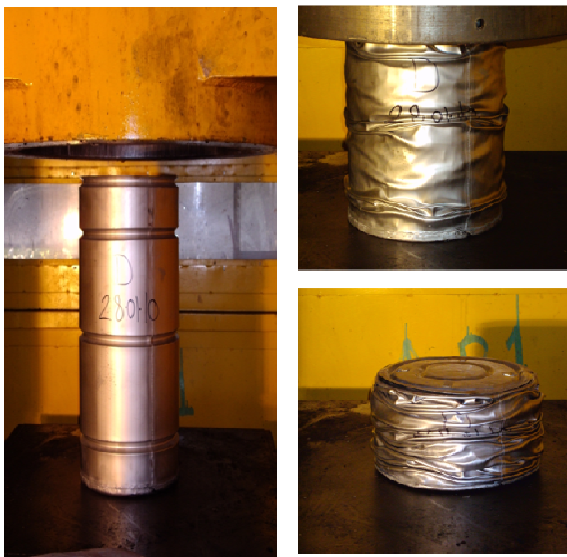
Fig 8B: Experimental work on Hull compaction

Linear Auto Sampler (LAS):

In conventional sampling system, there are several shortcoming i.e. time lag between decision to sample & actual sampling action, radiation exposure to operators, numbers of manual interventions resulting in human induced errors and requirement of skilled operators due to high dexterous activities involved in sampling. Linear Auto Sampler is intended to automate all the steps involved in conventional sampling and to address all the shortcomings. Linear auto sampler system can very well be integrated with existing pneumatic sampling bottle transfer system and thus enable potential of automation for whole sampling system at plant level. Positional interlocks are provided for safety and materials are compatible with process liquids. This system has given good performance at PRTRF, Trombay and is being replicated at INRP.

Fig. 9: Linear Auto Sampler

Continuous Rotary Dissolver:

Spent Fuel Dissolution is one of the important Head End operation of Reprocessing plant. Presently employed method of batch dissolution suits the requirement of plants of low and moderate capacity, however, for high through put plant with high burn up fuel continuous mode of dissolution is desirable due to higher specific dissolution capacity, automated operation including hull handling and uniform off gas generation etc. Hence to meet the requirement of future high throughput plants development of Continuous Dissolver has been initiated and is at progress in NRG.

The continuous dissolver being developed is based on concept of a bucket (perforated) wheel assembly (containing cut fuel pieces) indexing within a slab tank partially filled with nitric acid. The removable assembly consisting of drive components, rollers etc are amenable for remote handling for maintenance. The main drive is located outside the cell connected to equipment through wall penetration sleeve. The slab tank consisting of associated piping for solution transfer and instrumentation form the permanent part of hot cell.

A prototype equipment to meet the processing requirement of 400 teHM/Yr has been manufactured and installed in Engineering hall of CDCFT, Trombay. Mechanical loading trials, thermo hydraulic studies, mathematical modeling of dissolution in continuous mode based on batch dissolution trials and remote handling trials have been carried out.

Fig. 10: Continuous Rotary Dissolver

Hull rinser:

Future high through-put plants based on continuous process with automated head end process will require automated hull rinsing equipment. The equipment shall receive the hulls from continuous dissolver without disturbing the negative atmosphere, rinse it to remove any loose particulate sticking and discharge it into drum which can be sent for disposal. This will eliminate all the manual remote handling operation practiced in present operating plant.

A hull rinsing equipment was designed to meet the rinsing requirement by transfer of hulls through rinsing medium due to vibration created by vibratory motor. The equipment consisted of spiral flights about a central base cylinder and a pair of vibratory motors mounted in diametrically opposite on top of central base cylinder. The vibration caused by the motors mounted with 90 deg phase difference resulted in the transfer of hull through the spiral path in liquid medium, resulting in rinsing during transfer of hulls.

Considering these aspects an engineering scale prototype of hull rinser was designed, manufactured, tested with simulated hulls to match the processing capacity of Continuous Rotary Dissolver (Fig 11). The rinsing trials with simulated hulls yielded desired results in terms of rinsing time and effectiveness of cleaning. It was observed that hulls weighing 7.5 kg (corresponding to hulls of 5 numbers of 220 MW PHWR Spent fuel) would be rinsed in minimum time period. Multiple trials were carried to verify and establish the time period. This hull rinsing application is first of a kind developmental effort which has yielded desired

performance. The operation time, rinsing effectiveness and amenability to remote operation and maintenance makes it suitable for automation of head end operation for a large throughput plant.

Fig. 11: Hull Rinser

Centrifugal Clarifier:

Present mode of feed clarification is by means of vacuum assisted filtration using disposable filter elements. This system has a low filtration rate. It generates additional waste and requires extensive remote handling operation. The large reprocessing plants in operation elsewhere in world are reported to employ centrifugal clarifier for feed clarification in Head End Operation. Hence development of centrifugal clarifier for feed clarification application was taken-up jointly in coordination with MDD, BARC.

Based on the feed characteristics and process parameters available and initial trials with bowl and shaft assembly, an engineering scale prototype centrifugal clarifier amenable for remote operation and maintenance was designed, manufactured and installed (Fig 12). A test loop for carrying out the trials with necessary tanks and solution transfer system has also been erected in the engineering hall of CDCFT and trials were carried out with simulated feed. The centrifugal clarifier was able to separate particles of size greater than 2.5 microns from the actual feed at 1200 LPH when operated at a frequency of 50 Hz. At lower flow rates much better clarification was achieved. Further the prototype had a dirt holding capacity of approximately 20 batches of present 100 Te PHWR reprocessing plants, considering approximately 200 g fines are generated after processing of 1 Te. The self-cleaning system of the clarifier system also performed as desired. The

remote handling trials proved the amenability of the design for remote maintenance with available tools and tackles.

Fig. 12: Centrifugal Clarifier

Acknowledgement:

References:

1. Laser cutting for dismantling of PHWR fuel bundle- Dilip Kr, B.P. Badgujar, G.L Goswami-National welding Seminar, IIW-CAT Indore Jan-94 (1994)

2. Automated laser cutting system for disassembly of PHWR fuel bundle - A report on laser cutting trial - Sanjiv K. Jha AFD, BARC, Oct (1999)

3. Development of laser based disassembly and single shear system for reprocessing Thoria fuels-G.L. Goswami et al Proceedings symposium on Thoria Technology, Indian Nuclear Society, Mumbai, (2000)

4. Development of Hull Compaction System for Nuclear Recycle Facility; A.A. Manole, P.P. Karkhanis, Kailash Agarwal and Sekhar Basu; BARC Newsletter, Sep-Oct, 2013

5. Health Assessment of Existing Nuclear Fuel Cycle Facility: A Case Study Amit Varshney, Saha Dauji, Kapilesh Bhargava, Kailash Agarwal & Sekhar Basu, First International Conference on Structural Integrity (ICONS 2014).

6. Quantitative Determination of Plutonium in waste hull drums using passive Neutron Technique; T.C Kaushik, S.C. Andola, Satish C.Gupta, K. Agarwal, Raman Kumar, F.T. Quereshi and Sekhar Basu (A BARC Report BARC/2013/R/006)

7. Technological Innovations in Spent Fuel handling and their implementation for fuel reprocessing plants Kailash Agarwal; Founder's day special issue of BARC newsletter, Oct 2011

8. Innovations in Development of Head-End systems for Power Reactor Thoria Reprocessing Facility K.T. Badgujar, Raman Kumar, K. Agarwal. R.S. Soni and P.K.wattal National Conference on Power from Thorium: Present Status and future Directions, Dec 2014

9. Design Improvements in Spent Fuel Chopper at PREFRE-2, TarapurA.K.Jha, F.T.Quereshi and K.Agarwal, Founder's day special issue of BARC newsletter, Oct 2014

10. Management of spent fuel from PHWRs in India-An integrated approach, K. Agarwal & S. Basu IAEA Int conf on SFM June 15-19, 2015, IAEA, Vienna

11. Delayed Gamma Neutron & Photon Activation Analysis for Quantification of Shielded Fissile Materal P.M. Dighe, R. Verma, M. Vinod, A. Pathak, S.G. Thombare, L.P. Kamble, Raman Kumar, K.A. Datir, P.V. Bhatnagar, D. Das, K. Agarwal at Plutonium-75 , IGCAR, May, 2016

Dynamics of Novel Compounds

R. Mittal
Solid State Physics Division

We discuss lattice dynamical and inelastic neutron scattering studies on a variety of functional material to understand their anomalous thermodynamic properties. Our studies on negative thermal expansion (NTE) in variety of compounds provided understanding of the underlying mechanism. Specific anharmonic phonons have been identified that are responsible for NTE in terms of translation, rotation and distortion of atomic polyhedral units. Extensive studies on multiferroic and perovskite materials enable to identify the spin phonon coupling, structural distortions and their correlation to phonon instabilities, leading to phase transitions in these compounds. The studies on vibrational and thermodynamical properties of lithium-based superionic conductors provide a correlation between lithium diffusion and dynamical instability.

Introduction

The thermodynamical properties of materials like phase transition, thermal expansion, specific heat and many others are governed by the atomic dynamics in a solid. In crystalline solids, these motions are collective and coherent and forms travelling waves known as lattice vibrations. These vibrations are quantized in energy; the quantized vibrations are termed as "Phonons. To have a microscopic level understanding of solids, it is important to probe its structure and dynamics. Structure can be determined by various diffraction techniques while dynamics can be studied by inelastic scattering of light, X-rays or neutrons, etc.

Light scattering techniques can probe only long wavelength phonons hence give limited information, however inelastic neutron and X-ray scattering can probe the phonons of all wavelengths; hence provide the complete dynamical spectrum of the system. Experimental studies at high pressures and temperatures are often limited and accurate models for theoretical studies of various materials are of utmost importance. For this purpose, theoretical studies based on lattice dynamical methods are necessary for exploring the entire spectrum of thermal vibrations in crystals. The experimental data is used to validate the theoretical models. Once a model is validated successfully, this may further be used to predict the thermodynamic properties at various thermodynamical conditions. We have used the state of the art density functional theory methods to compute the total energy and forces, and hence the phonons in entire Brillouin zone for various compounds. To validate the theoretical results, the inelastic neutron scattering experiments have been performed. We have studied [1-21] variety of technologically important materials to understand the role of phonons in their functional properties like negative thermal expansion, super-ionic conduction, spin-phonon coupling and phase transitions in multiferroics etc. The motivation for studying the various compounds and significant results for some of our work is discussed below.

Negative Thermal Expansion Behaviour

The discovery of large negative thermal expansion (NTE) in ZrW_2O_8 over a very broad temperature range triggered a keen interest in the field [22-26]. The NTE behaviour was observed in several metal-oxide frameworks [25, 27, 28]. The observation of even larger NTE behavior in $Zn(CN)_2$ led to further impetus and discovery of NTE in a large number of

cyanide compounds[1, 29-34], e.g., $Cd(CN)_2$, $Ag_3Co(CN)_6$, $KMn[Ag(CN)_2]_3$ and MCN (M=Ag,Au,Cu). Usually materials contract in all directions under hydrostatic pressure; however, there exists a small number of materials known to expand along specific directions [23, 34-38].This unusual pressure behavior, known as negative linear compressibility (NLC), is remarkably rare but has potential applications in high-pressure environments, such as optical telecommunication lines, shock absorbers, and highly sensitive pressure detectors. Both NLC and NTE are practically relevant to pressure sensitive switches and temperature detectors for seismic, sonar and aircraft applications. $ZnAu_2(CN)_4$ is known to exhibit NTE and exceptionally large NLC simultaneously[23, 32]. The temperature dependence of the unit cell parameters of $ZnAu_2(CN)_4$ (space group $P6_222$) indicates[23, 32] that the thermal expansion is anisotropic and negative along the hexagonal c-axes($\alpha_a \sim 36.9 \times 10^{-6}$ K^{-1}, $\alpha_c \sim -57.6 \times 10^{-6}$ K^{-1}). The NLC along the c-axes at ambient pressure is reported to be~-42TPa^{-1}, which is much larger than any other compound showing NLC behavior[23]. The compound has a large positive linear compressibility (PLC) in a-b plane which compensates the NLC along the c-axes. The honeycomb structure of $ZnAu_2(CN)_4$ consists of polyhedral units and is believed to be responsible for its anomalous features. The compound also exhibits pressure driven structural phase transition at ~1.8GPa[23].

The measured inelastic neutron spectra[39] at various temperatures ranging from 150 K to 400 K as shown in Fig1. The spectra show sharp peaks at about 4,7, 12, 22, 25, 42, 50 and 70 meV. Modes between 20-30 meV are subject to a significant change in energy as a function of temperature, indicating the anharmonic nature of these modes. The measured spectra at 150 K and 225 K are shown only up to 55 meV due to the effect of the Bose-Einstein population factor affecting higher energy phonons when cooling down. The energy of the C-N stretching mode is about 280 meV, which is not captured in the present measurements, using a cold neutron spectrometer. Since thermal expansion and other thermodynamical properties are driven by low energy modes, the measured spectral range is quite appropriate.
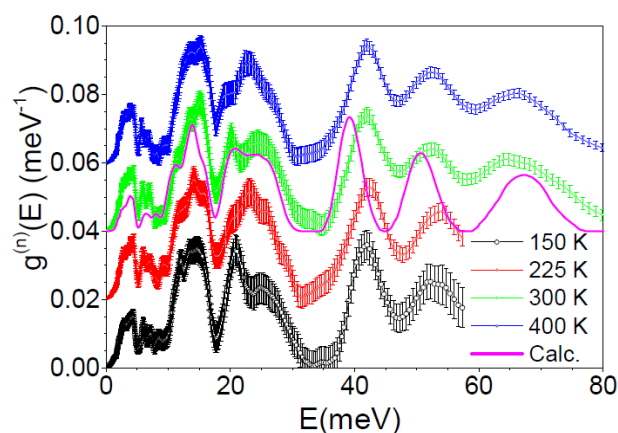
Fig. 1: The temperature-dependent inelastic neutron scattering spectra of the ambient pressure phase of $ZnAu_2(CN)_4$ along with the calculated neutron-weighted phonon spectrum.

The thermal expansion behaviour of a compound arises from anharmonic atomic vibrations. It is expected that some of the phonons contribute to NTE while others contribute to normal (positive) expansion of the material. The anomalous behaviour can be understood [39] by calculating the mode Grüneisen parameters and elastic compliance of the material [40]. We have calculated the anisotropic pressure dependence of phonon frequencies, and used it to derive the Grüneisen parameters, Γ_a and Γ_c, due to change in lattice parameters 'a' and 'c' respectively, as shown in Fig 2. The Grüneisen parameters show large negative values below 20 meV. The calculated linear thermal expansion coefficients at 300K are 44×10^{-6} K^{-1} and -55×10^{-6} K^{-1} along the a- and c-axes, respectively. The net volume thermal expansion coefficient is 33×10^{-6} K^{-1}. We have compared the experimentally measured [23, 32] fractional change in lattice parameters and volume with our calculated results as a function of
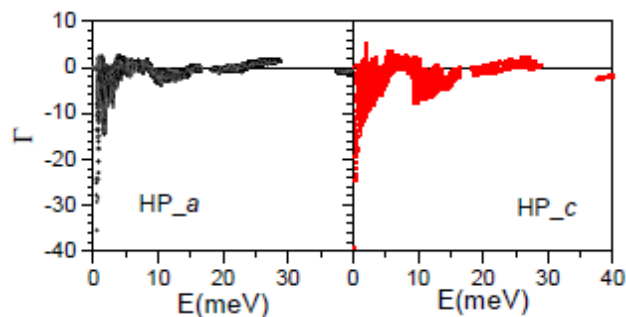
Fig. 2: The calculated Grüneisen parameters of $ZnAu_2(CN)_4$, Γ_a and Γ_c, averaged over the entire Brillouin zone on application of anisotropic pressure along a- (HP_a) and c-axes (HP_c), respectively.
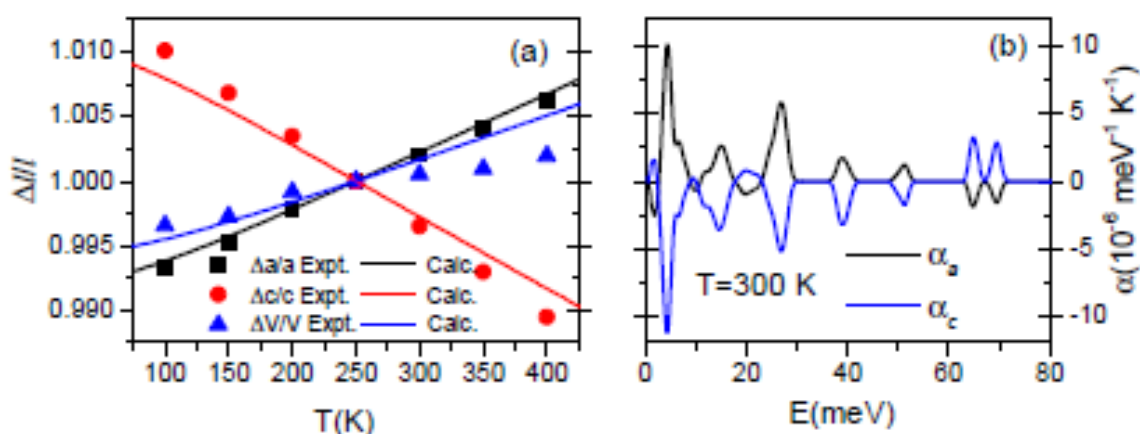
Fig. 3: (a) The calculated and measured[32] fractional change in lattice parameters and volume as a function of temperature, in the ambient pressure phase of $ZnAu_2(CN)_4$, and (b) the calculated contribution of various phonons of energy E to the linear thermal expansion along the a- and c-axes at 300 K.

Temperature (Fig 3(a)). We found that the calculated linear expansion along the *a*-axes is in a good agreement with the measurements; however, along the *c*-axes the calculations are slightly underestimated.

We have computed [39]the linear thermal expansion coefficient as a function of phonon energy at T=300 K (Fig 3(b)). It is interesting to see that modes which are contributing to the positive expansion in the *a-b* plane contribute to negative expansion along the *c*-axes. This unusual behaviour is attributed to large negative value of s_{13} (-0.057 GPa^{-1}) and hence related with NLC behaviour of the compound. It suggests that any change in *c*-axes would lead to change in the *a*-axes in opposite way. Hence as temperature increases the *c*-axes decreases and expands the *a*-axes. It is interesting to note that, although the anisotropic Grüneisen parameters are negative for compression along all the directions (Fig. 2), the combination of NLC and Grüneisen parameter leads to NTE (Fig. 3 (a)) only along the hexagonal-axis.

We find that the low energy modes dominated by dynamics of Au atoms play a major role in leading to anomalous behavior in thermal expansion. Analysis of the displacement pattern of these modes shows that all these modes involve perpendicular displacement of Au, C and N atoms to the -Zn-NC-Au-CN-Zn- linkage. The magnitude of this displacement is largest for Au in these modes. These kinds of anharmonic modes bend the -Zn-NC-Au-CN-Zn- linkage and contract the *c*-axes as well as expand the *a-b* plane.

Superionic Diffusion and Phonon Instability
The performance of energy storage devices depends crucially on the properties of their component materials. An excellent example of innovative materials science is the discovery of the rechargeable lithium battery. The materials research [5, 6, 18] based on computational methods now plays a vital role in characterizing and predicting the structures and properties of complex materials on the atomic scale. We have studied lithium based battery materials Li_2O, $LiAlSiO_4$ and $LiMPO_4$ (M=Fe, Mn). Here we present results obtained from our studies on $LiAlSiO_4$.
The compound β- eucryptite ($LiAlSiO_4$) is known to exhibit super-ionic conduction in the high temperature phase above 700 K. We have performed inelastic neutron scattering measurement and extensive molecular dynamics simulation studies to understand the mechanism of superionic conduction[18]. At high temperature, the anharmonic contributions are significantly large and broaden the phonon spectrum. The phonon spectra in energy range from 30 meV – 50 meV are highly contributed by Li dynamics. This region in the phonon spectra is highly broadened with increase in temperature, which can be seen from the experimental inelastic neutron scattering (Fig. 4) as well as calculated molecular dynamics phonon density of states. The mean square displacement (MSD) of various atoms has been calculated as a
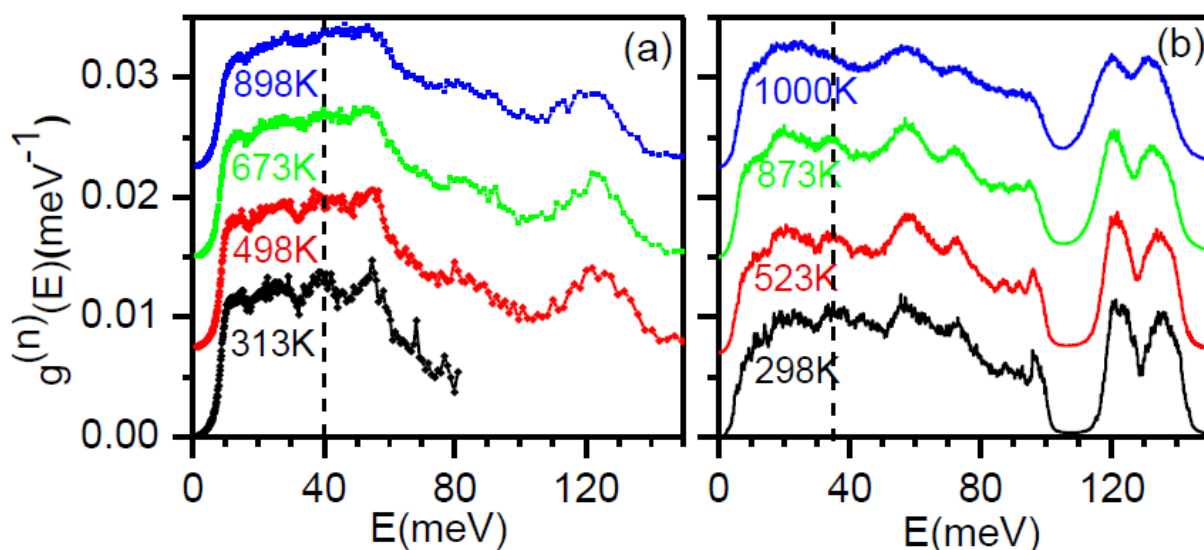
Fig. 4: Temperature dependent (a) experimental inelastic neutron scattering spectra, and (b) calculated neutron weighted spectra using MD simulations. For clarity, the spectra are shifted vertically. The peak corresponding to Li vibrations in the phonon spectra is highlighted by dotted line.

function of temperature. At high temperatures, the calculated MSD (Fig 5a) of Al, Si and O atoms saturate with time. However, for Li atoms it is found to increase with time, which is a clear signature of Li atom diffusion inside the crystal. We have calculated (Fig. 5(b) the diffusion coefficient at various temperatures for Li atoms from the slope of the mean square displacement as a function of time using the Einstein relation[41].
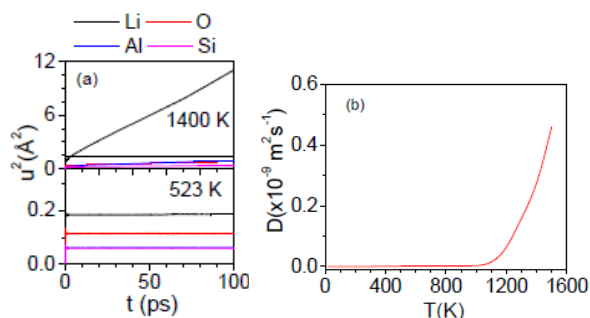
Fig. 5: (a) The calculated mean square displacement as a function of time for the different atoms of β-eucryptite. (b) The calculated diffusion coefficient as a function of temperature.

In order to understand the microscopic mechanism of superionic conduction phenomenon in β-eucryptite, the trajectories of Li atoms are analyzed at various temperatures up to 1400 K. We found that few Li atoms have high mean square displacements and show jump like behavior along the z direction (along the hexagonal c-axis) as compared to that

along the x- or y-axis (in the a-b plane). The diffusion process at 1400 K seems to be anisotropic. The analysis of pair correlation functions as a function of temperature indicates that the intrachannel correlated motion of lithium atoms along the hexagonal c-axis is the major process for Li conduction. This gives one dimensional superionic conduction along the hexagonal c-axis in β-eucryptite[18]. The work offers a fundamental microscopic framework with the perspective to improve the utilization of the studied material for practical applications.

Phonons and Phase transitions in Multiferroics and Perovskites

The interest in multiferroic materials continues for decades because of many attractive phenomena like structural phase transitions, magneto-electric coupling, magneto-elastic coupling charge and orbital ordering etc. We have studied [7-11] $GaFeO_3$ and $YMnO_3$ $PrMnO_3$, $CaMnO_3$ and $NaNbO_3$ to understand spin phonon coupling and phase transitions. Here we present summary of results obtained from our studies on multiferroic compounds $GaFeO_3$.

The compound $GaFeO_3$ belongs to the class of multiferroics and shows a magneto-electric coupling at low temperature. The orthorhombic structure [10, 42] of $GaFeO_3$ has eight formula units per unit-cell, with two different symmetry inequivalent sites of
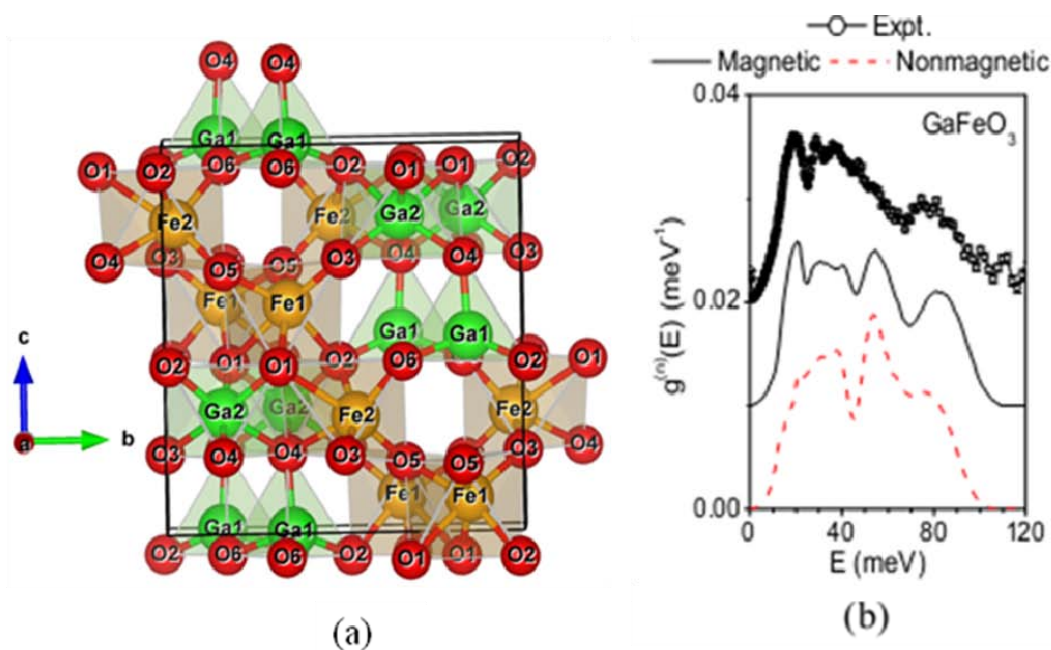
Fig. 6: (a) Crystal structure of GaFeO$_3$ in the Pc2$_1$n space group. (b) The calculated and experimental neutron inelastic scattering spectra of GaFeO$_3$. The experimental data consist of the "High Q" data collected at 315 K.

iron and gallium atoms; Fe1, Fe2, and Ga1 and Ga2, respectively. The tetrahedral sites are occupied by Ga1, while Ga2, Fe1 and Fe2 occupy all the octahedral sites (Fig. 6(a)). The electric polarization is found [42] to be along the b axis at ambient conditions. Anti-site disorder on the Fe and Ga sites [42] leads to a ferrimagnetic structure below 225 K [42]. We have performed a detailed analysis of lattice dynamics and spin phonon coupling in GaFeO$_3$. We have measured the phonon density of states over a wide temperature range 150-1198 K. We did not observe any anomalous change in spectra other than broadening of the spectra due to temperature. To investigate the material from microscopic scale we have computed the phonon spectrum from first principles density functional theory. The calculation is done in the ordered phase, by first considering the magnetic interactions and then neglecting them to better explore the possible interplay and effect of the spin degrees of freedom on the lattice dynamics.

In Fig. 6(b) we have compared the experimental and calculated phonon spectra[7]. The magnetic calculation shows a very good agreement with the experimental spectra. We notice some differences in the low energy part of the phonon spectra. The difference comes in fact from the value of the Fe magnetic moment in the two models. The main effect of the Fe spin degrees of freedom is to soften

the calculated phonon energies around 30 meV, bringing them closer to the experimental values. This demonstrates the role of magnetic interactions in GaFeO$_3$ and provides the signature of a spin-phonon coupling behavior in the compound.

The high pressure measurements [43], up to 70 GPa (increasing and decreasing cycles), revealed a very rich phase diagram of GaFeO$_3$. In order to understand the mechanism of phase transitions we have performed the ab-initio total energy calculation of different high pressure phase in various magnetic configurations. We found that the Pbnm phase is the most stable when adopting the G-type antiferromagnetic ordering, while the R3c phase stabilizes with the A-type antiferromagnetism. The calculated enthalpy difference in the various phases shows that the Pbnm phase is stable above 30 GPa (Fig. 7(a)) when comparing to Pc2$_1$n. The application of pressure leads to a change in the correlation between the electronic motions and affects the magnetic interaction. The pressure increase leads to a quenching of the Fe magnetic moment in the Pbnm phase at 36 GPa, resulting in an increase of the total energy and a sudden drop of the volume. We also find that the Fe magnetic moment is quenched in the R3c phase, when the pressure is raised to 45 GPa. A comparison of the experimental and calculated equation of state from calculations is shown in Fig. 7(b).
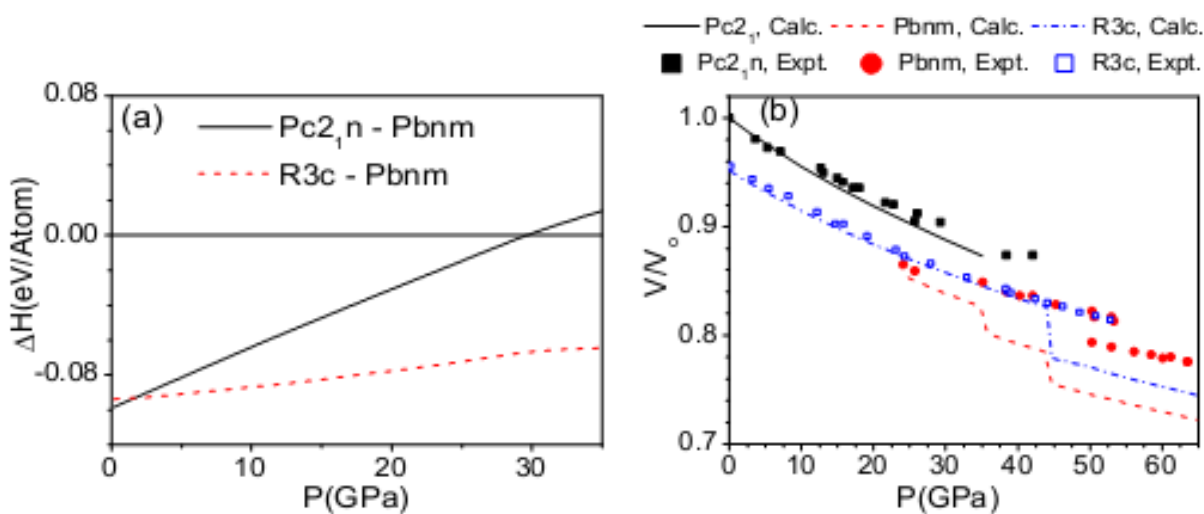
Fig. 7 (a) The calculated enthalpy difference in the $Pc2_1n$ and $R3c$ phases with respect to the $Pbnm$ phase of $GaFeO_3$ as a function of pressure. **(b)** The calculated equation of state of various phases of $GaFeO_3$ and a comparison with available experimental data [43]. V refers to the volume per formula unit at pressure P. V_o refers to the volume per formula unit of $Pc2_1n$ phase at ambient pressure.

Conclusions

We have studies a variety of functional materials using the techniques of lattice dynamics calculations and inelastic neutron scattering measurements to understand the thermodynamic properties of various compounds. We have successfully explained the role of phonons in various anomalous properties like thermal expansion, temperature- and pressure-driven phase transitions and super- ionic conductivity in various compounds.

References

1. M. K. Gupta, B. Singh, R. Mittal, S. Rols, and S. L. Chaplot, Physical Review B **93**, 134307 (2016).
2. M. K. Gupta, R. Mittal, S. L. Chaplot, and S. Rols, Journal of Applied Physics **115**, 093507 (2014).
3. M. K. Gupta, R. Mittal, and S. L. Chaplot, Physical Review B **88**, 014303 (2013).
4. M. K. Gupta, R. Mittal, S. Rols, and S. L. Chaplot, Physica B: Condensed Matter **407**, 2146 (2012).
5. M. K. Gupta, P. Goel, R. Mittal, N. Choudhury, and S. L. Chaplot, Physical Review B **85**, 184304 (2012).
6. P. Goel, M. K. Gupta, R. Mittal, S. Rols, S. J. Patwe, S. N. Achary, A. K. Tyagi, and S. L. Chaplot, Journal of Materials Chemistry A **2**, 14729 (2014).
7. M. K. Gupta, R. Mittal, M. Zbiri, R. Singh, S. Rols, H. Schober, and S. L. Chaplot, Physical Review B **90**, 134304 (2014).
8. M. K. Gupta, R. Mittal, M. Zbiri, N. Sharma, S. Rols, H. Schober, and S. L. Chaplot, Journal of Materials Chemistry C **3**, 11717 (2015).
9. S. K. Mishra, M. K. Gupta, R. Mittal, A. I. Kolesnikov, and S. L. Chaplot, Physical Review B **93**, 214306 (2016).
10. S. K. Mishra, M. K. Gupta, R. Mittal, M. Zbiri, S. Rols, H. Schober, and S. L. Chaplot, Physical Review B **89**, 184303 (2014).
11. S. K. Mishra, M. K. Gupta, R. Mittal, S. L. Chaplot, and T. Hansen, Applied Physics Letters **101**, 242907 (2012).
12. M. K. Gupta, R. Mittal, S. L. Chaplot, C. Tassel, H. Kageyama, K. Tomiyasu, and J. Taylor, Solid State Communications **241**, 43 (2016).
13. R. Mittal, M. K. Gupta, S. L. Chaplot, M. Zbiri, S. Rols, H. Schober, Y. Su, T. Brueckel, and T. Wolf, Physical Review B **87**, 184502 (2013).
14. P. P. Bose, M. K. Gupta, R. Mittal, S. Rols, S. N. Achary, A. K. Tyagi, and S. L. Chaplot, Physical Review B **84**, 094301 (2011).
15. T. Basak, M. N. Rao, M. K. Gupta, and S. L. Chaplot, Journal of Physics: Condensed Matter **24**, 115401 (2012).

16. P. Goel, M. K. Gupta, R. Mittal, S. Rols, S. N. Achary, A. K. Tyagi, and S. L. Chaplot, Physical Review B **91**, 094304 (2015).

17. N. P. Salke, M. K. Gupta, R. Rao, R. Mittal, J. Deng, and X. Xing, Journal of Applied Physics **117**, 235902 (2015).

18. B. Singh, M. K. Gupta, R. Mittal, M. Zbiri, S. Rols, S. J. Patwe, S. N. Achary, H. Schober, A. K. Tyagi, and S. L. Chaplot, Physical Chemistry Chemical Physics **19**, 15512 (2017).

19. A. M. Gopakumar, M. K. Gupta, R. Mittal, S. Rols, and S. L. Chaplot, Physical Chemistry Chemical Physics **19**, 12107 (2017).

20. B. Singh, M. K. Gupta, S. K. Mishra, R. Mittal, P. U. Sastry, S. Rols, and S. L. Chaplot, Physical Chemistry Chemical Physics **19**, 17967 (2017).

21. B. Singh, M. K. Gupta, R. Mittal, M. Zbiri, S. Rols, S. J. Patwe, S. N. Achary, H. Schober, A. K. Tyagi, and S. L. Chaplot, Journal of Applied Physics **121**, 085106 (2017).

22. W. Cao, Q. Huang, Y. Rong, Y. Wang, J. Deng, J. Chen, and X. Xing, Inorganic Chemistry Frontiers **3**, 856 (2016).

23. A. B. Cairns, J. Catafesta, C. Levelut, J. Rouquette, A. van der Lee, L. Peters, A. L. Thompson, V. Dmitriev, J. Haines, and A. L. Goodwin, Nat Mater **12**, 212 (2013).

24. V. Gava, A. L. Martinotto, and C. A. Perottoni, Physical Review Letters **109**, 195503 (2012).

25. T. A. Mary, J. S. O. Evans, T. Vogt, and A. W. Sleight, Science **272**, 90 (1996).

26. M. S. Senn, C. A. Murray, X. Luo, L. Wang, F.-T. Huang, S.-W. Cheong, A. Bombardi, C. Ablitt, A. A. Mostofi, and N. C. Bristowe, Journal of the American Chemical Society **138**, 5479 (2016).

27. R. L. Withers, J. S. O. Evans, J. Hanson, and A. W. Sleight, Journal of Solid State Chemistry **137**, 161 (1998).

28. Y. Yamamura, S. Ikeuchi, and K. Saito, Chemistry of Materials **21**, 3008 (2009).

29. K. W. Chapman, P. J. Chupas, and C. J. Kepert, Journal of the American Chemical Society **127**, 15630 (2005).

30. A. L. Goodwin, M. Calleja, M. J. Conterio, M. T. Dove, J. S. O. Evans, D. A. Keen, L. Peters, and M. G. Tucker, Science **319**, 794 (2008).

31. A. L. Goodwin, D. A. Keen, and M. G. Tucker, Proceedings of the National Academy of Sciences **105**, 18708 (2008).

32. A. L. Goodwin, B. J. Kennedy, and C. J. Kepert, Journal of the American Chemical Society **131**, 6334 (2009).

33. S. J. Hibble, B. Wood Glenn, J. Bilbé Edward, H. Pohl Alexander, G. Tucker Matthew, C. Hannon Alex, and M. Chippindale Ann, Zeitschrift für Kristallographie **225**, 457 (2010).

34. A. B. Cairns, A. L. Thompson, M. G. Tucker, J. Haines, and A. L. Goodwin, Journal of the American Chemical Society **134**, 4454 (2012).

35. J. W. E. Mariathasan, L. W. Finger, and R. M. Hazen, Acta Crystallographica Section B **41**, 179 (1985).

36. J. Haines, C. Chateau, J. M. Léger, C. Bogicevic, S. Hull, D. D. Klug, and J. S. Tse, Physical Review Letters **91**, 015503 (2003).

37. D. R. McCann, L. Cartz, R. E. Schmunk, and Y. D. Harker, Journal of Applied Physics **43**, 1432 (1972).

38. A. D. Fortes, E. Suard, and K. S. Knight, Science **331**, 742 (2011).

39. M. K. Gupta, B. Singh, R. Mittal, M. Zbiri, A. B. Cairns, A. L. Goodwin, H. Schober, and S. L. Chaplot, arXiv:1705.10215 (2017).

40. H. Zhou, M. Li, D. Li, J. Zhang, and X. Chen, Science China Chemistry **57**, 365 (2014).

41. H. Mehrer, *Diffusion in solids: fundamentals, methods, materials, diffusion-controlled processes* (Springer Science & Business Media, 2007).

42. T. Arima, D. Higashiyama, Y. Kaneko, J. P. He, T. Goto, S. Miyasaka, T. Kimura, K. Oikawa, T. Kamiyama, R. Kumai, and Y. Tokura, Physical Review B **70**, 064426 (2004).

43. R. Arielly, W. M. Xu, E. Greenberg, G. K. Rozenberg, M. P. Pasternak, G. Garbarino, S. Clark, and R. Jeanloz, Physical Review B **84**, 094109 (2011).

Design & development of Application Specific Integrated Circuits (ASICs) for High Energy Physics Experiment instrumentation

Menka Sukhwani, V B Chandratre and Sourav Mukhopadhyay
Bhabha Atomic Research Centre, Trombay
Megha Thomas
Electronics Corporation of India Ltd., Mumbai

Abstract: The contemporary High-Energy Physics experiments deploy variety of detectors, having high density readout channels for precise measurement of various experimental parameters. In such scenario, low power, high packing density, integrated complex functionalities, large dynamic range, good linearity and high speed are formidable constraints on the design of frontend (FEE) and data acquisition (DAQ) electronics. The efforts have been made by Electronics Division, BARC to design & develop the full-custom Application Specific Integrated Circuit (ASIC) based FEE and DAQ electronics in 0.7 um CMOS, 0.35 um CMOS and 0.35 um SiGe BiCMOS processes in presence of these challenges and trade-offs. The recent ASICs developed in this direction are ANUSANSKAR, ANUSMRITI and ANUSPARSH ASIC chipset. This article discusses these ASIC design aspects, applications and field deployed results achieved so far.

Introduction:

In a nutshell, high energy physics experiments intent to study the elementary particles and their interactions to interrogate the validity of Standard Model of physics and to search the answers to questions such as the origin of mass, the preponderance of matter over antimatter in the Universe, the identity of "dark matter," study of physics of the Big Bang, and the microscopic structure of space-time.

The most direct experimental path for such studies uses colliding particles of the highest achievable energies and building high density detectors along with suitable electronics to capture their interaction pattern data. The experimental parameters to be measured here mainly involve particle shower/track reconstruction, Time-of-Flight or arrival time-tagging, energy spectrum with respect to a valid trigger. The detector setup for such diverse measurements thus involves a combination of high density solid-state detectors; multi-channel Scintillator-PMTs, drift tubes and large area detectors like Resistive Plate chambers (RPC). For

the corresponding frontend (FEE) and data acquisition (DAQ) electronics, two approaches are being followed. In the first approach, two separate detector frontend channels, slow and fast, are used. The slow channel is dedicated to precise energy spectrum measurement and fast channel is designed for accurate TOF or time-tagging measurements. In the modern HEP instrumentation the second approach is being followed where the detector output is directly digitized after pre-amplification (if required) and rest of the processing is done digitally in DAQ. The similar kind of instrumentation setup is also deployed in medical and industrial imaging applications.

The Electronics Division, BARC is involved in the design and development of ASIC based FEE and DAQ modules for different detector setups following both the above approaches. The latest developments involve ANUSPARSH ASIC based FEE for readout of ~3.6 million channels of glass RPC detector of Iron Calorimeter (ICAL) experiment of India based Neutrino Observatory (INO) and ANUSANSKAR ASIC based FEE for

prototype Si pixel detector of Forward Calorimeter (FoCAL) proposed for ALICE upgrade experiments. As additional requirements high-speed analog memory ASIC, ANUSMRITI is also designed to implement the digital pulse processing based detector readout schemes.

INO-ICAL RPC detector readout electronics: ANUSPARSH ASIC Chipset, a low power, high speed frontend electronics

The INO-ICAL is an indigenous experiment being setup to study the atmospheric neutrinos by detecting muons, generated in the weak interactions of atmospheric neutrinos with target iron plates. The setup uses 2m x 2m glass RPC as active detector operated in avalanche mode. The INO-ICAL detector setup has total ~ 3.6 million readout channels with characteristic impedance of ~ 39 Ω providing single ended output of complimentary polarities from X & Y pickup strips with sub-nanosecond rise time. The critical design constraints for the FEE ASIC therefore involved high gain, very low power consumption, sub-nanosecond response, input-impedance matched to detector characteristic impedance, compact size, single-ended but complimentary input polarities and multiplexed analog output on 50 Ω load. There are very few ASICs developed so far worldwide catering to such requirements of RPC detector. Indigenous design efforts have led to development of novel topologies catering to readout of such class

of detectors, cumulating in ANUSPARSH ASIC chipset. The design of ANUSPARSH FEE ASIC has evolved through three versions to optimize between constrains and design trade-offs.

The ANUSPARSH-I [1] & II [2] ASICs are based on octal amplifier-discriminator with parallel LVDS digital output and multiplexed analog output, designed and fabricated in 0.35 um CMOS process. They comprised Regulated Cascode (RGC) trans-impedance topology based pre-amplifier. The use of RGC trans-impedance pre-amplifier has enabled achieving high gain, high speed response and matched input impedance over wide frequency range with minimum power consumption in a CMOS technology. Its use for readout of RPC detector was reported for the first time in ANUSPARSH-I & II ASICs. In the ANUSPARSH-II ASIC, the design of first version was enhanced with DC bias & gain stability across channels, differential inputs and reduced power dynamically biased analog 50 Ω driver.

The ASICs were successfully interfaced with 1mx1m RPC detector at TIFR and NPD, BARC [3] and tested for stable noise rate, detector efficiency, timing spectrum and HV scan for efficiency plateau using in-house developed ANUPAL TDC ASIC based DAQ module [4]. The ANUSPARSH-II ASIC architecture, layout, achieved specifications and test results with RPC detector are shown in Fig.1.
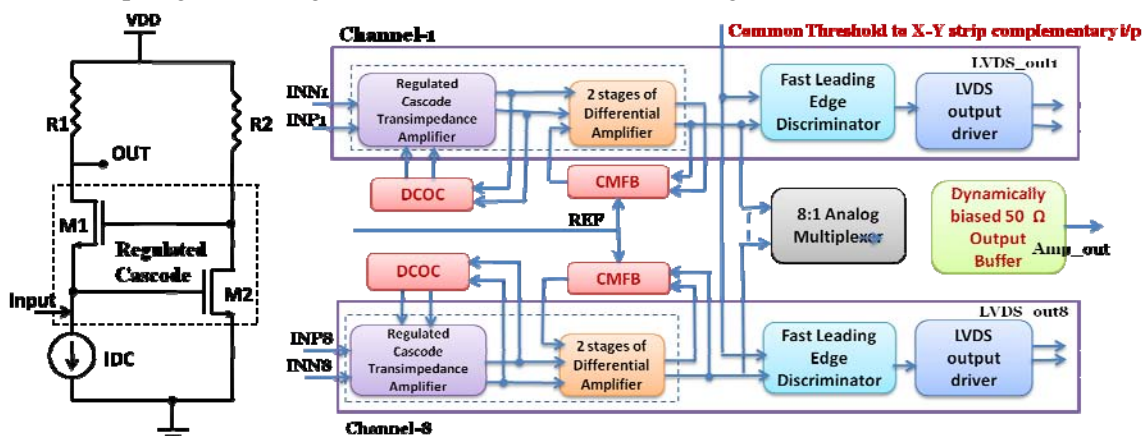
Fig. 1: ANUSPARSH-II ASIC architecture and simplified representation of RGC pre-amp

Tested Specification
- Channel Gain: 4 mV/uA
- Input Impedance @ 350MHz: ~ 50 Ω
- Linear Input dynamic range: +/- 100 uA
- LVDS output current: +/- 4 mA
- LVDS common mode voltage: 1.2 V
  (adjustable 0.8V to 1.6V)
- LVDS rise/fall time: ~ 700 ps on 100 Ω load
- Analog output rise time:
  ~ 1.2 ns on 100 Ω load for 1 ns i/p
- Power Supply: 3.3 V
- Power Consumption/Channel :
  without output buffer: ~ 38 mW
  with output buffer: ~ 40 mW
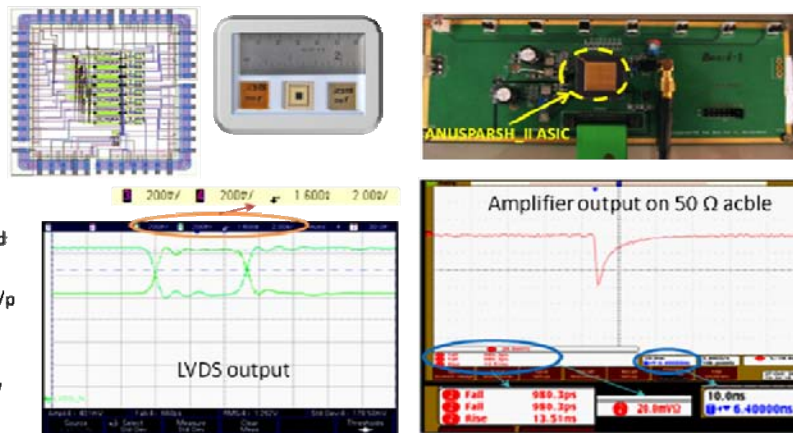
Fig. 2: Tested specifications, layout, packaged ASIC, FEE module and test results with RPC for ANUSPARSH-II ASIC
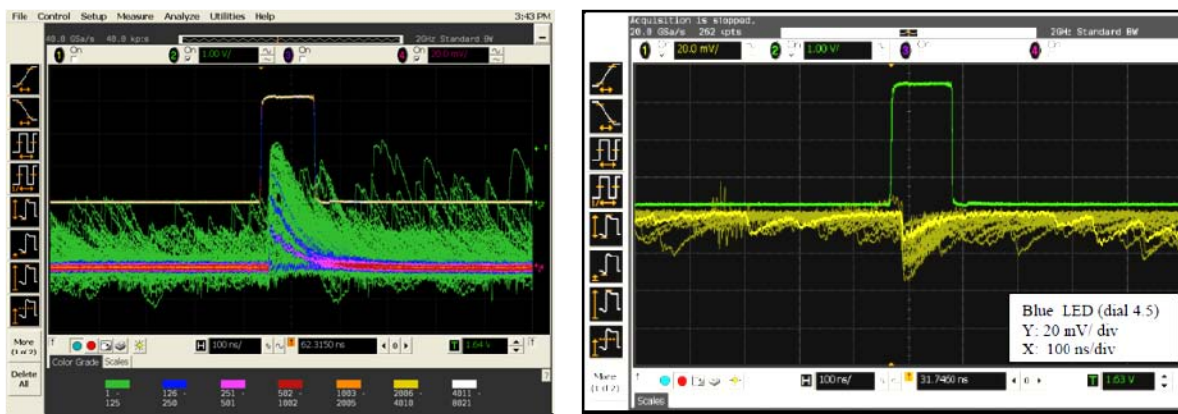
Fig. 3: Single and multi-photon response of ANUSPARSH-II ASIC with commercial MPPC and indigenous high gain photo sensor array

The versatility of the ANUSPARSH-II ASIC design was exhibited by successfully using it as FEE for in-house developed high gain photo-sensor array and commercial MPPC (Multi-photon Pixel Counters i.e SiPM) devices as shown in Fig.2 [5].

The ANUSPARSH-III ASIC was designed as a two-chip (chipset) solution of a quad amplifier with analog 50 Ω cable driver per channel and octal discriminator with LVDS driver and multiplexed daisy chained analog output in 0.35 um BiCMOS process. The two chip approach was chosen to ensure better system stability by isolating substrate coupling and regenerative feedback between amplifier and discriminator due to LVDS cable

mismatches and reflections. Further, the BiCMOS process based design has led to good reduction in power consumption besides achieving higher speed and higher gain requirements. The new BiCMOS design of dynamically biased analog buffer reduced the buffer power consumption to 1/8th as compared to the ANUSPARSH-II CMOS ASIC. This version of ASIC allows reading any strip analog signal and bringing it to the control room for monitoring or diagnostic by providing daisy readout support. This allows inaccessible detector strips buried deep in detector to be monitored as access to these signals is physically impossible. This is the unique and USP feature of the ASIC not found in its contemporary ASICs worldwide. The FEE modules
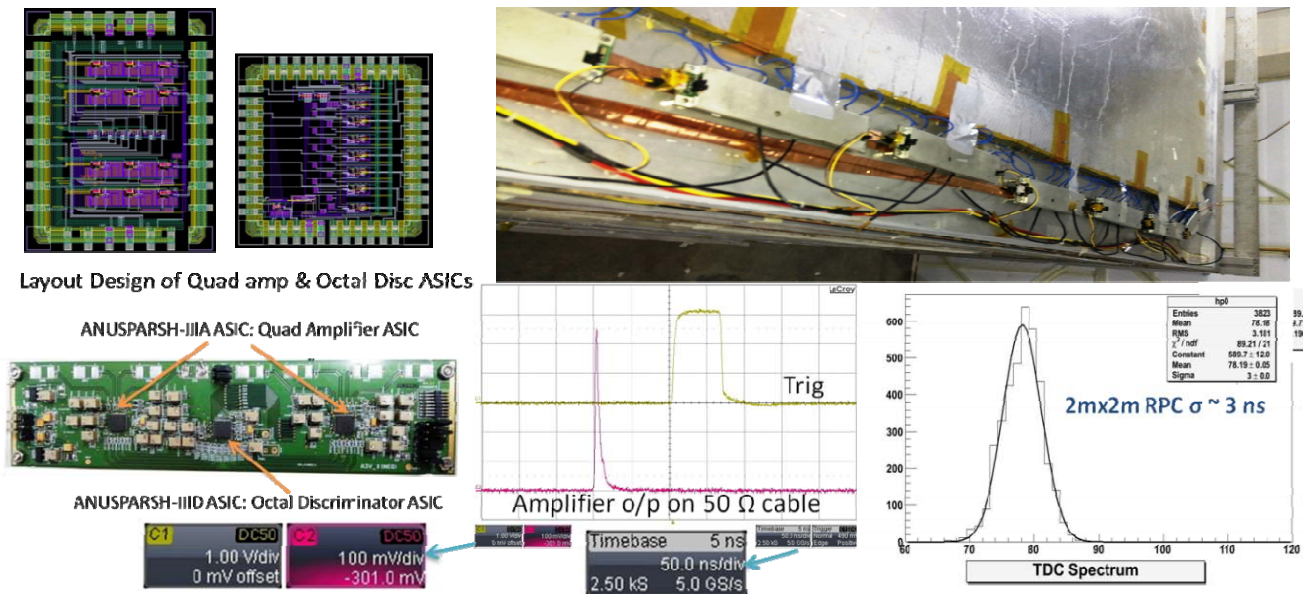
Figure 4 ANUSPARSH-III ASIC chipset layout design, FEE module PCB, shielded FEE module interfaced with 2mx2m RPC at Madurai, test results with RPC

based on ANUSPARSH-III ASIC chipset are successfully tested with 1mx1m and 2mx2m RPC detectors at TIFR, as shown in Fig. 4.

As an additional requirement of detector pulse profile analysis, a 128-bin, 500 MHz DLL based prototype switched capacitor analog waveform sampling analog memory ASIC ANUSMRITI was designed in 0.7 um CMOS process [6]. The test results in Fig. 5 illustrate the layout design of ANUSMRITI ASIC, storage of fast signal in 256 ns interval and subsequently readout in 128 µs.

ASICs for ALICE Upgrade: ANUSANSKAR ASIC, a sixteen channel pulse processing ASIC for Si-PAD detector:
Novel silicon tungsten based sampling type electromagnetic calorimeter, namely, FOCAL, has been proposed by India CERN Collaboration, as part of the ALICE upgrade at CERN, Geneva [7]. Prototype mini tower (four layers) and full length (twenty layers) FOCAL detector has been designed, developed and validated using indigenously developed silicon pixel detector and FEE ASICs ANUSANSKAR , MANAS (developed by VECC & SINP), ANUINDRA at PS and SPS beam line at
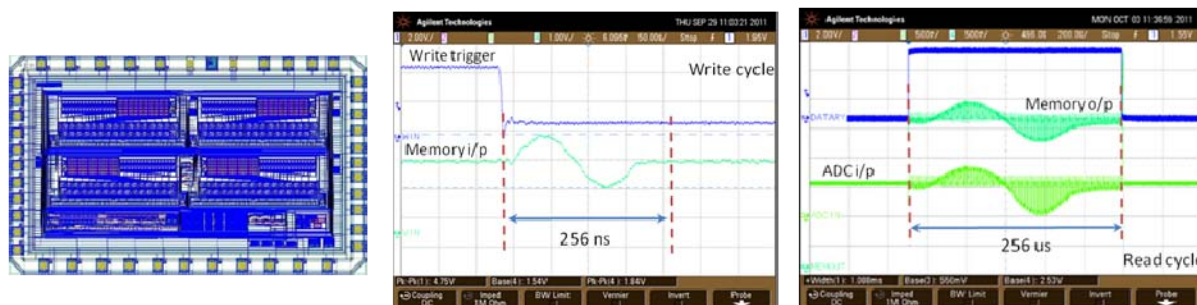
Fig. 5: ANUSMRITI ASIC layout design, Write and Read cycle test results
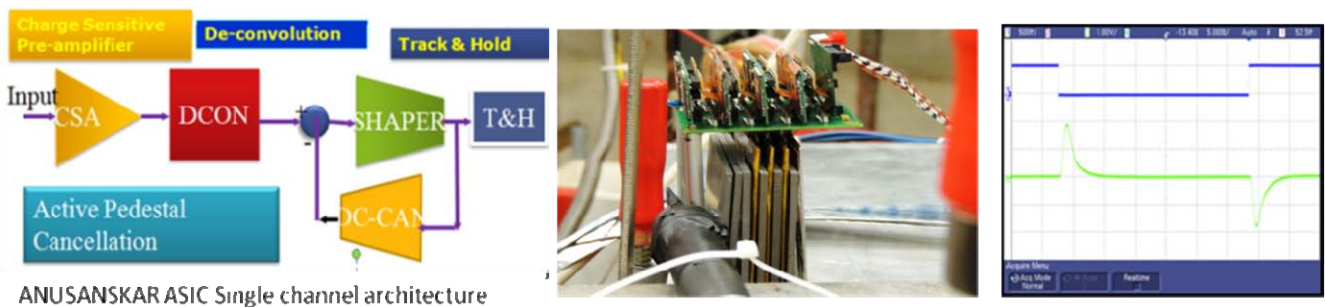
Fig. 6: ANUSANSKAR ASIC architecture, test setup with Si-pixel detector at CERN beam-line and test results

CERN. A 6x6 array of silicon pixel detector of 1 cm sq. individual pixel size, for the active layer of FOCAL, has been designed & developed by ED BARC and successfully fabricated at BEL, Bangalore. ASIC ANUSANSKAR [8] is designed and developed for readout of the prototype calorimeter in 0.7 um CMOS process as a 16-channel pulse processing ASIC, as shown in Fig. 6. It comprised charge sensitive amplifier (CSA), an optional g_m/C architecture based de-convolution filter, a Sallen-Key topology based fourth order semi Gaussian shaper (CR $-RC^4$) followed by a track & hold block. The key design constraints of FoCAL FEE are low noise to detect MIP (~ 4 fC) signal for tracking and large dynamic range ~ 3-4 pC for energy measurement. The ASIC provides parallel as well as multiplexed daisy chained output. The low noise performance is ensured by implementing the CSA feedback resistor by current conveyer topology.

Conclusion:
The critical requirements of frontend readout of various high density detector setups being used in modern HEP experiments could be efficiently met by ASIC based developments in latest technology nodes. In this direction, the ANUSPARSH ASIC chipset is designed as low power, high speed, and high gain frontend readout of ~ 3.6 million pickup channels of INO-ICAL RPC detector being operated in avalanche mode. The ASIC performance has been validated by the user, and now ready for low volume production. Similarly, ANUSANSKAR ASIC was designed as frontend of Si pixel detector based forward calorimeter of ALICE upgrade experiments. The ASIC was tested

in-field successfully in PS and SPS beam-line at CERN.

References:
1. Vinay Bhaskar Chandratre, Menka Sukhwani et. al.; "Regulated cascode preamplifier based frontend readout ASIC "ANUSPARSH" for Resistive Plate Chamber Detector", International Conference on VLSI, Communication, Advanced devices, Signals & systems And Networking, 2013 published by Springer for IEEE.
2. V.B.Chandratre, Menka Sukhwani, et.al; "ANUSPARSH-II frontend ASIC for avalanche mode of RPC detector using regulated cascode trans-impedance amplifier", Proceedings of the DAE-BRNS Symp. on Nucl. Phys. 60 (2015); pp 928-929.
3. V B Chandratre, Menka Sukhwani et.al; "Characterization of 1mx1m Glass RPC with

ANUSPARSH-II ASIC based Frontend & DAQ Electronics"; International Symposium on Nuclear Physics, pp-990, Vol 58, 2013.

4. K. Hari Prasad, et.al; "DAQ system for testing RPC front-end electronics of the INO experiment", DAE-BRNS Symp. on Nucl. Phys. 60 (2015); pp 916-917.

5. Sourav Mukhopadhyay, et.al; "Design and characterization of high gain photo sensors in standard CMOS process"; NSNI-2013, Nov 18-21, 2013, BARC Mumbai.

6. Menka Sukhwani, et.al; "500 MHz Delay Locked Loop based 128-bin, 256 ns deep Analog Memory ASIC "Anusmriti" Annual Symposium on VLSI-2011, IEEE Computer Society, Chennai, pp-72-77.

7. Sanjib Muhuri, et al; "Test and characterization of a prototype silicon-tungsten electromagnetic calorimeter", NIMA-764(2014)24–29.

8. Sourav Mukhopadhyay, et.al; "ANUSANSKAR: A 16 Channel Frontend Electronics (FEE) ASIC targeted for silicon Pixel array detector based prototype Alice FOCAL", National Symposium on Nuclear Instrumentation, 2013, BARC Mumbai.

Research and Development in Structural Integrity of Nuclear Components under Large Amplitude Cyclic Loads

Suneel K. Gupta
Reactor Safety Division
Vivek Bhasin
Nuclear Fuel Group

Abstract

The structural integrity assessment of the mechanical components is very essential for safe and reliable operation of nuclear power plants. The loads arising from a credible earthquake event are considered to design the Nuclear Power Plant components such as piping, vessels etc. Resent past has witnessed occurrence of many severe earthquake events with large numbers of significant pre and aftershocks. In view this, the adequacy of currently used assessment methodologies for structural integrity of nuclear components under large number of large magnitude reversing cyclic loads have been investigated. This has brought to limelight the gap/inadequacy of the existing design rules vis-à-vis the realistic failure modes under large magnitude reversing cyclic loads. Therefore, it is prudent to make/develop additional design provisions based on realistic failure mode to reliably assess structural safety of NPPs against extreme cyclic loads so that at least the basic safety functions for the NPPs are not impaired even under beyond design basis natural events (or extreme events).

Keeping above in mind, a large R&D programme was undertaken where over a period of time, about 70 number of pipes and elbows were tested under large cyclic loads anticipated during NPP operation and extreme events like severe earthquakes. The tests and analyses efforts has resulted in development of rational design criterion, simplified procedures / formulae for integrity assessment against Cyclic-Tearing and Ratcheting-Fatigue. These modes of failure are not explicitly addressed in the current design codes of nuclear components.

Keywords: Leak-Before-Break, Cyclic-Tearing, Ratcheting-Fatigue

Introduction

Defence in depth is the key design principle in nuclear reactor safety. The approach is to provide a series of philosophical and physical layers protection against the release of radioactivity to public. One of the aim of the first level of defence is to prevent failures of systems, structures and components (SSCs) of Nuclear Power Plants NPPs during the operational and postulated design basis accidents. This requires that the SSCs be robustly and conservatively designed, constructed, maintained using appropriate design codes, proven engineering practices, control over fabrication and in-service inspection etc. The SSCs are classified on the basis of their function and safety significance. They are designed/fabricated to achieve the quality and reliability in commensurate with their safety classification.

The primary heat transport piping system in the Nuclear Power Plant (NPP) carries high pressure coolant which removes the heat, produced in reactor core, during appropriate operational and accident conditions with the reactor coolant pressure boundary intact. Hence the primary piping system are of high safety significance and classified as class-1 components.

The primary components of Indian NPPs are designed to withstand a maximum credible earthquake event. The loading experienced by the nuclear components, during such design basis earthquake event, is one of the important and major load considered in the design. Here the pressurised primary piping system is subjected

high amplitude cyclic loads. In the current design philosophy/practices, these loads are considered in the *Leak-Before-Break (LBB) design* and *pressure boundary integrity assessment* of pressurized primary piping system of NPPs.

The current LBB [2-9] design assessment considers the earthquake as once applied non-cyclic load, which monotonically increases up to its maximum magnitude. The cyclic character of earthquake load and associated cyclic tearing failure mode (tearing-fatigue regime) are not explicitly considered while demonstrating stability of a through wall cracked pipe. However, it is known that the reversing cyclic load has deleterious effects on the fracture resistance of material [10-19].

The primary piping system pressure boundary undergoes high strain, low cycle fatigue conditions during severe earthquake. Here the pressurized piping may fail due to excessive accumulation of plastic strain by ratchet action along with ultra-low cycle fatigue damage. The present assessment methodologies intend to limit gross deformations and the average through thickness strain accumulations in SSCs during the design basis earthquake event. They do not account for the ratcheting-fatigue synergy while assessing the integrity under such loading conditions. The ratcheting-fatigue mode of failure has potential to cause breach in pressure boundary in limited numbers of large amplitude cycles.

In view of above facts, the adequacy of the currently used structural integrity assessment methodologies for above both mode of failures, that is, the LBB design and the primary pressure boundary integrity, have been investigated. In Indian NPP, one Safe Shutdown Earthquake (SSE) event (comprising of 10 cycles) and five Operating Basis Earthquake (OBE) events (comprising of 10 cycles per event) are considered in design. Same practice is followed in other NPP owner countries like USA, Japan etc. However, several recent earthquakes, such as, Tohoku Earthquake (Japan) of 11 March 2011, has shown that they are preceded and succeeded by large number of pre-shocks and aftershock cycles. In Tohoku Japan, the main earthquake duration was about 300 seconds, which is considerably greater than 60 seconds duration in typical earthquakes. During this earthquake, number of cycles (including aftershocks) was greater than 100 [1]. In general, it is difficult to pre-assess exact number of cycles during the design basis earthquake. This is owing to uncertainties associated in geological process. Hence, it is prudent to make/develop additional design provisions such that at least the basic safety functions for the NPPs are not impaired even under beyond design basis natural events (or extreme events).

Keeping this in mind, a large R&D programme was undertaken where large numbers of tests were conducted in two categories. The first category was 'Cyclic Tearing Investigations' where rigorous experimental work (about 50 tests on large size NPP pipes) were conducted on large size pipes of carbon steel (8", 12" & 16") and stainless steel (6" & 12") which are similar to those used in currently operating Indian reactors (PHWRs) other new reactors under design. The objective of the test programme was to evaluate the load capacities under displacement and load control extreme cyclic loading conditions (likely during severe earthquake event). Large number of tests on small size specimens also conducted to understand the material fracture behaviour under cyclic loading. This led to improved understanding of cyclic tearing failure behaviour of piping components (in presence of cracks) of Indian Nuclear Power Plants. The tests results directly led to development of a criteria and simple procedure for fracture stability / LBB assessment of NPP piping under extreme cyclic loading conditions. In the developed procedure reduction in fracture toughness / load carrying capacity and the number of cycles associated with severe earthquake loading is accounted in the failure criteria through a single parameter. None of the presently used codes/guides accounts for cyclic tearing failure mode in LBB assessment.

In second category, 'Ratcheting-Fatigue Investigation' were conducted on large size carbon steel and stainless steel pressurized pipes/elbows which are similar to those used in currently operating Indian reactors (PHWRs) other new reactors under design. These tests were conducted under reversing extreme cyclic loads as comes during a severe earthquake. These have resulted in development of crack initiation and cyclic plasticity models for realistic safety assessment under ratcheting-fatigue synergic conditions. The ratcheting-fatigue interactions causes drastic reduction in crack initiation life and also accelerate the growth of initiated crack resulting in through wall leakage in very few cycles. Such assessment was not possible by conventional procedures since they do not account for ratcheting-fatigue synergy. These developments also serve basis for arriving at optimized allowable seismic stresses in pressurized piping components.

The above tests/studies have helped in overall safety assessment of primary components of Indian reactors under extreme cyclic loading events. The outcome has provided important elements/methodologies for overall reactor safety assessment which were not adequately addressed in current design codes.

Cyclic Tearing Investigation: Leak-Before-Break Design for extreme cyclic loading

The "Leak-before-break (LBB)" concept is applied on the high energy primary coolant loop piping of nuclear power plant (NPP). The LBB approach through application of fatigue and fracture mechanics principles, demonstrates that the double-ended guillotine rupture or equivalent break of these piping is very unlikely. Implementation of LBB concept provides early warning before any major break in pressure boundary occurs; allows taking timely measures to prevent accident and keep the integrity of these piping intact, which in turn minimizes chances of radioactive material release inside the reactor building. The LBB demonstration therefore, serves as rational basis for robust and simple design. This in turn leads to reduced radiation exposure during operation and maintenance.

The presently available regulatory guides and documents on LBB, like USNRC LBB guide [2,3], IAEA-TECDOCs [4,5], Russian LBB guide [6], French RCC/MR A-16 LBB Guide [7], British R-6 method [8], German LBB practice [9] etc, considers the earthquake as once applied non-cyclic load, which monotonically increases up to its maximum magnitude during the fracture stability assessment of the leaking pipe. The cyclic character of earthquake load and associated cyclic tearing failure mode (tearing-fatigue regime) are not explicitly considered while demonstrating stability of a through wall cracked pipe. Code rules are silent on demonstration of fracture stability of a cracked pipe for a specified number of cycles of maximum load associated with an earthquake event which in turn requires consideration of the cyclic tearing failure mode. However, it is known that that the reversing cyclic load has deleterious effects on the fracture resistance of material [10-19]. Although some of them [2] have identified its importance, however, no suggestions have been made to account for the degradation during cyclic loading.

In past extensive experimental and analytical programmes, by International Piping Integrity Research Group (IPIRG, from 1986 - 1997),[10-15], and by Central Research Institute of Electric Power Industry (CRIEPI, from 1991-1997) Japan, [16-19], were undertaken to study/develop the fracture assessment under large reversing cyclic loads. These investigators have recognized the deleterious cyclic tearing damage under a cyclic loading event. However, they did not recommend any simplified rules, which could be directly implemented in fracture stability assessment for a specified number of cycles under cyclic loading event.

Various design codes like, American Society of Mechanical Engineers Boiler and Pressure Vessel (ASME B&PV) Code Section - XI (USA), RCC-M (France), DIN/KTA (Germany), and regulatory guides/techdocs of IAEA, USNRC etc., which deals with piping integrity assessment for LBB qualification or fitness for service demonstration, do not explicitly show that the recommended safety margins or procedures account for the potential fatigue-tearing damage in a seismic event and assure stability of cracked pipe for specified number of cycles. This may be due to un-availability of simple, reliable and easily implementable procedure to demonstrate the fracture stability of cracked pipes for specified number of cycles as required in the analysis.

All the current Leak-Before-Break (LBB) based design and fracture stability assessment method, considers the earthquake as once applied non-cyclic load, which monotonically increases up to its maximum magnitude. The cyclic character of earthquake load and associated cyclic tearing failure mode (tearing-fatigue regime) are not explicitly considered while demonstrating stability of a through wall cracked pipe.

In view of above and the fact that demonstration of the primary components integrity under the earthquake load is an essential / important element of NPPs safety analyses, a systematic, focused experimental programme [20-23] has been carried out to single out and quantify the deleterious effect of the cyclic character of applied load on stability assessment of a circumferential through wall cracked pipe.

Test details

The test program involved extensive number of cyclic tearing and corresponding monotonic fracture tests on large sized pipe components. Tests have been conducted on seamless pipes made from carbon steel (CS of SA-333 Gr.6) and austenitic stainless steel (SS of SA-312 Type 304LN) materials of primary piping of Indian Pressurized Heavy Water Reactors (PHWRs) and other new proposed reactors. The tests have been carried out

on two different base material (SSB and CSB) and three different girth weld configurations/combinations (CSW, SSW and NGW). The CSW and SSW are CS and SS weld using Shielded Metal Arc Welding (SMAW) with conventional groove while the NGW is SS weld obtained using Gas Tungsten Arc Welding (GTAW) with narrow Groove. The pipes specimens named as CSB, CSW, SSB, SSW and NGW, are regarded as five material categories and covered reasonable variation in fracture toughness. Monotonic fracture tests, corresponding to each cyclic tearing tests have also been conducted to obtain the base line data. The pipe sizes were considered are for SS (6" & 12") and for CS (8", 12" & 16"). Fig. 1 shows the schematic and photograph of the four point bend test setup for cyclic loading. These tests covered reasonable variation in pipe size, crack size, crack location, load history, loading control type, weld techniques and nuclear piping material etc. The piping system is subjected to mixture of load controlled and displacement controlled conditions. Therefore, the cyclic fracture tests were done under both the pure load controlled, Fig.2(b), as well as pure displacement controlled, Fig.2(a), loading conditions.
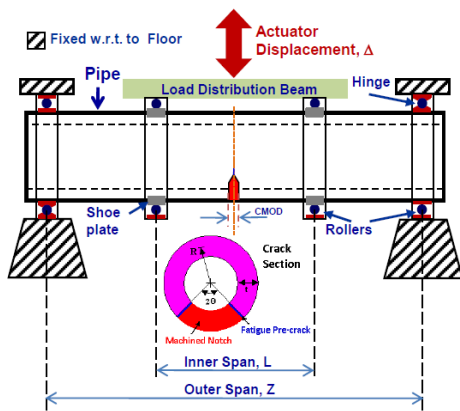
Fig. 1: Cyclic Tearing Tests- Four Point Bend Loading Setup

Test results

Fig.3 shows Moment (M) – rotation, history plots for four different tests namely SP-6-60-M-SSW (monotonic fracture test on SSW pipe), SP-6-60-M-NGW (monotonic fracture test on NGW pipe), QCSP-6-60-D1-SSW (incremental displacement controlled cyclic tearing test on SSW pipe) and QCSP-6-60-L2-SSW (load controlled cyclic tearing test on SSW pipe). All these tests were conducted on 6″NB Sch.120 SS 304LN pipes having nearly same size of circumferential TWC at weld centre line.
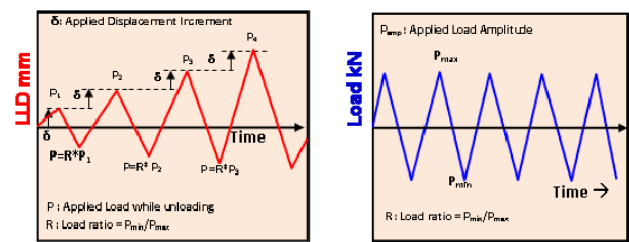
Fig.2: Schematic of the Loading Schemes (a) Incremental Displacement Controlled (b) Load Cycling
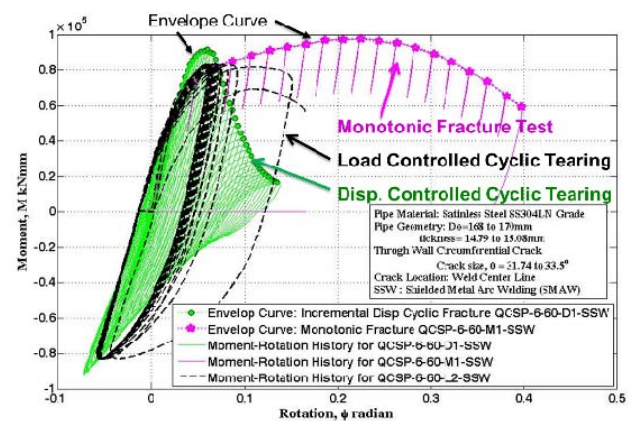
Fig.3: Typical Results under different loading conditions tests on identical pipe

The displacement controlled cyclic tearing tests of all five material categories along with corresponding monotonic fracture tests on identical pipes, have been analysed. The displacement controlled cyclic loading tests shown very high tearing crack growth leading to double ended guillotine break under step wise build-up of cyclic displacement loading. The relative comparisons of the pipe fracture behaviour, obtained from cyclic displacement and corresponding monotonic fracture tests, have shown significant decrease in fracture resistance under cyclic loading conditions in all five material categories tests.

The load controlled cyclic tearing tests have been conducted to assess the pipe crack growth and

fracture stability behaviour during an earthquake event and they in general are treated as load controlled and of fully reversing cyclic in nature. They revealed that the pipe may fail by unstable tearing in very few cycles under fully reversible load with a magnitude much below the monotonic capacity of pipe. The unstable failure of pipe was preceded by large crack growth. The crack growth and number of cycles before unstable failure are found correlated with applied loading. Larger compressive load in reverse direction (that is when larger negative load ratio) caused cyclic damage and resulted in accelerated crack growth.

Development of Cyclic Tearing Failure Assessment Diagram and New Design criteria for LBB

The load-controlled cyclic tearing test results were analysed to assess the importance of inclusion of load cycles as one of the parameters in fracture integrity assessment. The load controlled tests on carbon steel and stainless steel pipes (both base and weld) were investigated in relation to the corresponding monotonic fracture experiments. For each of the fully reversing load controlled cyclic tearing tests, a load reduction factor β was evaluated. The load reduction factor β is defined as ratio of magnitude of bending moment applied cyclically to bending moment capacity under monotonic loading condition, see equation given below:

$$\beta = \frac{Maximum\ Load\ In\ cyclic-tearing\ test}{Capcity\ Load\ under\ monotonic\ fracture\ test} \qquad (1)$$

The definition of β is based on monotonic capacity because in current pipe integrity assessment engineers adopt failure assuming monotonic load as basis of evaluation.

A Cyclic Tearing Failure Assessment Diagram (CTFAD) is developed where β-factors obtained for each cyclic tearing test is plotted with the number of cycles to failure, as shown in Fig.4. A lower bound CTFAD curve equation (β_L) is proposed for fracture stability assessment under cyclic loading. The β_L factor usage enables the existing procedures of stability assessment to demonstrate the integrity for specified number of load cycles. Based on the lower bound CTFAD curve, a criteria for fracture stability assessment under cyclic loading is proposed as given below:

Capacity Load (for N cycles) :β_L(N) * Montonic Capacity (2)

Here the β_L is evaluated from lower bound CTFAD curve, Fig.4, for a given number of cycles and equivalent maximum moment magnitude 'M_{Max}' of the cyclic loading event. The 'M_{Crit}' is the ultimate failure load/moment under monotonically increasing loading condition which may be evaluated experimentally or using any of the well documented existing practices or procedures. The Eqn. (2) enables the existing practices or procedures of stability assessment, to demonstrate the integrity for specified number of load cycles. To account for earthquake loading condition, the currently used of LBB qualification equations, have been modified with suitable β_L factor applied on M_{Crit}. The proposed modified equations are as given below:

Margin of 2 on Critical Crack Size:
Loads (normal operation + earthquake) < β_L × Monotonic Capacity for twice leakage size crack (3)

Margin of $\sqrt{2}$ on Loads:
Loads (normal operation + earthquake) × $\sqrt{2}$ < β_L ×Monotonic Capacity for leakage size crack (4)

The safety factor of 2 on crack and $\sqrt{2}$ on the Loads are current regulatory requirements intended to account for uncertainties in material properties, monotonic fracture evaluation procedures and specified loadings. The above LBB qualification equations may be used to demonstrate the stability for specified number of load cycles by suitability choosing β_L value.

Based on lower bound CTFAD, load reduction factors are proposed for different number of load cycles associated with different levels of earthquakes. For earthquake event without any significant aftershocks the β_L has to be at least 0.85 (that is. corresponding to 10 cycles). For the case of large duration earthquake event or earthquake with moderate number of aftershock cycles, value of β_L equal to 3/4 (=0.75) seems to be reasonable choice. However, if stability is to be demonstrated for large number of cycles, as in case of severe earthquake followed by large number of aftershock cycles β_L can equal to 2/3 (=0.67) is suggested. As can be seen in Fig.4 that beyond 75 cycles the rate of reduction of β_L with cycles is very small and hence its value beyond 150 cycles may not change appreciably with further increase in number of cycles.
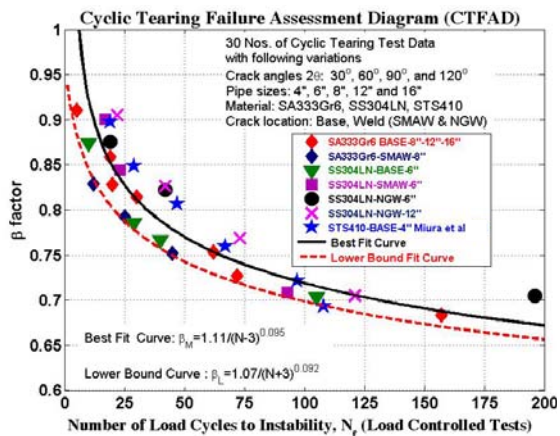
Fig.4: Cyclic Tearing Failure Assessment Diagram (CTFAD) developed from load controlled tests
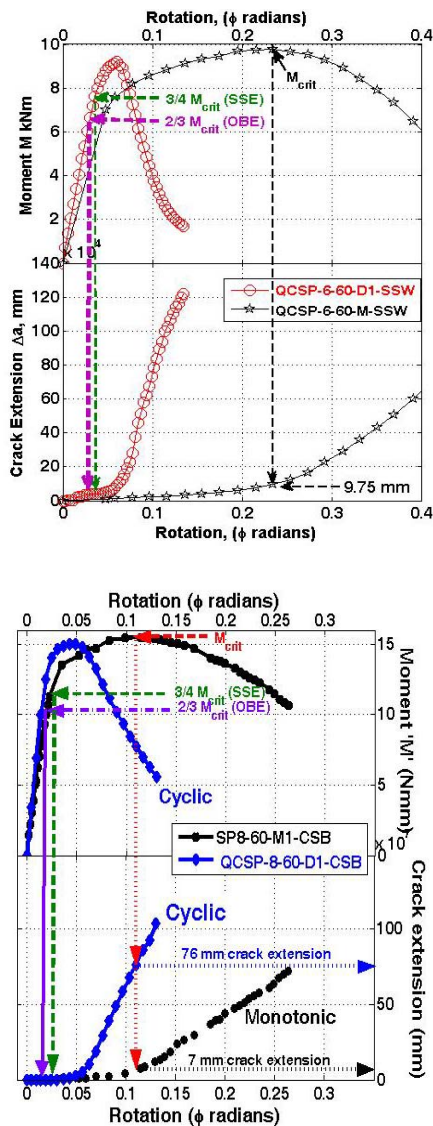
Fig. 5: Moment versus rotation and crack versus rotation plots for displacement controlled cyclic-tearing/monotonic tests

The displacement controlled cyclic deformations associated with an earthquake event, may lead to significantly higher crack tearing growth as compared to that in corresponding fracture tests under monotonic loading conditions. This is also highlighted in moment versus rotation and crack versus rotation plots, Fig. 5, of typical displacement controlled tests on carbon steel and stainless steel pipes. Hence the safety factor shall also guard against excessive tearing. The Fig. 5 also show that application of proposed β_L factor also ensures that under displacement controlled cyclic loading, the components will need significant cycles reach to maximum moment beyond which large tearing crack growth takes places. This fact shows that usage of suitable β_L factor ensures that excessive crack tearing growth is precluded.

Ratcheting-Fatigue Investigation: Pressure Boundary Integrity assessment under extreme cyclic loading

The primary coolant piping system in Nuclear Power Plant (NPP) carries high pressure coolant which removes heat from the reactor core and transfer it to secondary side fluid in the steam generator. The structural integrity of the primary coolant piping pressure boundary shall be demonstrated and shall possess adequate safety margin under loading arising from a severe earthquake event considered to design the NPP.

During such severe earthquake event, the primary piping system are subjected to large magnitude reversing cyclic loads. Here the pressurized piping may fail due to excessive accumulation of plastic strain by ratchet action along with ultra-low cycle fatigue (LCF) damage. The currently used code practices deal the ratcheting and the LCF damage independently. Moreover, the presently available cyclic plasticity models are inadequate to accurately assess the ratchet strain accumulation under complex loading conditions.

In view of above ratcheting-fatigue investigations, [24-25] were undertaken to assess the pressure boundary integrity of primary piping under the severe earthquake loading and to ensure the necessary margins against ratcheting failure. The ratcheting-fatigue studies were carried out on pressurized pipes and elbows made from carbon steel (CS) and austenitic stainless steel (SS). The elbows, among other piping components, exhibit highly strained regions in the piping system because of their high flexibility and are vulnerable to failure by ratcheting-fatigue. The tests were conducted

under different combinations of constant internal pressure and large amplitude quasi reversible cyclic displacement controlled loading.

Fig. 6 shows the picture of ratcheting fatigue tests setups for elbow and pipes.

In all these tests, significant accumulation of ratchet strain, that is, diametric growth (ballooning) of pressurized pipes/elbows, were observed over a number of applied cycles (see Fig. 7 for a typical CS elbow ratcheting test). The accumulation of hoop strain, i.e. ratcheting at crown location with number of loading cycles is shown in Figure-8. This clearly show that the ratcheting depends on both internal pressure and the amplitude of bending stress.

The ratcheting caused very early fatigue crack initiation (in some cases with in 30 cycles) in the component which finally grows rapidly to through thickness (in some cases within 60 to 80 cycles) leading to leakage (see

Fig. 6). In all the tests, the ballooning (that is, % increase in diameter) at time of failure was observed between 6 to 13.5%, the number of cycles to crack initiation, measured using ultrasound technique (test paused) and acoustic emission technique (online), was from 30-210. The number of cycles to final failure (that is when through wall crack occurred resulting into leakage) was from 62-625. Both the cycles to crack initiation and to failure, are found dependent on the internal-pressure and the amplitude of cyclic bending. The cyclic bending amplitude was varied from 0.9 to 2 times of Code Allowed (ASME B&PV Sec III Level D) while the internal pressure was varied from 0.9 to 1.4 times of Code Allowed (ASME B&PV Sec III). The local strain accumulation in 10 Cycles at crown location was observed as 1.7 to 8.0 %.
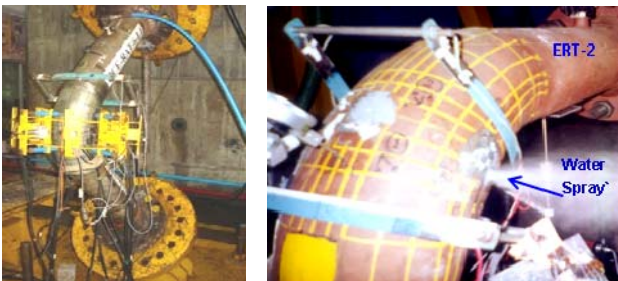
Fig. 6: Ratcheting Test pictures: SS Elbow (up), CS Elbow end of test (below)
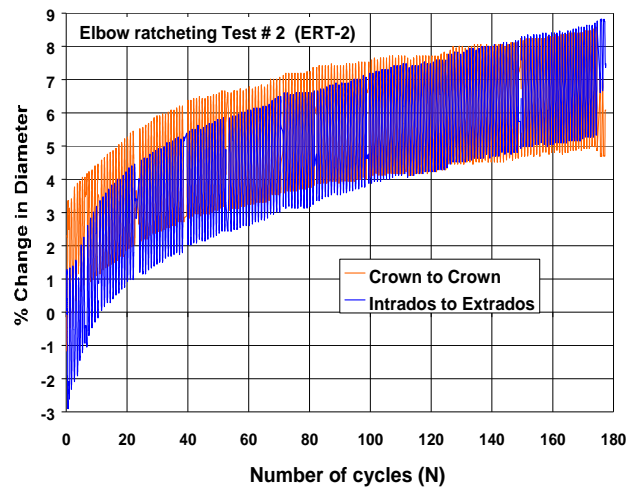
Fig. 7: Test results for ERT-2 on CS elbow: Change in diameter (%) versus Cycles

Predicted number of cycles for crack initiation using the current design codes practices were found orders of magnitude higher than that observed in tests. Even much higher than the cycles observed for complete failure by leakage in the tests.

The tests has clearly established presence of significant synergic damage owing to combined ratcheting-fatigue which causes crack initiation in as low as 30 cycles and through wall leak in 62 cycles. None of the currently available fatigue crack initiation methodologies were able to reasonably justify crack initiation in such a low number of cycles. It is observed that the progressive ratchet strain accumulation is causing a loss in ductility of material. The presence of non-relaxing internal pressure stress is acting as mean stress. In view of these observations, it is important to address the influence of ratcheting strain and pressure stress on fatigue behaviour. To understand the phenomena, a series of uniaxial ratcheting-fatigue experiments at specimen level have also been performed.

These specimen tests loading were given in two blocks. The first loading block of 100 cycles were to generate ratcheting strain (see Fig.9). The Stress amplitude was kept small so that the hysteresis loop will not open (insignificant plastic strain range) and there would be insignificant fatigue damage in 100 cycles. The second loading block of strain controlled were applied to obtain the LCF life (see Fig. 10). The LCF life obtained has clearly shown the strong synergy between ratchet strain accumulation and fatigue crack initiation life.

The fatigue life curve is generally represented by Basquin-Coffin Manson (BCM) equation as given below:

$$\frac{\Delta\varepsilon}{2} = \frac{\sigma_f^{'}}{E}(2N)^b + \varepsilon_f^{'}(2N)^c \qquad (5)$$

Here the $\Delta\varepsilon$, $\sigma_f^{'}$, c, $\varepsilon_f^{'}$, c, E and N are respectively, strain range, fatigue strength, fatigue strength exponent, fatigue ductility, fatigue ductility exponent, elastic modulus and fatigue life. Most of the design codes like, ASME, KTA, RCC-M/RCC-MR, PNAE employ above BCM equation to develop the basic fatigue life curve either on best fit or lower bound fit basis (to represent intrinsic scatter in fatigue test data). Further the design fatigue curves are then obtained from basic fatigue curve by applying recommended safety factors on stress and number of cycles.

The BCM equation does not account the influence of progressive ratchet strain accumulation and non-relaxing pressure stresses in the fatigue crack initiation assessment. The ratchet strain aspect is not accounted in any of the existing methodology used for fatigue crack initiation assessment. However during the ratcheting-fatigue damage, which occurs when the pressurized piping is subjected to large amplitude reversing cyclic bending loads, the ratcheting strain accumulates and causes a loss in ductility. Further the non-relaxing mean stress due to internal pressure is also not accounted in the Basquin-Coffin Manson fatigue life equation. To account for both of these aspects the BCM equation was modified for the mean stress 'σ_m' and ratchet strain 'ε_r' as given below:

$$\frac{\Delta\varepsilon}{2} = \frac{\left(\sigma_f^{'} - \sigma_m\right)}{E}(2N)^b + \left(\varepsilon_f^{'} - \varepsilon_r\right)\left(\frac{\sigma_f^{'} - \sigma_m}{\sigma_f^{'}}\right)^{\frac{c}{b}}(2N)^c \qquad (6)$$

In above equation the mean stress 'σ_m' correction is adapted from the proposal of Manson and Halford [26]. The crack initiation cycles for the elbow test were predicted using the BCM as well as the above proposed equations (modified BCM) and the same was plotted in **Fig**.11 . From this, it can be clearly seen that the classical low cycle fatigue procedure (BCM equation) over predicts the number of cycles to crack initiation even more than final rupture, in presence of ratcheting. The modified fatigue life prediction equation (modified BCM) accounts for ratcheting strain and non-relaxing mean stress, leads to conservative prediction of crack imitation.

The study has clearly highlighted that the ratcheting-fatigue Synergy may cause to very early crack initiation. Based on analysis of test data a mechanistic procedure has been developed to account the ratcheting-fatigue synergy.
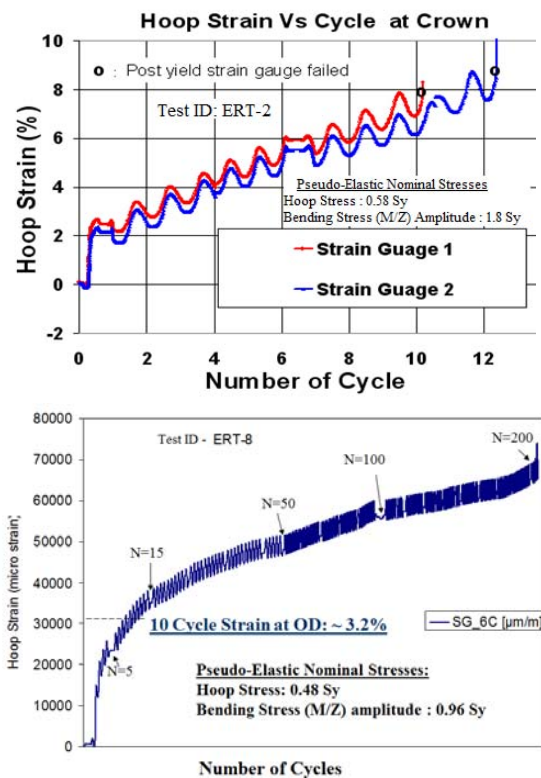
Fig.8: Carbon steel elbow ratcheting test results: Hoop strain (%) at crown versus number of load cycles
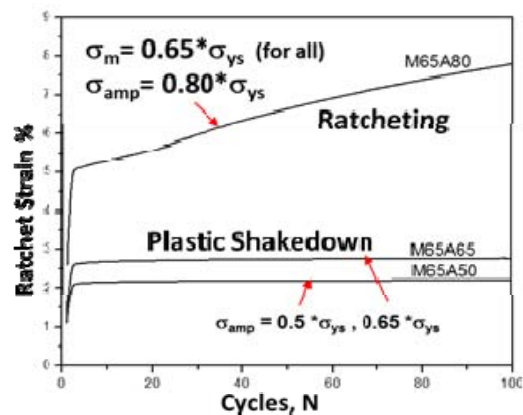
Fig.9: Uniaxial ratcheting test on small specimens: Ratcheting / plastic shakedown behaviour
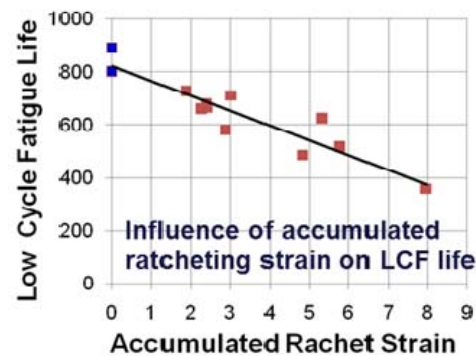
Fig. 10: LCF tests on ratcheting tested on small specimens: effect of ratcheting on fatigue life
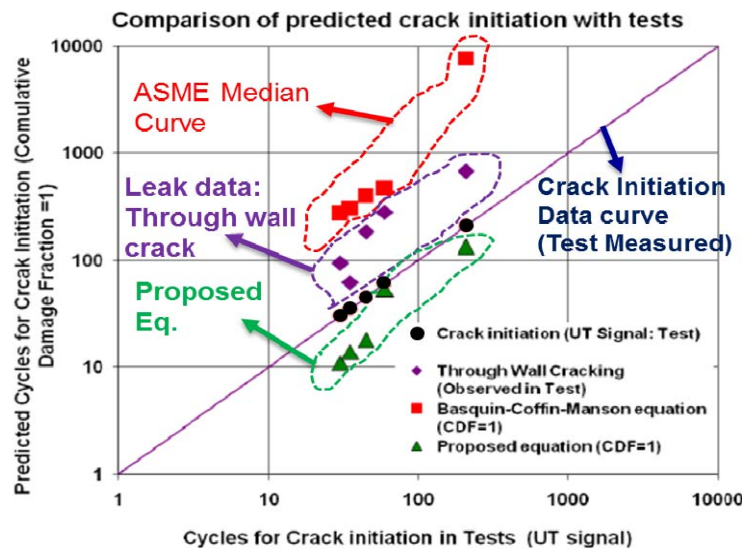
Fig.11: Predicted fatigue crack initiation life using BCM and the proposed equation

Conclusions

The paper covers the outcome of two systematic experimental programmes carried out in the area of cyclic-tearing and ratcheting-fatigue tests on large sized piping components. These programmes were initiated to study the structural integrity behaviour of cracked pipe (for LBB design) and pressurized elbows/pipes (for pressure boundary integrity) under large cyclic loading as experienced in large magnitude earthquakes.

The cyclic-tearing investigations resulted in original development of a Cyclic Tearing Failure Assessment Diagram (CTFAD). CTFAD has led to a simple but robust proposal for fracture integrity and LBB assessment of NPP piping components under extreme cyclic loading. The developed procedure, through a single parameter, implicitly accounts for the fracture toughness degradation and the number of cycles, which are associated with severe earthquake loading.

The ratcheting fatigue investigations has shown that the ratcheting-fatigue crack initiation in very few cycles is primarily due to the presence of non-relaxing mean stress (due to pressure load) and ductility exhaustion as result of accumulating ratchet strain. A mechanistic model has been developed to account these in the fatigue crack initiation calculations.

The above tests/studies have helped in overall safety assessment of primary components of Indian reactors under extreme cyclic loading events. The outcome has provided important elements/methodologies for overall reactor safety assessment which were not adequately addressed in current design codes.

References

1. Yoichi Fuji-ie, (2012) "A message 15 days after the 3.11 earthquake on the nuclear accident at Fukushima #1 NPS", Journal of Disaster Research Vol.1 No.sp , 2012
2. NUREG-1061-VOL.3, (1984), Evaluation of potential pipe break, USNRC Pipe Break Task Group
3. NUREG-0800, (2007), "Leak- Before - Break Evaluation Procedures", USNRC Standard Review Plan SRP 3.6.3
4. IAEA-TECDOC-710, (1993), Applicability of the leak before break concept, IAEA-TECDOC-710
5. IAEA-TECDOC-774, (1994), Guidance for the application of the leak before break concept, IAEA-TECDOC-774

6. Guidance for application of the "Leak Before Break" safety concept for NPP pipelines, 1999, R-TPR-01-99, RD-95 10547-99, MAE, Moscow

7. A16 LBB Guide, (2007), "Guide for Leak Before Break Analysis and Defect Assessment", RCC/MR, Section-1, Subsection-Z, Appendix A16.

8. R6, Revision 4, (2000), Assessment of the Integrity of Structures containing Defects, British Energy Generation Ltd

9. Gunther Barthome, (1997), "German leak-before-break concept", *Siemans/KWU Erlangen, Germany, Int. J. Pres. Ves. & Piping 71, pg 139-147*

10. Scott, P., Kramer, G., Vieth, P., Francini, R, and Wilkowski, G., (1994), "The Effect of Dynamic and Cyclic Loading During Ductile Tearing on Circumferentially Cracked Pipe—Experimental Results", *ASME PVP Vol.280, pp. 207-220.*

11. Wilkowski, G., Kramer, G., Vieth, P., Francini, R, and Scott, P., (1994),"The Effect of Cyclic Loading During Ductile Tearing on Circumferentially Cracked Pipe—Analytical Results", *ASME PVP Vol.280, pp 221-240.*

12. A. Hopper,G. Wilkowski, P. Scott, R. Olson, O. Rudland, T. Kilinski, R. Mohan, N. Ghadiali, and O. Paul, (1997), "The Second International Piping Integrity Research Group (IPIRG-2) Program- Final Report*", USNRC, NUREG/CR-6452*

13. D. L. Rudland, M. Scott, G. M. Wilkowski, (1996), The Effect of Cyclic and Dynamic Loads on Carbon Steel Pipe, *USNRC, NUREG/CR-6438*

14. D. L. Rudland, F. Brust, G. M. Wilkowski, (1996), The Effects of Cyclic and Dynamic Loading on the Fracture Resistance of Nuclear Piping Steels , *USNRC, NUREG/CR-6440*

15. G.Kramer, P. Vieth, C.Mm-schall, R. Francini, G. Wilkowski, (1997) "Stability of Cracked Pipe Under Seismic/Dynamic Displacement-Controlled Stresses", *USNRC, NUREG/CR-6233 Vol-2 ; Subtask 1.2 Final Report*

16. Naoki Miura, Terutaka Fujioka , Koichi Kashima, Satoshi Kanno Makoto Hayashi, Masayuki Ishiwata, Nobuho Gotoh, (1994)"Low cycle fatigue and ductile fracture for Japanese carbon steel piping under dynamic loadings", *Nuclear Engineering and Design 153 (1994) 57 69*

17. Kalsumasa Masayuki, Satoshi Kanno, Makoto Hayashi, , Masayuki Ishiwata, Nobuho Gotoh, Naoki Miura, Terutaka Fujioka , Koichi Kashima, (1995), "Fracture Behaviour under low cycle fatigue loadings in Japanese carbon steel welded pipe joints with a defect", *PVP-Vol.304, Fatigue and Fracture Mechanics*

18. Naoki Miura, Koichi Kashima, Kalsumasa Masayuki, Satoshi Kanno ,1997, "Effect of negative stress ratio on crack growth for cracked pipe subjected to cyclic loading with large scale yielding, *PVP-Vol.350, Fatigue and Fracture-1*

19. K.Kinoshita, K.Murayama, M.Yokota, K.Kitsukawa, and K.Kashima, "Effect of Dynamic Monotonic and Cyclic Loading on Fracture Behavior for Japanese Carbon Steel Pipe STS410", *NUREG/CP-0155, October 9-11, page 457-464*

20. Suneel K. Gupta, Vivek Bhasin, K. K. Vaze, A.K. Ghosh, H. S. Kushwaha, (2007), "Experimental Investigations on Effects of Simulated Seismic Loading on LBB Assessment of High Energy Piping ", *ASME-JPVT, Vol.-129*

21. Suneel K. Gupta, V. Bhasin, J. Chattopadhyay, K. K. Vaze, A.K. Ghosh, H. S. Kushwaha, (2009) "Cyclic Tearing of Through Wall Cracked Pipes made of Carbon Steel", *SMiRT 20, Division-II, Paper 1861*

22. Suneel K. Gupta, V. Bhasin, J. Chattopadhyay, A.K. Ghosh, K. K. Vaze, (2014) "A proposal on cyclic tearing based stability assurance for LBB demonstration of nuclear piping", *International Journal of Pressure Vessel and Piping, vol-119, pp 69-86*

23. Suneel K. Gupta, V. Bhasin, J. Chattopadhyay, A.K. Ghosh, K. K. Vaze, (2015) "Cyclic-tearing behavior and J-R curves of Indian NPP pipes under displacement controlled cyclic loading", *IJPVP, vol-132-133, pp. 72-86*

24. Sumit Goyal, S.K. Gupta, S. Sivaprasad, S. Tarafder, V. Bhasin, K.K. Vaze, A.K. Ghosh, (2013) "Low Cycle Fatigue and Cyclic Plasticity Behavior of Indian PHWR/AHWR Primary Piping Material", *Journal of Procedia Engineering, Volume 55, Pages 136-143*

25. S. K. Gupta, P. Arora, S. Goyal, V. Bhasin, K. K. Vaze, H. S. Kushwaha, (2011) "Recent Developments in Multiaxial Fatigue and Cyclic Ratcheting of Nuclear Power Plant Components", *37th MPA Seminar , MPA, University of Stuttgart Germany, Paper-6, pg. 6.1-6.30*

26. Manson, S. S. and Halford, G. R. (1981). Practical implementation of the double linear damage rule and damage curve approach for treating cumulative damage. *Int. Jour. Fract. Vol. 17. P. 169-172.*

Carbon Nanotubes: Applications in Atomic Energy

Kinshuk Dasgupta
Mechanical Metallurgy Division

Kinshuk Dasgupta is the recipient of the DAE Scientific & Technical Excellence Award for the year 2015

Carbon nanotube (CNT) is one of the most investigated materials since it was discovered by Ijimain 1991 [1]. Its attractiveness comes from its unique physical, chemical, mechanical and thermal properties originating from the small size, cylindrical structure, and high aspect ratio of length to diameter. CNTs have extremely high tensile strength ($\approx$150 GPa, more than 100 times that of the stainless steel), high modulus ($\approx$1 TPa), large aspect ratio, low density (1100-1300 kg/m^3, one sixth of that of stainless steel), good chemical and environmental stability, high thermal conductivity (~3000 W/m/K, comparable to diamond) and high electrical conductivity (comparable to copper). In Indian Atomic Energy program, CNTs find various applications, such as, (1) nanofillers in composites in order to improve mechanical or thermal properties, (2) to adsorb the gaseous products either from a reactor or as a storage medium (3) in separation of metal ions both in front end and back end of fuel cycle (4) as host for catalysts (5) in water purification etc. For all these applications CNTs have been produced in-house by fluidized bed CVD method. Depending on the applications they have been doped with other atoms or functionalized with other ligands. In this article a brief description of synthesis, functionalization and applications of CNTs have been outlined.

Synthesis of carbon nanotubes in a fluidized bed

Out of various techniques, catalytic chemical vapour deposition (CVD) in a fluidized bed has been proven to be a preferred route for large scale production of carbon nanotubes [2]. Here the carbon is deposited from a hydrocarbon (or other carbon bearing source) in the presence of a catalyst at temperatures lower than 1200°C. The CNT structure, such as its wall number, diameter, length, and alignment, could be well controlled during the CVD process. Thus, the CVD method has the advantages of mild operation, low cost, and controllable process, and is the most promising method for the mass production of CNTs. A fluidized bed CNT production facility having capacity ~ 1 kg/day has been created at S-30, south site (fig. 1).

Functionalization of carbon nanotubes

Pristine CNTs are inert in nature and thus do not make chemical bonding with others.It is mostly used in composites with ceramic or metal matrices, in electronics, field emission, gas storage etc.

Fig. 1: Fluidized bed furnace for CNT production

Functionalizing CNTs enables them to be used for various applications where bonding between carbon and the host atom is required, such as, polymer matrix composite, catalysis, metal ion adsorption, sensor application etc. At our laboratory

functionalization has been carried out by (i) replacement of atoms at lattice position, like doping with nitrogen or boron; (ii) side-wall and/or end cap functionalization with different groups; (iii) filling the inner capillary with different molecules or (iv)wrapping nanotube with big molecular chain.

Doping with nitrogen for hydrogen adsorption
Nitrogen doped CNTs (NCNTs) were produced in the fluidized bed reactor by using imidazole as the precursor nitrogen, acetylene as the precursor for carbon, ferrocene as catalyst and magnesia as support material. Fig. 2a shows a transmission electron microscopic (TEM) image of NCNTs produced at our laboratory at 850°C depicting typical bamboo-shaped structure. NCNTs were also characterized by FTIR and XPS (Fig. 2b) in order to verify and quantify N doping.
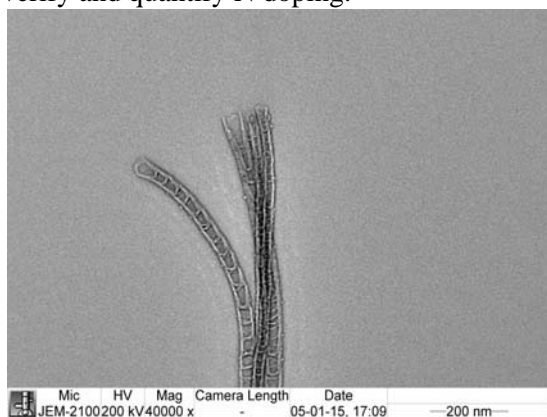
Fig. 2a: TEM image of NCNT
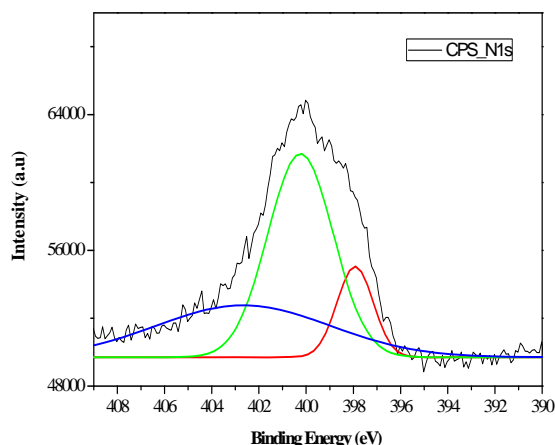
Fig. 2b: N 1s spectrum of doped CNTs

The hydrogen adsorption isotherms for pristine CNTs and NCNTs obtained by the volumetric method at different temperatures and pressures of up to 5MPa are shown in Fig. 3a and Fig. 3b, respectively. It indicates that the NCNTs adsorb higher amount of hydrogen at lower temperatures with respect to bare CNTs. When N atoms are located near C-C bonds, an electronic transfer of charge takes place towards the N-atoms that makes it favorable for interacting with the hydrogen atoms that surround its vicinity [3].
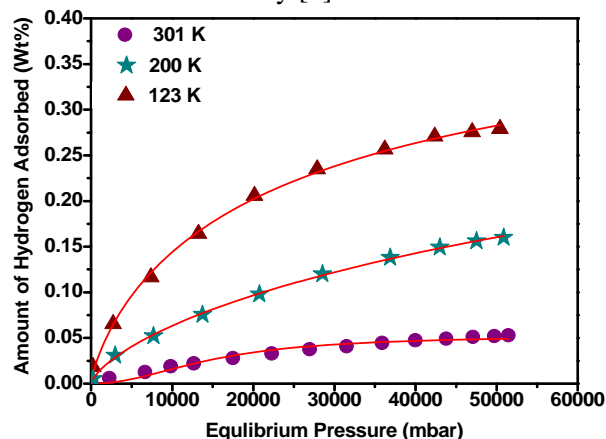
Fig. 3a: H adsorption isotherm of CNT
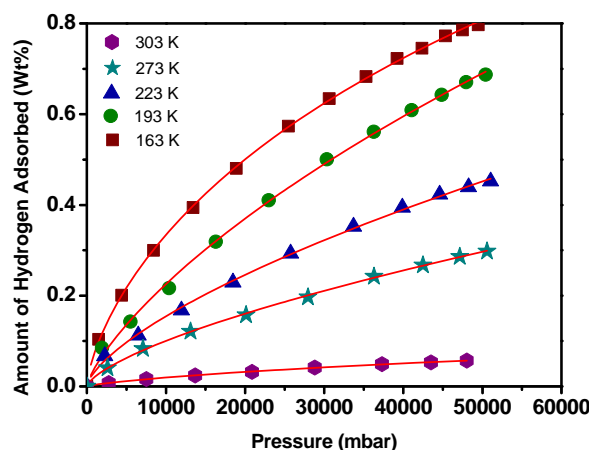
Fig. 3b: H adsorption isotherm of NCNT

Metal ion adsorbtion by functionalized CNT
Recovery of rare earth
-OH and –COOH functionalized CNTs were used for selective adsorption of Nd(III) in presence of Fe(III) from aqueous solution [Fig. 4] with ascorbic acid as complexing agent [4]. This process eliminates the use of hazardous organic solvents

and being solid-liquid extraction minimizes the use of effluent. CNT incorporated polymeric composite beads have been developed [Fig. 5] and successfully used for recovery of Dy and Y [5].
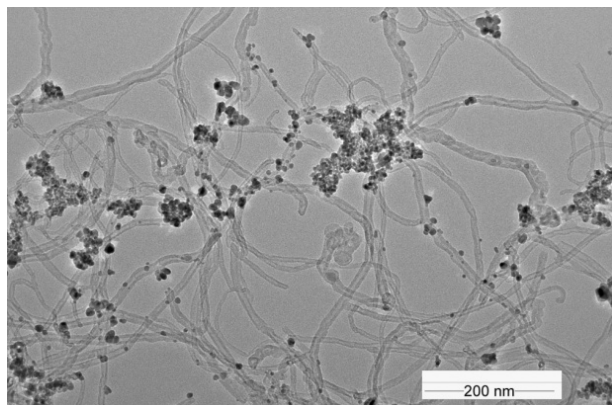
Fig. 4: Rare earth ions adsorbed on CNT
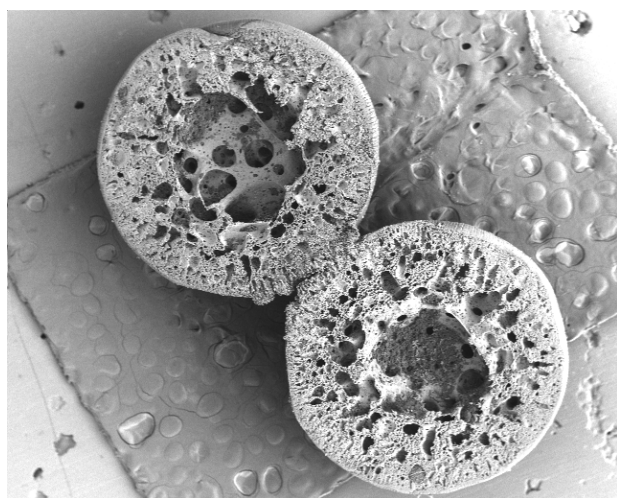
Fig. 5: Cross section of CNT-polymer composite bead

Sorption of actinides

Amido-amine (AA)and diglycolamic acid (DGA) functionalized CNTs [Figure 6] have been used to study the sorption behavior of Neptunium, Plutonium and Americium ions [6,7]. The results are very encouraging showing feasibility of using functionalized CNT for actinide partitioning.
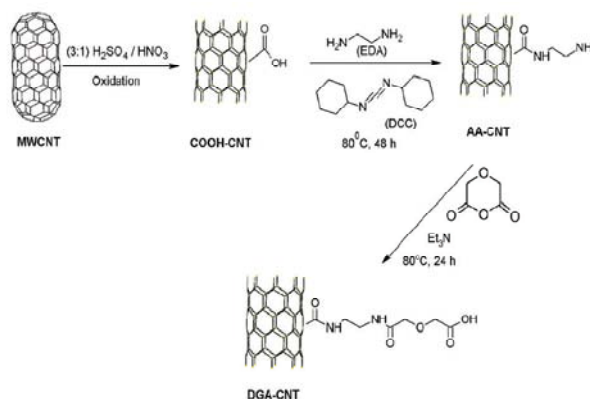
Fig. 6: Scheme for preparing AA and DGA functionalized CNT

Filling inner cavity of CNT

Samarium-cobalt intermetallic inside carbon nanotubes was formed by simultaneous filling of samarium and cobalt ions in a nitrate medium and heating the materials to a high temperature under reducing atmosphere. Under optimized conditions, $SmCo_5$ phase was produced inside the nanotubes without any metal attachment on the outer walls of the nanotubes [Figure 7]. The intermettalic filled CNT shows ferromagnetic property with the potential to be used as a hard nanomagnet [8].
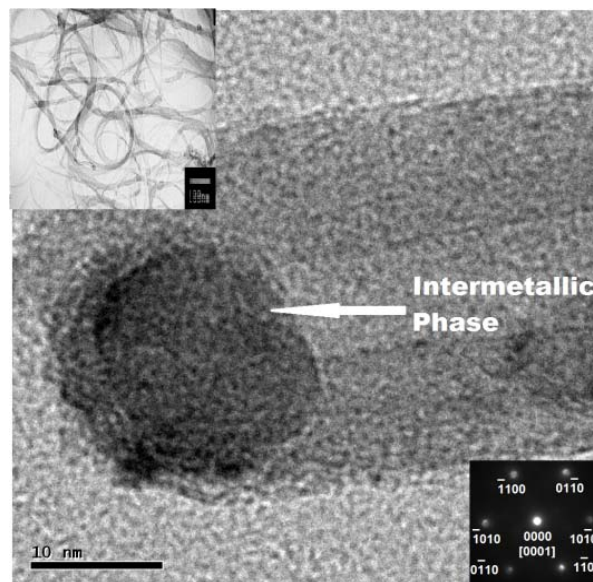
Fig. 7: Intermetallic filled CNT (left top corner inset –low magnification TEM; right bottom corner inset-nanodiffraction pattern showing hexagonal $SmCo_5$ phase)
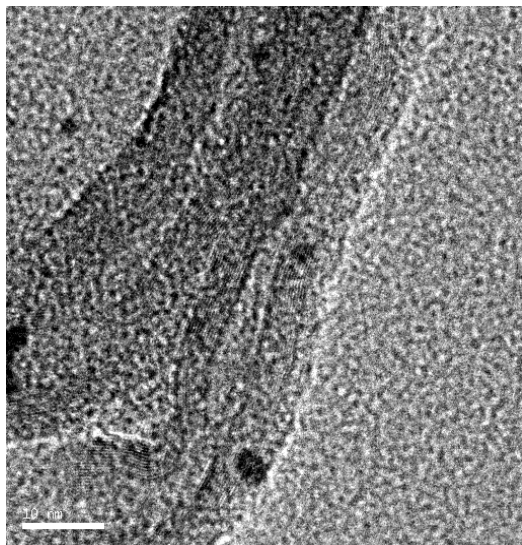
Fig. 8: High resolution TEM of Pt dispersed on CNT

Catalytic application of CNT

Nanoparticle dispersed CNT composite materials, such as Pt/CNT, Ag/CNT, Pd/CNT, Ru/CNT have been prepared [Figure 8]and used for various catalytic applications [9].

CNT based composites

CNT-boron carbide composite

Boron carbide is a hard and brittle ceramic material and finds applications in nuclear as well as defence industry. In order to improve the fracture toughness of boron carbide CNTs have been used at different volume percentage (up to 10 vol%) and composite tiles have been prepared by hot pressing at high temperature under vacuum. Results showed improvement in fracture toughness but decrease in hardness with CNT addition.

CNT-Polymer composite

CNT-aramid composite and CNT-polyethylene composite have been developed for body armour application. Fabric prepared with composite fibres showed improved ballistic properties. CNT-epoxy composite with better fracture toughness is being developed for high speed applications.

Acknowledgement

Reference

1. S. Iijima, Helical microtubules of graphitic carbon.Nature 354 (6348), 56 (1991)
2. K. Dasgupta, J. B. Joshi, S. Banerjee. Fluidized bed synthesis of carbon nanotubes-A review. *Chem. Eng. J.***171** (2011) 841-869.
3. A. Sharma, K. Dasgupta, S. Banerjee, A. Patwardhan, D. Srivastava, J. B. Joshi. In-situ nitrogen doping in carbon nanotubes using a fluidized bed reactor and hydrogen storage behavior of the doped nanotubes. *Int. J. Hydrogen Energy* **42** (2017) 10047-10056
4. K. Dasgupta, R. Vijayalakshmi, M. Anitha. Recovery of Nd(III) in coexistence with Fe(III) ions from aqueous phase using functionalized multiwalled carbon nanotubes: An environmental benign approach. *Journal of Environmental Chemical Engineering* **4** (2016) 2103-2113
5. K. K. Yadav, K. Dasgupta, D. K. Singh, M. Anitha, L. Varshney, H. Singh. Solvent impregnated carbon nanotube embedded polymeric composite beads: An environment benign approach to the separation of rare earths. *Separation and Purification Technology* **143** (2015) pp 115-124
6. A. Sengupta, A. K. Singha Deb, K. Dasgupta, V. C. Adya, Sk. M. Ali. Diglycolamic acid functionalized multiwalled carbon nanotube highly efficient sorbent for f-block elements: Experimental and theoretical investigation. *New Journal of Chemistry* **41** (2017) 4531-4545
7. P. Kumar, A. Sengupta, A. Singha Deb, K. Dasgupta, Sk. M. Ali. Sorption behaviour of Pu^{4+} and PuO_2^{2+} on Amido Amine functionalized Carbon nanotube: Experimental and Computational study. *RSC Adv.***6** (2016) 107011-20
8. K. Dasgupta**,** R. Tewari, H. Singh. Formation of samarium-cobalt intermetallic inside carbon nanotubes. *Materials Letters***101** (2013) pp 80-82
9. S. Biswas, K. Dasgupta, J. Bahadur, S. Mazumder. Green chemical approach for synthesis of Pt/MWCNT nano composite in trioctylmethyl ammonium hydrogen phthalate (TOMAHP) ionic liquid. *Materials Chemistry and Physics* **196**(2017) 1-8

Investigations of Incomplete and Total fusion in reactions with weakly bound nuclei

Vishwajeet Jha
Nuclear Physics Division

Abstract: The incomplete fusion (ICF) process, in which only a part of the nucleus fuses with the target, plays a crucial role in the reaction dynamics of weakly bound nuclei at the energies around the Coulomb barrier. We have developed a new quantum mechanical method to calculate the ICF cross sections based on the break-up of the projectile nucleus and subsequent absorption of its fragments. The present method enables us to study the coupling effects of break-up continuum and transfer on the total fusion cross sections and provides a consistent description of experimentally observed systematic behavior of the complete fusion suppression.

Introduction

Fusion using weakly bound nuclei present exciting opportunity for the synthesis of new nuclei away from the valley of stability and would possibly enable the production of the super-heavy nuclei in island of stability - the holy grail of nuclear physics. In addition, studies of fusion using weakly bound nuclei at low energies provide crucial information for the reactions of astrophysical interest. The fusion of two nuclei at energies around the Coulomb barrier is represented as the quantum mechanical tunneling phenomena through a multi-dimensional potential barrier. However, the couplings of various reaction processes to the internal degrees of freedom at energies around the barrier energies affects the fusion process.

Due to the low breakup threshold, the weakly bound projectile nuclei can easily break into fragments in the nuclear or Coulomb field and this has a significant influence on the fusion process [1]. The breakup may be followed by subsequent fusion of only a part of the projectile leading to incomplete fusion (ICF). The fusion process is classified as the complete fusion (CF), which refers to fusion of the whole projectile or all its fragments, and the total fusion (TF), where the ICF processes are also included. Experimentally, the measured CF cross sections in reactions induced by weakly bound projectiles show suppression compared with the theoretical calculationsthat explain the fusion cross sections involving tightly bound projectiles very well. Despite several theoretical efforts separate calculation of CF and ICF within a fully quantum mechanical model has been an open problem. The breakup process can be accounted for in a detailed way by using the continuum discretized coupled channel (CDCC) formalism, where breakup effects are modelled as excitation to the projectile continuum and its coupling effects on the fusion process are explicitly taken into account. We have developed a new method, which uses varied absorptions for the projectile fragments within the CDCC approach to evaluate the contributions of the ICF cross sections. Using this new method of calculation, we have carried out several investigations to understand the reaction mechanisms of the stable weakly bound projectiles, ^{6,7}Li and ^{9}Be, on a range of target nuclei and explain the experimentally observed features in the data, notably the fusion suppression in reactions with weakly bound nuclei. Some of the important results of the measurements and calculations are discussed here.

ICF calculations in ^{6}Li and ^{7}Li induced reactions:

For a comprehensive understanding of the fusion process with weakly bound nuclei, the separate contribution of the ICF and CF at energies around the Coulomb barrier needs to be calculated. The

breakup and transfer are the dominant direct processes which may contribute significantly at energies around the Coulomb barrier. The effect of couplings arising from breakup can be incorporated with the CDCC approach, while the transfer processes can be described by Coupled-reaction channel (CRC) calculations. A combined CDCC-CRC approach can be utilized to study the dynamic effects arising due to couplings of breakup and transfer. Earlier, the CDCC-CRC calculations have been utilized to provide the good descriptions of certain observables such as the total fusion (i.e., the sum of ICF and CF), elastic, and non-capture breakup cross sections [2, 3, 4]. Because, the ICF can be effectively defined as the absorption following the breakup, the breakup absorption model can be utilized for calculating the ICF components.

We have performed the detailed CDCC calculations to study the fusion process for the ^{6}Li and ^{7}Li nuclei on several targets [5]. An α-d cluster structure for the ^{6}Li [6] and α-t cluster structure for the ^{7}Li [7] were assumed for calculation of breakup. The continuum above break-up threshold were discretized and summed over momentum bins of sufficiently small widths with respect to the momentum of the relative motion of the clusters. The momentum bins were truncated at sufficiently high value of energy and angular momentum. In ^{6}Li, couplings to the 1^+, 2^+ and 3^+ resonances and $L = 0, 1, 2, 3$ α-d continuum were included. For the ^{7}Li to $1/2^-$ first excited state, the $5/2^-$ and $7/2^-$ resonances, and the $L = 0, 1, 2, 3$ α-t continuum was taken. The wave functions for generating the ground state, resonance states and continuum state of the projectile nuclei using the well known binding potentials for the clusters.

The radial wavefunctions $R_\alpha^J(r)$ of the projectile-target system are obtained by solving the coupled equations of the form [8, 9],

$$\left[-\frac{\hbar^2}{2\mu_{PT}} \left(\frac{d^2}{dr^2} - \frac{L(L+1)}{r^2} \right) + U_{PT} + E_\alpha - E \right] R_\alpha^J(r) = \sum_{\alpha'} i^{L'-L} \, V_{\alpha:\alpha'}^J R_{\alpha'}^J(r)$$

where, the required coupling potentials $V_{\alpha:\ \alpha'}^J$ were generated in the cluster-folding (CF) model, which used α-Target and d-Target potentials for the ^{6}Li, α-Target and t-Target potentials for the ^{7}Li. The total

fusion cross sections were calculated as the absorption of the flux from the coupled channels set by employing a short-ranged imaginary part of the complex ion-ion potential (U_{PT}) that describes the interaction of nuclei. The absorption represents the irreversible loss from the coupled channels set and is equivalent to the incoming wave boundary condition applied at the radius where the potential forms the pocket. The TF cross sections are taken as absorption cross sections are obtained from the S-matrix elements given by

$$\sigma_R = \sigma_D + \sigma_{abs} = \frac{\pi}{k^2} \sum_l (2l + 1)(1 - |S_l|^2).$$

where, σ_R is total reaction cross section and σ_D is cross section of all explicitly included direct reaction channels and $\hbar k$ represents the relative momentum of the two nuclei in the entrance channel. The ICF is subsequently calculated as the total absorption from the breakup channel only using the full CDCC wave function.

The results of the calculations for the TF, CF, and ICF cross sections are shown in In Fig. 1 with long-dashed, short-dashed, and dotted lines, respectively, along with the available measured data for ^{6,7}Li + ^{209}Bi systems, respectively. The bare calculations (without breakup couplings) were also performed and the calculated fusion cross sections are denoted by dash-dot-dotted lines in the above-mentioned figures. The Coulomb barrier positions are marked by arrows in figures. It is seen that at energies above the Coulomb barrier, the calculations which include the couplings and calculations that omit them have negligible difference, but at energies below the barrier, the coupled TF cross sections are enhanced in comparison to bare TF cross sections. This behaviour of enhancement of fusion cross sections due to inclusion of breakup couplings at energies below the Coulomb barrier is similar to coupling effects due to inelastic processes in tightly bound nuclei. The model calculations are able to describe the CF and ICF cross sections very well. From the calculations it is evident that the difference between the TF and CF cross sections at higher energy can be almost entirely ascribed due to the ICF cross sections. Hence, ICF cross sections can be taken as the measure of the suppression of the CF cross sections with respect to the calculations. The other important feature is the observation of dominance of

ICF process over the CF process at energies below the barrier, while the reverse is true at energies above the barrier.
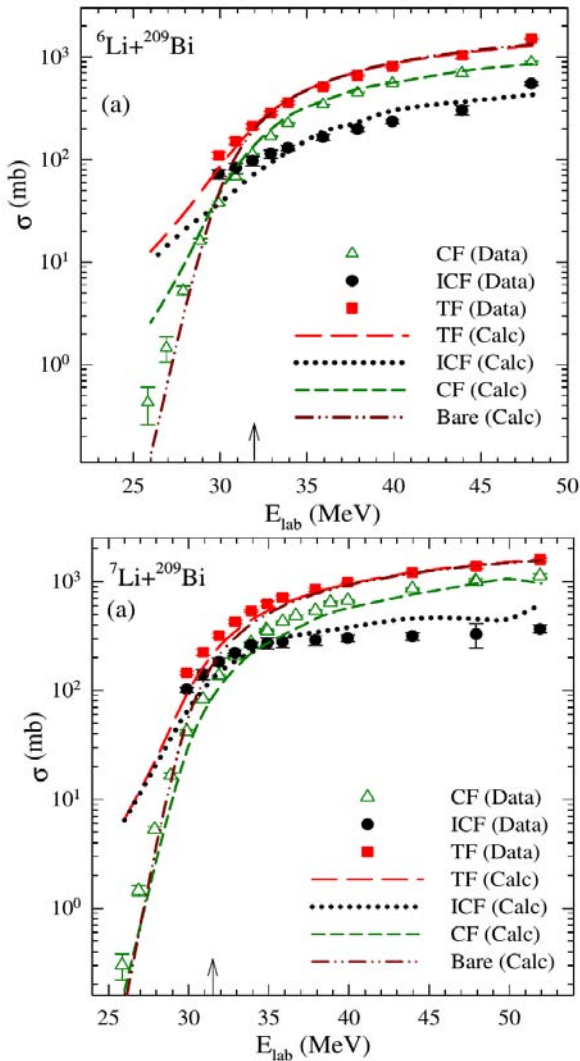
Fig. 1: The data of complete fusion (CF), incomplete fusion (ICF), and total fusion, (TF) = CF + ICF + fission, for ^{6,7}Li + ^{209}Bi reaction taken from Ref. [10] are compared with the calculations. The arrow indicates the position of Coulomb barrier.

Systematical behaviourof ICF and fusion suppression in ^{6,7}Li and ^{9}Be induced reactions:

There have been conflicting experimental results and theoretical interpretations regarding the suppression or enhancement of fusion cross sections for the weakly bound nuclei when the results are compared with the simplistic coupled-channel calculations. A large suppression of CF cross sections (~ 30%) has been inferred from most measurements in ^{6,7}Li induced reactions on different targets. Since the CF suppression observed in experiments with respect to coupled-channel calculations compares well with the ICF cross section, an indirect measure of CF suppression factors (F_{CF}) is obtained from the ICF probability ($P_{ICF} = 1 - F_{CF}$), which is defined as $P_{ICF} = \sigma_{ICF}/\sigma_{TF}$. Based on the ICF measurement for ^{9}Be on heavy targets, it was predicted that the complete fusion suppression factor will decrease with target charge. Even for the ^{6}Li and ^{7}Li projectile, the $F_{CF}$was expected to decrease with the target charge. Therefore, fusion measurements are necessary for light mass systems to study the systematic behavior of the CF suppression.
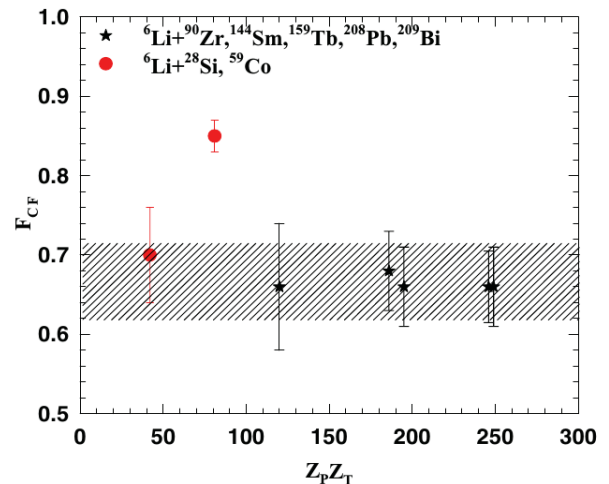
Fig. 2: Universal complete fusion suppression factor (F_{CF}) for ^{6}Li projectile with different targets [Ref. 11 and references therein].

The CF cross sections at energies around the Coulomb barrier for the ^{6}Li + ^{90}Zr around the barrier [11]. The above barrier CF cross sections were found to be suppressed by $34 \pm 8\%$ at all energies as compared to the conventional coupled-channel calculations. As shown in Fig. 2, a constant CF suppression from heavy to medium mass nuclei is observed. The calculations for ICF shown earlier are consistent with the suppression factors observed in the experimental data and a universal behaviour of P_{ICF} and F_{CF}can be deduced.

A larger body of experimental data for CF and ICF separately for ^{9}Be induced reactions on different

targets areavailable with the conflicting claim that the P_{ICF} and F_{CF} may monotonically decrease with the target charge Z_T[12, 13]. We utilize the experimental fusion cross section data available for fusion of ^{9}Be with ^{28}Si, ^{89}Y, ^{124}Sn, ^{144}Sm, and ^{208}Pb targets at energies around the Coulomb barrier. As the 1n-transfer is found to have a large contribution for the ^{9}Be induced reactions we studied the effect 1n-transfer couplings along with the breakup using the CDCC-CRC calculations [14]. A ^{8}Be + n cluster model has been found to correctly describe the low energy reaction dynamics of ^{9}Be [3]. The significant contributions of 1n transfer are obtained for the ^{9}Be + ^{208}Pb and ^{9}Be + ^{28}Si systems, specially at the lower energies.
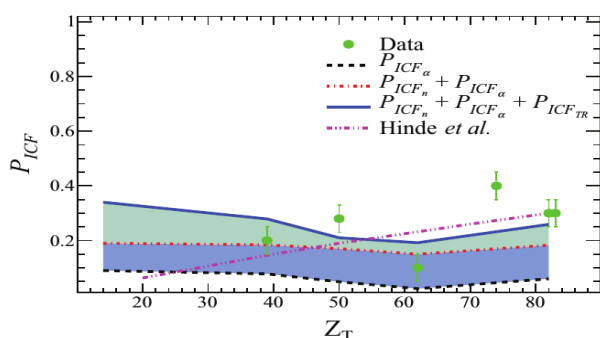
Fig. 3 : Calculated ICF probabilities (P_{ICF}) are compared with the suppression factors derived from the experimental data [Ref. 14 and references therein]. The behavior of ICF contribution due to transfer is included by adding P_{ICF-TR} to P_{ICF-n}+$P_{ICF-\alpha}$. For comparison, the calculations using the simplistic earlier model described in Ref. [13] are also plotted.

The ICF probabilities due to breakup (P_{ICF-n}+$P_{ICF-\alpha}$) and 1n transfer (P_{ICF-TR}) are in good agreement with the behavior of measured complete fusion suppression factors. The CF suppression factors calculated as the ICF probabilities show a systematic behavior with respect to different target masses and they remain approximately constant at energies above the barrier for all the systems considered. The ICF contribution due to transfer varies depending on the structure of the target and the residual nuclei.

Summary :
The simultaneous explanation of the measured experimental data for the CF, ICF, and TF cross sections over the entire energy range is obtained for the first time using calculations in the full quantum mechanical approach. The ICF probability, which signifies the suppression of CF in TF, is found to be constant at above-barrier energies and it is in agreement with the available data for several systems. The CF suppression factors calculated as the ICF probabilities show a systematic behavior with respect to different target masses and they remain approximately constant at energies above the barrier for all the systems considered. The exclusive measurements of ICF and CF cross sections with different weakly bound projectiles, especially in the light-target-mass region, wherever possible, are needed to further verify this proposition.

References:
1. L.F. Canto *et al.,* Phys. Rep. 596, 1 (2015)
2. V. Jha and S. Kailas*,* Phys. Rev. C 80, 034607 (2009)
3. S. K. Pandit, V. Jha*et al.,* Phys. Rev. C 84, 031601(R) (2011)
4. V.V. Parkar, V. Jha*et al.,* Phys. Rev. C 87, 034602 (2013)
5. V. V. Parkar, V. Jha and S. Kailas Phys. Rev. C 94, 024609 (2016)
6. V. V. Parkar, V. Jha*et al.*, Phys. Rev. C 78, 021601(R) (2008)
7. H. Kumawat, V. Jha*et al.*, Phys. Rev. C 78, 044617 (2008)
8. A. Diaz-Torres and I. J. Thompson, Phys. Rev. C 65, 024606 (2002).
9. A. Diaz-Torres, I. J. Thompson, and C. Beck, Phys. Rev. C 68, 044607 (2003).
10. M. Dasgupta et al., Phys. Rev. C 70, 024606 (2004).
11. H. Kumawat, V. Jha*et al.*, Phys. Rev. C 86, 024607 (2012)
12. P. R. S. Gomes *et al.*, Phys. Rev. C 84, 014615 (2011)
13. D. J. Hinde*et al.,* Phys. Rev. Lett. 89, 272701 (2002)
14. V. Jha, V. V. Parkar and S. Kailas, Phys. Rev. C 89, 034605 (2014)

Free radical induced redox reactions of organoselenium compounds: Insights from pulse radiolysis studies

Beena G. Singh

Selenium, a vital element in human body, plays an important role in maintaining the redox balance in cells. New selenium compounds are designed over the period to develop them as redox regulating antioxidants. One of the important roles of antioxidants is to neutralize free radical induced oxidative stress. Therefore to design selenium based antioxidant it is imperative to understand the effect of structure and substitution of organoselenium compounds on the free radical induced redox reactions. In the present article, molecular interactions responsible for the tuning of the reaction mechanism of three different types of selenium compounds belonging to the classes of selenoamino acids, diselenides and selenolane are discussed.

Introduction

Selenium the 34th element of the periodic table is an essential trace element, discovered exactly 200 years ago and the year 2017 is being celebrated as a bicentennial year of its discovery. Initially thought to be an absolute poison, today it is a micronutrient and around 25 selenoproteins are found to be present in biotic systems. Among all the selenoproteins, thioredoxin reductase (TrxR) and glutathione peroxidase (GPx) are the most studied selenoenzymes. The enzyme activity of selenium is attributed to its ability to participate in redox reactions with variety of substrates. In organoselenium compounds, selenium is the redox centre and many low molecular weight organoselenium compounds act as antioxidants either by GPx mimicking or by free radical scavenging activity, or by both and such compounds are being explored as novel class of antioxidants/radioprotectors.

In general, antioxidants act by arresting the uncontrolled generation of free radicals and molecular oxidants like in case of pathogenesis, exposure to pollutants, mutagens and radiation. Free radicals (molecules or fragments with an unpaired electron) are important intermediates in oxidative stress and are also active agents in radiotherapy. The only FDA approved radioprotector given during radiotheraphy is amifostine, an aminothiol. As sulfur and selenium belongs to the same group in the periodic table, selenium compounds are expected to participate in chemical reactions in similar manner as sulfur compounds. From the position of selenium in periodic table, it can be anticipated that selenium compounds have an advantage of easy oxidation by free radicals. Additionally, GPx is an oxidoreductase enzyme; it undergoes both oxidation and reduction during its catalytic cycle. Thus redox properties of organoselenium compounds must be one of the important factors that contribute to their overall GPx activity. Therefore it is important to study the redox reactions induced by free radicals/molecular oxidants in organoselenium compounds. The redox processes in organoselenium compounds can be mediated either by one or two electron transfer. Pulse radiolysis offers an excellent technique to follow one-electron induced redox processes, in nanosecond to microsecond timescale, especially those induced by free radicals which are often very short lived.

When sulfur and selenium compounds interact with oxidizing radicals, loss of electron occurs at the sulfur or selenium centers, producing their respective radicals. Sulfur and selenium centered radicals are unstable and acquire stability by interacting with the nearby heteroatoms having lone

pair of electrons. Such interactions are greatly influenced by the neighboring group participation. Radiation chemists with the help of pulse radiolysis have made extremely useful contributions to the understanding of sulfur and selenium centered transients and their interactions with heteroatoms. Some of the most interesting results from our research from different classes of organoselenium compounds are discussed below in brief. The transients were generated by hydroxyl ($^\bullet$OH) radical, a highly reactive radical implicated in oxidative assault to the biomolecules. It was generated by radiolyzing nitrous oxide saturated aqueous solution of the organoselenium compound by 7 MeV electron pulse (50/500 ns pulse width) obtained by the LINAC facility of RPC Division, BARC. The transients were monitored by absorption detection. Structure of the organoselenium compounds are given in scheme 1.

Selenide

Selenomethione (SeM)

Diselenide

where R = -COO⁻, R' = -NH₃⁺ : Selenocystine (SeCys)

R = -COO⁻, R' = -H : Diselenodipropanoic acid (DSePA)

R = -H, R' = -NH₃⁺ : Selenocystamine (SeCyAm)

Selenolane

3,4-Dihydroxy selenolane (DHS)
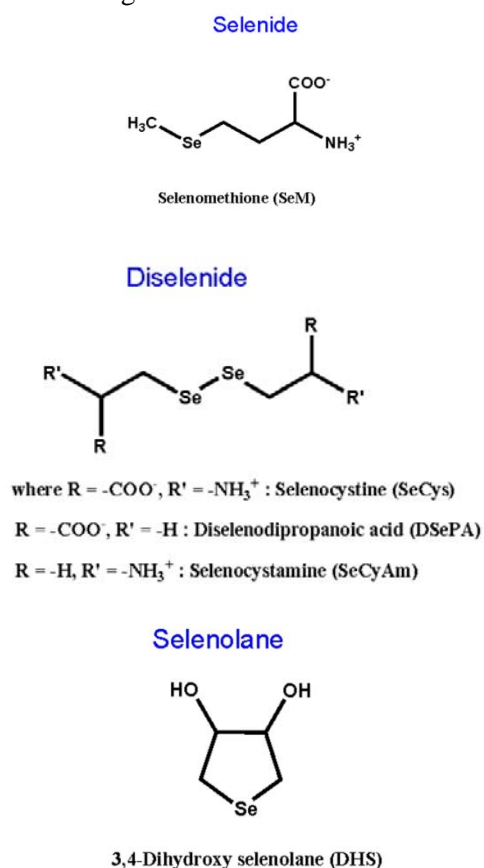
Scheme 1: Structure of organoselenium compounds

Selenomethionine:

Selenomethionine (SeM) is a naturally occurring selenium containing amino acid. Plants generally absorb inorganic selenium from the soil and store it in the form of SeM. It has been widely investigated as an anti-cancer reagent or an antioxidant. It exhibits free radical scavenging and GPx like catalytic activity.

$^\bullet$OH radical reacted with SeM to form radical adducts in which the $^\bullet$OH radical adds to Se atom forming the hydroxyselenouranyl radical (>Se∴OH). This primarily formed radical adduct was converted to selenium centred radical cation by intramolecular water elimination. The Se centered radical cations acquired stability by interaction of the unpaired electron in the p-orbital with the lone pair of electrons on suitable atoms like Se, N, O, P etc present either in the same molecule or in another molecule. In SeM, the lone pair available on N (amino group) or O (carboxylate group) can participate in such stabilization, forming either (Se∴N) or (Se∴O) type monomer radical cation. Based on theoretical and experimental studies, the radical cation structure in SeM has been attributed to the (Se∴N) monomer radical. Formation of this type of radical from (>Se∴OH) occurs by intramolecular water elimination involving the proton from the amino group. As the pH is decreased from 7, the proton from the solution (water) competes with that of the protonated amino group to react with (>Se∴OH) to form the selenium centred radical cation. Thus, at pH 1, as the lone pair on the protonated amino group is not available, the selenium centred radical cation interacts with the lone pair of the unoxidized Se in SeM, forming dimer radical cations (>Se∴Se<)⁺. The absorption maxima of (>Se∴Se<)⁺ and (Se∴N) type monomer radicals has been found to be at 480 and 380 nm, respectively. Similar radicals were observed during the oxidation by one-electron oxidants.[1]

Comparison of the results of SeM, with its sulfur analogue methionine (Met) showed that the initial reaction of $^\bullet$OH radical with both the chalcogenide amino acid was comparable resulting in similar type of transient. However, there was a significant difference between the radical cations of Met and SeM. The most important was the lifetime of the radical cation (SeM$^{\bullet+}$/Met$^{\bullet+}$). The half-life of
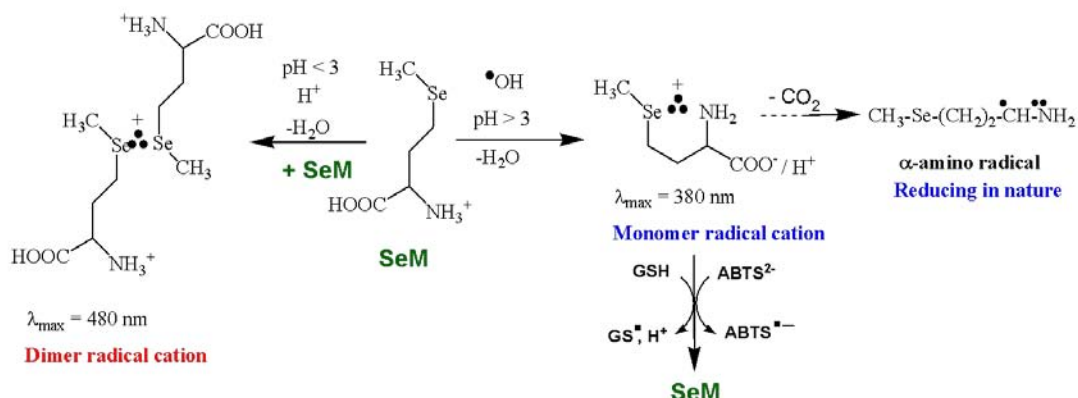
Scheme.2: Possible reactions of hydroxyl radicals with SeM

Met$^{\bullet+}$is reported to be 200 ns, while that of SeM$^{\bullet+}$ was found to be 70 µs. Due to comparably longer lifetime, the reaction between SeM$^{\bullet+}$ radicals and 2,2˗azino-bis(3-ethylbenzthiazoline-6-sulfonic acid) (ABTS^{2-}) was studied. The result indicated that SeM$^{\bullet+}$were oxidizing in nature and oxidized ABTS^{2-} with rate constant of $2.5 \pm 0.1 \times 10^8 M^{-1}s^{-1}$. Similar reactions with Met$^{\bullet+}$ could not be reported due to their short lifetime.

A fraction of SeM$^{\bullet+}$ was found to undergo decarboxylation and the liberated CO_2 was found be approximately half as that compared to Met$^{\bullet+}$. Due to decarboxylation, SeM$^{\bullet+}$is converted to 3-methyl-selenopropyl amino radicals (α-amino radicals), which were found to be reducing in nature. This α-amino radicals in comparison to analogous 3-methyl-thiopropyl amino radicals was a weak reductant. Also the pKa of the α-amino radicals derived from SeM is lower compared to Met. The lower reducing ability and pKa of the SeM derived α-amino radicals was attributed to the electron releasing nature of selenium atom. The $^{\bullet}$OH radical reaction with SeM has been summarized in Scheme.2. [1]

SeM$^{\bullet+}$ reacted with glutathione, the most abundant cellular thiol. Such reaction with Met$^{\bullet+}$ is not observed. This reaction in particular makes SeM a better antioxidant than Met as the oxidized product can be easily reduced back to SeM by GSH. Based on this reaction, it is proposed that SeM could provide an important line of defense against oxidative damage in proteins.

Selenocystine and its derivatives:
Selenocystine(SeCys) is a diselenide form of the 21st amino acid, selenocysteine. The diselenide moiety was essentially thought to be absent in proteins, till recently Gladyshev and his group discovered SeCys in SelL proteins present in zebrafish.[2] The protein showed redox activity and is proposed to function like TrxR. SeCys is reported to exhibit anti-cancer activity, by a redox mediated mechanism. The $^{\bullet}$OH radical reaction of SeCys was studied by pulse radiolysis and to understand the influence of the nature of functional group on the nature of transient formed, its two derivatives – diselenodipropanoic acid (DSePA) and selenocystamine (SeCyAm) were also studied.[3]

Reaction of diselenides with $^{\bullet}$OH radicals first leads to attachment to the diselenide moiety to form hydroxyselenouranyl radical adduct, which undergoes loss of H_2O or OH$^-$ion to form diselenide radical cations absorbing maximum at 560 nm. These diselenide radical cations showed different behaviour with substitution. The radical cations of DSePA accounted for >80% of the initial the $^{\bullet}$OH radicals generated and its spectrum did not change with the pH of the solution. In case of SeCys, the radical cations absorbing at 560 nm were observed only at pH 1, but at pH 7, a tranisent absorbing at 460 nm was observed. Similarly, in case of SeCyAm, the initially radical cation absorbing at 560 nm was observed, that decayed after 40 µs of the pulse, to form the 460 nm absorbing species. In case of SeCys and SeCyAm, only ~ 60% of the $^{\bullet}$OH radical adducts are converted to the radical cations.

Hydroxyselenouranyl radical

λ_{max} = 560 nm

Selenyl radical

+ Diselenide

Selenenic acid

where R_1 = -NH$_3^+$; R_2 = -COO$^-$ Selenocystine (SeCys)

where R_1 = -H; R_2 = -COO$^-$ Diselenodipropanoic acid (DSePA)

where R_1 = -H; R_2 = -NH$_3^+$ Selenocystamine (SeCyAm)

Selenouranyl radical
λ_{max} = 460 nm
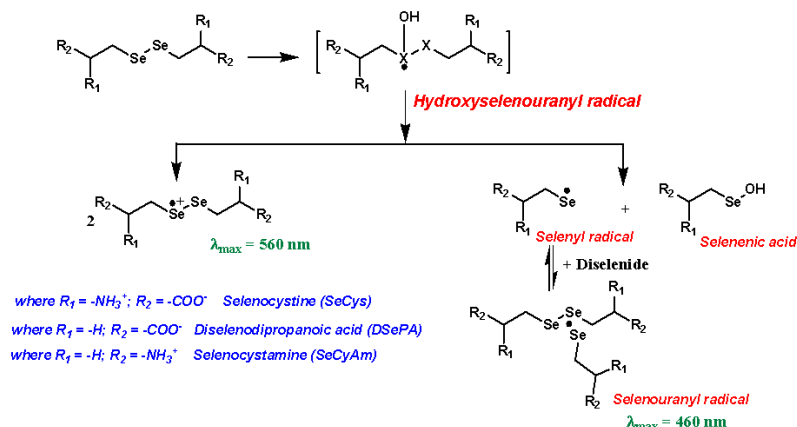
Scheme.3: Possible reactions of hydroxyl radicals with SeCys and its derivatives

The transient absorbing at 560 nm did not showed any concentration dependency on the diselenide, but that absorbing at 460 nm increased with increasing diselenide concentration. Such concentration dependent studies indicated that the 460 nm species was a selenuranyl radicals formed by the reaction of selenyl radicals with parent diselenide to form triselenide radical. In case of DSePA, due to the moderately electron donating carboxylate ion, there is substantial increase in the electron density on the diselenide moiety and this formed stable diselenide radical cations. The presence of electron withdrawing protonated amino group in SeCys and SeCyAm decreased the electron density at the diselenide moiety, resulting in the cleavage of the diselenide radical cation to form selenyl radical. The nature of functional group was also reflected on the lifetimes of the diselenide radical cations absorbing at 560 nm. It was observed that the radical cation of DSePA exhibited longer life time of about 70 µs, while that with SeCyAm had 4 µs at pH 7. The radical cation of DSePA due to longer half-life could react with water to form seleninic acid while those with shorter half-life cleaved to form selenyl radical, which formed triselenide and lead to further degradation of the compound. The $^\bullet$OH radical mechanism of diselenide is summarized in scheme 3.

The effect of functional group was observed on the one-electron reduction potential of the diselenide, which was found to be in the order, DSePA<SeCys<SeCyAm. The toxicity of diselenides compounds arises due to their higher reactivity with cellular thiols like glutathione (GSH), resulting forming redox active selenol. However in case of DSePA showed low reactivity with GSH as compared to SeCys and SeCyAm, making it comparatively stable in presence of reducing agents like thiol. Additionally, the presence of moderate electron donating carboxylate ion resulted in its easy oxidation by free radicals as compared to SeCys and SeCyAm. The higher stability and suitable redox potential resulted in anti-hemolytic and antioxidant activity of DSePA in red blood cells in presence of peroxyl radicals.[4]

3,4-dihydroxy selenolane :
3,4-dihydroxy selenolane (DHS) has been found to exhibit higher GPx like activity compared to its linear structural analogue, bis (2-ethanol) selenide (SeEOH) through the formation of a stable selenoxides. Formation of selenoxides is the rate determining step in the GPx-catalytic cycle where the selenoxide (DHS$_{ox}$) is recycled on the expense of thiol. DHS has been found to scavenge both free radical and molecular oxidants and can undergo both one-electron and two-electron oxidations.[5]
The initial reaction of $^\bullet$OH radical with DHS was similar as seen in selenide and diselenide compounds, forming the hydroxyselenuranyl adduct at the selenium centre. This radical adduct undergoes dehydroxylation to form the selenium
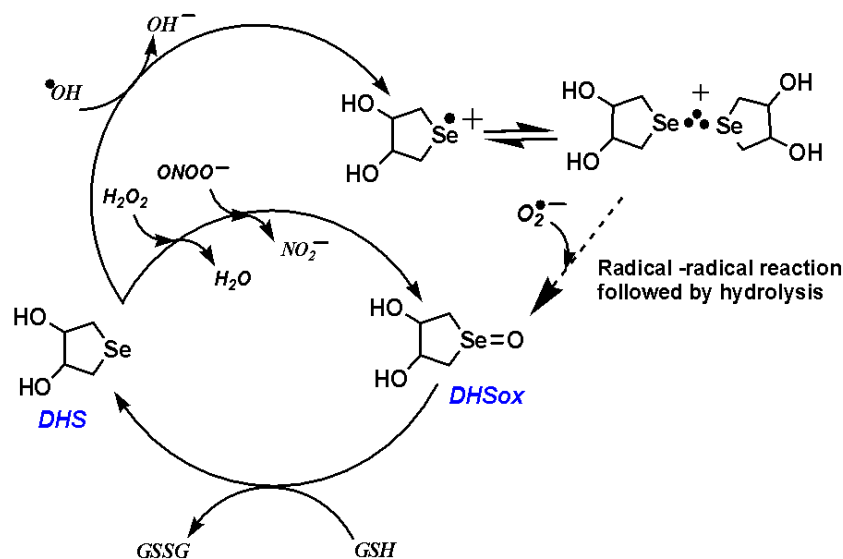
Scheme 4: Reaction of DHS with free radicals and molecular oxidants

centred radical cation that consequently formed the selenium centered dimer radical cation $(>Se\therefore Se<)^+$. Similar reaction was observed with trichloromethylperoxyl radical and specific one-electron oxidant like azide radical. The $(>Se\therefore Se<)^+$ exhibited absorption maximum at 480 nm and decayed by following second order kinetics. The $(>Se\therefore Se<)^+$ decayed mainly by disproportionation reaction followed by hydrolysis to form selenoxides. Also, the $(>Se\therefore Se<)^+$ radical reacted with superoxide anion to form the corresponding selenoxide, which was qualitatively and quantitatively estimated by mass and HPLC technique.[5]

Selenoxide is an important intermediate formed in the catalytic cycle of DHS and its formation on one-electron oxidation of DHS indicates that the free radical reaction of selenium compound can also be catalytic in nature. Additionally, the reaction of molecular oxidants like peroxynitrite and hydrogen peroxide with DHS generated selenoxides as major product. The antioxidant activity was evaluated in terms of GPx like activity and prevention of DNA damage, where DHS exhibited higher antioxidant activity as compared to SeM.

These results were complemented by quantum chemical calculations. The calculation indicated that the energy of non-bonding interaction (E_{nb}) between the selenium radical cation and the •-C-H bond is important in deciding the formation of the carbon centred reducing radical.[6] Higher E_{nb} value led to irreversible deprotonation of the radical cation forming reducing radical. In case of selenium compound due to the more diffused orbital on selenium leads to poor interaction between Se and •-C-H bond and thus lower E_{nb} value. Additionally, the higher covalent radius on selenium stabilizes the dimer radical cation which increased its stability and thus it's conversion to selenoxide. The reaction of DHS with different free radical and molecular oxidants is depicted in scheme 4.

Conclusions

Radiation chemistry with the help of pulse radiolysis has been found to be extremely powerful in understanding the free radical reactions of organoselenium compounds in real time scales. The studies were useful to identify the site of free radical attack on the organoselenium compound and characterize the nature and reactivity of the resulting transient. From these overall comparisons it can be concluded that the stability of selenium centred radical is crucial for its antioxidant activity. The selenium centered radical cations with electron donating (DSePA) and less interacting functional group (SeM and DHS) are less susceptible for free radical induced degradation. Formation of reducing

α-amino radicals or selenyl radicals is disadvantageous in their antioxidant action as such radicals can become source of peroxyl radicals under aerobic conditions. Formation of peroxyl radicals can increase oxidative stress in cells. Further, due to high propensity of the radical cation to form stable selenoxide, makes organoselenium compounds better antioxidants or radioprotectors than sulfur compounds.

Acknowledgements

Reference:

1. Mishra, B.; Sharma, A.; Naumov, S.; Priyadarsini, K. I. "Novel reactions of one-electron oxidized radicals of selenomethionine in comparison with methionine". J. Phys. Chem. B. 113 (21), (2009): 7709-15.

2. Shchedrina,V. A.; Novoselov, S. V.; Malinouski,M. Y.; Gladyshev, V. N. "Identification and characterization of a selenoprotein family containing a diselenide bond in a redox motif". Proc. Natl. Amer. Soc., 104(35), (2007): 13919-24.

3. Mishra, B.; Kumbhare, L. B.; Jain,V. K.; Priyadarsini, K. I. "Pulse Radiolysis Studies on Reactions of Oxidizing Radicals with Selenocystine Derivatives". J. Phys. Chem. B. 112 (14), (2008): 4441-46

4. Kumar, B. S.; Kunwar, A.; Singh, B. G.; Ahmad, A.; Priyadarsini, K. I. "Anti-hemolytic and radical scavenging activity of organoselenium compounds". Biol Trace Elem Res. 140, (2011):127–38

5. Singh, B. G.; Thomas, E.; Kumakura, F.; Iwaoka, M.; Priyadarsini , K. I. "One-electron redox processes in a cyclic selenide and selenoxide: A Pulse Radiolysis Study". J. Phys. Chem. A 114 (32), (2010): 8271–77

6. Kumar, P. V.; Singh, B. G.; Phadnis, P. P.; Jain, V. K.; Priyadarsini, K. I. "Effect of molecular interactions on reactivity of bis(alkanol)selenides: A radiation chemical study in the development of selenium antioxidants". Chem. Eur. J. 22(34), (2016): 12189 –98.

IGSCC crack growth rate of austenitic stainless steels in simulated LWR environment – effect of nitrogen content and mechanism

Supratik Roychowdhury, Vivekanand Kain
Materials Processing and Corrosion Engineering Division

Introduction:

Intergranular Stress Corrosion Cracking (IGSCC) of austenitic Stainless Steel (SS) and nickel based alloy components in Light Water Reactors (LWR) has been a serious issue affecting the safety, availability and cost of operation nuclear power plants and is generic in nature. Initial cracking incidences were attributed to weld induced sensitisation and Low Temperature Sensitisation (LTS) which was mitigated by the use of molybdenum and nitrogen containing nuclear grade SS (type 316NG). Non-sensitised grades of SS have also shown IGSCC in LWR environment which is attributed to strain hardening due to weld shrinkage of constrained welds. It is reported that abusive surface preparation leads to a surface deformed layer, scratch or local deformation, which aids in IGSCC initiation in LWRs [1-2]. Low Temperature Embrittlement (LTE) in type 316NG welds (delta ferrite in welds is richer in chromium and molybdenum) is a probable life limiting factor in future reactors with long design life of up to 100 years [3-5]. Problems due to LTE are expected to be less in type 304L/LN stainless steel making it suitable for use in reactors with long design life and also for the extended use of existing reactors [3, 5].

Nitrogen is an important alloying addition in the austenitic SS used in LWRs and it has a potential to affect the IGSCC susceptibility in LWR conditions. Study of the effect of nitrogen in SS, on the Crack Growth Rate (CGR) due to IGSCC in simulated LWR environment is pertinent as scant literature is available in this regard. This was the motivation for the present investigation and the results have significance to the future indigenous LWR/AHWR.

Experimental:

Material condition and specimens

Two heats of type 304LN stainless steels were used in this study with different levels of nitrogen, 0.08 and 0.16 wt%, referred to as SS 304LN1 and SS 304LN2, respectively. Both the stainless steels were used in heavily sensitised condition (675 °C for 24 hours, degree of sensitisation (DOS) measured by Double Loop Electrochemical Potentiodynamic Reactivation (DL-EPR) technique [6]) and in non-sensitised strain hardened condition for crack growth rate (CGR) studies in simulated LWR conditions. As both the SS are inherently resistant to sensitisation, severe heat treatments will make the effect of nitrogen on the susceptibility to IGSCC due to sensitisation, apparent. Strain hardening of non-sensitised plates of SS 304LN1 and SS 304LN2 was done by cross-rolling at 200 °C to achieve 20% thickness reduction. This was done to simulate the actual material condition which undergoes cracking in LWRs.

Both the SS in the strain-hardened non-sensitised condition (warm rolled) and after sensitisation (675°C, 24 hours) were used for the crack growth experiment in the experimental High Temperature High Pressure (HTHP) high purity water recirculation loop simulating an operating LWR environment, using 0.5T-C(T) samples. For the

rolled plates, specimens were fabricated from the mid-thickness of the plates to ensure uniform strain in the samples. The 0.5T-CT specimens, in the final material condition were fatigue precracked in air by applying a sinusoidal loading to an initial a/W of 0.45 [6]. Side grooving was done after fatigue precracking to obtain a total thickness reduction of 10 % (5 % thickness reduction on each side).

Crack growth rate experiments in HTHP experimental loop

Fatigue precracked C(T) specimens were used for the CGR experiments in the HTHP loop in demineralised water (outlet conductivity <0.1 µS/cm at 25 °C) at 288 °C, 10 MPa, at three levels of Dissolved Oxygen (DO), <10 (deaerated), 260 and 760 ppb (by weight). Figure 1(a) shows the photograph of the HTHP loop and the flow diagram is shown in the schematic in figure 1(b). After loading the specimen in the autoclave, fatigue precracking was done again in HTHP water at the test temperature and pressure. Subsequently a trapezoidal loading was applied for the IGSCC experiments [6-8]. All the CGR experiments were done within a stress intensity factor range of 30-40 MPa√m.

The loop contains a 200 litre capacity water storage tank which stores demineralised water (no chemical addition) of desired level of DO. A water recirculation pump circulates water in the low pressure side for achieving the desired DO and maintaining high purity. A reciprocating pump with pulsation dampener and a back pressure regulator is used for maintaining pressure in the high pressure section (maximum flow rate - 24 l/h). There is a 4 litre capacity autoclave made of type 316L stainless steel (effective volume 2.5 litres) in the high pressure side with a pressure balanced external Ag/AgCl reference electrode, platinum redox electrode and platinum counter electrode for electrochemical measurements. The electrode is designed to withstand maximum temperature of 300 °C and maximum pressure of 180 bar. There is a load cell of capacity 30 kN attached to the autoclave and a stepper motor with which very low strain rates can be applied on the specimens inside the autoclave

in HTHP water. Reversible Direct Current Potential Drop (DCPD) technique with a resolution of 8 µm was used for crack length monitoring in HTHP water. The purity of the water is maintained by continuously passing it through a mixed bed ion exchanger. The water chemistry (DO and conductivity only, no chemical addition) of either the water in the tank or the water coming out from the autoclave can be monitored at a time. There is an automatic control of the DO content in the water. All the wetted parts in the HTHP loop are made of type 316L stainless steel. All the relevant test parameters and the data are continuously monitored using a computer.

(a)

(b)

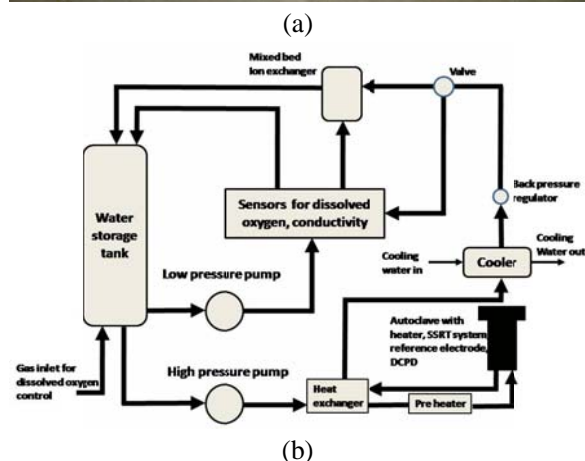**Fig. 1: a) Photograph showing the experimental HTHP high purity water recirculation loop used for simulating LWR water chemistry and b) flow diagram for the HTHP water recirculation loop [6].**

Crack length monitoring in HTHP water

DCPD wire (pure nickel wire having sleeves) connections were made to the C(T) specimens by spot welding using a tungsten inert gas welding machine and the specimens were immediately

dipped in cold water after welding to prevent any overheating of the specimens. A reference sample was used for the DCPD measurements which was another C(T) specimen of the same dimensions and not subjected to any loading. This reference sample was attached electrically in series to the test specimen. A current of 10 A was passed through both the reference and the test specimen and the DCPD signal was recorded for both the specimen (V_s) and the reference sample (V_{ref}). The initial values of the PD signal from the specimen ($V_{s,i}$) corresponding to the initial crack length (a_i) after fatigue precracking in air at the maximum load and the reference ($V_{ref,i}$) were noted at the test temperature and pressure. The PD from the reference was used for normalizing the PD signal from the specimen. This was done to eliminate any spurious DCPD signal due to variation in any of the operational conditions. The crack length (a) was calculated from the DCPD signal using equation 1 [6]. This equation assumes a linear variation in the PD signal with the crack length.

$$a = \frac{a_i}{K}\left(\frac{V_s}{V_{ref}}\right), K = \frac{V_{s,i}}{V_{ref,i}} \text{............ (1)}$$

Transmission electron Microscopic (TEM) examination

TEM examination was done of the SS in the warm rolled condition using JEOL 2000 FX microscope. A number of TEM micrographs and selected area diffraction patterns were recorded for analysis.

Results and discussion:

Sensitised SS

Studies revealed that SS 304LN2 (0.16% N) was more resistant to sensitisation as compared to SS 304LN1 (0.08% N). Comparison of Double Loop Electrochemical Potentiodynamic Reactivation (DL-EPR) values of these two grades of SS indicated the beneficial effects of reducing carbon levels and addition of nitrogen on resistance to sensitisation. The measured DL-EPR values were 22.5 (0.04 before heat treatment) for SS 304LN1 and 8.9 (0.07 before heat treatment) for SS 304LN2 [7]. The

objective was to establish the nitrogen levels in type 304L stainless steel which would impart resistance to sensitization to an extent that it has low CGR in LWR environment and the sensitisation levels too remain low. This would allow use of a SS that has sufficiently low DOS and also resist LTE.

CGR test results indicated that both the grades of SS in the sensitized (675 °C, 24 h) condition were susceptible to IGSCC at DO levels of 760, 260 and < 10 ppb. The CGR values did not vary much with reduction in the DO from 760 ppb to 260 ppb. This was attributed to the measured nominal change in the Electrochemical Pottential (ECP) (the main crack driving force) value by 55 mV only, on reducing the DO level from 760 ppb to 260 ppb. Substantial reduction in the CGR values was observed on reducing the DO levels to <10 ppb due to a reduction in the ECP value by 629 mV. The CGR values were higher by an order of magnitude in sensitized SS 304LN1 as compared to sensitized SS 304LN2 at all the three DO levels used in the test. This behaviour was attributed to the greater coverage by the chromium depleted regions and lower chromium levels in the depleted regions in SS 304LN1 as compared to SS 304LN2 [7]. Clear intergranular (IG) fracture was observed in both the SS. Figure 2(a) shows a typical plot showing crack length variation with time recorded during the experiment at different DO levels (and ECP), figure 2(b) summarises the effect of nitrogen in the SS and the effect of DO on the CGR in sensitised SS in HTHP water and figure 2(c) shows clear IG fracture in sensitised SS 304LN2 [7].

Warm rolled non-sensitised SS

Detailed material characterisation indicated that warm rolling did not induce any change in grain shape and also suppressed martensite formation [6]. This indicated that warm rolling of the plates successfully simulated the actual strain hardened regions adjacent to the weld which is susceptible to IGSCC in LWR conditions. Fatigue precracked C(T) specimens were used for CGR studies and the test conditions, loading schedule and DO levels were the same as that used for the sensitised SS.

(a)

(b)

(c)

Fig. 2. CGR experiments in HTHP water (288 °C, 10 MPa, DM water) (a) variation in crack length with time for sensitised SS 304LN1, b) IGSCC CGR for SS 304LN1 and SS 304LN2 (after a heavy sensitisation heat treatment at 675 °C, 24h) as a function of DO and c) clear IG fracture observed in both the SS in the heavily sensitised condition [7].

CGR studies in HTHP water indicated that both the grades of SS in the warm rolled condition were susceptible to IGSCC in HTHP water and the CGR

values measured were in the same range as those reported earlier for other grades of SS [8]. Clear IG fracture was observed in both the grades of SS in the non-sensitised strain hardened condition. The variation in the CGR with the three DO levels followed the same trend as observed in the sensitised SS. However, the CGR increased by three times in SS 304LN2 (0.16 wt% N) as compared to SS 304LN1 (0.08 wt% N). This variation was observed at all the three levels of DO. Figure 3(a) summarises the effect of nitrogen in the SS and DO on the CGR in HTHP water and figure 3(b) shows a typical IG fracture surface observed in SS 304LN2 in non-sensitised and strain-hardened condition [8].

(a)

(b)

Fig. 3. a) IGSCC CGR for SS 304LN1 and SS 304LN2 (in 20 % warm rolled condition) as a function of DO in high temperature (288 ⁰C) high pressure (10 MPa) pure water and b) predominant IG fracture in the strain hardened and non-sensitised SS 304 LN2 [8].
Mechanism of IGSCC

The present work clearly illustrates the effect of nitrogen on the IGSCC behaviour of SS in simulated LWR environment in both sensitised and non-sensitised (and strain-hardened) conditions. Results clearly indicate that nitrogen addition of 0.16 wt% to type 304L stainless steel improved its resistance to sensitization induced IGSCC in simulated LWR environment. However, the susceptibility to IGSCC in strain-hardened (non-sensitized) condition increased in SS containing 0.16 wt% nitrogen. In the heavily sensitised condition, the CGR in SS 304LN2 was lower than that in SS 304LN1 and this was attributed to differences in the pre-existing active path at chromium depleted regions at the grain boundary [7].

However, nitrogen level of 0.16 wt% is deleterious in comparison to 0.08 wt% in HTHP water for the SS in the non-sensitised, strain-hardened condition. The reason for this has been explained by the TEM study which revealed formation of twins and shear bands due to warm rolling and its intersection with grain boundaries as shown in figure 4 [9-12]. Twins and shear bands are linear features which terminate at the grain boundaries. Hence, the grain boundary prevents transmission of strain to the adjacent grain and local stresses as well as strain are expected to increase at the grain boundary. Figure 4 shows the original position and the final position of the grain boundary after intersection with twins/shear bands. The extent of grain boundary step formation due to intersection with twins and shear bands was observed to be more in SS with higher level of nitrogen and such increased localised stresses and strains at the grain boundary are expected to make these regions the preferred path for crack growth in HTHP water. These steps at the grain boundaries were also visible in the IG fracture surface as shown in figure 5. The distance between the steps seen on the fracture surface (figure 5) correlate well with the distance between the steps marked in fig. 4(a).

(a)

(b)
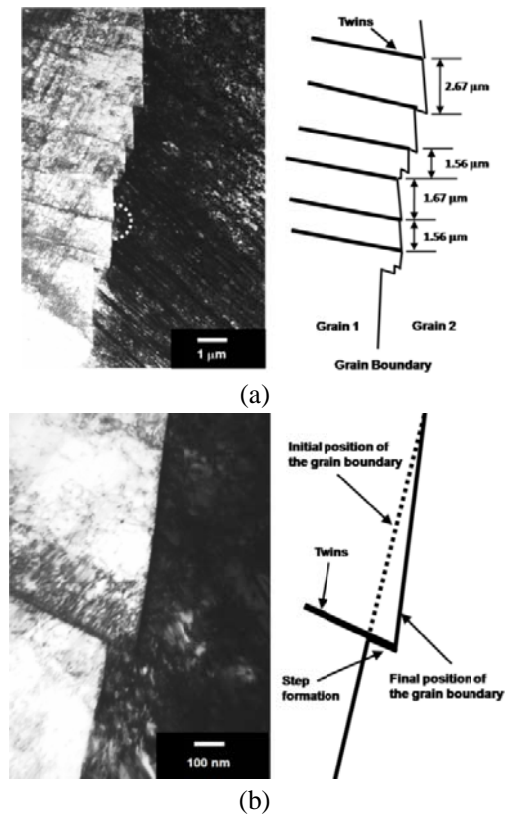
Fig. 4. Bright field image of SS 304 LN1 in the WR condition, a) steps observed where twins intersect with the grain boundary and a schematic showing the approximate distance between the steps measured, b) the region encircled in a) at a higher magnification and a schematic explaining the ledge formation [9].
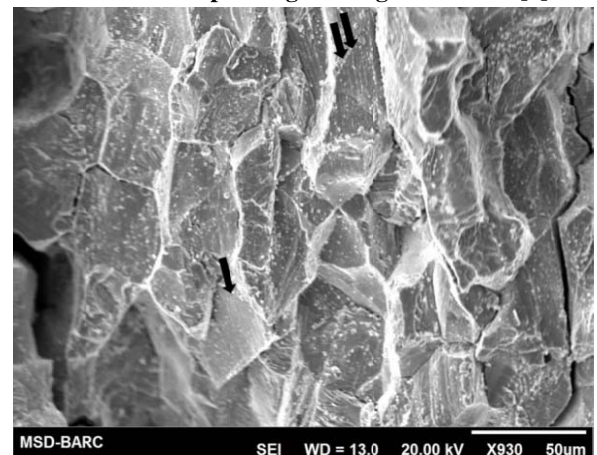
Fig. 5. Fracture surface of SS304LN1 showing clear IG fracture and the steps formed at the grain boundaries (black arrows) are marked. The distance between the steps seen on the fracture surface correlate well with the distance between the steps marked in fig. 4(a) [9].

Conclusions:

Based on this investigation the following conclusions can be made:

i) SCC experiments in HTHP water for SS 304LN1 and SS 304LN2 indicated that both the SS after a severe sensitization heat treatment or after warm rolling (simulating constrained weldment conditions) are susceptible to IGSCC at DO levels of 760, 260 and < 10 ppb.

ii) CGR values did not vary much with reduction in the DO from 760 ppb to 260 ppb for both the material conditions. This was attributed to the measured nominal change in the ECP value (crack driving force) on reducing the DO level. Substantial reduction in the CGR values was observed on reducing the DO levels to <10 ppb due to a substantial reduction in the ECP value.

iii) The CGR values were higher by an order of magnitude in sensitized SS 304LN1 as compared to sensitized SS 304LN2 at the three levels of DO used in the test. The greater coverage of the chromium depleted regions and lower chromium levels in the chromium depleted regions (due to higher nitrogen content) are the main reasons for enhanced CGR in SS 304LN1 as compared to SS 304LN2.

iv) The CGR increased three times in the SS with higher level of nitrogen (0.16 wt%). This effect was observed at all the three levels of DO. Based on TEM studies a mechanism was proposed explaining the effect of nitrogen content in SS on the CGR values in HTHP water. Higher CGR in SS 304LN2 was attributed to the accumulation of higher strain and stresses at the grain boundary due to warm rolling, as compared to SS 304LN1.

Acknowledgements

References:

1) R.M. Horn, G.M. Gordon, F.P. Ford, R.L. Cowan R L. Nucl. Engg. Des., 174 (1997) 313-325.

2) P.L. Andresen, M.M. Morra, J. Nucl. Mater., 383 (2008) 97-111.

3) V. Kain, K. Chandra, K.N. Adhe, P.K. De, J. Nucl. Mater., 334 (2004) 115-132.

4) H. Abe H, Y. Watanabe, Metall. Mater. Trans. A, 39 (2008) 1392-1398.

5) P. Auger, F. Danoix, A. Menand, S. Bonnet, J. Bourgoin, M. Guttamann, Mater Sci Technol, 6 (1990) 301-313.

6) S. Roychowdhury, "Effect of nitrogen content in austenitic stainless steels on intergranular stress corrosion crack growth rate and mechanisms in simulated BWR environment", PhD thesis, Indian Institute of Technology Bombay, Mumbai, 2011.

7) S. Roychowdhury, V. Kain, R.C. Prasad, J. Nucl. Mater., 410 (2011) 59-68.

8) S. Roychowdhury, V. Kain, M. Gupta, R.C. Prasad, Corrosion Sci., 53 (2011) 1120-1129.

9) S. Roychowdhury, V. Kain, S. Neogy, D. Srivastava, G.K. Dey, R.C. Prasad, Acta Materialia, 60 (2012) 610-621.

10) S. Roychowdhury, V. Kain, R.C. Prasad, 'Effect of nitrogen addition in 304L stainless steel on the IGSCC crack growth rate in simulated BWR environment', Proceedings of the 15th International Conference on Environmental Degradation of Materials in Nuclear Power Systems – Water Reactors, August 7-11, 2011: Colorado Springs, CO, USA.

11) S. Roychowdhury, S. Neogy, M. Gupta, V. Kain, D. Srivastava, G.K. Dey, R.C. Prasad, 'Effect of test temperature and prior straining on the deformation mode of austenitic stainless steel during tensile testing', Proceeding of the 2011 TMS Annual Meeting & Exhibition, February 27 - March 3, 2011: San Diego, CA, USA, Paper no.-0119.

12) S. Roychowdhury, V. Kain, M. Gupta, S. Neogy, D. Srivastava, G.K. Dey, R.C. Prasad, Mater. Sci. Forum, 702-703 (2012) 685–688.

Development of LOCA Qualified Absolute Pressure Sensors for Nuclear Reactor Applications

Partha Das, P. M. Geetha and P. R. Patil
Reactor Control Division

Abstract

LOCA qualified absolute pressure sensors with remotely mounted electronics are developed for nuclear reactor applications. The pressure sensor located inside the containment is connected to the electronics module located outside the containment through long screened cable. During accident, only the pressure sensor will encounter the accidental ambient conditions. The pressure sensors are designed to withstand and operate under the atmosphere of steam water mixture at 180ºC temperature, 10 bar pressure and high gamma radiation which may arise during Loss of Coolant Accident (LOCA). The pressure sensors are developed to meet stringent application requirements, high pressure, high temperature, nuclear radiation endurance, stringent environmental qualification requirements, EMI/EMC, Shock and vibration qualification requirements. The salient features and qualifications of indigenously developed LOCA qualified absolute pressure sensors are presented in this article.

Introduction

In nuclear power plant, for safety reasons, sensors used for pressure measurement of reactor coolant system (RCS) are located within the containment. The pressure sensors which are located inside the containment and used for actuation of reactor safety systems should function during accident and maintain their functionality after the accident to ensure safety of the plant. During normal plant operation, the temperature in the area of sensor installation is 30ºC – 40ºC, whereas during LOCA, these areas will encounter an atmosphere of steam water mixture at very high temperature, high pressure and high radiation.

Commercially available pressure transmitters cannot fulfill these requirements as they fail to perform under high temperature and high radiation conditions. In that harsh condition, the pressure transmitter fails mostly due to the failure of the electronics which is housed in the same enclosure along with the sensor. In view of the above, LOCA qualified pressure sensors are indigenously developed with Bi-bloc structure. Here the pressure sensing unit is designed to support remotely mounted electronics converter (signal conditioning electronics unit). It enables electronics module to

be brought out of containment to a conditioned atmosphere and connected with the pressure sensing unit mounted inside the containment through long screened cable. The pressure sensors which are to be mounted inside the containment have been designed to withstand and operate under the LOCA condition. Two types of LOCA qualified absolute pressure sensors have been developed based on two different operating principles.

LOCA qualified Absolute Pressure Sensor mark–I

Absolute pressure sensors mark–I are developed for 2 ranges, 0 – 250 kg/cm^2 and 0 – 100 kg/cm^2 with measurement accuracy of ± 1 % of span under normal ambient condition. The over range pressure of the sensor is 150% of full scale. The pressure sensor is qualified to operate under accident

condition of 180ºC, 10 bar saturated steam atmosphere and total integrated dose of 5 MRad of gamma radiation. The pressure sensors are connected to the reactor coolant system and high pressure system of the plant. Fully welded construction has been adopted for the pressure sensor to achieve zero leakage. LOCA qualified Absolute Pressure Sensor mark–I is shown in Fig.1. Bourdon tube is used as basic pressure sensing element for absolute pressure sensors mark–I. The deflection at the free end of the Bourdon tube due to the applied pressure is converted to electrical signal by customized high temperature Linear Variable Differential Transformer (LVDT). The pressure sensor is provided with back up pressure boundary to contain the process fluid in case of accidental rupture of Bourdon tube.

Remotely mounted electronics module shown in Fig.2 provides excitation signal to LVDT primary coil, receives the LVDT secondary output, conditions the mV ac output and provide 4 – 20 mA DC output proportional to input pressure. The electronics module is connected to the pressure sensor with the help of 4 core screened cable with copper conductor of cross section 1.5 mm^2 and length up to 100m. Remote health-check facility is provided in sensor electronic converters which enables electronic converter health check and ensures connectivity with the control system. On application of the test signal, healthiness of all the components of electronics module is checked and 12 mA output signal (50% of the output span with permissible error of ± 1% of span) is generated. After removing the test signal, the electronics returns to measurement mode and its output becomes proportional to the applied pressure.

LOCA qualified Absolute Pressure Sensor mark–II

Absolute Pressure Sensor mark–II is developed based on piezoresistive principle. The mark-II version has better accuracy than the mark-I version. Absolute pressure sensors mark–II is shown in Fig. 3. The measurement accuracy of mark-II pressure sensors is ± 0.25 % of span at normal ambient condition for both 0 – 250 kg/cm^2 and 0 – 100 kg/cm^2 ranges. This version of sensor is also designed with Bi-bloc structure, with field mountable pressure sensing unit and remotely mounted electronic unit. The pressure sensors are

qualified to operate under LOCA condition of 180 ºC, 10 bar saturated steam atmosphere and 5 MRad total integrated dose of gamma radiation.

Remotely mounted electronics module provides constant DC excitation signal to sensor bridge circuit, receives the mV DC bridge output and converts it to 4 – 20 mA DC output proportional to input pressure. The pressure sensor is connected to the remotely mounted electronics through 4 core screened cable of length up to 200m. Remote health-check facility is provided in electronic converters of mark-II pressure sensor also.

Qualification of Absolute Pressure Sensors

Qualification of the pressure sensors has been carried out to ensure that the sensors function reliably under high pressure, high temperature, high radiation conditions and perform satisfactorily throughout its life and meet the application requirements. Salient qualification tests carried out on absolute pressure sensor and the observations are given below.

For **environmental qualification**, the pressure sensor was subjected to high temperature test, low temperature test, high humidity test, and salt spray test. During all these tests, the functionality of the sensor was monitored. Fig. 4 shows the pressure sensor assembly placed inside the environmental chamber for qualification tests.

Accelerated thermal ageing test was carried out on the pressure sensor to ensure satisfactory operation of the sensor at 40°C ambient temperature for 10 years.

Radiation ageing test: Radiation aging test was carried out on the pressure sensors for total integrated dose of 5 MRad of gamma radiation at a dose rate of 0.1 MRad/ hr. After the test, the accuracy was found to be within their reference accuracy (± 0.25% of span for the mark- II version and ± 1% of span for mark-I version).

Over range pressure test at 150% full scale pressure was carried out on each pressure sensor.

Test for Protection against Water Jet was carried out on the pressure sensors as per IEC 60529 from a distance of 1.5metres for a period of 15 minutes. No traces of water were present in the enclosure of both versions of sensor after the test.

Vibration test was carried out on both types of absolute pressure sensors as per the application requirements. During and after the vibration test,

accuracy observed was within ± 1% of span for mark-I version and within ± 0.25% of span for mark- II version. Fig. 5 shows the vibration test of absolute pressure sensor.

Shock Test: The pressure sensors were subjected to shock test. After the shock test, accuracy observed was within their reference accuracy.

Steam Chamber test: Both mark-I and mark-II pressure sensors were subjected to steam chamber test for LOCA qualification. The sensors were exposed to 180°C, 10 bar saturated steam atmosphere for half an hour and exposed in moisture laden saturated air at 50 - 60° C for 24 hours. During and after the test, the pressure sensor functionality and operation was verified and it worked satisfactorily. Under harsh ambient conditions of steam chamber test, the accuracy of the absolute pressure sensor mark-I was within ± 4% of span. In case of absolute pressure sensor mark-II, enhanced performance was observed during steam chamber test. The accuracy of mark-II pressure sensor was ± 2.5% of span during the test. Fig. 6 shows the steam chamber test set up.

EMI / EMC qualifications were carried out on the electronic converters of the pressure sensors as per MIL-461 E.

Conclusion

LOCA qualified absolute pressure sensors based on two different operating principles have been developed for nuclear reactor applications. The LOCA qualified pressure sensors are designed such that they perform their intended functions reliably when exposed to normal and extreme service conditions. Manufacturing process, fabrication & assembly procedure and inter-stage testing methods have been developed for these sensors. Testing and qualification requirements for these pressure sensors have been formulated. The pressure sensors are fabricated with participation of indigenous industries and tested to meet the application requirements of nuclear reactor plant, high pressure, high temperature, nuclear radiation endurance, stringent environmental qualification requirements, EMI/EMC, Shock and vibration qualification requirements. The technical know-how is transferred to ECIL for manufacturing of these pressure sensors for future projects.

Fig.1: LOCA qualified Absolute Pressure Sensor mark-I

Fig.2: Electronic Converter for Absolute Pressure Sensor

Fig.3: LOCA qualified Absolute Pressure Sensor mark-II

Sensor under test

Fig.4: Absolute Pressure Sensor placed inside the environmental chamber for qualification tests

Sensor under

Fig.5: Vibration test of Absolute Pressure Sensor

Fig.6: Steam Chamber Test Set up

High Speed Cryogenic Turboexpanders and the Helium Liquefier/Refrigerator Development Program at BARC

Anindya Chakravarty

Abstract

Development of high speed cryogenic turboexpander based helium liquefaction/refrigeration systems of different capacities are taken up at Bhabha Atomic Research Centre (BARC), Mumbai, for present and anticipated future departmental programs. The work described in this article includes simulation of different thermodynamic cycles pertaining to turboexpander based helium liquefiers and refrigerators developed by CrTD, BARC. The basic specifications of key devices such as the turboexpanders and heat exchangers are generated from the simulation exercise. Based on these studies, three different series of turboexpanders, with speeds ranging from 2800 – 4500 Hz are developed and performance evaluated during field trials of the helium liquefaction/refrigeration systems.

Nomenclature

U	Turbine impeller tip speed	η	Turbine isentropic efficiency
D	Turbine impeller major diameter	θ	Turbine characteristic flow
P_{in}	Pressure at turbine nozzle inlet	ω	Turbine impeller angular speed
P_{out}	Pressure at turbine diffuser exit	Δh_{os}	Turbine isentropic enthalpy drop
T_{in}	Temperature at turbine nozzle inlet	$\dot{m}$	Mass flow rate through turbine
T_{out}	Temperature at turbine diffuser exit	a_1	Speed of sound at nozzle inlet
h_{in}	Enthalpy at turbine nozzle inlet	P_R	Pressure ratio across the turbine
h_{out}	Enthalpy at turbine diffuser exit	M_u	Ratio of impeller tip speed to sound speed at nozzle inlet
s_{in}	Entropy at turbine nozzle inlet	h_{out_isen}	Enthalpy (isentropic) at turbine diffuser exit
ρ_1	Density of helium gas at nozzle inlet	C_s	Isentropic velocity

1. Introduction

Superconducting magnets and RF cavities in cryomodules of large particle physics experiments (e.g. CERN, DESY, ESS) are maintained at temperatures in the range of 1.8 K – 2 K using large capacity helium refrigerators. Liquid helium cooled superconducting magnets are used for plasma confinement in thermonuclear reactors (e.g. ITER). Large helium refrigerators, at temperature ranges of 15 – 20 K, are also used to cool liquid hydrogen moderators for generating "cold neutron beam" in nuclear research reactors as well as for de-contamination of heavy water. With a view to similar current and future programs and requirements of the Department of Atomic Energy (DAE), India, helium liquefier/refrigerator development is considered a key focus area for BARC, Mumbai.

The underlying thermodynamic cycles employed in large helium liquefiers and refrigerators almost universally involve compression of process gas (helium) to pressures ranging from 13 – 25 bara followed by stage wise expansion of the high pressure (HP) stream (either in full or in part, depending on the cycle and the stage) to a lower pressure (LP) corresponding to compressor suction till liquefaction is achieved or desired refrigeration

temperature is reached by the process gas. A part of the cold expanded streams, from different stages, is returned to the process compressors through heat exchangers to cool down the HP incoming stream. Most modern helium liquefaction and refrigeration systems involve process compressor flows in excess of 50 g/s necessitating the use of expansion devices that can handle large flows. Gas bearing turboexpanders, owing to large flow handling capacity, high efficiency and low maintenance requirements are used as expanders in modern moderate to large capacity helium liquefaction/refrigeration systems.
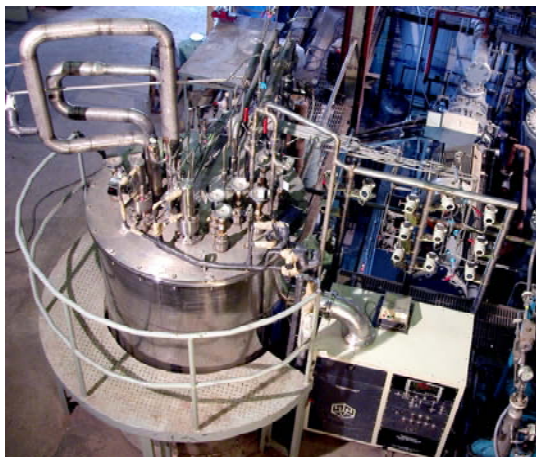
Figure 1. Reverse Brayton cycle based 20 K helium refrigerator [3].

2. Helium liquefier/refrigerator systems

Different helium liquefier and refrigerator thermodynamic processes are simulated to compute maximum refrigeration load capacity at lowest process gas temperature or maximum liquefaction capacity at saturation temperature, as the case may be, for known device efficiencies, process compressor pressure levels, flow rates and pressure drops in the process flow circuits. A set of equations are developed by applying conservation of mass and energy principles to each device (e.g. turboexpander, heat exchanger) control volume. Additionally, second law limitations are imposed through the use of assumed device effectiveness/efficiency values. The set of equations are solved to completely define each state point and compute the refrigeration load capacity/ liquefaction rate. Through the computed temperature and pressure of the state points, basis of design for

High speed cryogenic turboexpander based helium refrigerators/liquefiers are already developed and demonstrated at BARC [1, 2, 3]. Catering to the expansion stages of the developed refrigerators and liquefiers (figure 1, 2), three different series of turboexpanders, designated as Series A, B and C, are developed (table 1). The Series A and B correspond to the first expansion stage of the BARC helium refrigerator/liquefier while series C fits in the second expansion stage.

Figure 2. Modified Claude cycle based helium liquefaction/refrigeration system (4.5 K) [1].

devices such as turboexpanders and heat exchangers are arrived at.

2.1 Reverse Brayton cycle helium refrigerator

The thermodynamic process of a 2 – stage reverse Brayton cycle helium refrigerator consists of two turboexpanders in series interspaced with two heat exchangers (figure 3). Based on process compressor flow of 50 g/s and pressure levels of 2 bara to 17 bara, a 20 K reverse Brayton cycle refrigerator is conceived and developed. Through simulation runs, the inlet and exit state points for the first stage (Series A) turboexpander are arrived at. Consequently, the 20 K refrigerator is developed with Series A turboexpander as the first stage expander and a similar turboexpander for the second stage. During the trials, minimum temperatures (state point 7, figure 3) of 14.9 K and 16.5 K are registered without refrigeration load and with a load of 200 W, respectively. About 470 W of refrigeration load capacity is achieved at 20 K [3].

Figure 3. 2-stage reverse Brayton cycle helium refrigerator schematic [3].

2.2. Pre-cooled Collins cycle helium liquefier/refrigerator

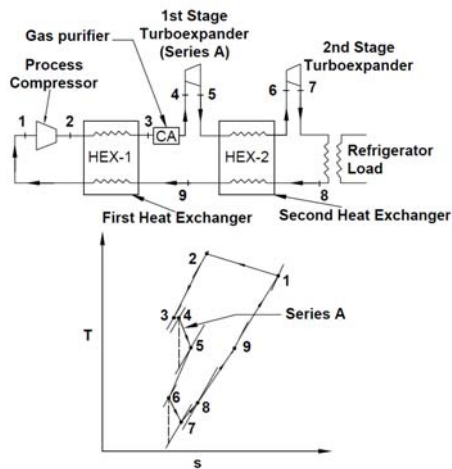The thermodynamic process of a pre-cooled Collins cycle helium liquefier/refrigerator is shown in figure 4. Effectively, parts of the HP process stream are bypassed to LP at two parallel expansion (turboexpander) stages at different temperatures, while the main stream, at the low temperature end, is finally expanded through a JT valve to the LP, forming helium mist. This two-phase helium flow is separated out to liquid helium in the helium receiver vessel while the single phase cold gaseous component is returned to the process compressor through a series of heat exchangers, cooling down the incoming hot HP stream in the process. An extra pre-cooling turbine stage as well as liquid nitrogen pre-cooling options are also provided for enhancing the liquefaction/refrigeration capacities.

A helium screw compressor with a maximum flow rate of about 67 g/s, measured at 1.05 bara suction pressure, is available at CrTD, BARC. The discharge pressure ranges from 13 – 17 barg. With the pre-cooling turboexpander handling a full compressor flow of 62 g/s, a maximum liquefaction capacity of about 57 l/hr at saturation temperature of 4.8 K, is computed [4]. With the pre-cooler turbine by-passed, the maximum liquefaction rate comes down to 29.4 l/hr [5]. For the same configuration, the refrigeration capacity is about 98 W at 4.8 K [5]. The computations also indicate that the turbine speed and diameter requirements are higher (due to low flow per stage and high stage pressure head) than that of Series A turboexpanders (table 1). However, due to the availability of only Series A
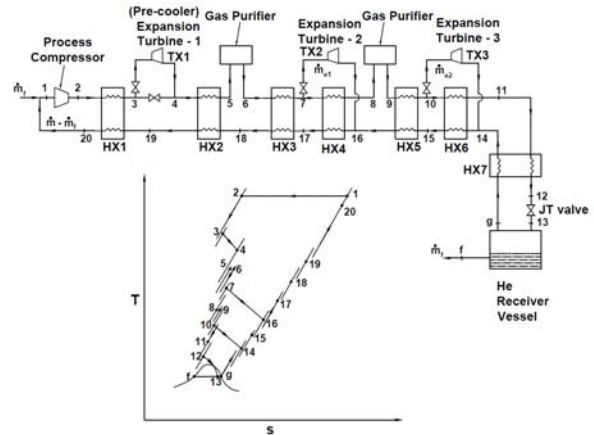
Figure 4. Pre-cooled Collins cycle helium liquefier / refrigerator schematic [4]

type turboexpanders, similar units are used in both the process stages of the system. A Collins cycle liquefier/refrigerator is built and during trial runs with liquid nitrogen pre-cooling, lowest temperature of about 7.8 K [6] is registered by a temperature sensor located downstream of the JT valve (state point 13, figure 4).

Poor thermodynamic performance of turboexpanders 2 and 3 (figure 4) emerged as one of the major issues during the trial runs. An operational domain far away from the design specifications is attributed to the poor performance of the turboexpanders. After a re-visit to the process simulation, coupled with analysis of the experimental results, the decision to re-configure the helium liquefier/refrigerator to a modified Claude cycle is taken. This particular thermodynamic cycle, due to process turbines placed in series in the expander circuit (figure 5), allows a larger (and equal) mass flow through both the turbines (coupled with lower head per stage) and hence is more suited to turboexpander based helium liquefaction / refrigeration systems.

2.3 Modified Claude cycle helium liquefier/refrigerator

During re-configuring the helium liquefier / refrigerator to modified Claude cycle (figure 5), it is decided to harvest all the existing equipment of the Collins cycle liquefier, such as the heat exchangers and cryogenic valves [5]. However, a multi-stream heat exchanger (HX8, figure 5), which is developed by CrTD, BARC [1, 5], is now added to the circuit. The pre-cooler turbine is retained in the cycle for enhancement of liquefaction capacity by utilizing

the higher process compressor pressures, when available. Assuming constant device efficiencies, liquefaction and refrigeration capacities computed from the simulation runs, for different turbine circuit flows, are presented in table 2. It is clear that the optimal flow rate in the turbine circuit for maximum refrigeration needs to be lower than that for the maximum liquefaction case. Maximum liquefaction rate and refrigeration capacity of 32 l/hr and 190 W (table 2), respectively, at 4.8 K, are realized during the experimental runs [1].

Table 1. Comparison of major design and operational parameters of expansion turbine series.

| Parameter	Series A		Series B		Series C	
	Design	Operation[*]	Design	Operation[*]	Design	Operation[*]
P_{in}(bara)	16.5	12.85	12	10.13	6.49	5.76
P_{out} (bara)	11	7.59	6.5	4.92	1.95	1.74
T_{in} (K)	70	67.81	50.09	46.00	13.56	14.45
T_{out}(K)	63.3	59.74	42.5	37.76	9.58	10.47
Rotational Speed (Hz)	4400	4295	4500	4447	2833	2826
Mass flow rate (g/s)	50	48.1	45	46.7	45	41.5
Power developed (W)	1820	2084	1824	2044	779	744
Velocity ratio, U/Cs	0.65	0.58	0.67	0.64	0.66	0.63
Isentropic efficiency	0.65	0.63	0.7	0.72	0.7	0.67
Characteristic flow	0.044	0.054	0.046	0.055	0.039	0.043

[*]Best Efficiency Point (BEP).
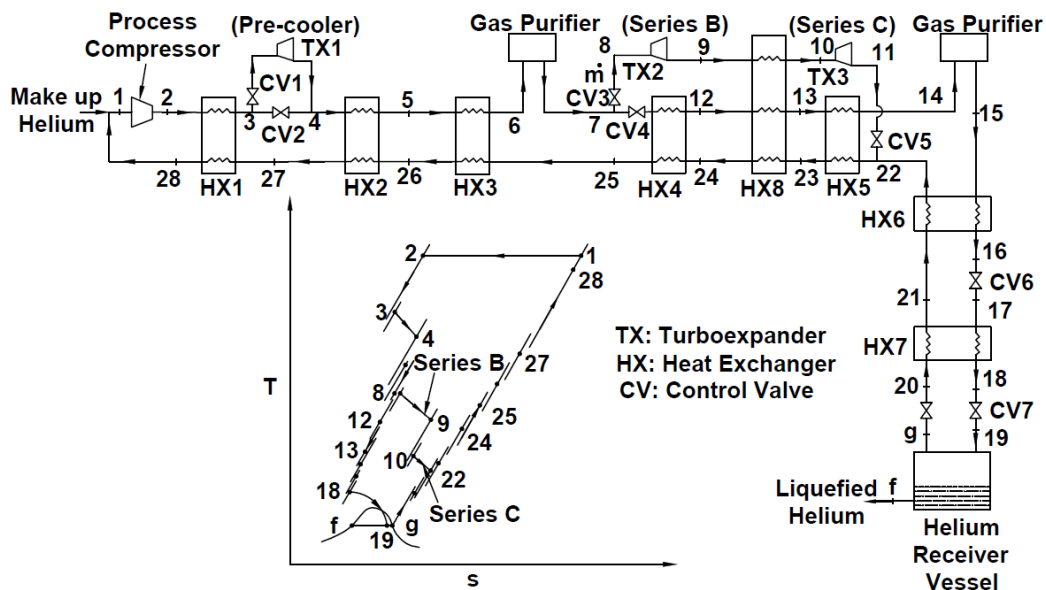
Figure 5. Process schematic of the pre-cooled modified Claude cycle helium liquefier/refrigerator

Table 2. Modified Claude cycle helium liquefier/refrigerator: simulation and experimental results.

Output					Parameters			
Liquefaction rate (l/hr)	Refrigeration capacity (W)	TX 1 efficiency (%)	TX 2 efficiency (%)	TX 3 efficiency (%)	Compressor flow (g/s)	TX 1 flow (g/s)	TX 2 flow (g/s)	TX 3 flow (g/s)
Simulation results								
47.5	315	50	65	65	62	62	40	40
49.4	325	60	65	65	62	62	40	40
51.3	250	50	65	65	62	62	45	45
53.8	250	60	65	65	62	62	45	45
37.5	235	NA	65	65	62	0	45	45
38.4	218	NA	65	65	62	0	47	47
Experimental results								
NA	193	NA	71.6	60.8	60	0	46.7	46.7
32.7	NA	NA	65.6	65.9	53.2	0	46.4	46.4

3. Cryogenic turboexpanders
3.1 Major features

The BARC turboexpander system consists of a shaft with a turbine and a brake compressor impeller mounted at the two ends (figure 6). The vertically oriented shaft consists of a collar, which together with the thrust bearings on its either side, forms the axial bearing system that takes up the thrust load due to difference of pressure between the expansion turbine and brake compressor ends. The radial bearing system is responsible for rotor alignment and stable operation at high speeds. The turbine expansion system consists of an inlet nozzle for flow guidance, a rotating expansion turbine impeller and a diffuser for pressure recovery. The brake compressor system consists of a compressor wheel, an inducer, an inlet throttle valve and a water-cooled heat exchanger unit (figure 6). The process gas helium expands through the turbine system, performs work on the turbine and thus cools down. This work is utilized by the brake compressor to increase pressure (and temperature, as a consequence) of flowing helium gas through its circuit. This circulating gas is throttled back to the inlet of the brake compressor inducer through the inlet valve. The heat generated through this compression process is dissipated via the water-cooled heat exchanger unit.

After initial investigations and studies based on literature on the subject [7, 8, 9, 10], a series of turbine impellers belonging to the 90° Inlet Flow Radial (IFR) turbine class are decided to be developed. The Series A turbines (figure 7) along with nozzles and diffusers are designed catering to the first expansion stage of the reverse Brayton cycle based 20K helium refrigerator (figure 1, 3). From design considerations, the number of impeller blades for this small size (major diameter: 16 mm) turbine are limited to 13, prompting the development of a second series (Series B) of turbine impellers with "splitter" blades (figure 8) for higher efficiency. A total number of 8 full blades are designed and 8 more "splitter" blades are interspaced at the inlet section (major diameter end) to eliminate the eddy and vortex losses [11, 12] within the blade passage. Moreover, a design feature in the form of negative incidence of −30° is introduced in the nozzle following reports [11, 12] that maximum efficiency is obtained at negative incidence values ranging from −20° to −30° at the inlet to IFR turbines. As another design enhancement, the nozzle and diffuser in Series B are combined together to reduce misalignment effects. In addition to the design aspects, the parameters of Series B turboexpanders are slightly altered (table 1) to cater to the first stage of the modified Claude cycle helium refrigerator/liquefier developed by BARC (figure 2, 5).

A third series of turbine (Series C) with a large pressure ratio (table 1) and computed major diameter 16.5 mm, catering to the 2nd expansion stage of the same Claude cycle liquefier/refrigerator, is also developed. The Series C turbines, with features similar to Series A, may also be used in the second stage of the Brayton cycle refrigerator. Brake compressor impellers are developed with designed major diameter of 28 mm for Series A & B (figure 9) and 35.5 mm for Series C (figure 10). The larger size of the Series C brake compressor impellers owes to the fact that the rotor design speed is lower and the compressor operates in a lower ambient

pressure domain. The material of construction of all the turbine and brake compressor impellers is high strength aluminium alloy (7075T6).
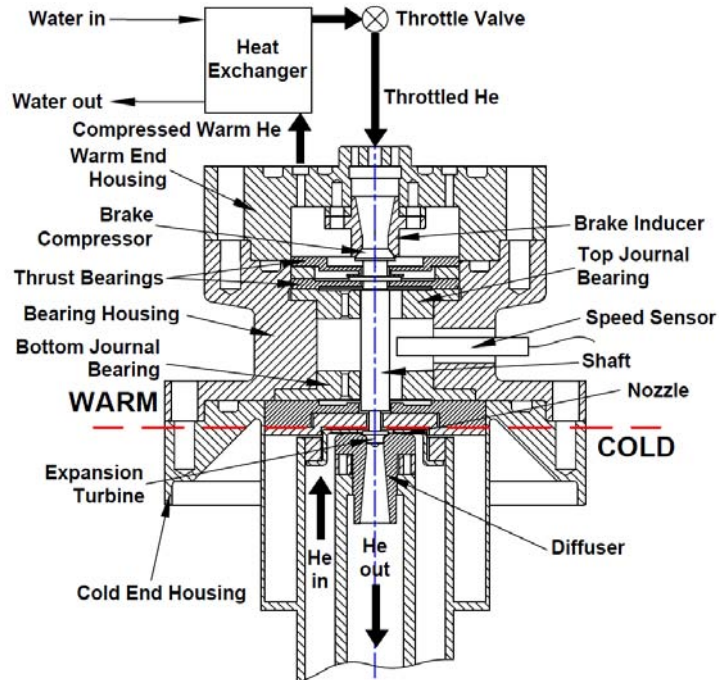

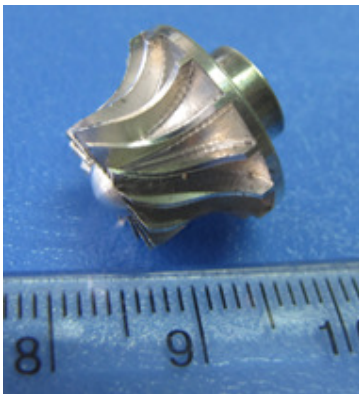**Figure 6.** Schematic of the BARC cryogenic turboexpander system.

Figure 7. BARC Series A turbine impeller.

Figure 8. BARC Series B turbine impeller (with splitter blades).
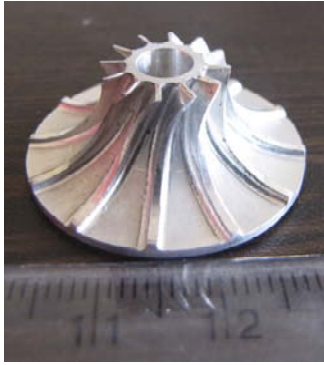
Figure 9. BARC Series A & B brake compressor impeller.

Figure 10. BARC Series C brake compressor impeller.

3.2 Performance evaluation during field trials

For applications restricted to a single working fluid and for high flow Reynolds numbers, the full non-dimensional performance characteristics of a turbomachine may be described by the following relationship [11]:

$$f(P_R, \eta, \theta, M_u) = 0 \qquad (1)$$

It is a common practice [11, 12] to present the isentropic efficiency, η, in relation to the isentropic velocity ratio, U/C_s, which is a combination of stage pressure ratio, P_R and rotor non-dimensional speed. The rotor tip speed, U and the isentropic velocity, C_s are defined as following:

$$U = \omega.\frac{D}{2} \qquad (2)$$
$$C_s = (2.\Delta h_{0S})^{1/2} \qquad (3)$$

The isentropic enthalpy drop across the turboexpander, Δh_{os}, is expressed as:

$$\Delta h_{0s} = h_{in} - h_{out\_isen} \qquad (4)$$

The turbine isentropic efficiency, η, is computed as follows:

$$\eta = \frac{h_{in} - h_{out}}{h_{in} - h_{out\_isen}} \qquad (5)$$
$$h_{in} = h(P_{in}, T_{in}) \qquad (6)$$
$$h_{out} = h(P_{out}, T_{out}) \qquad (7)$$
$$h_{out\_isen} = h(P_{out}, s_{in}) \qquad (8)$$

The non-dimensional mass flow parameter (characteristic flow) [11], θ, is defined as:

$$\theta = \frac{\dot{m}}{\rho_1 a_1 \pi D^2/4} \qquad (9)$$

For thermal performance evaluation of turboexpanders, the enthalpies corresponding to the inlet and exit temperatures and pressures are computed using HEPAK® software. The discrete data points of computed isentropic efficiencies are presented in figures 11 and 12 against the computed isentropic velocity ratios and characteristic flows at different (quasi) steady state operating conditions. A comparison between design and BEP operational parameters of all the series is presented in table 2.

Figure 11. Variation of isentropic efficiency of turboexpanders with isentropic velocity ratio [3].

Figure 12. Variation of isentropic efficiency of turboexpanders with characteristic flow [3].

Founder's Day Special Issue October 2017

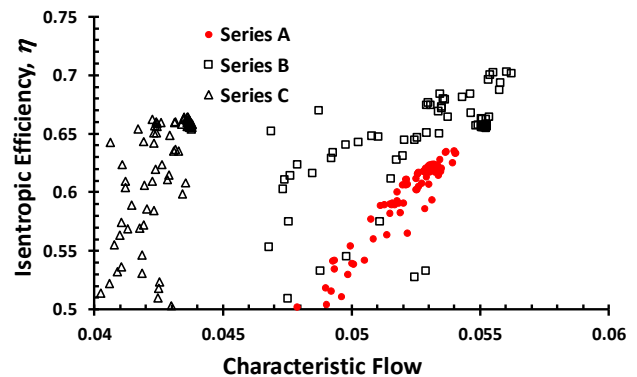It is evident from figure 11 that the isentropic efficiency rises with U/C_s ratio for all the turbine series. In general, the efficiencies computed for Series B are a notch higher than those of Series A for same U/C_s ratios, hence, it appears that Series B is more efficient than Series A, which may be attributed to the described design modifications undertaken for Series B. The Series C turbine efficiency is found to be the lowest, which may be attributed to the fact that it operates (and is designed for) a much larger pressure ratio than what is normal for IFR turbines. The efficiency values of Series B and C peaks out at around U/C_s ratio of $0.63 - 0.65$. On the other hand, since it is not possible to reach the design U/C_s ratio (table 2) for Series A during operation, its efficiency shows an upward trend without any sign of peaking.

What is interesting is that all the turbine series exhibit best efficiencies at characteristic mass flows much higher than design (table 2, figure 12). In fact, the plot in figure 12 seems to indicate the possibility of even larger swallowing capacity of the turbine Series A and B, than that achieved during field trials, without affecting the efficiency. The cluster of data at lower efficiencies (corresponding to liquefier/refrigerator transient conditions) are quite spread out for Series C, however, if only the data corresponding to higher turbine efficiencies are looked into, it seems that the efficiency of Series C turbine is also quite unaffected by the characteristic flow.

4. Conclusion

Simulation studies on different helium liquefaction and refrigeration thermodynamic cycles are taken up at BARC. Based on the studies, helium liquefaction and refrigeration systems of different capacities are developed and demonstrated at BARC, Mumbai. High speed turboexpanders (BARC turboexpander series A, B and C), suited for the expansion circuit of the liquefaction/refrigeration systems are designed and developed. During the experimental runs of the liquefaction/refrigeration systems, successful field trials of the turboexpanders exhibiting highest isentropic efficiency of around 70%, is achieved. More off-design experimental data as well as further studies are required to develop turbines in future with even higher efficiencies.

References

[1] Ansari N A et al. 2017 Development of helium refrigeration/liquefaction system at BARC, India *IOP Conf. Series: Materials Science and Engineering* **171/1/012007**

[2] Kumar J et al. 2017 Helium refrigeration system for hydrogen liquefaction applications *IOP Conf. Series: Materials Science and Engineering* **171/1/ 012029**

[3] Chakravarty A et al. 2017 Development and performance evaluation of high speed cryogenic turboexpanders at BARC, India *IOP Conf. Series: Materials Science and Engineering* (presented at CEC/ICMC 2017, Madison, WI; accepted for publication)

[4] Chakravarty A et al. 2013 Conceptualization and development of a helium liquefier at BARC, Mumbai *Indian Journal of Cryogenics* **38** 144 – 149

[5] Chakravarty A et al. 2016 Operational analysis and update on modifications to a helium liquefier under development at BARC *Indian Journal of Cryogenics* **41** 18 – 25

[6] Chakravarty A et al. 2014 Recent trials with the experimental helium liquefier developed by BARC *Indian Journal of Cryogenics* **39** 19 – 23

[7] Balje O E 1981 *Turbomachines* (USA: John Wiley and Sons)

[8] Kun N C and Sentz R N 1985 High efficiency expansion turbines in air separation and liquefaction plants *Int. Conf. of Production and Purification of Coal Gas and Separation of Air, Beijing, China* 1 – 21

[9] Hasselgrüber H 1958 Stromungsgerechte gestaltung der laufrader von radialkompressoren mit axialem laufra deintrict (in German) *Konstruction* **10** 22

[10] Balje O E 1970 Loss and flow path studies on centrifugal compressors Part - II *Trans. ASME J. Eng. Power* **70** 287 – 300

[11] Whitfield A and Baines N C 1990 *Design of radial turbomachines* (England: Longman Scientific & Technical)

[12] Baines N C and Sieverding C H 1992 *Radial Turbines* (Belgium: von Karman Institute for Fluid Dynamics)

Development of ^{177}lu-Based Agents for Targeted Radiotherapy: Laboratory to Clinics

Tapas Das

Radiopharmaceuticals Division

Tapas Das is the recipient of the DAE Scientific & Technical Excellence Award for the year 2015

Abstract: In the last one and half decade, ^{177}Lu has emerged as one of the most important and useful radionuclides for the development of a wide variety of targeted radiotherapy agents owing to its suitable nuclear decay characteristics, comparatively longer half-life and production feasibility using medium flux research reactors. Radiopharmaceuticals Division (RPhD), BARC has done pioneering work in the field of production of clinical-grade ^{177}Lu and development of ^{177}Lu-based agents for targeted radiotherapy and palliative care. The efforts undertaken by the author and his colleagues in the past 15 years have paved the way towards the development of several potential radiopharmaceuticals and freeze-dried kits. A few of these radiotherapeutic agents and lyophilized kits are being regularly used in various hospitals of our country for the treatment of cancer patients. This has not only ensured the availability of some state-of-the-art radiopharmaceuticals in our country, but also helped to make such radiotherapeutic modalities affordable to the cancer patients.

Key words: ^{177}Lu, Bone pain palliation, Targeted radiotherapy, EDTMP, DOTMP, DOTA-TATE, PSMA-617, Freeze-dried kit

Introduction: Radionuclide therapy (RNT) using target-specific radiopharmaceuticals has been in existence for over sixty-five years for the treatment of thyroid cancer primarily due to the efficacy and ease of using radioiodine (^{131}I) [1]. Other than the applications in tumor therapy, targeted RNT finds applications in certain other diseased states, such as bone pain palliation for improving the quality of life of cancer patients, locoregional applications for treatment of liver cancer and radiation synovectomy for patients with rheumatoid arthritis [2]. The development of new and improved approaches for targeted radionuclide therapy is currently one of the most intensively pursued areas of radiopharmaceutical research. Recent advances in this area exploit the diversity of receptor-avid and immune-derived molecular vectors as well as a plethora of therapeutic radionuclides. In order to ensure the wider use of radiopharmaceuticals, it is essential to carefully consider the choice of radionuclides for a particular application. The criteria for the selection of a radionuclide for radiotherapy are suitable nuclear decay characteristics, ability to produce with high radionuclidic purity and specific activity as well as amenable chemistry [1,3]. However, the practical considerations in selecting a radionuclide for targeted therapy are the possibility to produce the radionuclide with high specific activity at low production cost and comfortable delivery logistics.

In the last one and half decade, therapeutic radionuclide ^{177}Lu has emerged as one of the prime candidate for developing various types of radiotherapeutic agents [4]. Suitable nuclear decay characteristics [$E_{\beta(max)}$ = 0.49 MeV, E_γ = 208 keV (11%), 113 keV (6.4%)], comparatively longer half-life ($T_{1/2}$ = 6.71 d) along with its easy and cost-effective production feasibility with adequately high specific activity and radionuclidic purity using medium flux research reactors have made this isotope as one of the most widely used radionuclide, a close next to ^{131}I, for non-thyroidal applications in RNT [4]. Moreover, possibility of using ^{177}Lu for theranostic applications, which enables the use of same agent for diagnosis or staging of the disease during the course of

radionuclide therapy, are added advantages while using it for targeted RNT applications [5].

While the use of ^{177}Lu for radiotherapy has been reported earlier by a few researchers, the concerted efforts to explore the potential applicability of this isotope in designing agents for therapeutic applications, more specifically targeted radiotherapy, was initiated in 2000, in the Radiopharmaceuticals Division, BARC [1]. A logical outcome therefore led to research towards envisaging methods to produce this logistically suitable radioisotope in adequate quantities and specific activities using the present reactor facilities in our Institute. The first (n,γ) irradiation of natural Lu_2O_3 target to produce ^{177}Lu was carried out in 2000, following which the production of high specific activity ^{177}Lu from enriched target was attempted in mid 2001 [6]. Owing to the extensive research on standardizing the production methodology of this isotope, high specific activity clinical-grade ^{177}LuCl$_3$ had emerged as a new radiochemical for commercial deployment to nuclear medicine centres all over India.

^{177}Lu-based agents for bone pain palliation: Skeletal metastasis is one of the most common complications experienced by the patients suffering from prostate, breast and lung cancer at the advanced stage of their disease [7]. It is reported that 80-85% of patients with advanced breast or prostate cancer are likely to develop bone metastases [8]. These metastatic skeletal lesions often lead to excruciating pain and have a very detrimental impact on the quality of life of these patients. This clinical condition can lead to pathological fractures, immobility, hypercalcemia, neurological deficits and severe psychological trauma [7,8]. Such patients are subjected to palliative care, the major objective of which is to alleviate the pain and thus improving the quality of life enjoyed by these patients.

Clinical management of bone pain arising out of skeletal metastases is a challenging task and usually carried out through a multimodality approach which includes use of analgesic medications, cytotoxic chemotherapy, hormone-deprivation therapy, radiation therapy as well as administration of bisphosphonates and bone-seeking radiopharmaceuticals [7,8]. Although the

conventional treatment modalities such as administration of analgesics and external beam radiotherapy are continuing practices, these approaches have multiple side effects. It is reported that amongst the methodologies usually employed for metastatic bone pain palliation, use of bone-seeking radiopharmaceuticals is considered to be the most desirable for the patients having multiple metastatic lesions, as it is most well tolerated by the patients [9].

The major challenge in developing effective agents for palliative treatment of bone pain arising from skeletal metastasis is to ensure the delivery of adequate dose of ionizing radiation at the site of skeletal lesion with minimum radiation induced bone marrow suppression [10]. These *in-vivo* features are governed by the tissue penetration range and hence on the energies of the β$^-$ particles of the radionuclides used in the radiopharmaceutical preparations [10]. The important attributes of ^{177}Lu as an attractive radionuclide for bone pain palliation emerge from its suitable β$^-$ energy which is adequately low and thereby it is expected to cause minimum bone marrow suppression on accumulation in skeletal lesions [4]. Therefore, attempts were made for the development of potential bone pain palliation agents based on ^{177}Lu.

^{177}Lu-EDTMP: It is well reported in the literature that EDTMP (ethylenediaminetetramethylene phosphonic acid, Figure 1) forms stable complexes with different radionuclides [10] and ^{153}Sm-EDTMP (Quadramet$^®$) is an already well-established radiopharmaceutical for bone pain palliation [7]. Since Lu^{+3} has similar coordination chemistry as that of Sm^{+3}, it is pertinent to envisage EDTMP complex of ^{177}Lu, expecting the pharmacokinetic properties of the agent to be similar to that of ^{153}Sm-EDTMP. Therefore efforts were directed to develop ^{177}Lu-EDTMP as an agent for metastatic bone pain palliation.

EDTMP was synthesized in-house following the reported procedure [11] and characterized by standard spectroscopic techniques. The radiolabeling protocol for the formulation of ^{177}Lu-EDTMP was standardized and subsequently scaled-up to prepare patient dose equivalent of ^{177}Lu-EDTMP. Preliminary biological studies were

performed in normal Wistar rats, normal New Zealand white rabbits as well as in diseased dogs [10]. Clinical studies with the agent were carried out in collaboration with AIIMS (All India Institute of Medical Sciences, New Delhi) and KMCH (Kovai Medical Centre and Hospital, Coimbatore).
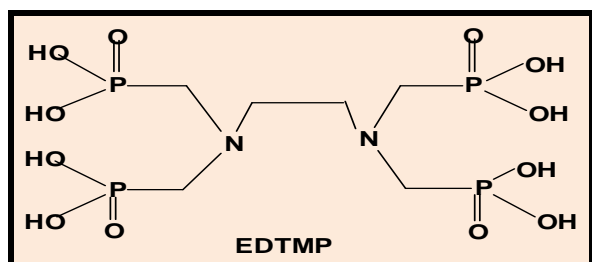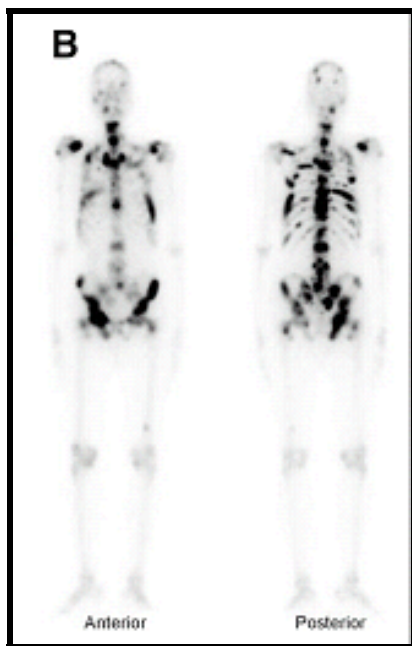

Figure 1: Structure of EDTMP

Figure 2: Whole-body scintigraphic images of a patient treated with ^{177}Lu-EDTMP
(Image courtesy: Dr. Sandip Basu, RMC, BARC)

On the other hand, for the easy and convenient preparation of ^{177}Lu-EDTMP patient dose at the hospital radiopharmacy, formulation of suitable lyophilized EDTMP kit was also attempted. As the preparation of the agent using the kit requires only the addition of normal saline and [177]LuCl$_3$ in the kit vial prior to incubation at room temperature, the formulation becomes relatively simple at the end user. This also reduces the possibility of contamination, radiation exposure, batch failure as well as the preparation time of the radiopharmaceutical [12]. Freeze-dried EDTMP kits, each comprising a lyophilized mixture of 35 mg EDTMP, 14.1 mg NaOH and 5.8 mg of CaCO$_3$ was prepared in our facility [12]. The kit was successfully used for the preparation of up to 3.7 GBq (100 mCi) patient dose of ^{177}Lu-EDTMP with high radiochemical purity [12]. Clinical potency of ^{177}Lu-EDTMP, formulated using the freeze-dried EDTMP kit, was evaluated in human cancer patients in collaboration with KMCH, Coimbatore and RMC (Radiation Medicine Centre), BARC, Mumbai. Figure 2 shows the post-therapy whole-body scans of a prostate cancer patient recorded after administration of ^{177}Lu-EDTMP (anterior and posterior views). It has now been proven that ^{177}Lu-EDTMP is effective in providing significant pain relief to patients and the treatment considerably increased their mobility, resulting in an overall improvement in the quality of life [13]. A similar pain response efficacy, similar hematological toxicity profile and absence of renal toxicity exhibited by ^{177}Lu-EDTMP coupled with almost identical improvement in the quality of life in comparison to those reported with [153]Sm-EDTMP provided conclusive evidences that the agent is clinically safe for pain palliation of patients with disseminated skeletal disease [14].

It is important to mention that the use of both the ^{177}Lu-EDTMP preparations, namely ready-to-use and that formulated using freeze-dried EDTMP kit, have been approved by the RPC (Radiopharmaceuticals Committee) of DAE (Department of Atomic Energy) for human application. Both these products are now being supplied from BRIT (Board of Radiation and Isotope Technology) for the benefit of the patients needing palliative care.

^{177}Lu-DOTMP: Lutetium-177-labeled DOTMP (1,4,7,10-tetraazacyclododecane-1,4,7,10-tetramethylene phosphonic acid) is another bone pain palliation agent whose clinical evaluation has recently been initiated. DOTMP (Figure 3), the macrocyclic analog of EDTMP, is reported to form complex with ^{177}Lu with superior thermodynamic stability and improved kinetic inertness [15]. The

agent can be prepared following a simple wet-chemistry protocol akin to that of ^{177}Lu-EDTMP mentioned above [15] or more conveniently using freeze-dried DOTMP kits [16]. Patient dose of ^{177}Lu-DOTMP was prepared by using freeze-dried DOTMP kit, developed in-house, comprising 20 mg of DOTMP and 8.75 mg of NaOH in the lyophilized form [17]. Clinical evaluation of this agent is presently being carried out in collaboration with three nuclear medicine centres in India, namely, KMCH (Coimbatore), PGIMER (Post Graduate Institute of Medical Education and Research, Chandigarh) and AIIMS (New Delhi). Figure 4 shows the post-therapy whole-body scans of a patient recorded after administration of ^{177}Lu-DOTMP (anterior and posterior views). Satisfactory pain palliation was achieved starting from 6th day post-administration and none of the patients have shown any significant hematological toxicity till date. Although the clinical studies, conducted till date, are limited by the number of patients recruited, the preliminary data obtained so far indicates the potential of the agent to emerge as an alternative radiopharmaceutical for bone pain palliation. The proposal seeking clearance of using freeze-dried DOTMP kits for the formulation of ^{177}Lu-DOTMP for human administration has already been submitted to RPC. It is expected that RPC approval for the regular manufacture and supply of lyophilized DOTMP kits for the clinical use of ^{177}Lu-DOTMP will be obtained in the near future.
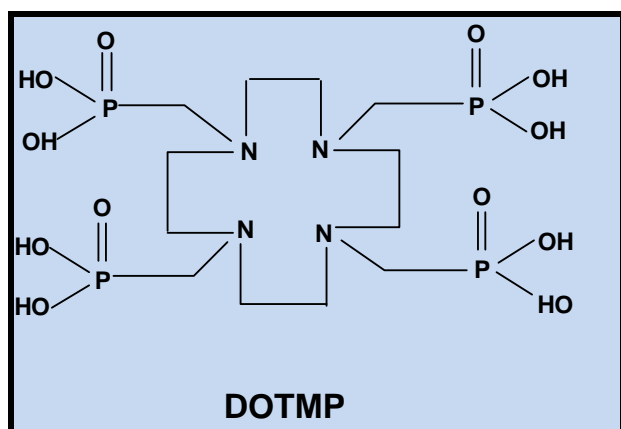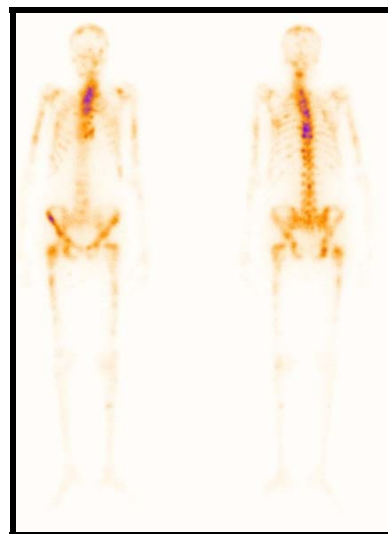

Figure 3: Structure of DOTMP

Figure 4: Whole-body scintigraphic images of a patient treated with ^{177}Lu-DOTMP
(Image courtesy: Dr. Ajit Shinto, KMCH, Coimbatore)

^{177}Lu-DOTA-TATE for peptide receptor radionuclide therapy: Peptide receptor radionuclide therapy (PRRT) using radiolabeled somatostatin analogues is a novel therapeutic modality for the treatment of somatostatin receptor-positive tumors [18]. PRRT using ^{177}Lu-DOTA-TATE, (TATE is a somatostatin analog octapeptide, Tyr3-Octreotate, Figure 5) is now an established therapeutic modality for the treatment of patients suffering from a wide variety of inoperable neuroendocrine cancers [18]. In the last decade, PRRT has gained momentum and at present is being routinely used as a therapeutic regimen in a limited number of countries. In India, PRRT employing ^{177}Lu-DOTA-TATE has been in regular use since 2008 and till date few thousand patient doses have been administered in thirteen nuclear medicine centres across the country [19]. India, with a large population, has a significant number of patients who require PRRT and the treatment needs to be provided at a reasonable cost due to the poor affordability of a large mass of population. This required the formulation of the agent using ^{177}Lu obtained via the more economical and indigenously produced direct (n,γ) route using enriched ^{177}Lu as the target [4]. However, specific activity of ^{177}Lu produced following this route varies significantly from batch to batch due to the

variable operating conditions of the reactor (scheduled and unscheduled shut-downs, power fluctuation etc.) and variation in irradiation cycles used. Additionally, variation in logistical factors such as transportation delay, the distance of the hospitals from the radionuclide production site, date and time of actual administration etc. contribute to the variation in the specific activity of ^{177}Lu available to the end user [19]. Therefore, the radiopharmaceutical challenge associated with PRRT using ^{177}Lu-DOTA-TATE lies in its preparation with adequately high specific activity so that the required dose could be deposited in the cancerous lesions without saturating the limited number of receptors available on the target [20]. Accordingly, a suitable method for the preparation of patient dose of ^{177}Lu-DOTA-TATE was developed in our laboratory [21] and the methodology had been successfully demonstrated to various nuclear medicine centres in India. Figure 6 shows the post-therapy whole-body scans of a neuroendocrine cancer patient recorded after administration of ^{177}Lu-DOTA-TATE (anterior and posterior views)
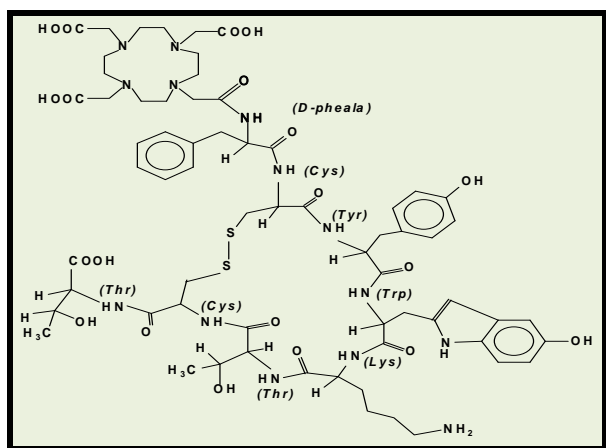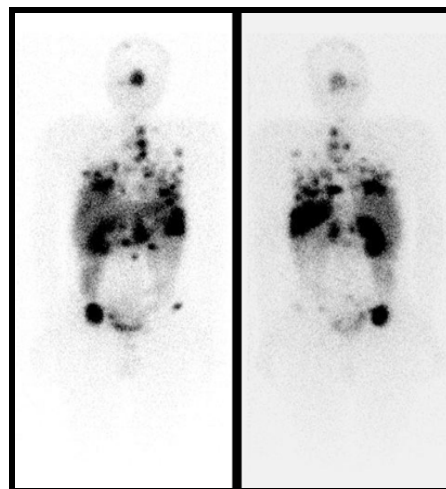

Figure 6: Whole-body scintigraphic images of a patient treated with ^{177}Lu-DOTA-TATE
(Image courtesy: Dr. Kumar G. Kallur, Bangalore Institute of Oncology, Bengaluru)

Figure 5: Structure of DOTA-TATE

^{177}Lu-PSMA-617 for treatment of prostate cancer: Prostate cancer is the sixth leading cause of cancer related deaths and is estimated to be the second most frequently encountered cancer in males worldwide [22]. Therefore, development of suitable and efficient therapeutic agents is of high clinical importance, specifically, to combat the metastatic and hormone refractory prostate carcinoma. Prostate-specific membrane antigen (PSMA) is a surface protein that is usually present on healthy prostate cells and significantly over-expressed on prostate cancer cells [23]. In prostate cancer, PSMA expression has been shown to correlate with disease progression, with highest levels expressed in hormone-refractory and metastatic disease [24]. Moreover, pathology studies have shown that PSMA is expressed by virtually all types of prostate cancers and PSMA-negative prostate carcinoma are relatively rare [25].

During the last two decades, significant work has been carried out in order to develop suitable low molecular weight prostate-specific ligands, which can be labeled with diagnostically or therapeutically important radionuclides [26]. Amongst these prostate-specific ligands, PSMA-617 (Figure 7) developed at the German Cancer Research Center of Heidelberg (DKFZ), has emerged as the most promising PSMA vector till-date. This molecule is reported to exhibit strong binding affinity to PSMA and demonstrated highly

efficient internalization in prostate carcinoma cells [26]. Therefore, use of DOTA (1,4,7,10-tetraaza-cyclododecane-1,4,7,10-tetraacetic acid) coupled PSMA-617, which enables its labeling with either diagnostically (^{68}Ga) or therapeutically (radiolanthanides) useful radionuclides, have opened up a new avenue in the management of prostate cancer.
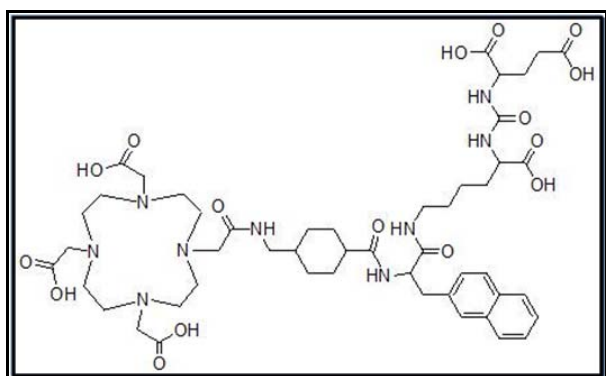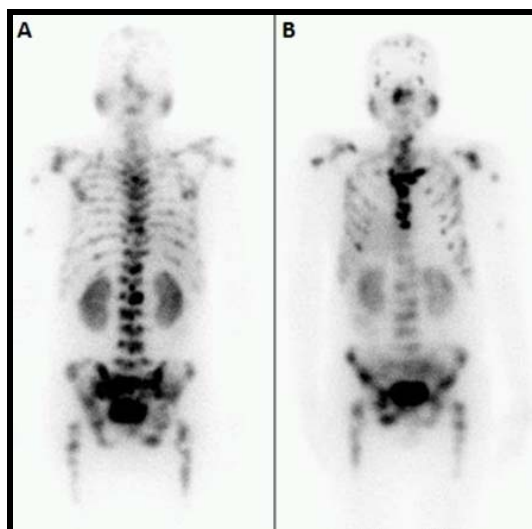

Figure 7: Structure of PSMA-617

Figure 8: Whole-body scintigraphic images of a patient treated with ^{177}Lu-PSMA-617
(Image courtesy: Dr. Vikram R. Lele, Jaslok, Hospital, Mumbai)

In the last couple of years, clinical evaluations carried out with ^{177}Lu-labeled PSMA have shown encouraging results in targeted RNT of patients suffering from prostate cancer [27]. Therefore, efforts were directed to standardize the methodology of formulation of patient dose of ^{177}Lu-PSMA using the indigenously produced ^{177}Lu. Patient dose of 7.4 GBq (200 mCi) of ^{177}Lu-PSMA-617 was prepared with high radiochemical purity under the optimized reaction protocols and necessary biological evaluations were carried to facilitate the clinical translation of the agent [26]. Clinical evaluation of the agent in prostate cancer patients, having proven PSMA expression in primary and metastatic lesions, was initiated in collaboration with Jaslok Hospital and Medical Research Centre, Mumbai. Figure 8 shows the post-therapy whole-body scans of a prostate cancer patient (with extensive skeletal metastases) recorded after administration of ^{177}Lu-PSMA-617 (anterior and posterior views). Our effort towards clinical translation of this potential agent using the indigenously produced ^{177}Lu has ensured the availability of this agent at a comparatively much lower price to the cancer patients of India within 1-2 years of its first clinical utilization. The therapeutic efficacy of ^{177}Lu-PSMA in treating prostate cancer patients is presently being evaluated in few reputed nuclear medicine centres of India.

Conclusion

^{177}Lu has been pursued with great interest for therapy in many countries all over the world, owing to its attractive features detailed earlier and in the last one and half decade it has emerged as one of the prime radioisotopes for developing agents for targeted radiotherapy. Our modest beginning in clinical deployment of this radioisotope for treating patients a decade ago has now grown into a robust program, which is reflected in the continuous increase of demand of clinical-grade ^{177}Lu, presently supplied through BRIT. Extensive research carried out with this radionuclide in the Radiopharmaceuticals Division, BARC in the past ten years has helped in development of several important radiopharmaceuticals, such as ^{177}Lu-EDTMP and ^{177}Lu-DOTMP for bone pain palliation, ^{177}Lu-DOTA-TATE for treatment of neuroendocrine cancers, ^{177}Lu-PSMA-617 for treatment of prostate cancer. This has ensured the availability of state-of-the art ^{177}Lu-based radiopharmaceuticals in India at an affordable cost and thus helped the much-needed radiotherapeutic intervention to reach a wider mass of cancer patients of our country.

References

1. Banerjee S, Das T, Chakraborty S, Venkatesh M. Emergence and present status of Lu-177 in targeted radiotherapy: The Indian scenario. *Radiochim. Acta* 100 (2012): 115-126.

2. Volkert WA, Hoffman TJ. Therapeutic radiopharmaceuticals. *Chem. Rev.* 99 (1999): 2269-2292.

3. Volkert WA, Goeckeler WF, Ehrhardt GJ, Ketring AR. Therapeutic radionuclides: Production and decay property considerations. *J. Nucl. Med.* 32 (1991): 174-185.

4. Das T, Pillai MRA. Options to meet the future global demand of radionuclides for radionuclide therapy. *Nucl. Med. Biol.* 40 (2013): 23-32.

5. Das T, Banerjee S. Theranostic applications of Lutetium-177 in radionuclide therapy. *Curr. Radiopharm.* 9 (2016): 94-101.

6. Pillai MRA, Chakraborty S, Das T, Venkatesh M, Ramamoorthy N. Production logistics of ^{177}Lu for radionuclide therapy. *Appl. Radiat. Isot.* 59 (2003): 109-118.

7. Das T, Banerjee S. Radiopharmaceuticals for metastatic bone pain palliation: Available options in the clinical domain and their comparisons. *Clin. Exp. Metastasis* 34 (2017): 1-10.

8. Palma E, Correia JDG, Campello MPC, Santos I. Bisphosphonates as radionuclide carriers for imaging or systemic therapy. *Mol. Biosyst.* 7 (2011): 2950-2966.

9. Paes FM, Serafini AN. Systemic metabolic radiopharmaceutical therapy in the treatment of metastatic bone pain. *Semin. Nucl. Med.* 40 (2010): 89-104.

10. Chakraborty S, Das T, Banerjee S, Balogh L, Chaudhari PR, Sarma HD, Polyák A, Máthé D, Venkatesh M, Janoki G, Pillai MRA. ^{177}Lu-EDTMP: A viable bone pain palliative in skeletal metastasis. *Cancer Biother. Radiopharm.* 23 (2008): 202-213.

11. Moedritzer K, Irani RR. Direct synthesis of α-aminomethyl phosphonic acid: Mannich type reactions with *o-* phosphorus acid. *J. Org. Chem.* 31 (1996): 1603-1607.

12. Das T, Sarma HD, Shinto A, Kamaleshwaran KK, Banerjee S. Formulation, pre-clinical evaluation and preliminary clinical investigation of an in-house freeze-dried EDTMP kit suitable for the preparation of ^{177}Lu-EDTMP. *Cancer Biother. Radiopharm.* 29 (2014): 412-421.

13. Shinto AS, Shibu D, Kamaleshwaran KK, Das T, Chakraborty S, Banerjee S, Thirumalaisamy P, Das P, Veersekar G. ^{177}Lu-EDTMP for treatment of bone pain in patients with disseminated skeletal metastases. *J. Nucl. Med. Technol.* 42 (2014): 55-61.

14. Thapa P, Nikam D, Das T, Sonawane G, Agarwal JP, Basu S. Clinical efficacy and safety comparison of ^{177}Lu-EDTMP with [153]Sm-EDTMP on an equidose basis in patients with painful skeletal metastases. *J. Nucl. Med.* 56 (2015): 1513-1519.

15. Das T, Chakraborty S, Sarma HD, Banerjee S. ^{177}Lu-DOTMP: A viable agent for palliative radiotherapy of painful bone metastasis. *Radiochim. Acta* 96 (2008): 55-61.

16. Das T, Chakraborty S, Sarma HD, Banerjee S. Formulation and evaluation of freeze-dried DOTMP kit for the preparation of clinical-scale ^{177}Lu-DOTMP and [153]Sm-DOTMP at the hospital radiopharmacy. *Radiochim. Acta* 103 (2015): 595-604.

17. Das T, Shinto A, Kamaleshwaran KK, Banerjee S. Theranostic treatment of metastatic bone pain with ^{177}Lu-DOTMP. *Clin. Nucl. Med.* 41 (2016): 966-967.

18. Dong C, Liu Z, Wang F. Peptide-based radiopharmaceuticals for targeted tumor therapy. *Curr. Med. Chem.* 21 (2014): 139-152.

19. Das T, Banerjee S. Formulation of patient dose of ^{177}Lu-DOTA-TATE in hospital radiopharmacy in India: Preparation using *in-situ* methodology vis-a-vis freeze dried kit. *Cancer Biother. Radiopharm.* 29 (2014): 301-302.

20. Breeman WAP, de Jong M, Visser TJ, Erion JL, Krenning EP. Optimising conditions for radiolabelling of DOTA-peptides with ^{90}Y, ^{111}In and ^{177}Lu at high specific activities. *Eur. J. Nucl. Med. Mol. Imaging* 30 (2003): 917-920.

21. Das T, Chakraborty S, Kallur KG, Venkatesh M, Banerjee S. Preparation of patient doses of

^{177}Lu-DOTA-TATE using indigenously produced [177]Lu: The Indian experience. *Cancer Biother. Radiopharm.* 26 (2011): 395-400.

22. Jemal A, Bray F, Center MM, Ferlay J, Ward E, Forman D. Global cancer statistics. *CA Cancer J. Clin.* 61 (2011): 69-90.

23. Akhtar NH, Orrin P, Saran A, Tyrell L, Tagawa ST. Prostate-specific membrane antigen-based therapeutics. *Adv. Urol.* (2012): http://dx.doi.org/10.1155/2012/973820.

24. Mannweiler S, Amersdorfer P, Trajanoski S, Terrett J, King D, Mehes G. Heterogeneity of prostate-specific membrane antigen (PSMA) expression in prostate carcinoma with distant metastasis. *Pathol. Oncol. Res.* 15 (2009): 167-172.

25. Bostwick DG, Pacelli A, Blute M, Roche P, Murphy GP. Prostate specific membrane antigen expression in prostatic intraepithelial neoplasia and adenocarcinoma: A study of 184 cases. Cancer 82 (1998): 2256-2261.

26. Das T, Guleria M, Parab A, Kale C, Shah H, Sarma HD, Lele VR, Banerjee S. Clinical translation of ^{177}Lu-labeled PSMA-617: Initial experience in prostate cancer patients. *Nucl. Med. Biol.* 43 (2016): 296-302.

27. Kwekkeboom D. Perspective on ^{177}Lu-PSMA therapy for metastatic castration-resistant prostate cancer. *J. Nucl. Med.* 57 (2016):1002-1003.

Effective and Economically Viable Rhenium-188 Radiopharmaceuticals for Liver Cancer Therapy and Bone Pain Palliation: BARC Contributions to Rhenium-188 Radiopharmaceuticals Program in India

Madhava B Mallia
Radiopharmaceuticals Division

Abstract

Rhenium-188 is an important therapeutic radioisotope, available from a commercial Tungsten-188/Rhenium-188 generator (^{188}W/^{188}Re generator). Its high energy beta emission [$E_{\beta max}$ - 2.12 MeV, E_γ - 155 keV (15%), half-life - 16.9 h] is especially useful for the therapy of large tumors in organs such as liver. Trans arterial radioembolization (TARE) using rhenium-188 labeled lipiodol is an effective and economically viable alternative to imported radiotherapeutic agents for liver cancer therapy. The ^{188}ReN(DEDC)$_2$ complex (hence forth written as ^{188}ReN-DEDC complex, DEDC – diethyl dithiocarbamate) extracted into lipiodol is one such radiopharmaceutical, which has proven its clinical efficacy for the therapy of liver cancer. ^{188}Re-HEDP (1-Hydroxy Ethylidene-1,1-Diphosphonic Acid) is another effective radiopharmaceutical for palliation of bone pain due to osseous metastasis. In-house development of freeze-dried kits for the preparation of ^{188}ReN-DEDC/lipiodol and ^{188}Re-HEDP will eliminate the dependence on imported kits, that had been a major impediment for its wide spread clinical application in India. This article highlights the contributions from BARC to clinical ^{188}Re-radiopharmaceutical program in India.

Key words: Rhenium-188, Radiopharmaceuticals, Therapy, Theranostic isotope, Liver cancer, Bone pain palliation, ^{188}ReN-DEDC, ^{188}Re-HEDP, Freeze-dried kits.

INTRODUCTION

Rhenium belongs to group-VII of the periodic table, same as that of technetium-99m, the isotope which is called the workhorse of nuclear medicine. It has two important radioisotopes, ^{186}Re [half-life - 3.71 days, $E_{\beta max}$ - 1.09 MeV, E_γ - 136 keV (9%)] and ^{188}Re [half-life - 16.9 h, $E_{\beta max}$ - 2.12 MeV, E_γ - 155 keV (15%)] [1]. Both radioisotopes have beta energies suitable for therapy with associated gamma emissions, which permits monitoring the distribution of the radiotracer in vivo. While relatively low-energy beta particles of ^{186}Re are useful for therapeutic applications requiring low tissue penetration, high-energy beta emissions from ^{188}Re are particularly useful for therapy of cancer in large organs like liver.

Being in the same group of the periodic table, technetium and rhenium may be expected to share similar chemistry. For example, pertechnetate (TcO_4^-) and perrhenate (ReO_4^-), in which both the metals are in their most stable oxidation state of +7, are iso-structural. With suitable ligands, both metals form complexes in +5 oxidation state. Both metals form *fac*-tricarbonyl complexes, ($[M(CO)_3]^+$; M = Tc, Re), in which the metal is in +1 oxidation state. Similarity in chemistry of technetium and rhenium prompt us to believe it is possible to have theranostic radiopharmaceutical pair with ^{99m}Tc and [188]Re radionuclides, wherein the ^{99m}Tc-radiopharmaceutical will be used for diagnosis and corresponding [188]Re-analogue for therapy. However, practically, rhenium in +7 oxidation is more difficult to reduce than technetium. Rhenium often requires acidic conditions for its efficient reduction, while technetium can be reduced under neutral or slightly acidic/basic conditions, ideally suited for radiopharmaceutical preparation. This is one of the reasons, we do not see rhenium analogue of all successful technetium radiopharmaceuticals.

Like the [99]Mo/^{99m}Tc generator, which had a significant role in making ^{99m}Tc the workhorse of nuclear medicine, the [188]W/[188]Re generator has the potential to popularize the use of [188]Re-radiopharmaceuticals for therapy. Commercial availability of [188]W/[188]Re generator fulfils the primary criteria to achieve this objective. However, unlike a [99]Mo/^{99m}Tc generator, a [188]W/[188]Re generator is several times costlier. At present in India, cost of a 500mCi [188]W/[188]Re generator is approximately 18 lakhs. For any nuclear medicine centre, economic viability of the services they provide is vital for their existence. Initial investment, a [188]W/[188]Re generator, necessary to start [188]Re-therapy program in a nuclear medicine centre being high, availability of sufficient number of effective [188]Re-radiopharmaceuticals for prime oncological applications is essential for efficient utilization of [188]Re-activity from the generator, which will make the therapy program sustainable.

Freeze-dried kits remarkably simplify the preparation of radiopharmaceuticals in a busy hospital radiopharmacy. Radiopharmaceuticals division, BARC, recognized the importance of in-house development of freeze-dried kits for the preparation of [188]Re-radiopharmaceuticals to boost [188]Re-therapy program in India. By carefully analyzing the trends in clinical nuclear medicine scenario, two [188]Re-radiopharmaceuticals, which could provide an effective and economically viable alternative to existing nuclear medicine practice, were selected. The first one was [188]ReN-DEDC/lipiodol for the therapy of unresectable primary liver cancers such as hepatocellular carcinoma (HCC) or intrahepatic cholangiocarcinoma (ICC) [2]. The second radiopharmaceutical was [188]Re-HEDP, a palliating agent for pain arising from bone metastasis [3]. At the time of conceptualizing this work, freeze-dried kits for the preparation of both of these [188]Re-radiopharmaceuticals were not available commercially. In this article, author briefly describe the development of freeze-dried kits for the preparation of the two selected radiopharmaceuticals starting from laboratory bench, culminating in its application in the clinic.

THERAPY OF LIVER CANCER
Background

HCC and ICC are the two most common primary liver cancers and represents the second most common causes of cancer death worldwide [4]. Patients presented with late stage HCC/ICC are often unresectable, and therefore, recommended for loco-regional therapies such as Trans arterial chemoembolization (TACE), TARE or sorafinib therapy, depending on the stage of the disease [5]. TARE is one of the minimally

invasive, image-guided loco-regional liver therapies in clinical practice today [6]. Primarily, this procedure embolizes the blood vessels feeding the tumor to deny vital nutrients and oxygen. Additionally, the radiotherapy agent in the embolizing medium delivers effective loco-regional therapy while sparing neighboring normal liver cells.

Some of the clinically available options for TARE include ^{90}Y-labeled microparticles [7, 8], ^{131}I-lipiodol [9, 10] and [188]Re-lipiodol [2, 11, 12]. Recent studies have proved the efficacy and safety of ^{90}Y-microparticles for TARE [13]. However, high cost of ^{90}Y-microparticle therapy limits its application to a small fraction of patients who can afford it. Though ^{131}I-lipiodol therapy provides an economically viable alternative, long half-life, low β-energy [$E_{\beta max}$ - 0.61 MeV (89.3%), 0.33 MeV (7.3%), 0.25 MeV (2.1%), half-life – 8.02 days] and the need for isolation of the patient post therapy, makes it a less preferred clinical choice.

[188]Re-Radiopharmaceuticals for TARE

Rhenium-188 radiopharmaceuticals for liver cancer therapy combine the low-cost benefit of ^{131}I-lipiodol therapy and, the safety and efficacy of ^{90}Y-microparticle therapy. Rhenium-188 has beta energy comparable to that of [90]Y [$E_{\beta max}$ - 2.28 MeV, half-life - 64.1 h] and hence comparable tissue penetration range could be expected. As mentioned earlier, presence of gamma emission, which permits monitoring the localization of radiopharmaceutical in the target tissue, is an added advantage of [188]Re-radiopharmaceutical over ^{90}Y-counterpart.

A common approach for the preparation of [188]Re-radiopharmceutical for liver cancer therapy involves preparation of a stable, lipophilic complex of [188]Re and its extraction into lipiodol (poppy seed oil). Subsequently, [188]Re-loaded lipiodol is used for TARE.

Jeong et al. reported a freeze-dried kit procedure for the preparation of a lipiodol solution of [188]Re-TDD (TDD - 2,2,9,9-Tetramethyl-4,7-diaza-1,10-decanedithiol) for therapy of liver cancer [11]. This method involved preparation of a lipophilic [188]Re-TDD complex and its extraction into lipiodol. Though [188]Re-TDD/lipiodol could be prepared in good yields, its retention in liver was not good enough for the therapy of liver cancer. The same group subsequently reported a modified form of [188]Re-TDD, the [188]Re-HDD (HDD - 4-hexadecyl-2,2,9,9-tetramethyl-4,7-diaza-1,10-decanedithiol), which showed higher retention in liver. In an IAEA-sponsored clinical study, Kumar et al. concluded that TARE with [188]Re-HDD/lipiodol is a safe and effective option for the therapy of inoperable hepatocellular carcinoma [12].

Though [188]Re-HDD/lipiodol is clinically used for the therapy of liver cancer, efficiency of extraction of [188]Re-HDD into lipiodol is poor (~50%). Lower extraction efficiency is an impediment to prepare higher patient doses of [188]Re-HDD/lipiodol and, quite often, the radiopharmacist is forced to do multiple preparations of [188]Re-HDD to obtain the required patient dose. Moreover, freeze-dried HDD kits are not available locally and have to be imported.

The [188]ReN-DEDC complex reported by Boschi et al. had higher extraction efficiency into lipiodol (>80%) and combined with excellent clinical efficacy for the therapy of HCC and ICC by TARE, it presents itself as an effective alternative to existing clinical option. Based on these facts, we decided to develop these kits in-house to ensure uninterrupted local availability at an affordable cost.

[188]ReN-DEDC/lipiodol for liver cancer therapy

Preparation of [188]ReN-DEDC complex involves two steps [2]. First step involves the preparation of $[^{188}ReN]^{2+}$ (rhenium nitride) intermediate, the precursor for the preparation
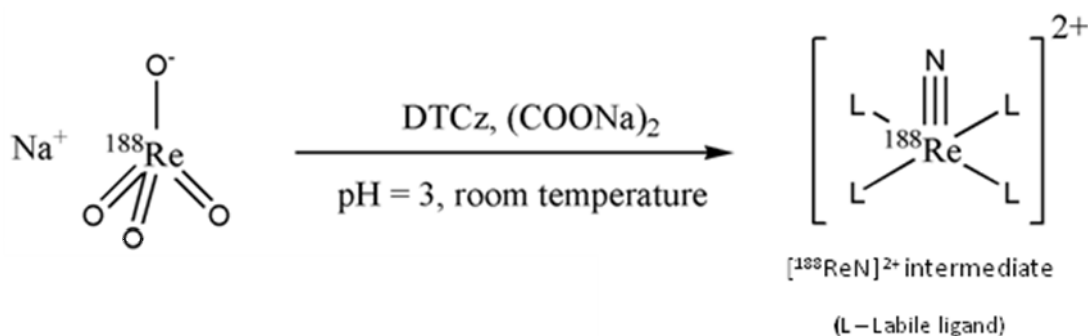
Figure 1. Preparation of [^{188}ReN]$^{2+}$ intermediate

Figure 1. Preparation of [^{188}ReN]$^{2+}$ intermediate

of ^{188}ReN-DEDC complex (Figure 1). The reaction involved reduction of [^{188}ReO$_4$]$^-$ by stannous chloride dihydrate (SnCl$_2$.2H$_2$O) followed by attack of the nitride (N^{3-}) ion from N-methyl-S-methyl dithiocarbazate (DTCz). This reaction is highly facilitated under acidic conditions (pH = 3) and kinetics of [^{188}ReO$_4$]$^-$ reduction is enhanced in the presence of oxalate ligand. Therefore, glacial acetic acid and disodium oxalate are added in the reaction mixture while preparing [^{188}ReN]$^{2+}$ intermediate.

The [^{188}ReN]$^{2+}$ intermediate has square pyramidal structure with 'N' atom occupying the apex of the square pyramid and four labile ligands (L) occupying the four corners of the basal plane. It should be noted that nitride ion donor, DTCz, itself can act as a ligand in the present case.

The second step involves the preparation of ^{188}ReN-DEDC complex from [^{188}ReN]$^{2+}$ intermediate prepared in the first step (Figure 2) by incubating with DEDC ligand at 70°C for 20 min. The pH of the reaction mixture was maintained at 6.

The neutral, lipophilic, ^{188}ReN-DEDC complex thus prepared was subsequently extracted into lipiodol and used for TARE procedure for the therapy of liver cancer.

Kit procedure for the preparation of ^{188}ReN-DEDC/lipiodol

Freeze-dried kits are designed to prepare radiopharmaceuticals in minimum time, following simple procedures, in a busy hospital radiopharmacy. A freeze-dried kit contains all the necessary reagents, except radioactivity, for the preparation of a radiopharmaceutical. A two-vial freeze-dried kit for the preparation of ^{188}ReN-DEDC complex was made in-house following a previously optimized procedure. Kit vial 1 for the preparation of [^{188}ReN]$^{2+}$ intermediate contained DTCz (2 mg), disodium oxalate (28 mg) and stannous chloride dihydrate (0.8 mg). Kit vial 2 contained DEDC ligand and carbonate buffer. To prepare the complex using freeze-dried kits, glacial acetic acid (0.1 mL) and freshly eluted Na^{188}ReO$_4$ (3 mL, ~185 MBq) from a ^{188}W/^{188}Re generator was mixed and transferred into kit vial 1. The vial was gently shaken to dissolve the contents and then incubated at room temperature for 30 min to obtain [^{188}ReN]$^{2+}$ intermediate. In step two, kit vial 2 was reconstituted with sterile saline (2 mL) and 1.5 mL of the reconstituted solution was transferred into vial 1 containing [^{188}ReN]$^{2+}$ intermediate. The two solutions are thoroughly mixed and incubated at 70°C for 20 min to obtain ^{188}ReN-DEDC complex. After cooling the vial to room temperature, lipiodol (3 mL) was added to kit vial 1. The contents of
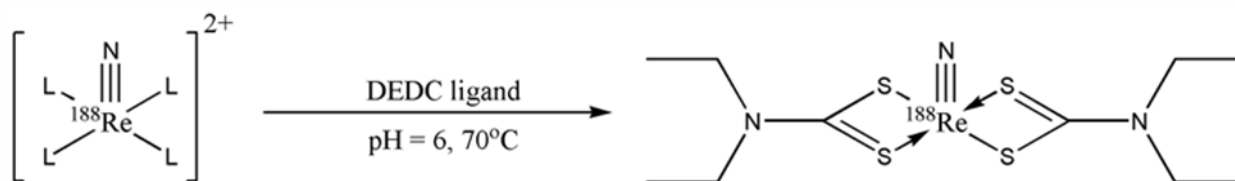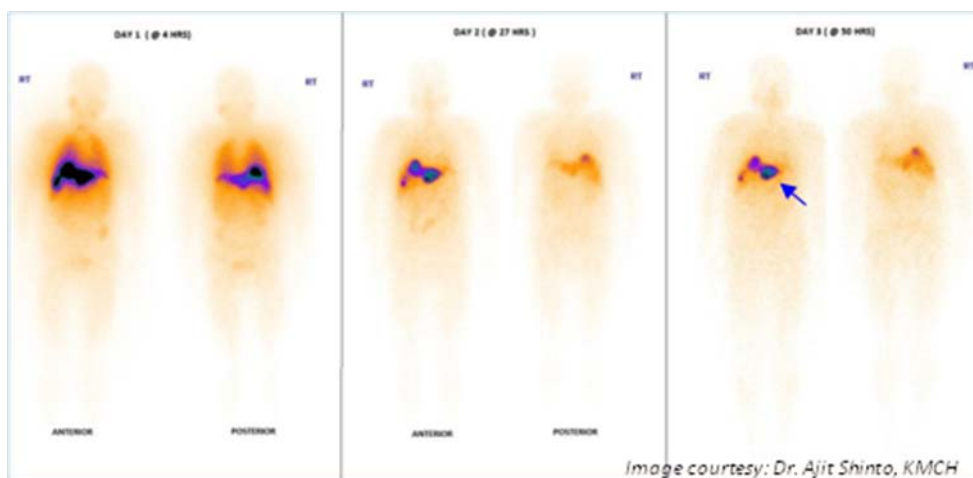
Figure 2. Preparation of ^{188}ReN-DEDC complex

Figure 3. Typical clinical images of a liver cancer patient obtained at
4h, 27h and 50h after injecting ~50mCi of ^{188}ReN-DEDC/lipiodol by TARE procedure

the kit vial were thoroughly agitated in a vortex mixture to effect maximum extraction of the lipophilic ^{188}ReN-DEDC complex into the lipiodol phase. The lipiodol phase containing ^{188}ReN-DEDC complex is used for therapy of liver cancer by TARE procedure. Using this kit, ^{188}ReN-DEDC complex could be prepared in >80% radiochemical purity and >95% extraction in lipiodol phase could be achieved.

The two-vial kit for the preparation of ^{188}ReN-DEDC/lipiodol is in the process of obtaining regulatory approval from Radiopharmaceuticals Committee (RPC) for its production and supply to various nuclear medicine centers across India through Board of Radiation and Isotope Technology (BRIT), Vashi.

Limited clinical Evaluation

After obtaining necessary hospital ethical committee clearance, limited clinical trials of ^{188}ReN-DEDC/lipiodol, prepared using the two-vial kits developed in BARC, was carried out in Tata Memorial Hospital (TMH), Mumbai, and, Kovai Medical Centre and Hospital (KMCH), Coimbatore. Preliminary results of the clinical trials are satisfactory and as per expectations. Typical clinical images of a liver cancer patient obtained at different time intervals during the course of therapy are shown in Figure 3.

From Figure 3, it could be noted that activity deposited in liver by tare procedure is retained even after 50h post injection (blue arrow). It is

also important to note that there is no significant accumulation of activity in any other part of the body, especially the lungs and kidneys. At present, extensive dosimetric studies of this agent is being carried out at KMCH, Coimbatore.

Making the two-vial kit more user-friendly!
As mentioned in the previous section, the preparation of [188]ReN-DEDC complex using two-vial kit required addition of stipulated volume of glacial acetic acid for efficient preparation of the $[^{188}ReN]^{2+}$ intermediate. An error by the radiopharmacist in this step can potentially affect the formation of $[^{188}ReN]^{2+}$ intermediate as well as the optimum pH required for the reaction mixture in the crucial second step, leading to low radiochemical purity of [188]ReN-DEDC complex. In routine conventional radiopharmacy operations, an "acetic acid free" procedure for the preparation of [188]ReN-DEDC complex could be more reliable and reproducible, thus helping to avoid any inappropriate usage of the radiopharmaceutical.

In Radiopharmaceuticals division, we devised a simple strategy to solve this problem by including a buffer of pH 3 in the kit vial itself to create a conducive environment for $[^{188}ReN]^{2+}$ intermediate formation. The basis of this strategy was the observation that disodium oxalate, salt of oxalic acid, is a constituent of kit vial 1 discussed above [2] and by including calculated amount of oxalic acid, it is possible to construct a buffer of pH = 3, which would then eliminate the need of adding glacial acetic acid.

We prepared a freeze-dried oxalate buffer kit of strength 0.5M and used it for the preparation of $[^{188}ReN]^{2+}$ intermediate. The only difference in the procedure for the preparation of $[^{188}ReN]^{2+}$ intermediate using oxalate buffer kit was that there is no need to add glacial acetic acid. The formation of $[^{188}ReN]^{2+}$ intermediate using oxalate buffer kit

and its radiochemical purity was determined by HPLC. Figure 4 shows the formation of $[^{188}ReN]^{2+}$ intermediate as a function of incubation time at room temperature. For comparison, $[^{188}ReN]^{2+}$ intermediate prepared by glacial acetic acid method is also shown in Figure 4. It could be noted that using 0.5M oxalate buffer kit, ~96% formation of $[^{188}ReN]^{2+}$ intermediate was complete as early as 5 min. No further improvement in RCP was observed. By conventional method, however, only about 28% $[^{188}ReN]^{2+}$ intermediate formation was complete during the same time interval. After 30 min incubation at room temperature, RCP of $[^{188}ReN]^{2+}$ intermediate prepared by conventional method approached that of 0.5M oxalate buffer kit. Typical HPLC elution profile of $[^{188}ReN]^{2+}$ intermediate prepared by glacial acetic acid method and oxalate buffer method is shown Figure 5. It could be noted that there is no difference in the HPLC elution profile of $[^{188}ReN]^{2+}$ intermediate prepared by either methods.
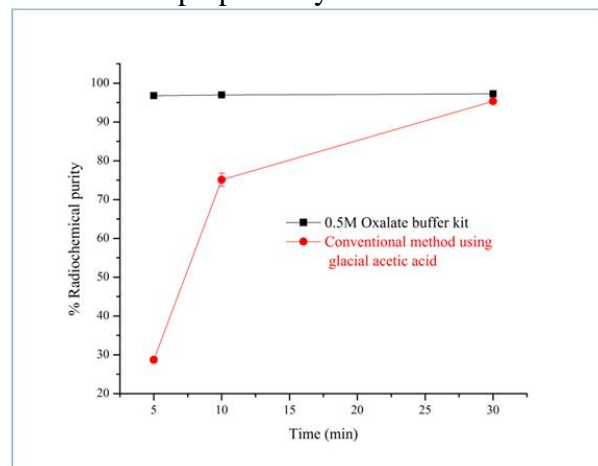

Figure 4. Variation in radiochemical purity of $[^{188}ReN]^{2+}$ intermediate prepared by conventional glacial acetic acid method and using 0.5M Oxalate buffer kit as a function of time

Subsequently, the [188]ReN-DEDC complex was prepared from $[^{188}ReN]^{2+}$ intermediate prepared using oxalate buffer kit (0.5M). We
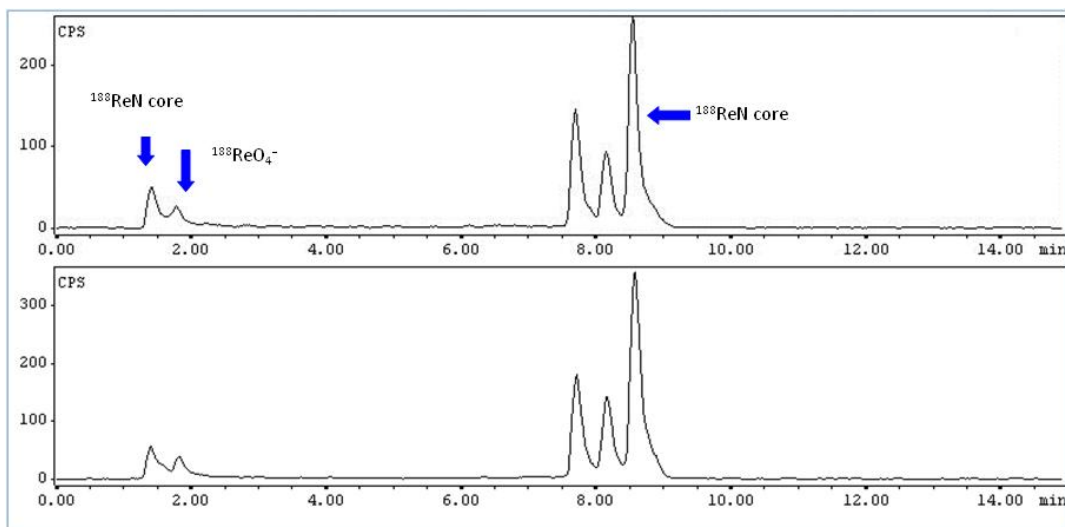
Figure 5. Typical HPLC elution profile of [^{188}ReN]$^{2+}$ intermediate prepared by (Top) glacial acetic acid method and (Bottom) 0.5M Oxalate buffer after 30 min incubation at room temperature

observed that ^{188}ReN-DEDC complex could be consistently prepared in >80% RCP. In addition, the ^{188}ReN-DEDC complex prepared by both methods showed >95% extraction into lipiodol phase.

The novel oxalate buffer method has led to a significant simplification of the procedure required for in-house production of this therapeutic agent. Considering that routine manipulation of high-energy β-emitters always constitutes a significant health hazard for operators involved in this type of radiopharmaceutical preparations, the more user-friendly kit described here could contribute to drastically decrease the radiation exposure, particularly when used in a busy hospital radiopharmacy. Process to obtain regulatory clearance for the manufacture and supply of oxalate buffer kits for the preparation of ^{188}ReN-DEDC/lipiodol has been initiated.

BONE PAIN PALLIATION
^{188}Re-HEDP for bone pain palliation

Bone metastasis is common in patients with cancer of prostrate, breast, lung, bladder and thyroid. Problems associated with bone metastasis include severe pain, pathological fracture, spinal cord compression etc., which can compromise the quality of life of the patient by affecting mobility and sleep. Clinical management of pain itself can significantly improve the quality of life of the patient. Radionuclidic therapy is one of the modalities widely being practised for bone pain palliation. This involves selective delivery of radiation dose to the affected bone lesions, which are responsible for pain to the patient.

Bisphosphonates are by far the most widely explored molecules for preparing bone seeking radiopharmaceuticals [14]. HEDP is one such phosphonate which has shown strong adsorption on hydroxyapatite, the major constituent of bone, *in vitro* [15]. Liepe et al. reported a comparative study of surface bone-seeking radiopharmaceuticals ^{186}Re-HEDP, ^{188}Re-HEDP, ^{153}Sm-EDTMP (EDTMP – ethylene diamine tetramethylene phosphonic acid) and the volume seeker ^{89}Sr (as ^{89}SrCl$_2$) for the treatment of skeletal metastases [15]. This study concluded that all the radiopharmaceuticals are helpful in rendering pain relief to the patient with no significant

difference in their therapeutic efficacy or toxicity [15]. The clinical efficacy of the above radiopharmaceuticals for bone pain palliation being similar, the choice may be made on the basis of relative logistical advantage and cost factor of the radiopharmaceutical. In this context, ^{188}Re-HEDP enjoys advantage since it can be prepared "on demand" in any hospital radiopharmacy housing a ^{188}W/^{188}Re generator. In this context, availability of a freeze-dried kit for the preparation of ^{188}Re-HEDP would be of great help for easy and efficient preparation of this radiopharmaceutical in a busy radiopharmacy.

Freeze-dried HEDP kits

Formulation of a lyophilized HEDP kits for the preparation of ^{188}Re-HEDP was initially reported by Verdera et al [16]. Later, Marczewski et al. reported a liquid kit preparation for the same purpose [17]. Practical difficulty associated with liquid kit formulation involved its shelf-life (approximately 9 days) and logistics associated with its transport to distant places.

There is a wide variation in the amount of HEDP, gentisic acid and stannous chloride dihydrate in the freeze-dried HEDP kits reported by different groups for the preparation of ^{188}Re-HEDP [16-18]. In the present work, although the amount of reagents used were similar to that reported by Verdera et al., there is significant difference between the two formulations. While rhenium carrier (300 µg potassium perrhenate; total rhenium metal content 193 µg) was included in the lyophilized kit formulated by Verdera et al., no rhenium carrier is included in the kit vial reported herein. This was done to avoid the possibility of the Sn^{+2} ions being consumed by carrier rhenium in the kit, which could ultimately affect the shelf-life of the kit.

Procedure for the preparation of freeze-dried HEDP kits without carrier rhenium was optimized. Six consecutive batches of freeze-dried HEDP kits were prepared to demonstrate the robustness of the procedure. Randomly selected kits from all the six batches were subjected to thorough quality control tests before declaring fit for use in clinical applications. A proposal was submitted to RPC to obtain regulatory approval for the manufacture and supply of these kits to various nuclear medicine centres through BRIT, Vashi. Freeze-dried HEDP kit is now a RPC approved radiopharmaceutical kit for the preparation of ^{188}Re-HEDP for bone pain palliation (Fig. 6).

Figure 6. Freeze-dried HEDP kits

Kit procedure for the preparation of ^{188}Re-HEDP

Typical procedure for the preparation of ^{188}Re-HEDP using freeze-dried HEDP kit is as follows. About 1 µmol (in ~100 µL) of perrhenic acid ($HReO_4$) or ammonium perrhenate (NH_4ReO_4) supplied along with the freeze-dried HEDP kit was thoroughly mixed with 1 mL of freshly eluted Na^{188}ReO$_4$ from a ^{188}W/^{188}Re generator. This solution was aseptically transferred to the sterile HEDP kit vial. Subsequently, the kit vial was heated at 100°C for 15 min. After cooling the vial to room temperature, pH of the preparation was adjusted to physiological level by adding sodium acetate solution (0.5 mL) supplied with the kit. The ^{188}Re-HEDP complex thus prepared should pass the necessary quality control tests before it can be injected into the patient.

Table 1. Quality control check list for [188]Re-HEDP prepared using lyophilized kit

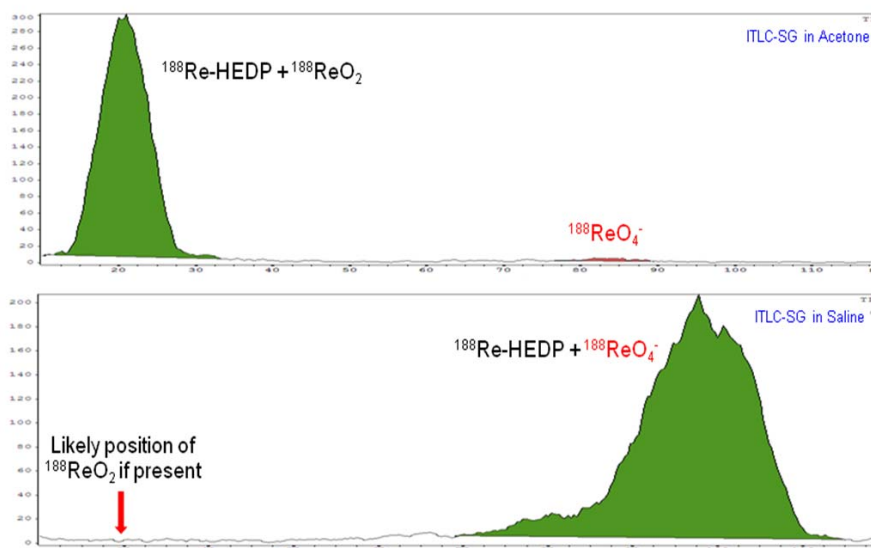| QC parameter	Results obtained	Determined by
Appearance	Clear	Visual inspection
Colour	Pale yellow - amber	Visual inspection
pH	5 - 6	Non-bleeding pH paper
Radiochemical purity	>95%	ITLC-SG

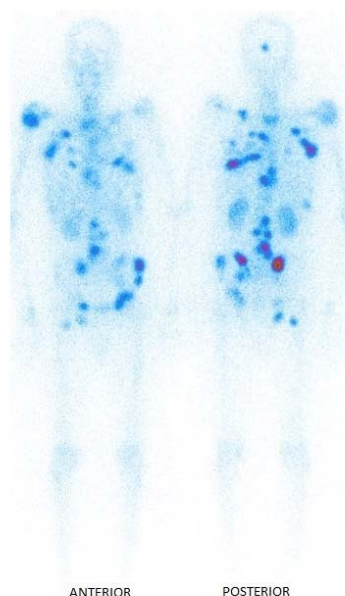**Figure 7**. Typical ITLC-SG pattern of [188]Re-HEDP in acetone and saline

Fig. 8. Typical whole-body scan of a patient obtained 24 hours after [188]Re-HEDP injection. The scan shows extensive bone metastasis.

Quality control parameters (Table 1) for [188]Re-HEDP include visual inspection of the preparation to determine clarity and colour, followed by determination of pH and RCP. The RCP of [188]Re-HEDP should be >95% to pass the quality control check. Typical ITLC-SG pattern of [188]Re-HEDP in saline and acetone is shown in Figure 7.

Clinical evaluation

Clinical evaluation of [188]Re-HEDP prepared using freeze-dried HEDP kits were carried out in various nuclear medicine centers in India, including, Tata Memorial Hospital, Mumbai, Radiation Medicine Center, Mumbai and Kovai Medical Centre and Hospital, Coimbatore. The clinical results are satisfactory and in expected lines. Patients injected with [188]Re-HEDP experienced the onset of pain relief within a week and pain-free period lasted for several weeks. A typical clinical image obtained with [188]Re-HEDP is shown in Figure 8.

A significant advantage with BARC HEDP kits discussed here compared to the commercial HEDP kits is that the former kit can be used with up to 5 mL of freshly eluted [188]Re-activity while the latter kit is restricted to use only 2 mL of activity. This feature of BARC HEDP kits comes in handy at the fag end of generator-life when radioactive concentration (RAC) or activity per millilitre available from the generator decreases drastically. It can be explained further with a real scenario in a hospital radiopharmacy. A hospital radiopharmacy having access to [188]Re-activity of RAC 10 mCi/ml requires just a single BARC HEDP vial to prepare a patient dose of ~50 mCi (5 mL x 10 mCi). At the same time, due to volume limitation in commercial HEDP kit vial which is 2 mL, the radiopharmacist will be forced to use two HEDP vials to prepare the same patient dose. This may result in escalation of cost of therapy as well as dose received by the radiopharmacist during radiopharmaceutical preparation.

Conclusions

In a nuclear medicine centre, initial investments required to start a diagnostic or therapeutic program and the returns expected from the program are prime considerations. Considering relatively high cost of [188]W/[188]Re generator, it is important to use the generator for as many applications as possible so that the program is self-sustainable. Therefore, improving the [188]Re-radiopharmaceutical portfolio for therapeutic applications is very essential. The rhenium radiopharmaceuticals development program in Radiopharmaceuticals Division, Bhabha Atomic Research Centre, is essentially aimed at improving the [188]Re-radiopharmaceutical portfolio at an affordable cost. Development of freeze-dried DEDC kits for the preparation of [188]ReN-DEDC/lipiodol for the therapy of inoperable HCC, along with other freeze-dried kits such as HEDP kits, is a timely step in the right direction, which will help boosting [188]Re-radiopharmaceuticals program in India.

Sarma at various stages of kit development. The author also take this opportunity to thank clinical collaborators, Dr. V. Rangarajan, Tata Memorial Centre, Mumbai, Dr. Ajit Shinto, Kovai Medical Centre and Hospital, Coimbatore, and Dr. Sandeep Basu, Radiation Medicine Centre, Parel, for their help in clinical evaluation of rhenium-188 radiopharmaceuticals.

References

[1]. Singh, B, Viggars, DA. (1981). Nuclear data sheets for A = 188. Nuclear Data Sheets, 33(2), 275-387.

[2]. Boschi A, Uccelli L, Duatti A, Colamussi P, Cittanti C, Filice A, Rose AH, Martindale AA, Claringbold PG, Kearney D, Galeotti R, Turner JH, Giganti M. A kit formulation for the preparation of 188Re-lipiodol: preclinical studies and preliminary therapeutic evaluation in patients with unresectable hepatocellular carcinoma. Nucl Med Commun. 2004;25(7):691-9.

[3]. Maxon HR. 3rd, Schroder LE, Washburn LC, Thomas SR, Samaratunga RC, Biniakiewicz D, Moulton JS, Cummings D, Ehrhardt GJ, Morris V. Rhenium-188(Sn)HEDP for treatment of osseous metastases. J Nucl Med 1998;39(4):659.

[4]. Ferlay J, Soerjomataram I, Dikshit R, Eser S, Mathers C, Rebelo M, et al. Cancer incidence and mortality worldwide: sources, methods and major patterns in GLOBOCAN 2012. Int J Cancer 2015;136:E359-E386.

[5]. European Association For The Study Of The Liver; European Organisation For Research And Treatment Of Cancer. EASL-EORTC clinical practice guidelines: management of hepatocellular carcinoma. *J Hepatol* 2012;56:908-943, Maida M, Orlando E, Cammà C, Cabibbo G. Staging systems of hepatocellular carcinoma: a review of literature. World J Gastroenterol 2014;20:4141-4150.

[6]. Gbolahan OB, Schacht MA, Beckley EW, LaRoche TP, O'Neil BH, Pyko M. Locoregional and systemic therapy for hepatocellular carcinoma. J Gastrointest Oncol. 2017; 8(2):215-228.

[7]. Fidelman N, Kerlan RK Jr, Hawkins RA, Pampaloni M, Taylor AG, Kohi MP, Kolli KP, Atreya CE, Bergsland EK, Kelley RK, Ko AH, Korn WM, Van Loon K, McWhirter RM, Luan J, Johanson C, Venook AP. Radioembolization with (90)Y glass microspheres for the treatment of unresectable metastatic liver disease from chemotherapy-refractory gastrointestinal cancers: final report of a prospective pilot study. J Gastrointest Oncol. 2016;7(6):860-874.

[8]. Hoffmann RT, Paprottka PM, Scho n A, Bamberg F, Haug A, Du rr EM, Rauch B, Trumm CT, Jakobs TF, Helmberger TK, Reiser MF, Kolligs FT. Transarterial hepatic yttrium-90 radioembolization in patients with unresectable intrahepatic cholangiocarcinoma: factors associated with prolonged survival. Cardiovasc Intervent Radiol. 2012;35(1):105-16.

[9]. Lintia-Gaultier A, Perret C, Ansquer C, Eugène T, Kraeber-Bodéré F, Frampas E. Intra- arterial injection of 131I-labeled Lipiodol for advanced hepatocellular carcinoma: a 7 years' experience. Nucl Med Commun. 2013;34(7):674-81.

[10]. Ahmadzadehfar H, Habibi E, Ezziddin S, Wilhelm K, Fimmers R, Spengler U,Palmedo H, Strunk H, Schild HH, Biersack HJ, Risse J. Survival after 131I-labeled lipiodol therapy for hepatocellular carcinoma. A single-center study based on a long-term follow-up. Nuklearmedizin. 2014;53(2):46-53.

[11]. Jae Min Jeong, Young Joo Kim, Yoon Sang Lee, Jun Il Ko, Miwon Son, Dong

Soo Lee, June-Key Chung, Jae Hyung Park, Myung Chul Lee, Lipiodol solution of a lipophilic agent, 188Re-TDD, for the treatment of liver cancer, Nucl Med Biol, 2001;28(2):197- 204.

[12]. Kumar A, Srivastava DN, Chau TT, Long HD, Bal C, Chandra P, Chien le T, Hoa NV, Thulkar S, Sharma S, Tam le H, Xuan TQ, Canh NX, Pant GS, Bandopadhyaya GP. Inoperable hepatocellular carcinoma: transarterial 188Re HDD-labeled iodized oil for treatment--prospective multicenter clinical trial. Radiology. 2007;243(2):509-19.

[13]. Wang EA, Broadwell SR, Bellavia RJ, Stein JP. Selective internal radiation therapy with SIR-Spheres in hepatocellular carcinoma and cholangiocarcinoma. J Gastrointest Oncol. 2017;8(2):266-278.

[14]. Lam MG, de Klerk JM, van Rijk PP. [186]Re-HEDP for metastatic bone pain in breast cancer patients. Eur J Nucl Med Mol Imaging 2004;31(Suppl 1):S162.

[15]. Liepe K, Kotzerke J. A comparative study of [188]Re-HEDP, [186]Re-HEDP, [153]Sm-EDTMP and ^{89}Sr in the treatment of painful skeletal metastases. Nucl Med Commun 2007;28(8):623.

[16]. Verdera ES, Gaudiano J, León A, Martinez G, Robles A, Savio E, León E, McPherson D W, Knapp FF(Russ) Jr. Rhenium-188-HEDP kit formulation and quality control. Radiochimica Acta 1997;79:113.

[17]. Marczewski B, Dias CR, Moraes V, Osso JA Jr. Liquid kit for preparation of [188]Rhenium-etidronate. Braz Arch Biol Technol 2005;48(2):137.

[18]. El-Mabhouh A, Mercer JR. [188]Re-labeled bisphosphonates as potential bifunctional agents for therapy in patients with bone metastases. Appl Radiat Isot 2005;62(4):541.

Fuel management in AHWR

Amit Thakur and Baltej Singh

Reactor Physics Design Division

Amit Thakur is the recipient of the DAE Young Applied Scientist /
Technologist Award for the year 2015

Abstract: The Advanced Heavy Water Reactor(AHWR) [1-2] is being designed with advance safety features and closed fuel cycle, where full length fuel cluster is designed to have high discharge burn-up fuel (40-60 GWd/Te) with on-power refueling. The in-core fuel management and initial core optimization problems for AHWR are quite different from conventional reactors like Pressurized Heavy Water Reactors (PHWRs) and Light Water Reactor (LWRs). The in-core fuel management of AHWR needs to be a suitable combination of fuel management practices observed in PHWRs and LWRs. Therefore, on-power refueling scheme for in-core fuel management of AHWR was developed. Different modern algorithms like Genetic Algorithm (GA) [3-4] and Estimation of Distribution Algorithms (EDA) [5] were applied to optimize the initial core of AHWR.

Introduction

As a step towards developing technologies for Th-^{233}U based next generation reactors, AHWR is being designed. Purpose of AHWR is to design a unique reactor with all the advanced safety features, where Thorium based reactor technologies will be used and developed by utilizing past experience and expertise of PHWRs & LWRs. The distinctive fuel cycle of AHWR necessitates the development of on-power refueling scheme for efficient fuel utilization in initial phase, transition phase and equilibrium phase. Brief descriptions of the problems like in-core fuel management for AHWR as well as initial core loading pattern optimization (LPO) of AHWR and development of optimization techniques to address the problems is given below.

In-core fuel management for AHWR

Reactors with batch refueling like pressurized water reactors (PWRs) and boiling water reactors (BWRs) require loading pattern optimization (LPO) for proper utilization of fuel. In case of heavy water reactors like PHWRs, the refueling scheme is relatively simple mainly due to on-line refueling, use of small length bundle and NU as fuel. The use of NU as fuel, small length fuel bundle and flexibility of multi-bundle shift scheme helps in controlling the ripples in power due to on-power

refueling. The AHWR has features of both PWRs (high discharge burn-up fuel) and PHWRs (on-power refueling) and has several inherent passive safety features. The AHWR has flexibility to use (Th, U, Pu) MOX or (Th, LEU) MOX as fuel with boiling light water as coolant and heavy water as moderator. However, during on-power refueling with full length channel and high enrichment fuel, the challenge is to control the on-power refueling ripples and maintaining the power distribution close to design power distribution and maintain all the operational parameters within their design limits. The on-power refueling strategy with an objective to control the flux distribution and hence power peaking was developed for AHWR. In the AHWR refueling scheme, each refueling operation should be followed by one or two reshuffling operations so that refueling ripples are contained within their design limit. The on-power refueling scheme requires selection of two / three channels (one for refueling and one/two for reshuffling) at each refueling. For selecting two appropriate channels from a core consisting of ~444 fuel channels, we have to study $^{444}P_2$ number of possible combinations. Simulation of all these combinations and finding out the best one seems very cumbersome and time consuming. The best combination found out this way will be used for one refueling only. For every refueling one has to

simulate same number of combinations. Selection of suitable channels for refueling and reshuffling is a complex problem. In our work, we have introduced a concept of refueling factor and reshuffling factor for each channel in reactor.

We have defined refueling factor (*RF)* as:-

$$RF = K \frac{B}{D \cdot CP \cdot C1 \cdot C2} \qquad (1)$$

Here, '*K*' is proportionality constant. The value of *K* can be taken as 1. Where '*CP'* is channel power of channel, '*C1'* is average power of 1st neighbors of channel and '*C2*' is average power produced by 2nd neighbors of channel. All the channels are arranged in descending order of their refueling factors. The preference order for channels to be discharged has been decided.

We have defined reshuffling factor *(Resh F)* as:-

$$\text{Resh F} \quad = 0 \qquad \text{if } B < \frac{G}{5} \text{ or B} > (1.5 \cdot G)$$

$$= K \frac{D}{B \cdot CP \cdot C1 \cdot C2} \qquad \text{if } \quad \frac{G}{5} < B < (1.5 \cdot G) \qquad (2)$$

Where 'G' is core average burnup.

It is to be noted that in the above burnup range, the channels which are having lower burnup and present in low flux regions will be more suitable candidates for reshuffling. These factors will give the priority for a particular cluster for refueling and reshuffling and are assigned to each fuel cluster of the core. A computer program CARS (Code for Automated Refueling Strategy) [6] has been developed, where the selection of fuel channels for refueling/reshuffling has been automated. The program was developed such that the fuel cluster which has achieved its target discharge burn-up is selected for discharge on priority keeping the power peaking in control. Fig 1 shows the maximum channel power (MCP) behavior with full power days (FPDs) for simulations carried out using CARS. Several 3D diffusion calculations are required for simulating all these refueling schemes.

Parallel processing on shared memory interface has been used to reduce the time for fuel cycle study for AHWR. Table 1 shows the comparison study of design parameters before using CARS and after using CARS.
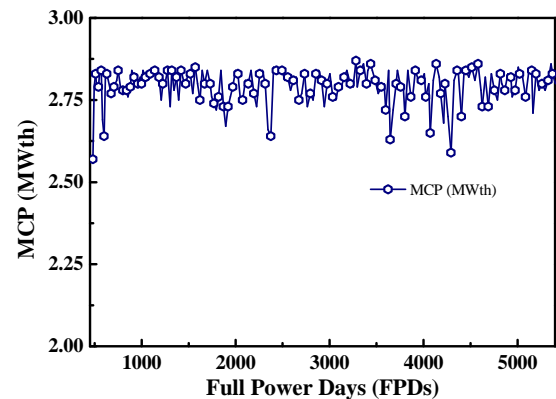

Fig 1: MCP vs full power days using CARS

Initial core Optimization of AHWR
The loading of only one type of fresh fuel (say equilibrium core cluster) in the initial core shall give centrally peaked flux distribution. However, flat flux distribution is required for maximizing the power output from a given initial core loading. Therefore, initial core loading needs at least two types of differentially reactive clusters to achieve flat flux distribution from the initial core. Moreover, the equilibrium core cluster is highly reactive as it has been designed for a discharge burn-up of 40 GWd/Te, therefore its loading in initial core of AHWR will require a large quantity of neutron poison in moderator to suppress its excess reactivity. Presence of large amount of neutron poison in moderator will adversely affect different reactivity feedbacks and worth of reactivity devices and shut down system (SDS). Therefore, two initial core clusters (containing lesser fissile content) namely type-1 and type-2 were designed for initial core loading of AHWR.
The loading of two types of initial core clusters in the AHWR initial core is a combinatorial optimization problem. The objective is to find out the location and number of channels of different types of fuels to be loaded for a flat power distribution and maintain reactivity worth of

Table-:1 Comparison of core key parameters for different refuelling schemes

Refueling Scheme adopted	MCP (MW)	MMP (kW)	Discharge burnup achieved (GWd/Te)	In-core excess reactivity maintained (mk)
Without CARS	2.5<MCP<6.9	140<MMP<380	55	~10
With CARS	2.5<MCP<2.85	140<MMP<180	59	~10

Table-2 Properties of optimized loading pattern

Max. Objective function	K-eff	MCP (MW)	MMP (KW)	Worth of SDS-1 (mk)	Type-1 Clusters	Type-2 Clusters
1.00953	1.00953	2.58	154	63.1	356	88

reactivity devices close to or better than the design values while maximizing core excess reactivity or k-effective. This type of problem can be solved by defining one objective function and then maximize or minimize it. For AHWR initial core, penalty method has been used to define the objective function [7-8].

The objective function (OF) for this problem is defined as

$$OF = (A_1 \cdot keff) - A_2(MCP - 2.6) - A_3(MMP - 200) - A_4(63.0 - worth\ of\ SDS1) \quad (3)$$

Where A_1, A_2, A_3 and A_4 are constants and its value is based on few test simulations [9]. The maximum channel power (MCP), maximum mesh power (MMP) and shut-down system (SDS) worth limit for initial core have been considered as 2.6 MWth, 200 KWth and 63.0 mk respectively.

Modern optimization methods based on evolutionary algorithms are frequently being used for fuel loading pattern optimization problems. In modern optimization algorithms, a two step procedure is followed. In first step, a pool of randomly generated solutions is evaluated and in second step, new set of solutions is generated by considering feedback from the current evaluations. We have developed a computer code based on estimation of distribution (EDA) [7-8] to optimize the initial core of AHWR. The distributed memory parallel computer system AGGRA at BARC was used for parallelization. In EDA, we start with an initial probability distribution function and generate probable pool of candidate solutions based on this probability distribution function. After evaluation of the objective function value for all the candidates in the present sample, the probability distribution function is modified by giving some weight to current best solutions. The most basic form of EDA has been given below:-

Step-1: Generate a population (N) of different loading patterns based on initial distribution function. This population consists of solution candidates for fitness estimation. In each generation, same population size (N) is maintained and is evaluated. However, the candidates in the pool are modified from the feedback given by previous generation.

Step-2: Simulate all the candidates of this population by solving diffusion equation using FEMINA [10] and objective function for all the candidates are evaluated.

Step-3: Select best $M < N$ candidates based on objective function values

In present study, M is considered as 25% of N.

Step-4: The distribution function (DF) for generating loading pattern is modified

DF (t+1) = DF (t) · (1-α) + α · X

where, 'α' (weighing factor) is a constant and its value is between 0 and 1. 't' represents the generation.

Where $X = \frac{1}{M} \cdot \sum_{i=1}^{M} X_i(t)$

$X_i(t)$ is 0 or 1 based on the loading of a particular fuel in fuel lattice location.

Step-5: Again generate the population of different loading patterns based on new distribution function

Step-6: Go to step-2 and repeat the cycle till optimization is achieved

Suitable values for various internal parameters like population size and weighing factor (α) in each generation for AHWR initial core loading pattern optimization problem have been estimated in EDA.

The same problem of AHWR initial core LPO was also solved by using Genetic algorithm (GA) [7]. The first two steps of the GA are similar to EDA, however, in the third step, two person tournament, the selection is done for creating the mating pool. New candidates of population size N is generated by using uniform cross-over operator between different candidates of mating pool. And this process is repeated till optimization is achieved. In the study, we have observed that by considering proper choice of internal parameters for GA too, same initial core loading pattern is achieved. Table-2 describes the properties of optimized loading pattern. It is observed that the optimized LP meets the design conditions of MCP and SDS worth. The excess reactivity observed is also better than earlier optimized two zone patterns by hit and trial.

Conclusions

A computer code CARS (Code for AHWR Refueling Strategy) for the in-core fuel management is developed. The CARS provides a set of fuel clusters for replacement with fresh ones and another set of fuel clusters for reshuffling within the core at their pre-determined locations at every stage of core follow-up. The CARS has reduced all the manual work for the selection of fuel clusters for refueling. It has been able to enforce the selection criteria strictly to improve the quality of fuel management and reduce the time taken for completing the job by a few order of magnitudes.

For initial core optimization problem for AHWR, two modern optimization algorithms based on GA and EDA have been developed for AHWR initial core loading patterns. The optimum value of internal parameters for both the algorithms was estimated and the initial core of AHWR was optimized.

References

1. Sinha, R.K., Kakodar, A., 2006. "Design and development of AHWR-the Indian thorium fueled innovative reactor". Nuclear Engineering and Design 236, 683–700.
2. Amit Thakur, Baltej Singh, Neelima Prasad Pushpam, Vishal Bharti, Umasankari Kannan, P. D. Krishnani and R. K . Sinha, "Fuel cycle flexibility in Advanced Heavy Water Reactor (AHWR) with the use of Th-LEU fuel", Int. Conf. on Future of Heavy Water Reactors (FHWR -2011), Ontario, Canada, Oct. 02-05, 2011.
3. Goldberg, D.E., 1989. "Genetic Algorithms in Search Optimization and Machine Learning". Addison-Wesley, Reading, New York.
4. Parks G. T., 1996. "Multiobjective pressurized water reactor reload core design by non domindated genetic algorithm search". Nucl. Sci. and Eng. 124,178-187.
5. S. Jiang, A. K. Ziver, J. N. Carter, C. C. Pain, A. J. H. Goddard, S. J. Franklin, and H. Phillips. "Estimation of distribution algorithms for nuclear reactor fuel management optimization". Annals of Nuclear Energy, 33(12):1039-1057, 2006.
6. Amit Thakur, Baltej Singh and P.D. Krishnani, "In-core fuel management for AHWR", Annals of Nuclear Energy 57, 47-58, 2013
7. Amit Thakur, Baltej Singh, Anurag Gupta, Vibhuti Duggal, Kislay Bhatt and P.D. Krishnani, "Performance of Estimation of distribution algorithm for initial core loading optimization of AHWR-LEU", Annals of Nuclear Energy 96, 230-241, 2016
8. Amit Thakur, Baltej Singh, Anurag Gupta, Vibhuti Duggal, Kislay Bhatt and P.D. Krishnani, "Improvement in estimation of distribution algorithm (EDA) for fuel loading pattern optimization in AHWR", Int. Conf. on Thorium Energy 2015 (ThEC15) Mumbai, India, Oct. 12-15, 2015
9. Amit Thakur and Baltej Singh, "Sensitivity study about the variations in the elements of objective function used in GA for initial core loading pattern optimization of AHWR", Technical Note: RPDD /AHWR /347/ June 09, 2016
10. A. Kumar and R. Srivenkatesan, "Nodal expansion method for reactor core calculation", Technical report No. BARC-1249, 1984

Infrared Spectroscopy of Molecular Solids under Extreme Conditions

Himal Bhatt

High Pressure & Synchrotron Radiation Physics Division

Abstract. The first infrared beamline at the Indian synchrotron radiation source, Indus-1 has been designed, fabricated and installed based on extensive beam extraction and propagation simulations and a comprehensive facility for spectroscopy has been developed. The development of beamline, lab based facilities and research on technologically and bio-geologically important molecular solids were taken up in parallel. The proton dynamics of strong hydrogen bonds across the potential barrier under extreme thermodynamic conditions of high pressure (upto 30 GPa) and low temperature (upto 4.2 K) were examined in the family of oxalic acid, the simplest dicarboxylic acid and glycine, the simplest amino acid, which are abundant in planetary gasses and ices. Upon reaching the symmetrization limits, the subtle, drastic and as well as rare high pressure behaviours depicted by these systems, of great relevance to basic physics, crystal engineering and biology, indicate that they can be the model systems to study proton dynamics in complex bio-geological processes.

Keywords: Hydrogen bond, dynamics, infrared beamline, spectroscopy, synchrotron, glycine, oxalate, high pressure.

Introduction

Hydrogenous materials such as water, organic acids and minerals (the fundamental constituents of life) under extreme thermodynamic conditions are of immense importance to the understanding of bio-geological processes in earth's interior as well as other celestial bodies. Hydrogen bonds play a decisive role in their structural stabilization. For example, at high pressures, the structure of non-molecular phase of ice (~100 GPa) is predicted to be stabilized by a symmetric hydrogen bond formed through translational proton tunneling. However, because of the high barrier in the potential energy, in general, localized proton at the hydrogen bond centre and proton transfer are rare events or dynamical bottlenecks. These fundamental problems have direct relevance with various bioprocesses and applications.

Glycine, the building block of proteins, provides vast opportunities to understand proton dynamics in the complex bio-geological processes in nature where inter-molecular interactions are governed by diverse chemical environments. Among various carboxylic acids, only oxalic acid yields crystallized salts with glycine in different stoichiometries from either slow evaporation or other techniques. The hydrogen bonded networks in these complexes are also ideal to look for novel structures like ferroelectric/ non-linear optic materials or dynamic polymers through hydrogen bond assisted supramolecular assembly, a path adopted in nature for bio-material synthesis.

Glycine and oxalic acid complexes form a special class as these compounds contain very strong hydrogen bonds which are in the limit of symmetrization even at ambient conditions. Infact, oxalates are capable of forming strong hydrogen bonds in various complexes including in its ambient structure as dihydrate. Oxalic acid dihydrate (OAD), although a benchmark hydrogen bonding and crystallographic system, remains one of the most debated compounds in molecular solids for nearly a century with regard to proton dynamics.

The present work reviews the proton dynamics studies under high pressure in glycine and oxalic

acid family of crystals [1-5], we claim to have solved the long standing debate on proton dynamics in oxalic acid dihydrate (OAD) by demonstrating a complete mechanism of proton transfer and effects on the cooperative molecular structure. In addition, a novel mechanism of the 'rare' pressure induced hydrogen bond symmetrization has been proposed in glycinium oxalate (GO) using experiments as well as theory. Possible phase transitions to the technologically important structures in feroelectricity and supramolecular engineering has also been discussed in Bis(glycinium)oxalate (BGO) and GO respectively. For such studies on proton dynamics and its influence on molecular structure under pressure, Infrared (IR) spectroscopy is the preferred technique because of the difficulty with structural methods, viz. X-ray/neutron, to monitor hydrogen positions at high pressures (even deuteration can vary wavefunctions and dynamics). However, high pressure IR investigations using diamond anvil cells demand a high brilliance of the probing beam to be focused on a spot of the order to tens of microns. Synchrotron radiation is the ideal source for IR microscopy and therefore a new IR lab for comprehensive condensed matter research and an IR beamline have been developed at Indus-1 synchrotron source. Hence, both the works of development of the IR beamline and initiating the studies on proton dynamics were taken up in parallel and are described in this paper.

Development of IR beamline:

The high brightness of synchrotron radiation in the infrared region as compared to the thermal sources comes from the very small size of the source and the directional property of the emitted radiation (narrow emission angles). The spectrum of a bending magnet radiation is uniform in the horizontal plane of emission. But in the vertical plane, it is strongly wavelength dependent and the cross section of the 'fan' emitted is systematically filled with higher wavelength contributions as one moves away from centre (Fig.1). For wavelengths significantly longer than the critical wavelength (λ_c = 61 Å, i.e. ~ 202 eV for Indus-1) of the storage ring, the characteristic angle θ_v depends upon the wavelength λ as ~ $(\lambda/\rho)^{1/3}$, where ρ is the radius of curvature of electron trajectory. Hence an optimization of the acceptance angle becomes

crucial to extract the high wavelength infrared components from the storage rings.
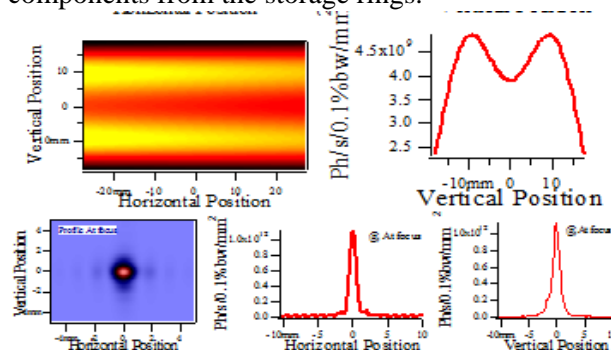

Fig. 1: (Top to bottom) Extracted beam profiles (cross section) as calculated for λ= 50 μm at Indus-1 with 35 mradbeamport opening; focussed spot (nearly 300 μm)

Indus-1 commissioned in 1999, operates at 100 mA beam current with beam lifetime of ~1.8 hours. The IR beamline is installed at the $10^°$ port of dipole (DP-4) and integrated with a FTIR end-station (Fig. 2). The first mirror can be conveniently placed close to the beamport so that the radiation can be
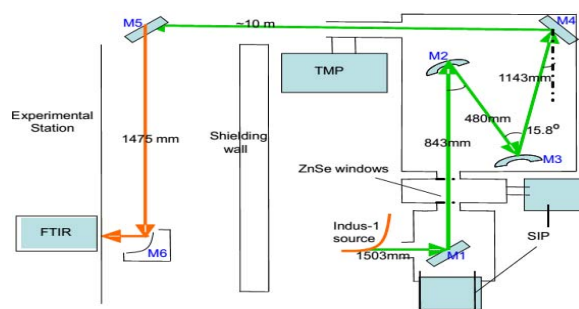

Fig. 2: (top to bottom) Optical layout of beam extraction and transport upto the experimental station of beamline - showing IR microscopy for high pressure, cryogenic system, FTIR interferometer, Liq. He Bolometer detector etc.

collected over a large vertical and horizontal emission angle, which makes it possible to obtain both horizontal and vertically polarized IR radiation from the source, which is very difficult to obtain from a thermal source. With the acceptance angle of 35 mrad, vertical collection of radiation covering the complete mid infrared region became possible at Indus-1.

An analysis of the 100% gold reflection lines shows that for synchrotron source, the signal to noise ratio (SNR) depicts relatively much smaller decline as compared to the thermal source, upon reducing the microscopic aperture. This gives nearly an order of magnitude higher signal to noise ratio for smaller focused spots. Various other developments have been carried out at the experimental station, which make it a unique national facility for in-situ high pressure, low temperature, imaging and polarization dependent IR measurements (Fig. 2). The above efforts are well complemented with the development of a very high resolution (~ 0.0012 cm^{-1}) IR lab at BARC for spectroscopic studies of molecules and transient species in absorption (using normal and indigenously developed long path cell) and transmission (using electrodeless discharge lamps and hollow cathodes) modes.

High pressure studies of molecular crystals
Colourless single crystals were grown by slow evaporation from an aqueous solution containing stoichiometric ratios of glycine and oxalic acid. The samples were characterized using single-crystal XRD, neutron diffraction, Raman and IR spectroscopy.

For IR studies, an indigenously developed clamp type symmetric DAC was used with an IR microscope coupled to Bruker Vertex 80V FTIR equipped with various sources and beamsplitters, installed at the experimental station of IR beamline at Indus-1. LN$_2$-cooled MCT detector was used for the complete mid-IR range. All the studies were initially carried out using thermal source, which was followed by using the synchrotron source in some of the cases. Polycrystalline sample in CsI matrix along with a couple of ruby balls was loaded in a 150 μm hole of a tungsten gasket preindented to a thickness of ~60 μm for absorption studies.

Pressure calibration was done using ruby fluorescence.

High pressure Raman studies were carried out in an existing facility, based on confocal micro Raman setup in back scattering geometry, configured around JobinYuon (HR 460) spectrograph. Mao Bell DAC was used for Raman and support studies using XRD. The results are well complemented with first principles molecular dynamics simulations using VASP code.

Proton Migration in OAD
Oxalic acid dihydrate, an important molecular solid in crystal chemistry, ecology and physiology, is being studied for nearly 100 years now. The most debated issues regarding its proton dynamics have arisen due to an unusually short hydrogen bond between the acid and water molecules ($d_{O1\cdots Ow}$ ~ 2.43 Å, $\angle O_1 HO_w$ ~ 177°). In O_1-H_t---O_w, the acceptor O_w (oxygen atom of water) also acts as a donor for the carbonyl group of subsequent OA molecule, forming a chain, –C-O_1-H_t---O_w-H_w---O_2=C-. The alternate hydrogen bonded chain causes a net decrease in O---O through the well knowncooperativity effect of hydrogen bonds. Due to this enhanced strength, the initial beliefs, which date back to 1930s, of observing a proton transfer state of oxalic acid dihydrate at ambient conditions were ruled out by a number of studies in subsequent decades. Though, X-ray and neutron studies have also been reported under pressure, hydrogen atom positions could not be unambiguously determined which could affirm the thermodynamic conditions for proton motion.

Using combined in-situ spectroscopic studies and first-principles simulations at high pressures, we found that the structural modification associated with this hydrogen bond is much more significant than ever assumed [1]. Initially, under pressure, proton migration takes place along this strong hydrogen bond at very low pressures of 2 GPa (Fig. 3). This results in the protonation of water with systematic formation of hydronium ion and dianionic oxalate, thus reversing the hydrogen bond hierarchy in the high pressure phase II (Fig. 3). The resulting hydrogen bond between hydronium ion and carboxylic group shows remarkable strengthening under pressure, even in the pure ionic phase III as seen from the softening and dampening

of the ν1 hydronium mode (Fig. 3). The oxalic acid molecule also shows various changes due to transition from neutral to dianionic species, for example vanishing of Fermi resonance between C-O and C=O as observedfrom the merging of the two IR modes into one band. The loss in the cooperativity of H- bonds leads to another phase transition at ~ 9 GPa through reorientation of other hydrogen bonds. High pressure phase IV is stabilized by a strong hydrogen bond between the dominant CO_2 and H_2O groups of oxalate and hydronium ions respectively. The findings suggest that oxalate systems may provide useful insights on proton transfer reactions and assembly of simple molecules under extreme conditions.
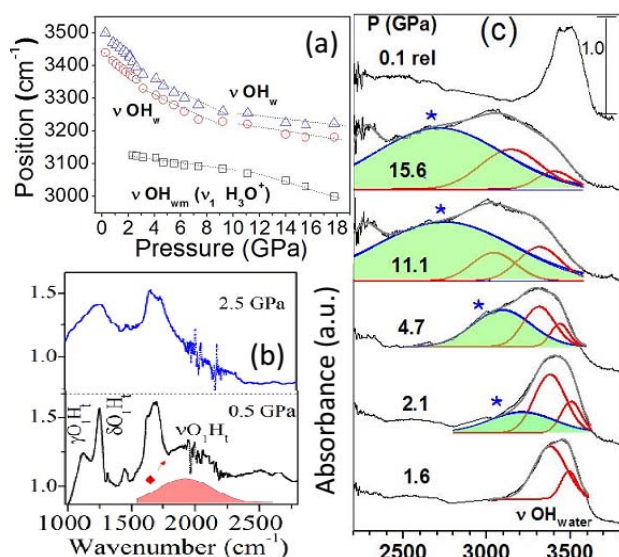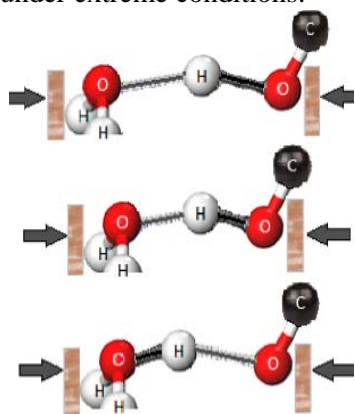

Fig.3: (top) Asymmetrization of H-bond on proton transfer, (bottom) High pressure IR spectra shows (a) softening of O-H stretch modes, (b) vanishing of OH signatures from OA and (c) evolution of H_3O^+ IR mode

Hydrogen bond symmetrization aiding supramolecular assembly in GO

Glycinium oxalate (GO), the simplest amino acid-carboxylic acid complex crystallizes in monoclinic structure with space group $P2_1/c$ and four formula units per unit cell (Z=4). It possesses a nearly linear and strong O3-H7---O6 hydrogen bond (d_{O---O} ~2.54 Å, d_{H---O} ~1.65 Å and $\angle OHO$ =177°) between semioxalate molecules in a columnar arrangement along the *b*-axis (Fig. 4). These semioxalate (HC_2O_4) columns hold the head to tail linked glycine (NH_3CH_2COOH) sheets in the *ac*-plane via other hydrogen bonds to form the three dimensional network. We have studied the proton dynamics of this strong O3-H7---O6 hydrogen bond under pressure, beyond the symmetrization limit up to ~ 20 GPa [2].

Under compression when the proton moves close to the mid-point of a very strong hydrogen bond O-H---O, the system becomes highly anharmonic leading to OH instability and resulting in remarkable dampening of νOH (stretching) mode (~2360 cm^{-1} for GO) (Fig. 4). A large red shift of ~ 250 cm^{-1} up to 2.5 GPa in νOH mode (from theory and ambient reflectance) and a substantial reduction in the O3---O6 distance (d_{O3--O6} < 2.5 Å, see Fig. 4) implies that this hydrogen bond is strengthened under pressure and is on the verge of approaching symmetrization limit. The bond parameters obtained from MD calculations (total 12000 equilibrated configurations, in 1 femto-second time steps used at each pressure to generate the dynamical picture) show that the spread of proton distribution reduces with pressure and shifts towards the bond mid-point. The large softening of νOH mode, as approximated by a power law fit (ν ~ $[A(P_c-P)]^{0.5}$) for the soft mode gives P_c ~ 8.15 GPa as the pressure corresponding to νOH mode instability. At pressures close to 10 GPa, the distance between oxygen atoms, $d_{O3---O6}$ continuously reduces to ~2.4 Å, accompanied by an increase in the covalent bond length (d_{O3-H7}), decrease in the hydrogen bond length ($d_{H7---O6}$). However, $\angle OHO$ remains close to ~180°. The probability of crossing the mid-point through proton hopping increases with pressure and is already significant at ~ 10 GPa. This implies proton sharing between the closely overlapped potential minima in which the proton hops between the two

sites, which mimics the proton being at the mid-point. The consequent proton sharing between the two semioxalates would result in the emergence of neutral oxalic acid like spectral features, which have also been confirmed from the Raman and infrared modes.

We also note a relative increase in the background of the observed IR band profile above 2 GPa (See Fig.4). Such broad envelopes, resembling a continuum arise due to large νOH dampening and ride over the background of various other fundamentals. Its centroid shifts to lower frequencies (up to ~ 1000 cm^{-1} at 18 GPa), at an increased rate above 8 GPa and the extent of this band crosses the lowest 600 cm^{-1} mark to enter even in the far IR regions at higher pressures.Above 12 GPa, the evolution of broad envelopes in N-H stretching regions, behavior of N-H---O H-bonds and the observed transition in glycine conformation from bent to planar have suggested the formation of a supramolecular assembly in GO assisted by N1-H4---O4=C3 interactions at high pressures where glycine hammocks (in *ac*-plane) are tied to the infinite symmetric H-bonded oxalate poles (*b*-axis).

Novel phase transitions in BGO

Bis(glycinium)oxalate, another organic complex of glycine and oxalic acid family has a very short and strong O-H---O hydrogen bond (H---O=1.3 Å, O---O=2.461 Å) between glycinium and oxalate ions. Our high pressure studies of BGO indicate structural transformations across 1.6 and 4.5 GPa due to reorientation of H-bonds [3]. The appearance of Raman active modes in the IR spectra (Fig. 5) and vice versa above 1.6 GPa confirms that glycine molecules have become non equivalent leading to loss of centre of symmetry (implies breakdown of principle of mutual exclusion) and hence a non centrosymmetric high pressure phase. Softening followed by discontinuous shift of νO-H mode suggest that, in the high pressure phase above 1.6 GPa, though relatively weaker compared to that in the parent phase, yet strong O-H---O bonds exist. Further, high pressure dielectric studies suggest that the pressure induced transition results in a possible ferroelectric phase above 1.6 GPa, whereas low temperature spectroscopic and single crystal X-ray studies indicate that there is no phase transition occurring at low temperatures.
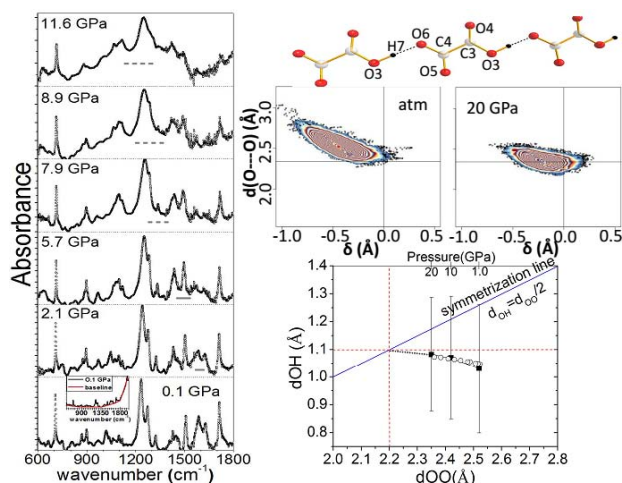

Fig. 4. Left: IR spectral features (broad absorption background shown as dashed lines) of the soft mode; Right (top to bottom): O3-H7---O6 hydrogen bond which symmetrises under pressure; Proton position at high pressures, here δ=0 is bond mid point; O-H and O---O lengths with pressure (vertical bars-hopping probability)
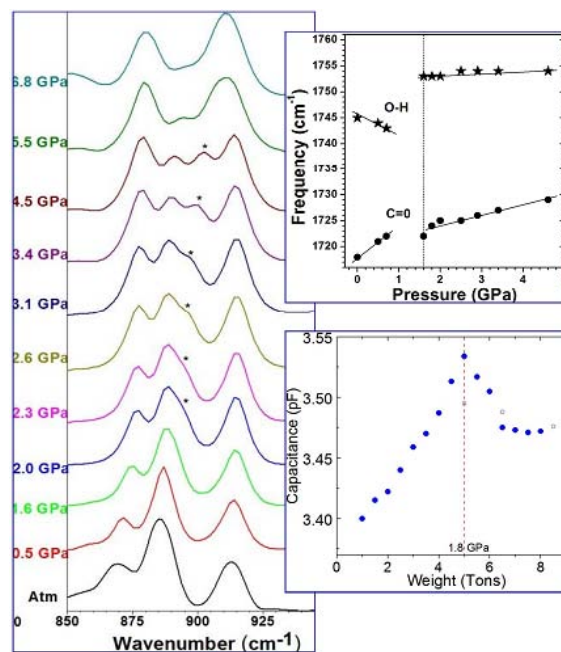

Fig 5. (Left) IR spectra showing new modes emerging due to phase transition, (Right) selected IR mode variations and capacitance with applied pressure in BGO

Conclusion

To summarize, we have studied proton dynamics of strong hydrogen bonds under pressure in glycine and oxalic acid family of complexes and set up various state-of-the-art national experimental facilities for IR spectroscopic studies covering a wide scientific domain. The findings of different high pressure studies carried on these crystals suggest that these systems can be the model systems to understand proton dynamics as they have depicted all the three and rare events of proton transfer across the barrier (relevant to enzymatic catalysis), a symmetric hydrogen bonded state (relevant to water transport in earth's crust and basic physics) and hydrogen bond reorientation inducing phase transformation to a possible ferroelectric state at moderate pressures.

Contributors

Dr. S. M. Sharma, Dr. M. N. Deo, Dr. S. K. Deb, Dr. C. Murli, Shri S. R. Vishwakarma, Dr. A. K. Verma, Dr. N. Garg, Dr. A. K. Mishra, Dr. R. Chitra, Dr. V. N. Rai.

References

1. Himal Bhatt, A. K. Mishra, ChitraMurli, Ashok K. Verma, NandiniGarg, M. N. Deo, S. M. Sharma, *Phys.Chem.Chem.Phys.***18** (2016) 8065.
2. Himal Bhatt, ChitraMurli, A. K. Mishra, Ashok K. Verma, NandiniGarg, M. N. Deo, R. Chitra, S. M. Sharma, *J. Phys.Chem.B***120** (2016) 851.
3. Himal Bhatt, C. Murli, N. Garg, M. N. Deo, R. Chitra, R. R. Choudhury and Surinder. M. Sharma, *Chem. Phys. Lett.***532** (2012) 57.
4. R. Chitra incl. H. Bhatt, *J.Mol.Str.***1049** (2013) 27.
5. Himal Bhatt,M.N. Deo,*Spectrochim..Acta A (ICOPVS2016)*, **185** (2017) 45.

Development of solvent encapsulated polymeric beads for rare earth separation

Kartikey Kumar Yadav

Rare Earth Development Section, MP&CED

Abstract: Novel polymeric composite beads encapsulating organic extractant (di-2-ethyl hexyl phosphoric acid (D2EHPA) and 2-ethyl hexyl phosphonic acid (PC88A)) has been developed to separate and purify rare earths (yttrium, dysprosium) from lean and secondary sources. The polyethersulfone(PES) based beads were synthesized by non-solvent phase inversion technique. Rare earth separation studies by extractant encapsulated polymeric beads revealed better (>97% Y(III)) recovery of rare earth elements from aqueous media when compared with ion exchange process and have shown loading capacity upto 100mg of Dy / gram of dry beads. These polymeric beads also have excellent stability and reusability under harsh experimental conditions (vigorous mixing, strong acidity >50% HCl/H_2SO_4 and 100 cycle application) with minimal loss of encapsulated extractant (<2%) and has excellent potential for commercialization

The rare-earth elements (REEs) are becoming increasingly important due to their essential role in permanent magnets, lamp phosphors, catalysts, rechargeable batteries etc. Careful examination of the current scenario in the field of rare earths separation and purification including environmental concerns indicates that there is an urgent need to develop effective and efficient processes which not only maximizes the separation but also minimizes the environmental hazard associated with the conventional processes[1]. Presently, the most commonly used hydrometallurgical concentration and purification methods in the mining industry for rare earths separation are precipitation, liquid-liquid extraction and ion exchange [2]. However, the traditional solvent extraction process has limitations such as requirement of large volumes of organic solvents, diluents and saponification agent. Solvent extraction is a complex process and creates environmental concerns due to the use of hazardous diluents [3]. Due to vexed problems of separation of rare earths, last decade has seen phenomenal growth in interest for developing a new extraction system, including novel extraction material, synergistic extraction system, membrane based techniques and ionic liquid extraction, with improved efficiency and elimination of organic waste release in aqueous streams. In this context, solvent impregnated resins/beads are being developed as attractive alternatives in separation technology nowadays. The aim of the present work is to prepare and evaluate the extractant encapsulated polymeric beads for the sorption of rare earths under variable experimental conditions. Based on the batch experimental results, it was also of interest to employ these polymeric beads for the recovery of rare earths in continuous column operation mode, which may establish the materials potential to industrial level scale up.

An experimental set up (Fig.1) was prepared for synthesis of extractant encapsulated polymeric beads [4]. Initially, a PES solution was prepared by dissolving polymer in n- methyl pyrolidone (NMP) in a desired w/v ratio. This prepared solution was then added to suitable organic extractant (D2EHPA) at definite polymer to extractant ratio under stirring condition. The mixed polymer solution was gradually dropped into the anti-solvent (deionised water) bath through a nozzle of syringe needle at an appropriate height. In the anti-solvent bath the instantaneously formed droplets slowly

precipitated due to the phase inversion of relatively dense polymeric backbone resulting in the formation of PES beads impregnating extractant [5]. These beads were then immersed and stabilized in the water bath for 24 hours prior to their use. Various types of polymeric composite beads with different additives were prepared by the above mentioned method under optimized preparatory conditions.
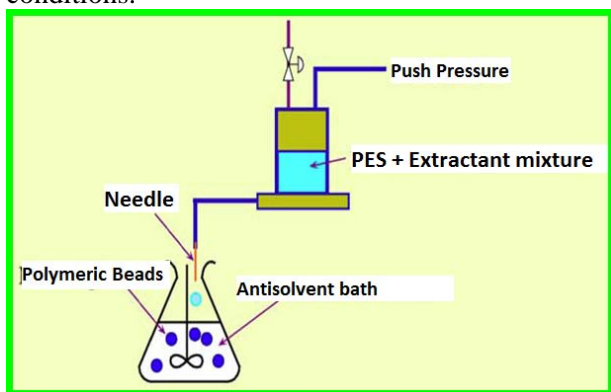

Fig. 1 Preparation set up for extractant encapsulated PES based polymeric beads

The concentration of the constituents was optimized in such a way that the resultant composite beads resulted in spherical shape. The concentrations of additives in different polymeric beads were 1.5, 0.25, 1, and 1 % w/w for lithium chloride (LiCl), multiwall carbon nanotube (MWCNT), polyvinyl alcohol (PVA) and polyethelene glycol (PEG) respectively. Morphology and internal structure of the synthesized composite beads were examined by SEM and optical images. Fig. 2 shows the optical images of PES/D2EHPA, PES/PVA/D2EHPA and PES/PVA/MWCNT/ D2EHPA beads respectively.

Whereas, Fig. 3 (a–f) illustrates the cross sectional SEM images of the polymeric composite beads with different additives which also reveals that the additives play vital roles in changing the internal microstructure of the bead in terms of porosity and pore size distribution which in turn affect their sorption capacity considerably [6].

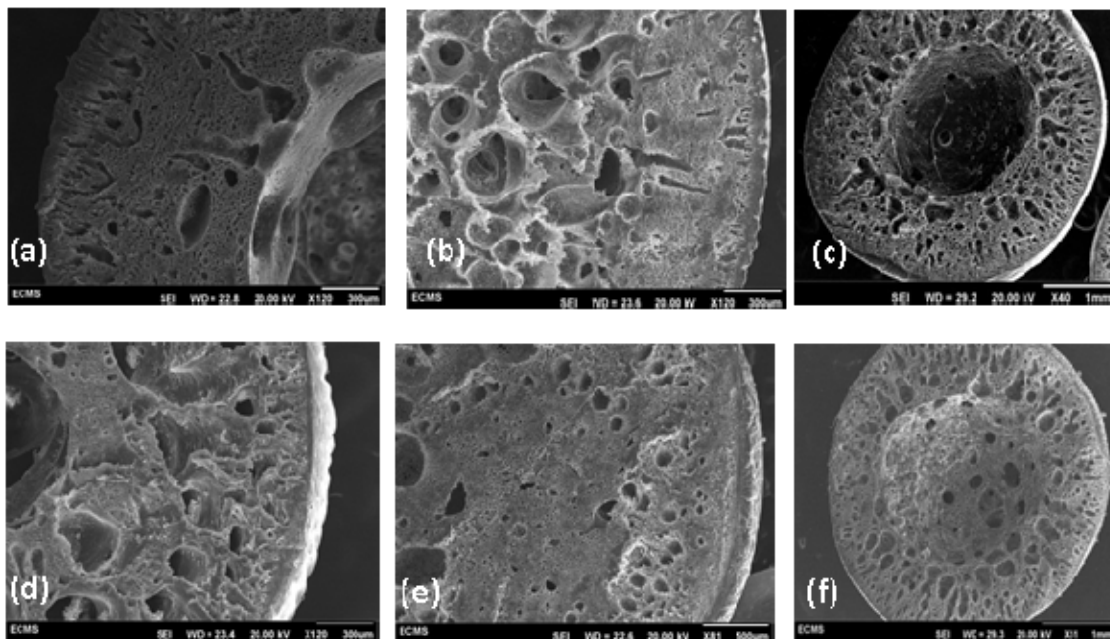Fig. 2: Images of PES/D2EHPA, PES/PVA/ D2EHPA and PES/PVA/MWCNT/ D2EHPA

Fig.3: SEM images of cross-section of beads (a) PES blank, (b) PES/D2EHPA, (c) PES/PVA/D2EHPA (d) PES/PEG/D2EHPA (e) PES/LiCl/D2EHPA, (f) PES/PVA/MWCNT/D2EHPA.

Subsequent characterization by thermo-gravimetry was performed to determine the encapsulation capacity of different types of beads developed. Fig. 4 shows the weight loss profiles of blank PES bead (line a), PES/D2EHPA/PVA bead (line b) along with PES/D2EHPA/PVA/MWCNT beads and 3M D2EHPA liquid phase (line c and d respectively) as references while heated in nitrogen atmosphere. Comparison of TG profiles resulted in evaluation of chemical interaction among the constituents and extractant encapsulation capacity.
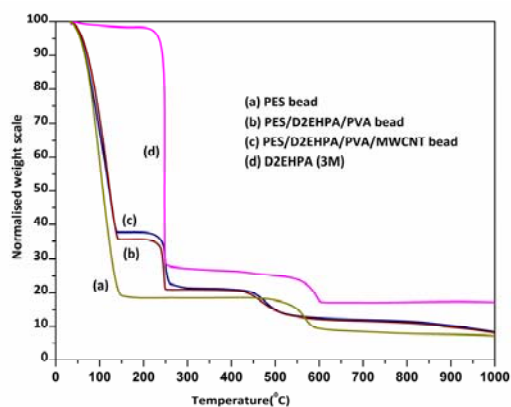

Fig. 4 TG profiles of (a) PES bead (b) PES/D2EHPA/PVA (c) PES/D2EHPA/PVA /MWCNT bead and (d) D2EHPA (3M)

Sorption (uptake) study of Y(III) or other rare earths by developed polymeric beads were investigated in batch mode to evaluate the role of different additives from aqueous chloride medium with PES/D2EHPA composite beads embedded with additives like polyvinyl alcohol (PVA), multiwall carbon nanotube (MWCNT), lithium chloride (LiCl) and polyethelene glycol (PEG) under comparable experimental conditions was investigated. Sorption studies have been performed by contacting known amount of all the types of polymeric beads separately with aqueous solutions containing rare earths (80 to 3300 mg/L) at varying concentrations at an appropriate solid to liquid ratio for 8 hours to make sure that the system had reached the equilibrium. Once the system reached the equilibrium the polymeric beads were removed and the aqueous phase was analyzed for its metal ion content by ICP-AES (JY Ultima 2). The weight distribution coefficient, K_d were evaluated using equation 1.

$$K_d = \left(\frac{C_0 - C_e}{C_e}\right)\frac{V}{w} \qquad (1)$$

Where C_0, and C_e are concentration of Y(III) in mg/L or ppm at initial time and at equilibrium, respectively; w is the weight of

polymeric beads (polymer and extractant); and V is the volume of aqueous phase in mL. The results are shown in Fig. 5. The sorption of Y(III) with additive embedded composites followed the order: PES/D2EHPA/PVA/MWCNT > PES/D2EHPA/PVA > PES/D2EHPA. The better distribution of D2EHPA in the PES/PVA/MWCNT bead along with favorable pore size distribution resulted in the enhancement in Y(III) sorption. Not only the additive enhances or suppress the equilibrium sorption amount of Y(III) but also influences the rate of sorption.
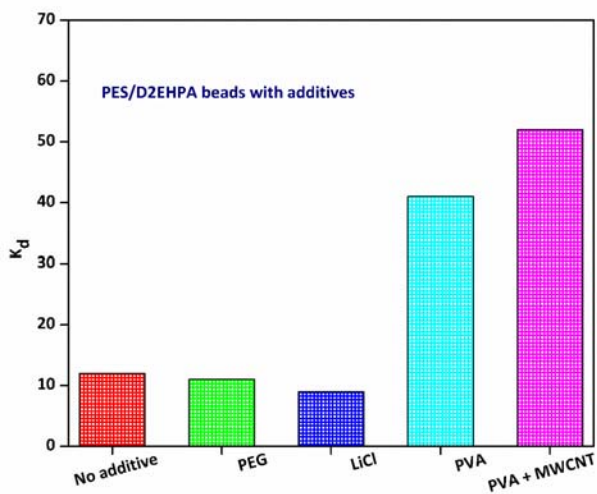

Fig. 5 Effect of additives in polymeric composite beads on weight distribution ratio of Y(III) by PES/D2EHPA beads.

Based on the batch experimental results, the developed polymeric beads were successfully deployed for the recovery of rare earths in continuous column operation mode, to establish its potential to industrial level scale up [7]. Sorption and desorption experiments were performed in column (Fig. 6 c) to evaluate the performance of these beads for the recovery of yttrium from aqueous chloride medium. The sorption profile of Y(III) from the feed having 160mg/L at 0.3M HCl is shown in Fig. 6 for PES/D2EHPA/PVA and PES/D2EHPA/PVA/MWCNT beads [8].

The studies on the synthesis, characterization, evaluation and application of polymeric beads for the recovery of REEs have promising potential to be harnessed in the fields like toxic metal removal, concentration of metal ions from lean sources and removal of entrained impurities. The developed bead not only addresses the environmental issues but also offer selective and efficient separation of rare earths. Moreover, they have added advantage of extraordinary stability and recyclability. The developed solvent encapsulated polymeric composites for rare earths separation has the potential to be adopted at commercial scale as an alternate to ion exchange process in rare earths industry due to its dual advantage in terms of higher loading capacity and comparatively faster kinetics.
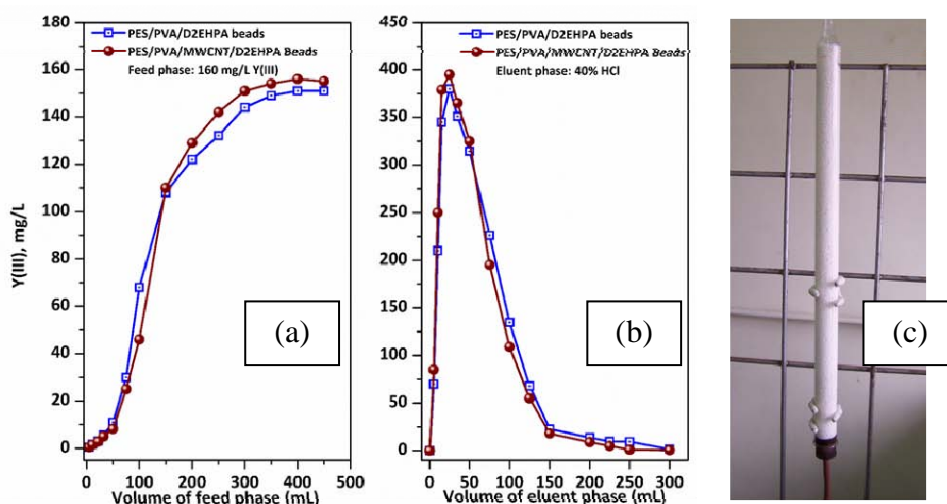

Fig.6 Breakthrough profile of (a) Y(III) uptake (b) Elution profiles PES/D2EHPA/PVA and PES/D2EHPA/PVA/MWCNT beads (c) column used in study

Acknowledgements

References

1. Alonso E, Sherman AM, Wallington TJ, Everson MP, Field FR, Roth R, Kirchain RE. Evaluating Rare Earth Element Availability: A Case with Revolutionary Demand from Clean Technologies. Environ. Sci. Technol. 2012: 46: 3406– 3414.
2. Zhang J, Zhao B, Schreiner B. Separation Hydrometallurgy of Rare Earth Elements, Springer International Publishing, Switzerland; 2016.
3. Sun XQ, Waters KE. Development of industrial extractants into functional ionic liquids for environmentally friendly rare earth separation. ACS Sustainable Chem Eng. 2014; 2: 1910–1917.
4. Gong XC, Luo GS, Yang WW, Wu FY, Separation of organic acids by newly developed polysulfone microcapsules containing trioctylamine, Sep. Purif. Technol. 2006; 48: 235–243.
5. Yadav KK, Singh DK, Anitha M, Varshaney L, Singh H. Studies on separation of rare earths from aqueous media by polyethersulfone beads containing D2EHPA as extractant, Sep. Purif. Technol. 2013; 118: 350-358.
6. Yadav KK, Dasgupta K, Singh DK, Anitha M, Lenka RK, Varshaney L, Singh H. Sorption behavior of Y(III) from chloride medium with polymer composites containing di-2-ethyl hexyl phosphoric acid and multiwall carbon nanotube, Sep. Sci. Tech. 2015; 50:463-470.
7. Yadav KK, Dasgupta K, Singh DK, Varshney L, Singh H. Dysprosium sorption by polymeric composite bead: Robust parametric optimization using Taguchi method. J. of Chromatography A. 2015; 1384: 37-43.
8. Yadav KK, Dasgupta K, Singh DK, Anitha M, Varshney, L.; Singh, H. Solvent impregnated carbon nanotube embedded polymeric composite beads: An environment benign approach for the separation of rare earths. Sep. Purif. Technol. 2015; 143: 115-124.

Compact Pulsed Plasma based Underwater Shock Wave Generator

Rohit Shukla, Premananda Dey, Avaneesh Kumar Dubey, Karuna Sagar, K. Apparao, Archana Sharma

PPEMD, BARCF, Vizag

Dr. Rohit Shukla is the recipient of the DAE Young Applied Scientist / Technologist Award for the year 2015

Abstract

Electrically exploding-wire phenomenon was invented in the last century and has found several applications since then and hence was adapted to different geometries of the pulsed power generators depending upon its applications. Marx generator based inductive storage type compact and light-weight 500MW and 1.5 GW [1-3] electrical power generators were developed and were reported demonstrating the explosions of exploding copper wire of 9cm and 11cm respectively of two different diameters. The systems were table-top tested and subsequently the first one is made standalone system by introducing some up-gradations facilitating the structural rigidity and better usability. The system for the generation of underwater shocks is being reported in this article.

Introduction

A detailed study is reported on underwater exploding wires [4-10] and it is suggested that if the discharge time from the capacitor bank to the wire is sub-microseconds in the underwater discharges, then the estimated pressures generated are much higher than the estimated pressures generated in the microseconds discharges. Interesting convergence of shock waves is also reported in their study to enhance the shock pressures in underwater experiments. The pressure in their study is experimentally found to be fitting with the distance from shock wave origin with the power of -0.7. It is good to recall [10] here that in underwater experiments the radial expansion is slowed down by two orders of magnitude and hence the energy density going inside the wire is enhanced in the case of underwater experiments. Loeffler et al [11] suggested the aluminum underwater exploding wire techniques to be used as alternative of blasting techniques and proposed the various schemes to amortize the investments in the technology within short time. Reduction in electrical energy required (using aluminum water reaction), reduction of average power requirement (by preheating the wire upto melting) and multiple use of energy supply are

three areas in which their study aims. Pashchenko [12] et al have proposed the application of pulsed plasma elastic waves to the field of Enhanced Oil Recovery as one among several methods to do so. It is further mentioned to be innovative approach to enhanced oil recovery. J. Wojtowicz [13] et al have proposed to generate seismic wave simulation conditions by exploding wire which results in the creation of shock wave front in water which is finally emitted to the geological environments in the form of acoustic waves. Lisitsyn et al [13,14] have estimated from pressure and shock wave velocity measurements that upto 90% of the energy of capacitor bank is dissipated in the wire in fast discharges with optimum length of the wires. The discharge power is calculated to be nearly 800MW in these experiments. The application in these experiments is the destruction of solids by the shock waves generated in underwater electric wire explosions. In other experiments [16,17] it is estimated with the help of pressure diagnostics that at the Discharge Plasma Channel (DPC) boundary the boundary velocity is ~2km/s and pressure is 10GPa for specified wire dimensions. Additionally, the peak pressure is reported to be satisfying a law of the radial propagation distance (r) to the power

of -0.74. Nelson et al [18] have interestingly shown the addition of energy of aluminum water combustion to that deposited electrically with experiments. In these experiments enhancement of an order was observed in the peak pressures achieved.
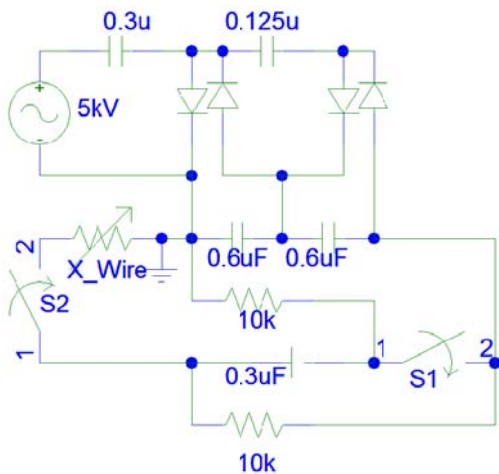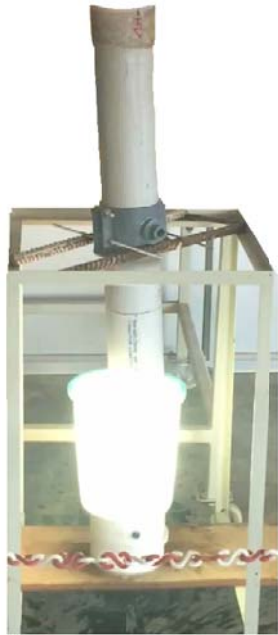

Fig. 1: Compact underwater shock wave generator and its electrical equivalent

Experimental Details

The feasibility of operating several spark gaps (nearly 10 nos) was not a practical solution [1-3] so the structure has to be reduced to use lesser number of spark gaps so that the standalone rigid structure may be practically realized. The reduction in the number of spark gaps of the Marx generator, on the other hand, demanded series connections of the capacitors and charging them to a higher/multiplied voltage from the power supply. For this purpose two high voltage upliftment schemes were coupled. The first one being voltage multiplier and other one being the two stage Marx generator. Additionally the one stage of the Marx generator is made common to the voltage multiplier output stage in order to further reduce the number of electrical components in the complete generator assembly. The complete electrical assembly is molded in Epoxy resin/ hardener mixture to restrict a final geometrical shape of 115mm of diameter and 1.6meters of total length in cylindrical shape. The system is shown in figure 1 while in action underwater. The figure is taken at the time of wire explosion when the light is also emitted from the wire. The figure 1 also shows the electrical schematic of the generator. The wire exploded is copper wire of 184 micron diameter in this experiment. The generator along with its power supply is light weight (40kgms) and can be handled by single person. The charging time for the generator is less than 10 seconds.

The electrical scheme of the generator is quite interesting in which a voltage multiplier (four stage) charges a capacitor to a peak voltage of-30kV and the voltage multiplier output arm and external capacitor arm (equal capacitance) makes a two-stage Marx generator using two self breaking spark gap switches. One switch is adjusted to break at nearly -30kV and the other one is set to break nearly-45kV of the voltage. As soon as first spark gap switch closes the other one sees double the voltage and hence it also closes. This way the -60kV impulse voltage appears across the connected exploding wire and causes the phase changes from solid to liquid to gas and then to the plasma. The electrical feed to the system is ~5.4kV rms from a high voltage transformer which takes 230volts as its input. The charging voltage of the multiplier and the discharge current from the system is monitored with a high voltage divider output and a Rogowski coil respectively. The total energy of the capacitor bank at 30kV of charging voltage is ~290joules.

Results

The fig.2 represents di/dt signal and indicates that in the air the higher di/dt is being generated inside

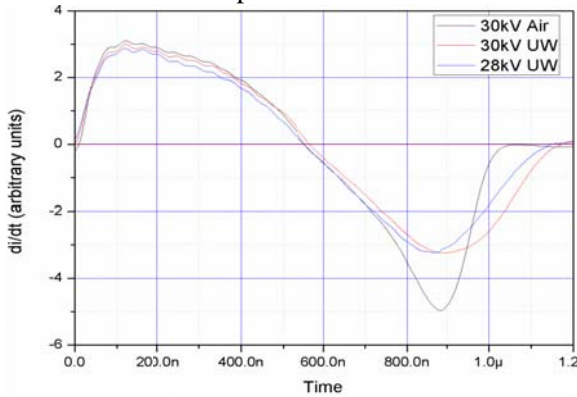the wire. The copper wire used is 184micron diameter in these experiments.

Fig. 2: di/dt vs time for wire explosion from the compact shock wave generator

di/dt waveform also indicates that the rate of rise of resistance is higher in air during the time of wire explosion. The same can be observed from the integrated waveforms of the wire explosion which are shown in fig. 3. It additionally indicates that there is no considerable change of peak current amplitude which suggests of no significant shunting effect when the wire is blown inside the water as compared with the air experiment. The discharge currents are ~23kA at the time of occurrence of its maximum and are seen to be occurring at 550ns from the beginning of the current discharge. The current ceases to flow in the wire at ~1µs from the beginning of the discharge.
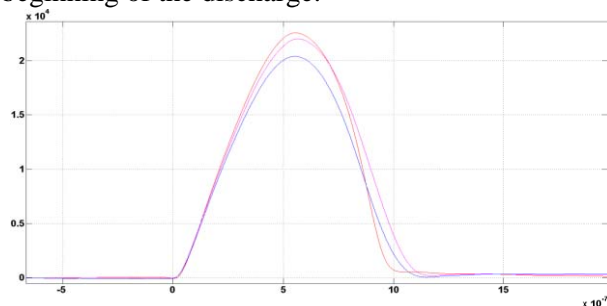

Fig. 3: Time(seconds) on X axis and Current (Amperes) Y axis [Red 30kV Air, Magenta 30kV UW, Blue 28kV UW]

The energy of the capacitor bank is discharged in the wire in sub-microsecond duration in order to utilize the dielectric strength of the water under the pulsed conditions. The sequential shots of its underwater experiments are shown in fig. 4.

Fig. 4: sequential images of prototype being experimented for underwater experiments (184micron diameter copper wire)

Conclusion

The developed compact pulsed plasma based underwater shock wave generator system is negatively charged to utilize higher underwater resistivity of water for the pulse negative voltage discharge in water as compared to the pulsed positive voltage discharges. It means the shunting effects caused by the environmental conditions (mainly water) around wire are further minimized. Additionally since in our experiments the wire used is aluminum (in subsequent experiments after initial use of copper), an effective enhancement of generated pressure is also observed leading to a conclusion of thermite reaction assistance (by release of energy) in underwater experiments. The 240micron diameter enameled aluminum wire is exploded in the experiments. The length of the aluminum wire is 11cm in these experiments.

Acknowledgements

References

1. R. Shukla, P. Banerjee, S. K. Sharma, R. Das, P. Deb, T.Prabahar, B. K. Das, B. Adhikary, A. Shyam "Inductive storage type pulsed power driver for the generation of Electromagnetic Radiations" International Symposium on Microwaves (ISM-2010) Bangalore India

2. R. Shukla, P. Banerjee, S.K.Sharma, P. Deb, T. Prabaharan, R. Das, B. Das, B. Adhikari, A. Shyam "Low-Cost, Inductive storage type, Indigenous & Compact 500MW pulsed power driver for 12.5ohm load" Poster presentation in School on Pulsed Power Technology (SPPT-2010) BARC , Mumbai India

3. Rohit Shukla, A. Shyam "Compact, reusable inductive storage cum opening switch based 1.5GW single shot pulsed power generator" Notes: Review of Scientific Instruments 85 Issue 3 (2014)

4. Yakov E. Krasik, Sergei Efimov, Daniel Sheftman, Alexander Fedotov-Gefen, Oleg Antonov, Daniel Shafer, David Yanuka, Michael Nitishinskiy, Maxim Kozlov, Leonid Gilburd, Gregory Toker, Svetlana Gleizer, Eran Zvulun, Victor Tz. Gurovich, Dmitry Varentsov, and Maria Rodionova "Underwater Electrical Experiments of Wires and Wire Arrays and Generation of Converging Shock Waves" IEEE Transactions on plasma science, VOL. 44, NO. 4, (2016)

5. S. Efimov L Gilburd A Fedotov-Gefen V. Tz. Gurovich, J. Felsteiner, Ya E. Krasik "Aluminum micro-particles combustion ignited by underwater electrical wire explosion" Shock Waves 22 pp 207-214 (2012)

6. Ya Krasik, S. Efimov, A Fedotov, D. Sheftman, A. Sayapin, V.TzGurovich, A. Grinenko "Underwater Electrical Wire Explosion" 29th ICPIG Cancun Mexico (2009)

7. Dekel Veksler, Arkady Sayapin, Sergei Efimov, Ya. E. Krasik "Characterization of different wire configurations in underwater electrical explosion" IEEE Transactions on Plasma Science 37 No 1 2009

8. A Grinenko, S. Efimov, A Fedotov & Ya. E. Krasik I. Schnitzer"Addressing the problem of plasma shell formation around an exploding wire in water" Physics of Plasmas 13 052703 (2006)

9. A Sayapin, A Grinenko, S Efimov, Ya. E. Krasik "Comparison of different methods of measurement of pressure of underwater shock waves generated by electrical discharge."

10. D. Sheftman and Ya. E. Krasik "Evaluation of electrical conductivity and equations of state of non-idealplasma through microsecond timescale underwater electrical wire explosion" Physics of Plasmas 18, 092704 (2011)

11. M. Loeffler, H.A. Wieland J Neumann C Dreecen "Electrical wire explosions as a Basis for Alternative Blasting Techniques?" International conference on pulsed power applications March 27-29 2001

12. A. F. Pashchenko and P.G. Ageev "Elastic Waves and Plasma- a new era of enhanced oil recovery" International Conference of Numerical Analysis and Applied Mathematics 2015 (ICNAAM 2015) AIP conference proceeding 1738

13. Jolantla Wojtowicz, Hubert Woztowicz, Wieslaw Wajs "Simulation of electrohydrodynamic phenomenon using computational intelligence methods" Procedia computer science 60 (2015) 188-196

14. Igor V Lisitsyn, Taishi Muraki, Hidenori Akiyama "Characterization of a shock wave generated by a wire explosion in water" Journal of Acoustic society of Japan (E) 18,2,1997

15. I. V. Lisistsyn, T. Muraki, H. Akiyama "Wire induced flashover as a source of shock waves for destruction of solid materials" 11th IEEE Pulsed Power Conference, 1997, Baltimore MA, USA

16. Xingwen Li, Youchuang Chao, Jian Wu Ruoyu Han, Haibin Jhou, &AiciQiu "Study of the shock waves characteristics generated by underwater electrical wire explosion" Journal of Applied Physics 118 023301 (2015)

17. Haibin Zhou, Youngmin Zhang, Ruoyu Han, Yan Jing, Jiawei Wu, Qiaojue Liu, Weidong Ding "Signal analysis and waveform reconstruction of shock waves generated by underwater electrical wire explosions with Piezoelectric Pressure Probes" Sensors (2016) 16, 573

18. Llyod S. Nelson, Steve R Hogeland and Thomas C. Roth "Aluminum-Enhanced Underwater Electrical Discharges for Steam Explosion Triggering" SAND99-0796 (1999)

Design, development and testing of a 300 mm diameter horizontal room temperature bore 4-Tesla superconducting magnet

S. Sundar Rajan, U.G.P.S. Sachan, Vijay Harad, A.K. Sinha and Sanjay Malhotra
Accelerator Control Division
Multidisciplinary Research Group

Shri S.Sundar Rajan is the recipiennt of the DAE Young Applied Scientist / Technologist Award for the year 2015

Abstract: A 4-Tesla warm bore superconducting magnet is required for corrosion and Magneto hydrodynamic studies related to the development of Lead Lithium Cooled Ceramic Breeder (LLCB) test blanket module. The magnet bore is 300 mm and is accessible from both ends. Magnet is immersed in liquid helium bath at 4.2K. The cold mass is surrounded by a thermal shield to reduce the radiation heat losses and is supported inside the vacuum vessel with high thermal resistivity support rods to reduce the conduction losses. Conduction cooled current leads are used to power the magnet. The superconducting magnet has been developed and tested for its design performance.

Index Terms: Superconducting Solenoid Magnet (SC Magnet), thermal shield, G-M cryocoolers, MHD, Conduction cooled current leads.

I. Introduction

Electromagnetic Applications Section, ACnD is involved in the development of superconducting solenoid room temperature bore electromagnet. The magnet needs to produce a field of 4-Tesla in a room temperature bore of 300 mmdiameter. The magnet is made out of multi-filamentary Nb-Ti composite superconducting wires developed at BARC. The critical current density of wire is 2600 A/mm^2 at 5-Tesla magnetic field and 4.2 K temperature. The magnet is supported inside avacuum vessel to minimise convective heat losses. To reduce radiative heat losses into the vessel, a thermal shield is placed between the vacuum vessel and the liquid helium cryostat. The thermal shield is cooled by an 80K G-M cryocooler. The magnet is powered via conduction cooled current leads made of copper from 300K to 80K and High Temperature superconductors from 80K- 4.2K. The magnet is passive quench protected using cold diodes and resistors. Stored energy in the magnet is 800KJ at the rated current. The magnet is developed and tested for its operating performance.

II. Electromagnetic Design

The superconducting magnet is made of NbTi copper composite wire developed at AFD, BARC. The characteristic properties of the wires are discussed in Ref [1]. Electromagnetic analysis was carried out using OPERA TOSCA module. The parameters of the solenoid magnet are listed in Table-1.
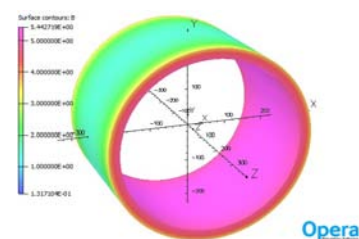

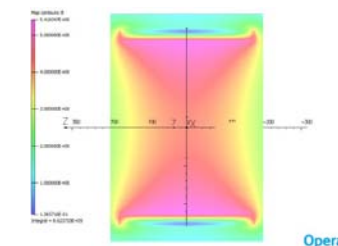
Fig. 1: Electromagnetic design
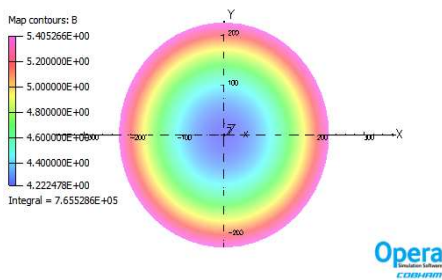

Fig. 2: Fieldprofilein r-z plane

Fig. 3: Field profile in the r-Øplane

Table 1: Superconducting solenoid magnet -EM design parameters

Inner diameter	458 mm
Magnet length	350 mm
Wire diameter	1 mm
Inter layer insulation thickness	0.1 mm
Number of turns per layer	350
Number of layers	24
Operating Current	240 A
Central magnetic field	4.2 Tesla
Maximum magnetic field	5.5 Tesla
Stored energy	840 KJ

The superconducting strands are wound directly onto the inner shell of liquid helium vessel. To avoid movement of the wire due to huge Lorentz forces, the wire is wound on the mandrel with pre-stress. Ground insulation is provided by 0.5mm thick G10-CR grade sheets and inter layer insulation is provided by glass fibre cloth of 0.1mm thickness. Winding is impregnated by wet hand layup technique. Banding by 0.5 mm of brass wire is done over the magnet winding, to provide pre-stress to the winding.

Fig. 4: SPM developed to carry out winding

Superconducting magnet has to be protected from temperature and voltage rise in the event of quench. Quench is a transition of the magnet from Superconducting state to normal state. The quench initiates at a point in the winding and grows by thermal conduction. Stored energy of the magnet is dissipated as heat. The highest integrated heat dissipation is at the quench initiation point. Passive quench elements comprising resistance and diode network is used for quench protection [2-4]. Detailed quench analysis was carried out in QUENCH module of vector fields [5] to estimate the temperature rise and the number of sub divisions required for safe operation of magnet.

Heat input of 0.2Joules provided to initiate a quench
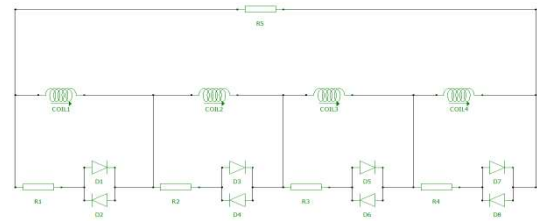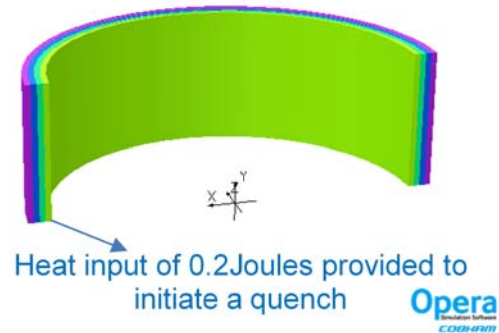

Fig. 4: SC magnet quench analysis

The nonlinear thermal and electrical properties required for the quench simulations are obtained from ROXIE material database reference [7].
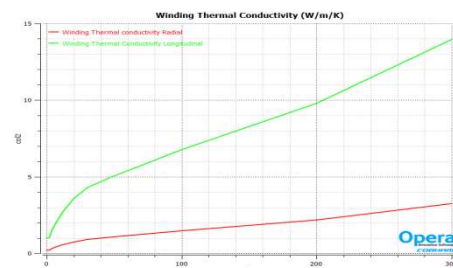
Fig. 5: Nonlinear thermal conductivity
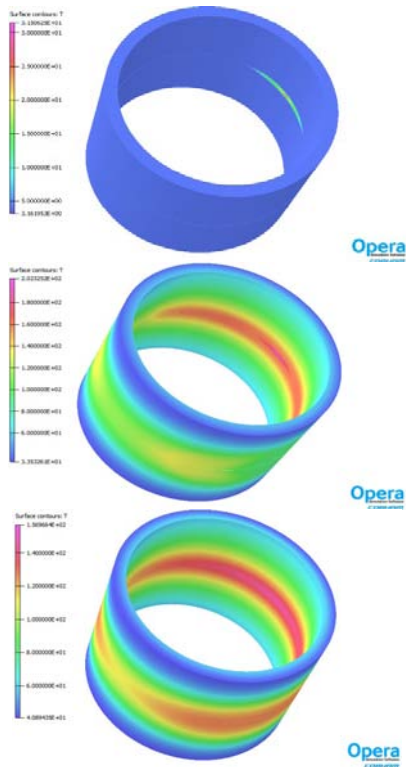
Fig. 6: Propagation of heat at t=0.1sec, 1 sec and 10 sec
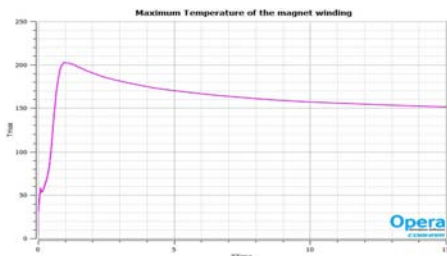
Fig:7 Maximum temperature in the winding
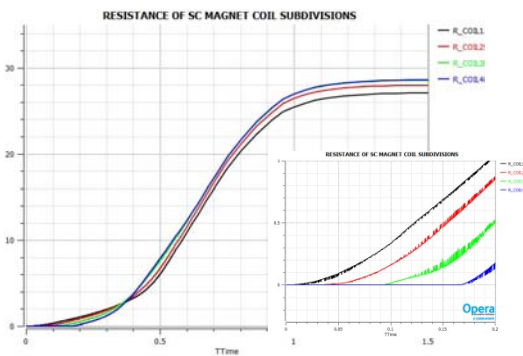
Fig:8 Growth of resistance of the winding
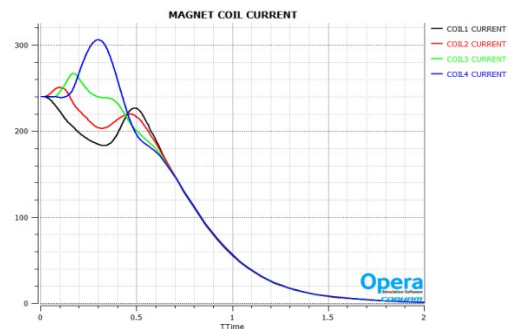
Fig: 9 Decay of current in the magnet coils

Fig:10 Assembly of quench protection diodes

III. Mechanical design

The conceptual design of the superconducting magnet is shown in Fig 11.
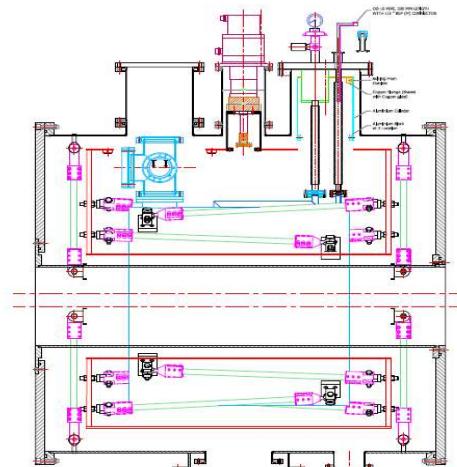
Fig:11 Cross sectional details of liquid helium cooled SC magnet

The liquid helium vessel is made of AISI 316L and designed in compliance with the guidelines stated in ASME Section VIII [6]. The helium vessel is

designed for an operating pressure of 1 bar and maximum pressure of 2 Bar. The welding procedure was qualified with Charpy impact test at 77K. The welding filler material was 316L with ferrite number less than 5. The vessel was tested for helium leak rate after cold thermal shock testing (spraying 77K). As the expansion ratio of liquid helium is 740, pressure relief valves were designed as per API and CGA guidelines. The vessel was tested for helium leak rate of less than 10^{-8} Torr.l/sec.

The vacuum vessel is designed and developed as per the guidelines of ASME Section VIII for external pressure of 1 Bar and internal pressure of 1.5 Bar. The material of construction is AISI 304 and the operating pressure is less than 5x10-5 Torr.

Relief valve and rupture disc are provided for safety of the vessel. The vacuum vessel is tested for helium leak rate of less than 10^{-9} Torr.l/sec.

IV. Thermal design

The operating temperature of the helium vessel is 4.2K and that of the vacuum vessel is 300K. The helium vessel is supported inside the vacuum vessel through tie rods. To reduce conduction heat loss, the tie rods are made up of cryogenic grade glass fibre composite, and thermalized to the thermal shield which is cooled to 80K[7-8]. The total conduction loss is less than 0.1 watts at 4.2K and 3 watts at 80K.

Fig:12 Support tie rods

To reduce the radiation loss, intermediate thermal shield is used which is cooled by G-M cryocooler to 80K. To further reduce the radiation losses, helium vessel and thermal shields are wrapped with MLI (Multilayer insulation) blanket. The total radiation loss is less than 0.5 watts at 4.2K and 10 watts at 80K.

Fig:13 MLI blanket wrapped over thermal shield

The superconducting magnet is energised by conduction cooled current leads, consisting of composite HTS leads and copper leads. The composite HTS leads are made up of BSCCO and thermalized to the thermal shield (80K). The conduction cooled leads from 80K to 300K is made up of ETP copper. Optimisation of the current lead cross sectional area was carried out for minimum heat leak [10].
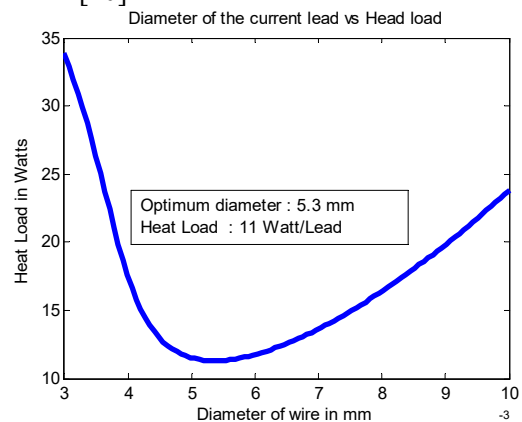

Fig:14 Optimised current lead for an operating current of 240A

V. Assembly of SC Magnet

The superconducting magnet is assembled vertically and then tilted horizontally for its normal operation. Suitable jigs were developed to carry out the assembly.

Fig:15 Assembly of SC magnet

VI. Testing of SC magnet

The liquid helium vessel is pre-cooled with liquid nitrogen. After purging out liquid nitrogen, helium was transferred. The magnet was energised and tested to its rated current.

Fig: 16 Transfer of liquid helium

VII. Conclusion

A room temperature bore, liquid helium cooled, superconducting magnet is designed, developed and tested for its performance. The authors are indebted to Materials Group, BARC (Dr Krishnamurthy, Dr G.K Dey) for their initiation and support in the indigenous development of thislarge horizontal warm bore superconducting magnet.

VIII. References

1. Low Temperature Superconductor - Fabrication and Application A.K. Singh, M. M. Hussain, S. P. Singh and V. G. Date, Atomic Fuels Division, Bhabha Atomic Research Centre, BARC Newsletter 2003.

2. Y. Torun, D. Huang, J. Norem, R. B. Palmer, A. Bross, M. Chung, A. Jansson, A. Moretti, K. Yonehara, D. Li, and R. Rimmer, "The MuCool test area and RF program," in *Proc. IPAC*, Kyoto, Japan, pp. 3780–3782, THPEA046.

3. M. N. Wilson, *Superconducting Magnets*. Oxford, U.K.: Oxford Univ. Press, 1983.

4. G. Gregoire, G. Ryckewaert, and L. Chevalier, MICE and InternationalMuon Ionization Experiment Technical Reference Document 2001.

5. Vector Fields, Reference manual.

6. ASME Section-VIII & Section-IX

7. Ph. Leburn "Design of A Cryostat for Superconducting Accelerator Magnet: The LHC Main Dipole Case".

8. G. Vandoni: "Heat Transfer"; in CERN, European Organization for Nuclear Research, Geneva Switzerland.

Indigenous Efforts on the Development of Samarium-Cobalt based Permanent Magnets

D .K. Sahoo and V. Kain

Material Processing and Corrosion Engineering Division,
Materials Group

D.K. Sahoo is the recipient of the DAE Young Applied Scientist/ Technologist Award for the year 2015

Abstract:

The present invention deals with process of producing samarium-cobalt alloy powder which is useful as raw material in developing permanent magnets having high magnetic properties. A modified reduction- diffusion process has been adopted here to produce the alloy by choosing appropriate raw material and performing reduction process in a controlled way. The process essentially involves the calciothermic reduction of samarium oxide in presence of cobalt under argon atmosphere, followed by decalcification to get desired alloy product. The effect of processing parameters in obtaining the desired magnetic phases and on residual calcium has been studied in details.It was observed that the alloy powder with optimum samariumand lower calcium contentis suitable to have improvedthe magnetic properties in the final product. The process has been successfully scaled up from 100g to 10kg batch level.

Introduction:

Permanent magnets i.e. hard magnetic materials are of great technological importance because they can maintain high level of constant magnetic fluxes without applying an external magnetic field or electrical current. Rare earth based permanent magnets are technologically important materials and have got significant uses in industry and science, i.e.electric motors, NMR scanners, wind-mills, compact discs, actuators for robotics and flight control, etc [1-3].After the discovery of magnetic anisotropy in yttrium cobalt compound (YCo_5) in 1966, an insurgent interest had been developed in the researchers to explore the magnetic properties of other rare earth metals with cobalt. The extensive research on this area has led to the discovery of $SmCo_5$ based magnets with energy product which was referred to the first generation of rare earth based permanent magnets. Later Sm_2Co_{17} and NdFeB type of magnets were discovered. Although NdFeB type of magnets are widely used in the market on account of their superior magnetic properties and low cost but they have some shortcomings like low curie temperature, low thermal stability and corrosiveness which often limits their uses [4-6].Samarium-cobalt based magnets with high energy product and excellent coercive force are suitable to be used in highly efficient machine and components in which higher operation temperature, higher corrosion and oxidation resistance are crucial [7-8].These magnets find use in atomic energy, space and defence industries for a variety of strategic and non-strategic applications. Industrially, rare earth alloys are produced by melting pure rare earth metals at high temperatures. It is, however, expensive due to high cost of rare earth metals, high melting temperature, and rare earth losses in the process. Moreover, it is obtained as a dense ingot, which requires further crushing and grinding before magnet making. All these processes are energy intensive. On the other hand, reduction-diffusion process yields the alloy powders directly from inexpensive oxides at much lower temperature, thereby resulting in lower cost magnets.The object of this invention is to develop indigenous technology for preparing Sm-Co magnetic alloy powder from the raw materials found in India suitable to make permanent magnets.

Experimental:

In the first step of process, the samarium oxide (99% pure) was thoroughly mixed with cobalt powder (99.4% pure) supplied by Indian Rare Earths Limited (IREL). The mixture was then admixed with calcium metal granules (99% pure procured from local market) to affect the reduction of the samarium oxide. Mixing of calcium into the charge mixture was carried out under protective cover of argon gas inside a glove box. In the process 10-100% stochiometric excess of calcium was used to ensure that all of the samarium metal oxide is reduced to samarium metal. The mixtureof Sm_2O_3, Co and Ca was then charged into a specially designed crucible and then kept inside the furnace chamber. The furnacechamber was purged with argon gas for one hour to remove water moisture and entrained air before keeping the crucible containing charge mixture in it. The furnace was heated up to 1100-1200 °C and nominal flow of argon gas was maintained throughout the course of experiment. Optimum soaking period was given depending upon the quantity of charge mixture taken to ensure the complete diffusion of samarium into cobalt matrix. The crucible along with the reaction mixture was taken out after the furnace cool down to room temperature.

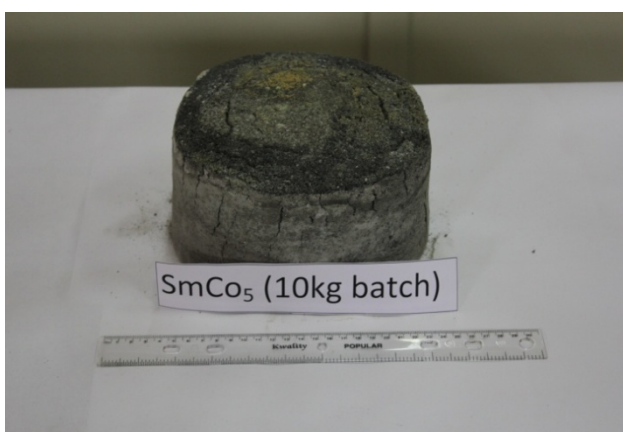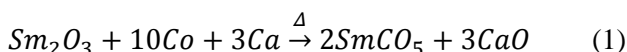The reactions involved in the RD process are given below:

$$Sm_2O_3 + 10Co + 3Ca \xrightarrow{\Delta} 2SmCO_5 + 3CaO \qquad (1)$$

Fig.1: Sm-Co product obtained by R-D process

Fig.1 shows the product obtained after RD process. It is essentially a hard, black, clinker-like cake comprising Sm-Co intermetallics and Cao along with some unreacted calcium. The undesired Ca and CaO sometimes forms Ca (OH)$_2$ upon exposure to atmosphere. The main aim in the second step was to effectively leach out Ca from the RD products safeguarding the Sm and Co values. The reaction product was first cooled to room temperature and then subjected for leaching process.

To start the process, the resulted mass of the RD product was first crushed into smaller pieces with particle size of around 1 to 2 mm size. For small scale batch (up to 1 kg scale) crushing was carried out in mortar pestle,where as for large scale batch (more than 1 kg scale) jaw crusher was used for this purpose. After crushing into small pieces, the next step was to grind the small pieces to fine powder having particle size of 200 μ. For small scale batch (up to 100g scale) grinding was carried out in mortar pestle,where as for large scale batch (more than 1 kg scale) planetary ball mill was used.

The resulting mass after crushing and grinding is hydrated with water to alkalize the Ca/CaO to form calcium hydroxide according to following equation.

$$2SmCo_5 + 3CaO + H_2O \xrightarrow{yields} 2SmCo_5 + 3Ca(OH)_2 \qquad (2)$$
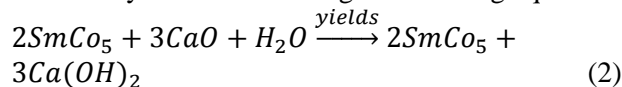
Here, the solution was stirred using a mechanical stirrer keeping a fixed rpm for optimum duration. In the process, the heavier intermetallic settled out while dissolved and un-dissolved Ca(OH)$_2$ floating in the supernatant liquid was removed by decantation. Water wash treatment was carried out in repeated cycles keeping with affixed solid to liquid ratio. In addition to water wash, the RD product is also subjected to acid treatment with solution of weak acid to get desired level of calcium content in the final product.

X-ray diffraction (XRD) (Inel France make, using Cr Kα radiation (λ= 2.29 Å) was employed to identify the phases of the alloy powder before and after the Ca leaching. Similarly, ICP-AES (Inductively Coupled Plasma-Atomic Emission Spectroscopy) technique was used to analyze residual calcium of the intermetallic powder.Wavelength Dispersive X-ray fluorescence (WD-XRF) spectroscopy was used to analyze the composition of Sm and Co in the alloy .The various phases and composition of the alloy were identified

by means of scanning electron microscopy (SEM) analysis. Oxygen content in the alloy powder was determined by inert gas fusion method.

Results and Discussion:

Fig.2 shows the XRD pattern of final product obtained after leaching. It was evident from the XRD pattern that the decalcified under optimum conditions has peaks corresponding to required $SmCo_5$ and Sm_2Co_7 only. Results obtained from WDXRF were also found to be consistent with the XRD result. Residual calcium and oxygen content in the alloy powder were found to be well within the permissible limit for making magnets.
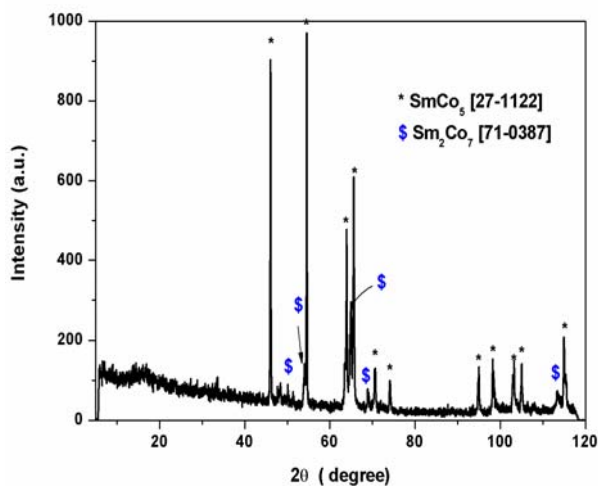

Fig.2: XRD of final powder

Optimization of parameters in the RD process:

To study the effect of temperature on the performance of RD process, experiments were carried out at different temperature ranging from 900^0C to $1300°C$. It was observed that the reduction was incomplete when it was carried out below $1050°C$ and there was loss of samarium value when temperature crossed $1200°C$. It was evident from the study that temperature must be kept above the melting point of samarium i.e.$1070°C$ for faster diffusion to happen.

A number of experiments were carried out to arrive at the optimum charge composition to get desired phases of the alloy. It was found that 5% excess Sm_2O_3 and 20% stoichiometric excess of Ca were necessary to get the desired phases.

Optimization of leaching conditions:

In the decalcification step, it was observed that almost 95% CaO was removed by leaching the product with demineralized (DM) water. For further decrease of residual calcium, leaching with acid solution was found to be necessary. In the leaching process, pH control is very important in the removal of trace amount of calcium by chemical reaction. High acidity may facilitate calcium removal but it leads to corrosion of alloy powder resulting in the deviation from targeted composition. Improper leaching results in loss of rare earth values. Typical SEM image the decalcined powder is shown in Fig.3.
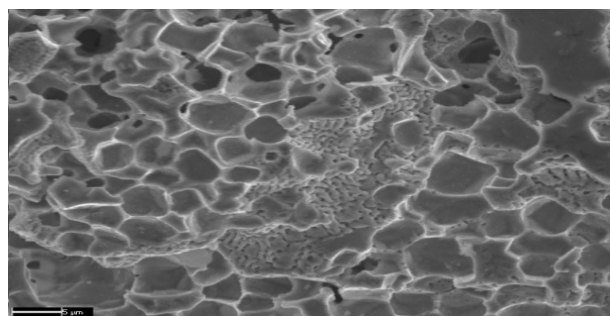
Fig.3: SEM image of the leached powder

To select the effective leaching conditions for maximum yield of $SmCo_5$ with minimum residual Ca in the alloy powder, four parameters have been identified. These are number of water wash cycle, number of acid wash cycle, pH of the solution and digestion time in each cycle. A number of experiments were carried out to reach at optimum conditions of leaching. These standardized leaching conditions were also experimentally validated for one kg and 10 kg scale batch.

Magnets were made out of this alloy powder and magnetic properties of these magnets were found to well match with the properties of the imported $SmCo_5$ magnet (Recoma-18) with typical values of Br= 8.4 kGauss ,H_c = 8.1 kOe ,H_k = -12 kOe ,BH_{max} = 19 MGOe.

Conclusion

Synthesis ofSm-Co (1:5) alloy powder by reduction-diffusion process has been optimized. Leaching conditions were also standardized for successful

removal of calcium from the products. XRD analysis confirmed the presence of required phases and WD-XRF analysis ensured the desired contents of the elements in the alloy powders. Oxygen and residual calcium content in the final products were well within the permissible limit for magnet preparation. Magnets made out of this material were found to be par with the recoma-18 grade magnets. The process has been successfully scaled up from 100g to 10kg batch level.

References:
1. C.Yamahata,C.Lotto, E.Assaf,M.Gijs, Nanofluid, A PMMA valvelessmicropump using electromagnetic actuation, Microfluid Nano fluid (2004) 197-2007.
2. H.R. Kirchmayr, Permanent magnets and hard magnetic materials, J. Phys. D.Appl.Phys.29 (1996) 2763-2778.
3. S. Sugimoto, Current status and recent topics of rare-earth permanent magnets, J. Phys. D: Appl. Phys. 44 (2011) 1-11.
4. S. D. Bhame, V. Swaminathan, P. K. Deheri, R. V. Ramanujam, Exchange coupled Nd2Fe14B/α-Fe nanocomposite by novel autocombustion- reduction-diffusion synthesis, Adv. Sci. Lett. 3 (2010) 1-6.
5. D. Brown, B. M. Ma, Z. Chen, Developments in the processing and properties of NdFeB-type permanent magnets, J. Magn. Mag. Mater. 248 (2002) 430-440.
6. M. Sagawa, S. Hirosawa, H. Yamamoto, S. Fujimura, Y. Matsuura, Nd-Fe-B Permanent Magnet Materials, Jap. J. Appl. Phy. 26 (1987) 785-800.
7. S.R. Trout, Permanent magnets based on the lanthanides: Raw materials, processing and properties, Proc. The International Symposium on Magnetics, Seoul, Korea, Nov 8-10, (1990) pp 79- 90.
8. S.J. Heh, S.K.Chen, F.T.Jin,L.K.Chen, Process for producing rare earth-cobalt permanent magnet, US patent, 4875946,1989.

Development of customized strategies for improving the efficacy of cancer radiotherapy

Sundarraj Jayakumar, Deepak Sharma and S. Santosh Kumar

Radiation Biology and Health Sciences Division

Abstract

We have developed DNA damage and DNA damage based gene expression as predictive markers of radiosensitivity in cancer cells which would find application in customized radiotherapy. We have identified Nrf2 as a target for modulating radiosensitivity in cancer cells and normal cells. We have also developed Nrf2 centric drugs for mitigation of radiation injury.

Introduction

Cancer is one of the major causes of death worldwide. Radiation therapy is an important treatment modality employed for cancer. But due to the inter-individual differences in radiosensitivity of cancer cells, the efficacy of the radiotherapy is affected. Further, normal tissue toxicity is also a major concern to the clinicians during radiotherapy. The efficacy can be improved by prediction of radiosensitivity of cancer cells and through modulation of radiation responses of normal and cancer cells. Clonogenic assay is considered as gold standard for predicting radiosensitivity.However, this assay cannot be used under clinical settings because the tumor samples derived from patients seldom grow in a petri dish to form colonies. Hence there is a need for development of rapid and reliable assay for predicting the radiosensitivity, which will help in designing personalized radiotherapeutic regimen. Apart from prediction, modulation of radiosensitivity is also important for improving the outcome of radiotherapy. For modulation of radiation response, understanding the molecular players governing radiosensitivity of cell is pivotal. Drugs which target the proteins that are contributing to radioresistance of cancer cells can be effective sensitizers and the drugs which activate survival proteins specifically in normal cells can be potential radioprotectors. When cells are exposed to gamma radiation, free radicals are formed as a result of water radiolysis and these free radicals in turn cause damage to cellular macromolecules like protein and DNA. Damage to DNA (double strand breaks) is the most critical lesion, which if unrepaired can lead to cell death. Cells activate many signaling mechanisms and repair pathways which help in salvaging the DNA damage. These factors can be used as targets for predicting and modulating the radiosensitivity. One ubiquitous transcription factor which gets activated during the radiation exposure is Nrf2. Under normal conditions, this transcription factor is sequestered in the cytoplasm and during oxidative stress,Nrf2 is translocated to the nucleus and thereby transactivates the target genes which are involved in anti-oxidant response leading to the survival of the cell. Targeting Nrf2 can be a good strategy for radiosensitization of tumor cells and radioprotection of normal cells. Drugs whichtarget this molecule can be good radio-modulators.

Materials and Methods

Tumor cells were obtained from National Centre for Cell Science, Pune. Chemicals and reagents were procured from Sigma-Aldrich.

Clonogenic assay

Clonogenic assay determines the ability of a cell to divide multiple times and form a macroscopic colony. Tumor cells were cultured in the petri dish for 12 h and then they were exposed to radiation. They were further cultured for two weeks for the colony development. The colonies were fixed using

methanol, stained with crystal violet and counted using a colony counter.

Assessment of DNA damage by comet assay

When a cell containing DNA damage is subjected to electrophoresis the movement of DNA will be higher as compared to that from control cell. Comet assay measures the DNA damage using this principle. For this assay, the cells are mixed with agarose gel and layered on to the slide. After solidification, the cells were lysed using lysis buffer, and electrophoresis was carried out in Tris-Borate-EDTA buffer.The cells were stained with a SYBR-Green dye (a DNA binding fluorescence dye), visualized using fluorescence microscope and the images were used for calculating the extent of DNA damage by analyzing the tail formation.

Assessment of DNA damage by gamma-H$_2$AX foci

H$_2$AX is a histone variant found as a part of the nucleosome, on which DNA is coiled around. When the DNA is damaged, this histone gets phosphorylated and it can be detected as foci using antibody staining. By analyzing the number of foci present at different time points after radiation, the extent of DNA repair was studied. For performing this assay, cells were grown on a coverslip, given respective treatments, fixed using 4% paraformaldehyde, permeabilized by treating with Triton-X-100, stained with γ-H$_2$AXantibody and secondary antibody labelled with fluorescent dye. The cells were counterstained with DAPI and visualized under fluorescence microscope and average number of foci present in each nucleus was counted as a marker for DNA damage.

Results and Discussion

Correlation between clonogenic assay and comet assay for predicting the radiosensitivity of tumor cells

To know the usefulness of comet assay in predicting the radiosensitivity of tumor cells, the radiosensitivity profiles of seven different cancer cells were established using clonogenic assay indicating their respective survival fraction. The radiation induced DNA damage was quantified using comet assay (% DNA in tail).The correlation between survival fraction and % DNA in tail was

calculated and we found that these two parameters showed significant correlation (Fig.1). This correlation was also valid under fractionated dose regimens. Out of several time points analysed, the comet assay performed immediately after irradiation showed best correlation with radiosensitivity. Moreover, neutral comet assay, which preferably assesses DNA double strand breaks showed better correlation with radiosensitivity than the alkaline comet assay which quantifies total DNA damage (single and double strand breaks). In conclusion, our results established that the neutral comet assay performed immediately after radiation exposure can be a good predictive markerfor radiosensitivity.
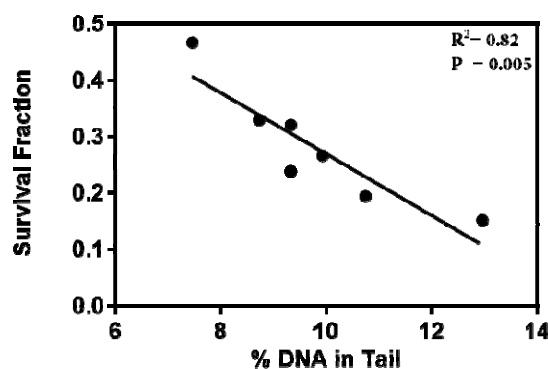

Fig:1: Correlation between clonogenic assay (survival fraction) and neutral comet assay (% DNA in tail) was obtained in seven different cancer cell lines.

Role of Nrf-2 in radioresistance of cancer cells

Apart from predicting radiosensitivity, understanding the underlying molecular mechanisms is also important for identifying druggable targets in the cells. For this purpose, a microarray analysis was performed in two cancer cell lines which exhibited differential radiosensitivity measured in terms of survival fraction and apoptosis. From the microarray data, the genes which are differentially expressed in radioresistant cells were identified. Thioredoxin family of genes was upregulated in radioresistant cells as compared to radiosensitive cells. Since thioredoxin family genes are regulated by Nrf2, we analysed the expression of Nrf2 in these cells. The radioresistant cells showed higher expression of basal as well as radiation induced Nrf2. Accordingly, the levels of radiation induced reactive

oxygen species were higher in radiosensitive cells as compared to radioresistant cells. To further confirm the role of Nrf2 in radioresistance, we have used chemical inhibitor (all-*trans* retinoic acid) or knocked down approach by shRNA and then examined their effect on the radiosensitivity of cancer cells. Pharmacological inhibition or knockdown of Nrf2 synergistically enhanced the radiosensitivity of cancer cells implying that Nrf2 overexpression in tumor cells can lead to radioresistance.

Involvement of Nrf2 in DNA repair

To further understand the possible mechanism through which Nrf2 is regulating radioresistance, the effect of Nrf2 on DNA repair was studied. When Nrf2 was inhibited or knocked down, DNA repair was slowed down, as found by γ-H$_2$AX foci (Fig.2). The influence of Nrf2 on DNA repair was not dependent on its downstream genes involved in anti-oxidant activity. This was confirmed by studying the DNA repair in the presence of a known anti-oxidant N-acetyl-cysteine. Further, involvement of the non-homologous end joining pathway was ruled out by combining DNA-PK inhibitor along with Nrf2 inhibitor. When the upstream regions of DNA repair genes were probed, RAD51 family of genes (involved in homologous DNA repair) showed
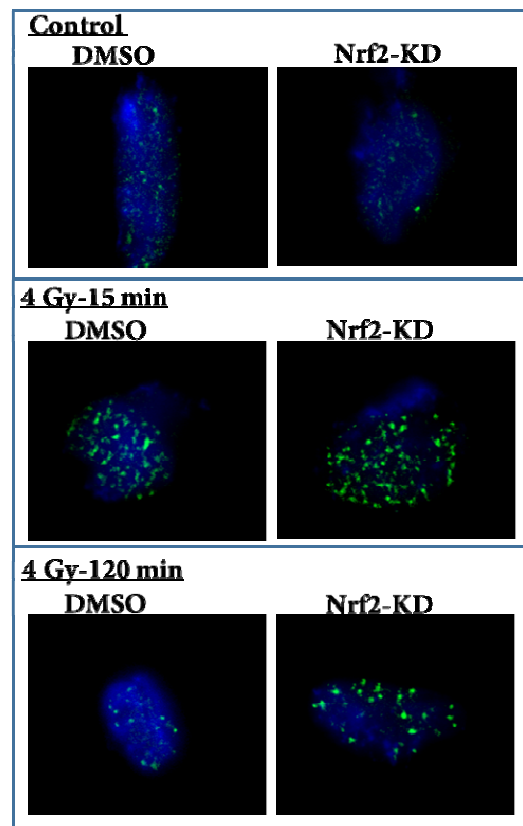

Fig:2. Effect of Nrf2-knockdown (Nrf2-KD) on DNA damage repair as compared to control (DMSO) as analysed by γ-H$_2$AX foci formation.
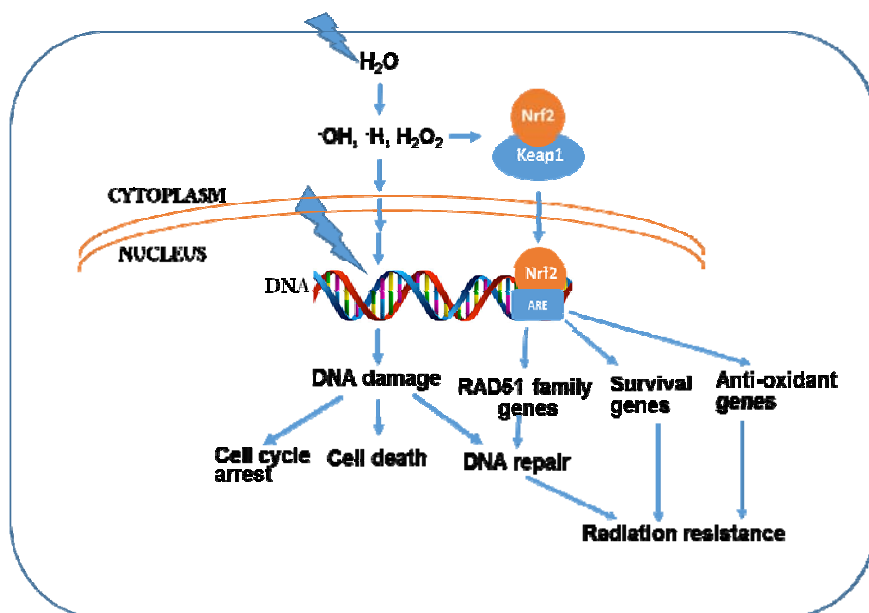

Fig:3: Role of Nrf-2 in the DNA repair and in radioresistance of cancer cells.

the presence of antioxidant response elements (ARE) in their promoter region. The expression of RAD51 family of genes was decreased in Nrf2 knockdown cells, suggesting that the Nrf2 is involved in DNA repair through the homologous recombination repair. Hence our results clearly indicated that apart from involvement in anti-oxidant response, Nrf2 is also modulates DNA repair and thereby contributes to radiation resistance in cancer cells (Fig.3).

Development of new drugs for modulation of cellular radio-sensitivity

Many phytochemicals and their derived compounds were screened to modulate the radiosensitivity of cancer cells and normal cells. We found that dimethoxy curcumin (DIMC), a synthetic analogue of curcumin, modulated radiosensitivity of cancer cells. The bio-availability and stability of DIMC is more as compared to curcumin.Our studies revealed that DIMC at 2.5 µM concentration increased the radiosensitivity of the cancer cells and cancer stem cells. This effect was due to inhibition of thioredoxin reductase- an Nrf2 dependent gene. We have also identified another drug which is a derivative of green plant pigment chlorophyll (BARC Radio Modifier-BRM). Preclinical studies using BRM demonstrated its radioprotective efficacy against lethal doses of radiation in mice. Safety and toxicological studies in multiple species of rodents have been completed under GLP conditions. BRM is well tolerated up to 5g/Kg body weight. This technology has been incubated with Innovative Drug Research Solutions Ltd., Bangalore. The formulation has been optimized and 2 lakh tablets have been manufactured under GMP conditions for human clinical trials.

Conclusion

Our efforts have identified a simple, fast and efficient protocol for predicting the radio-sensitivity of patient derived cancer cells. This protocol will be useful for customized radiotherapy. Further, we have identified Nrf-2 and thioredoxin reductase as druggable targets for modulation of radiosensitivity. Based on these studies, we have developed new radio-modifying drugs for use in clinic.

Dynamics and Structure of Pollutants in Gas Phase and at Air-Liquid Interface

Ankur Saha, Awadhesh Kumar and P. D. Naik

Radiation & Photochemistry Division

Abstract: In recent time, studying the dynamics and structure of pollutants in gas phase and as well as at air-liquid interface has got considerable interest in view of both environmental and fundamental research. In this context, in our division we have developed and installed a Molecular beam-Resonance Enhanced Multiphoton Ionization - Time of Flight (MB-REMPI-TOF) set up to understand the UV-photodissociation of halogenated volatile organic compounds (VOCs) in gas phase. We have also installed Vibrational Sum-frequency Generation (VSFG) set up to study the structure, dynamics and interaction of molecules having environmental and biological importance, at surfaces and interfaces. Applications of these two techniques with specific examples are presented in this article.

Photodissociation dynamics of halothane: A REMPI-TOF study

Introduction

Halothane (2-bromo-2-chloro-1,1,1-trifluoroethane), which contains three different halogens as substituent on a simple ethane skeleton, was a widely used general inhalation anesthetic and one of the major man-made bromine-containing species found in the free troposphere. Since Br atom is predicted to have several times more efficiency in depletion of ozone in stratosphere than Cl atom, photodissociation studies on bromohalides are of importance. The photodissociation dynamics of halothane have been studied near 234 nm, in a molecular beam environment, employing resonance-enhanced multiphoton ionization with time-of-flight mass spectrometer (REMPI-TOF-MS). Both bromine and chlorine atoms are detected in both the ground and spin-orbit excited states. Translational energy distributions, the recoil anisotropy parameter (β) and the spin-orbit branching ratios of these channels have been measured. Based on the combined experimental results and theoretical calculations the mechanisms of bromine and chlorine formation channels have been proposed.

Experimental

Halothane in a molecular beam was irradiated at ~234 nm and the photoproducts, $Br(4P\ ^2P_{3/2})$, $Br^*(4P\ ^2P_{1/2})$, $Cl(3P\ ^2P_{3/2})$ and $Cl^*(3P\ ^2P_{1/2})$ atoms, detected state-selectively, employing (2+1)-REMPI with TOF mass spectrometer. A detailed description of the experimental setup (Fig.1.1) is given in our previous publications.[1,2] A TOF-MS (two-stage Wiley–McLaren type)was mounted vertically, perpendicular to the horizontal MB, with microchannel plates (MCP) as detector. The vapour of the reactant, seeded in helium, was obtained by bubbling helium through a sample maintained at room temperature. A single laser was used for both photodissociation of the parent molecule and ionization of the atomic photoproducts. A Nd:YAG laser pumped dye laser, using rhodamine 101 dye, was employed for generating the requisite laser beam in the range of 230-236 nm. For measuring TOF spectra, the MCP signal was fed to an oscilloscope, which was interfaced to a Pentium PC. A double Fresnel rhomb was used for rotation of the laser beam polarization entering the chamber. TOF profiles were taken for three different experimental configurations (vertical, horizontal and magic angle), and are shown in Fig.1.2. The measured TOF

profiles correspond to the component of the photofragment that speeds along the TOF-MS axis, which defines the lab frame Z axis and is given as,

$$f(v_z, \chi) = \int_{|v_z|}^{\infty} \frac{g(v)}{2v} \left[1 + \beta P_2(\cos\chi) P_2\left(\frac{v_z}{v}\right) \right] dv,$$

where v_Z is the velocity component along the Z axis, v is the recoil speed of the fragments, β is the anisotropy parameter, $P_2(\cos\chi)$ is the second Legendre polynomial, and the $cos(\chi) = \hat{\varepsilon} \cdot \hat{z}$, is the projection of the pump laser electric field, $\hat{\varepsilon}$, on the detector axis, $\hat{z}$, which is also defined as the angle between the dissociation laser polarization and the Z axis. The major task of the analysis procedure is to extract the photofragment speed distribution, $g_i(v)$, and anisotropy parameter, β_i, of each decay channel i active in the photodissociation. The detail of the adopted procedure has been described elsewhere.[2] The photofragment speed distribution, $g(v)$, thus obtained was converted into the center-of-mass translational energy distribution, $P(E_T)$ and the average translational energy was calculated. Also, the spin-orbit ratio of the halogen atom formed is evaluated, which eventually gives information about the dynamics occurring in the exit channel of the photodissociation process.
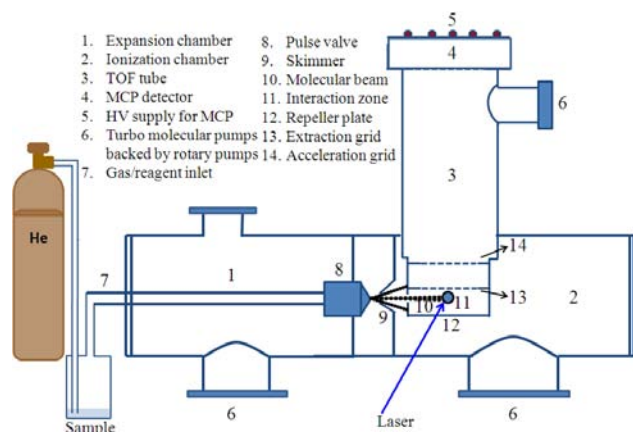

1. Expansion chamber
2. Ionization chamber
3. TOF tube
4. MCP detector
5. HV supply for MCP
6. Turbo molecular pumps backed by rotary pumps
7. Gas/reagent inlet
8. Pulse valve
9. Skimmer
10. Molecular beam
11. Interaction zone
12. Repeller plate
13. Extraction grid
14. Acceleration grid

Fig. 1.1: Schematic of MB-REMPI-TOF-MS setup.

Results and Discussion

The TOF profiles of Br* and Cl* are similar to that of Br and Cl(shown in Fig.1.2), respectively. The analysis of TOF spectra results in the β values of 0.6±0.2 for Br and Br*, and 0.3±0.1 for Cl and Cl* fragments. The non-zero β values imply an anisotropic angular distribution of the fragments,
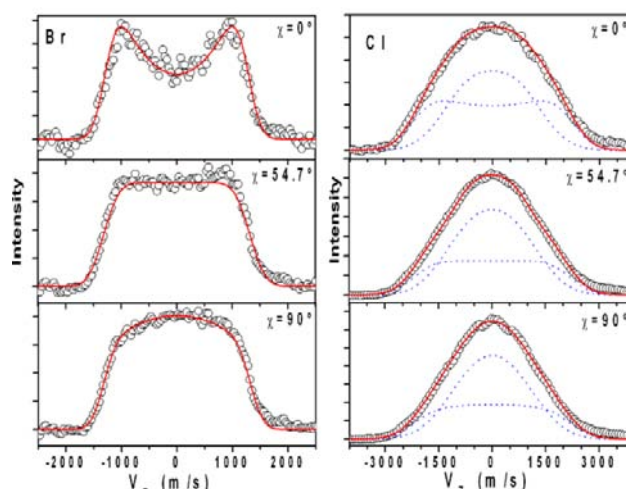

Fig.1.2: TOF profiles of Br($^2P_{3/2}$) and Cl($^2P_{3/2}$) produced from the 234 nm photodissociation of Halothane at different laser polarization. The circles are the experimental data and the solid and dashed lines are forward convolution fit.

suggesting fast formation of Br and Br*, and also probably for Cl and Cl*. The photofragment speed distributions reveal only one velocity component (fast) for both Br and Br*, but two components (fast and slow) for both Cl and Cl*. Thus, each of two bromine channels (Br or Br*) originates from a single pathway, whereas each of two chlorine channels (Cl or Cl*) originates from two different dissociation pathways. The relative translational energies of Br and Br* channels are 10.5±1.0 and 8.5±0.9 kcal/mol, respectively. The relative translational energies for the fast (high energy) and slow (low energy) Cl channels are 17.5±2.0 and 7.5±1.0 kcal/mol, respectively. Similarly, the average translational energies for the fast and slow Cl* channels are 21.0±2.0 and 9.5±1.0 kcal/mol, respectively. The excitation energy (122 kcal/mol) is greater than the bond dissociation energies of both the C-Br (60.5 kcal/mol) and C-Cl (73.2 kcal/mol) bonds of halothane. Thus, in principle, both the bonds can be cleaved on excitation at 234 nm. But, at this wavelength only the σ^*(C-Br)←n(Br) transition of halothane is directly excited, and not the σ^*(C-Cl)←n(Cl) transition. Thus, the direct C-Br bond dissociation can take place from the repulsive state to produce Br atoms in both the ground and spin-orbit excited states. This impulsive bond scission is characterized by partitioning of a greater

fraction of the available energy in the relative translation ($f_T = 0.17$) of the products associated with high recoil anisotropy parameter (β) of 0.6. However, the mechanism of chlorine atom formation cannot involve direct C-Cl bond rupture. The locally excited nσ*(C-Br) surface can transfer energy to the nσ*(C-Cl) surface, from which Cl and Cl* can be produced. The observed f_T values of 0.37 and 0.46 for high kinetic energy (fast) Cl and Cl* channels, respectively, and the β parameter value of 0.3±0.1 for both the channels suggest that this mechanism is responsible for the fast chlorine atom channels. The translational energy distributions of low energy (slow) Cl and Cl* with the observed f_T values of 0.16 and 0.21, respectively are much greater than the statistical value of ~0.07. The slow chlorine atom channel cannot be assigned to occur from the ground electronic state of halothane after fast internal conversion, or involving a secondary reaction. Thus, the mechanisms of formation of slow chlorine atoms also involve the impulsive C-Cl bond scission. These mechanisms are supported by molecular orbital calculations.

Conclusions

The UV photodissociation dynamics of halothane is investigated on excitation at ~234 nm to the n(Br)σ*(C-Br) surface. Both bromine and chlorine atoms are detected using (2+1)-REMPI with TOF mass spectrometer. The C-Br bond scission is observed predominantly due to direct σ*(C-Br)←n(Br) transition, with translational energy distribution described with a soft impulsive model. The diabatic crossing from the [n,σ*(C-Br)] surface to the [n,σ*(C-Cl)] diabatic surface is responsible for an unexpected chlorine formation via the stronger C-Cl bond fission. Thus, the presence of the bromine atom has a pronounced effect on the C-Cl bond dissociation dynamics. Moreover, the energy transfer between the two modes is fast enough to produce anisotropic distribution of the chlorine atoms.

Aggregation of mixed surfactants at air-water interface: A VSFG study

Introduction

Surfactants are widely used for several industrial applications. Hence, the adsorption of these molecules at interfaces, particularly air-water interface, is an important area of research in surface science. Among several techniques employed to investigate the microscopic structure and morphological properties of surfactant at interfaces, the vibrational SFG is ideally suited because of its inherent surface specificity and high sensitivity. In the present work we have investigated effects of various compositions in mixed surfactant solutions of SDS (sodium dodecyl sulfate) and CTAB (cetyltrimethylammonium bromide), at air-water interface using VSFG nonlinear optical spectroscopy. The main objective of this study was to investigate ordering of interfacial water molecules at the charged air-water interface and aggregation behaviour of the catanionic system of CTAB and SDS with varying compositions in aqueous solutions.

Experimental

The experimental setup of VSFG (Fig. 2.1) is described in details elsewhere.[3]However, a brief description is as follows. Vibrational SFG spectroscopy is based on a coherent second order non-linear process, which involves two input beams of fixed visible (v_{vis}) and tunable infrared frequencies (v_{IR}). The visible beam at 532 nm is generated by frequency doubling of the fundamental output of a Nd:YAG laser (PL2241B, Ekspla, Lithuania). The tunable IR beam is generated in a difference frequency generator (DFG) by mixing the output of an optical parametric generator (OPG) with the fundamental output (1064 nm) of the Nd:YAG laser in a silver thiogallate ($AgGaS_2$) crystal. The OPG (PG401, Ekspla) was pumped by the third harmonic (355 nm) beam of the Nd:YAG laser, using lithium triborate (LiB_3O_5) as a non-linear crystal. These two input beams are passed through apertures, energy attenuators and polarizers, and finally partially focused at the interface. The angles of incidence were kept at 55° and 60° for the IR and visible laser beams, respectively. The SFG signal beam was separated and detected with a photomultiplier tube (PMT) after spatial, polarization and spectral filtering. Four different polarization schemes (*ssp*, *sps*, *pss* and *ppp*) are possible for SFG experiments, and these are denoted based on the polarization states of the SFG, visible and IR beams in the sequence. For measuring the vibrational spectra at an interface, the IR frequency

was scanned in the appropriate range. The CH and OH vibrational stretching regions were scanned in the range of 2750-3000 cm^{-1} and 3000-3600 cm^{-1}, respectively.
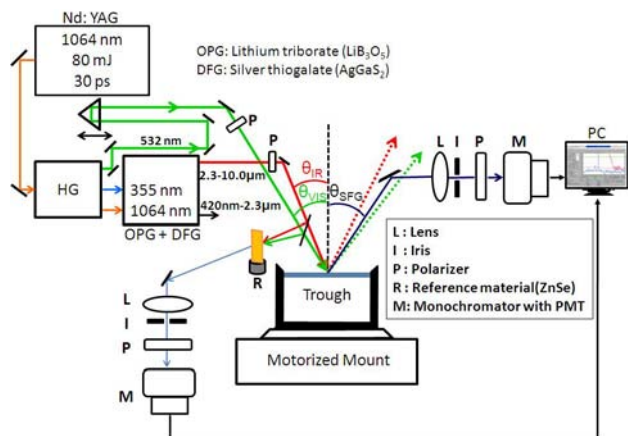

Fig. 2.1: Schematic diagram of the VSFG set up

Results and Discussion

In the presence of either CTAB or SDS aqueous solution, we observed a significant enhancement in the intensities of the OH stretching modes (broad peaks at ~3200 cm^{-1} and ~3400 cm^{-1}) of interfacial water molecules in the VSFG spectra. This implies an ordering of the H$_2$O molecules at interfaces, induced by the large electrostatic field of the charged surfactants. However, with a mixed surfactant solution of SDS and CTAB in 1:1 ratio (Fig. 2.2), opposite charges on these surfactant molecules get cancelled and consequently the OH peaks disappear. One can assume that for this composition approximately half of the interfacial water molecules are oriented with oxygen atoms towards the bulk water phase, and the other half are oriented with oxygen atoms towards the air. This results into null orientation of interfacial water molecules, leading to disappearance of the OH peaks. A significant change was also observed in the CH spectral region of the mixed surfactants (SDS and CTAB in 1:1 ratio) with respect to the individual surfactants (Fig. 2.2). The vibrational frequencies in VSFG spectra of surfactants with their assignment are given in Table 2.1. For the 1:1 composition, the intensity of the v_s(CH$_2$) band at ~2850 cm^{-1} is reduced and that for the v_a(CH$_2$) band at ~2917 cm^{-1} (due to CTAB) is negligibly small. But the intensities of the CH$_3$ modes are very much

enhanced. In addition, the v_s(CH$_2$) band at ~2850 cm^{-1} has shifted to a lower wavenumber of 2846 cm^{-1}. Even the new peak at ~2940 cm^{-1} has shifted to lower wavenumber by about 3 cm^{-1}, and this peak can be assigned to the v(CH$_3$-FR) band of a complex between CTAB and SDS surfactant molecules. Thus, the observed VSFG spectra from the mixed surfactant system are dominated by the v_s(CH$_3$) and CH$_3$ Fermi-resonance bands positions, suggesting highly ordered conformation and low gauche conformation with respect to individual surfactant component.
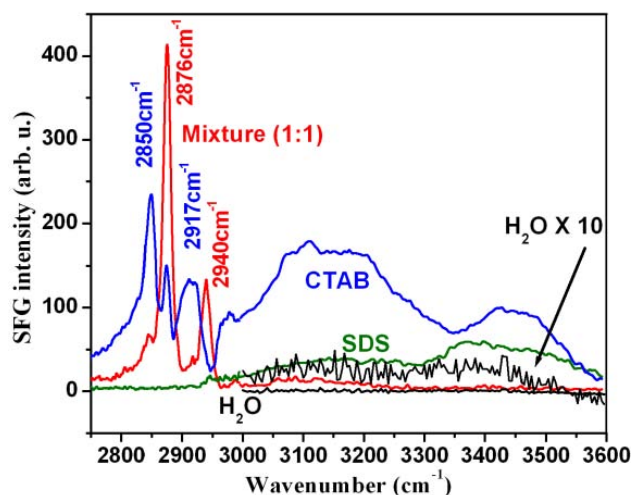

Fig. 2.2: VSFG spectra of aqueous solution of individual and mixed (1:1) surfactants of SDS and CTAB at the air-water interface.

Vibrational region of the CH stretching frequencies at the air-water interface was also probed to investigate the time evolution of the alkyl chain of the surfactant molecules in the insoluble 1:1 complex. The complex is characterized by two major vibrational peaks at 2876 and 2940 cm^{-1}. The temporal profiles show an induction time before the appearance of these two peaks of the complex (Fig. 2.3). Subsequently, there is a fast growth (within ~30s) followed by a slow growth up to more than 3 hrs. The induction time and the growth kinetics strongly depend on the total bulk concentration and the relative compositions. With increasing bulk concentrations of the 1:1 ratio of CTAB and SDS surfactants, the induction time decreases (from ~2000 s to nil) and the adsorption kinetics become

| Table 2.1: Assignment of vibrational frequencies in VSFG spectra of surfactants at air-water interface under SSP polarization.			
Assignment of vibrational frequencies	**Observed vibrational frequencies/cm^{-1}**		
	SDS	CTAB	1:1-Complex
CH$_2$ symmetric stretch, $\nu_s(CH_2)$	2850-2857	2848	2846
CH$_3$ symmetric stretch, $\nu_s(CH_3)$	2879-28881	2876	2876
CH$_2$ antisymmetric stretch, $\nu_a(CH_2)$	~2924	2914-2920	--
CH$_3$ Fermi-resonance, $\nu(CH_3\text{-FR})$	2944-2947	--	2940
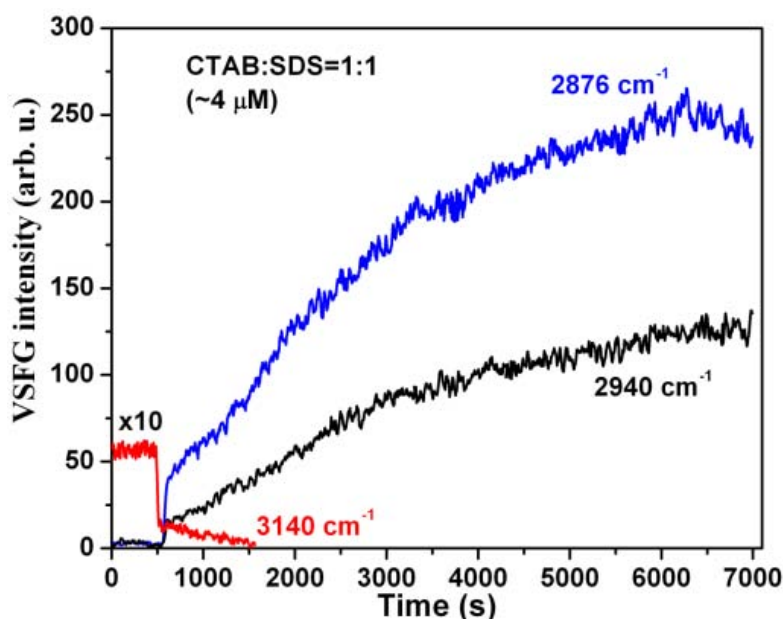
Fig. 2.3: *Temporal evolution of the OH (3140 cm^{-1}) and CH (2876 and 2940 cm^{-1}) vibrational bands of the complex between CTAB and SDS*

faster. Among all the compositions with the same total bulk concentration, the 1:1 ratio exhibits the smallest induction time and the fastest adsorption kinetics. Under similar conditions, the OH peak decays much faster, whereas the CH peaks keep on growing for a longer time. The slow growth can be due to re-arrangement of the complex forming a monolayer. The presence of the fast growth in VSFG profile is explained based on the formation of surface aggregate domains due to the adsorption of catanionic surfactant molecules.

Conclusions

The effects of various compositions in mixed surfactant solutions of SDS and CTAB at air-water interface were investigated using vibrational sum-

frequency generation (VSFG) nonlinear optical spectroscopy. In the presence of either SDS or CTAB aqueous solution, we observed a significant enhancement in the intensities of the OH stretching of interfacial water molecules in VSFG spectra, due to ordering of these molecules induced by the large electrostatic field of the charged surfactants. However, with a mixed surfactant solution of SDS and CTAB in the 1:1 ratio, opposite charges on these surfactant molecules get cancelled and consequently the OH peaks disappear. The time evolution of the vibrational region of the CH stretching frequencies at the air-water interface indicates formation of the insoluble 1:1 complex of CTAB and SDS.

References
1. Naik, P.D., Upadhyaya, H. P., Kumar, A., Bajaj, P.N., Sinha, A.K., Bhatt, S. and Gupta, M.D.P., "Development of Resonance-Enhanced Multiphoton Ionization System", BARC Report No.: BARC/2009/E/011.
2. Upadhyaya, H. P., Saha, A., Kumar, A., Bandyopadhyay, T., Naik, P.D. and Bajaj, P.N. "Photodissociation Dynamics of Phosphorus Trichloride (PCl_3) at 235 nm Using Resonance Enhanced Multiphoton Ionization (REMPI) with Time-of-Flight (TOF) Mass Spectrometry"*J. Phys. Chem. A*, 114, (2010): 5271-5278
3. Saha, A., Upadhyaya, H. P., Choudhury, S., Kumar, A. andNaik, P.D."Sum-Frequency Generation Spectroscopy of Adsorbed Monolayer of Mixed Surfactants at Air-Water Interface" *J. Phys. Chem. C*, 118, (2014): 3145-31

Enhancement of Charge Carrier Mobility in Organic Semiconductor and their Gas Sensing Properties

Soumen Samanta
Technical Physics Division

Introductions:

Semiconducting organic materials, both polymeric and small molecule based, have gained worldwide attention during last two decades owing to their several interesting electrical and optical properties, and therefore, are being used in various devices, such as, organic field effect transistor (OFET), organic photovoltaics, organic light emitting diodes (OLED) and bio- and gas sensors etc [1,2]. Presently some of these organic devices are available in the market. Although these devices are having low charge carrier mobility but still these can be used in some special cases like in low cost flexible electronics, large area devices application etc [3,4]. For better performance of these organic semiconductor devices, it is very important to understand the charge transport mechanism in these organic semiconductors. A considerable amount of efforts have been devoted to study the charge transport mechanism(s) in organic semiconductor thin films, particularly at low temperatures (300-4 K). However it is very difficult to measure electrical conductivity at temperatures below 150 K. This is because no measurable electrical current is obtained atlow temperatures due to the very low mobility (μ), which are usually in the range of 0.01-0.1$cm^2V^{-1}s^{-1}$. The low value of μ in organic semiconductor thin films mainly arises due to theweak van der Waals forces between adjacent molecules. In addition, the μ is also affected byenergetic disorders (diagonal and non-diagonal), nature of molecular stacking (face-on oredge-on), adsorbed oxygen species and impurities [5].

Clearly, in order to investigate the lowtemperature charge-transport properties of organic semiconductor films, the major issue ishow to improve the mobility of films. Similar to the conventional inorganic semiconductorfilms, the μ can be enhanced by improving the crystalline structure of the films and reducingthe impurities.

Thiswork deals with growth and characterization of FePc and CoPc (chemical structure shown in figure 1a) thin films with a motivationof improving the charge carrier mobility and to study their charge transport and gas sensing properties.

Effect of substrate on the growth of organic semiconductor:

We have deposited metal-phthalocyanine (MPc) films using organic molecular beam epitaxy (OMBE) system on a variety of substrates viz. glass, (100) $SrTiO_3$, (100) $LaAlO_3$, (0001) Al_2O_3 and along the 38.6° bi-crystal boundary of bicrystal $SrTiO_3$. Generally, growth of MPc epitaxial films on inorganic substrates is difficult due to (i) large lattice mismatch between film and substrate, and (ii) extended (planar) nature of the MPc molecules. Nevertheless, it has been found that the chemical nature of substrate as well as its surface roughness strongly influences the growth of the MPc films. The growth mode of large planar molecules is governed by a competition between "molecule-molecule" and "molecule-substrate" interactions. If the molecule-substrate interaction is dominant then molecules arrange in the face-on stacking mode, otherwise the stacking mode will be edge-on.
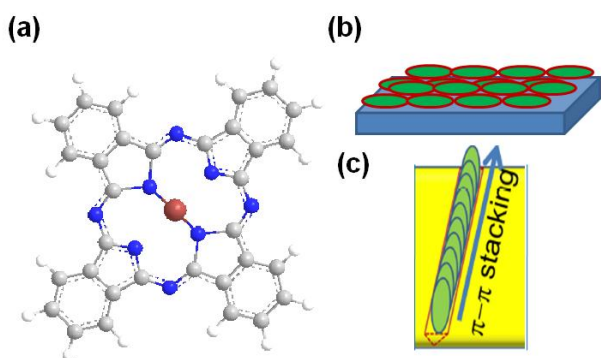
Fig. 1: (a) Structure of phthalocynine molecule, (b) Schematic of face-on and (c) edge-on staking of molecule.

The glass substrates are widely used to deposit organic films. Glass substrates are amorphous in nature and are chemically non-interactive to MPc molecule. Thus there is minimum substrate-molecule interaction between phthalocyanine and glass substrate. However, the morphology and the structure of the films strongly depend on various growth parameters, such as substrate temperature, film thickness, and deposition rate. For example, MPc molecule deposited with various substrate temperatures ranging from 25°C to 300°C, the morphology changes from amorphous to densely packed grains to nanowires [6]. Overall due to the less substrate-molecule interaction and high roughness, MPc molecules stack 'edge on' and results disordered films on glass.

On the other hand the (0001) sapphire surface has extremely low roughness and has aluminium termination which interact very strongly with the π-cloud of MPc molecules. This results 'face on' staking of molecules (shown schematically in figure 1b) on the sapphire surface upto certain thickness (~ 20 nm). However, as film thickness increases, the influence of molecule-substrate interaction becomes weaker and molecule-molecule interaction dominates, which allows edge-on stacking of molecules. As a result, the film grows in thepolycrystalline form at higher film thickness. It may be added here that the thesepolycrystalline films are likely to be better in terms of the molecular packing as compared to the polycrystalline films grown on the glass substrate in which molecules randomly stack inthe edge-on configuration.

The high mobility along charge transport direction demands face to face staking of molecule which enhances the overlapping of charge clouds. Thus we need to deposit MPc molecule on such a substrate so that it can induce ordering in some direction as well as molecule stack face to face along charge transport direction. For this purpose we choose twined (001) $LaAlO_3$ which has very low roughness of less 1 nm and natural twin boundaries. These natural twin boundaries act as template for the molecule to order along the twin boundary with edge-on configuration. The high degree of ordering is confirmed by X-ray rocking curve of (200) Bragg peak.Taking a clue from the growth of MPc films on (001) $LaAlO_3$ substrate, we have selected a bi-crystal (001) $SrTiO_3$ substrate for the deposition of CoPc films. The bicrystal has a single boundary, which consists of periodic triangularly shaped grooves (depth of 2–3 nm). Since the bicrystal boundary has a very small width of 2-3 nm, therefore, in the film CoPc molecule grow with edge-on stacking along this narrow bi-crystal boundary (as schematically depicted in figure 1c.). At rest of the place the molecules will stack randomly similar to the glass substrate.

Effect of molecular ordering on charge transport:

The charge transport of MPc films depends on the molecular ordering which in turn depends on the substrate on which they are deposited. In this section, we will discuss the charge transport behaviour of MPc films on different substrates. The MPc films on glass substrate shows a hysteretic current-voltage characteristic (*J-V*) at room temperature. The hysteretic *J-V*characteristic is explained by space charge limited conduction (SCLC) with deep charge traps created by chemisorbed oxygen. The presence of chemisorbed oxygen is confirmed by *XPS*. The amount of hysteresis in *J-V* characteristic depends on the amount of chemisorbed oxygen which further depends on the crystallinity of the films [7, 8].In these films, the transport at low temperature is governed by the Poole-Frankel mechanism which is nothing but the promotion of localized charge

Table 1. Different parameters calculated from temperature dependent *J-V* characteristics of CoPc films grown on glass and (0001) sapphire substrate.

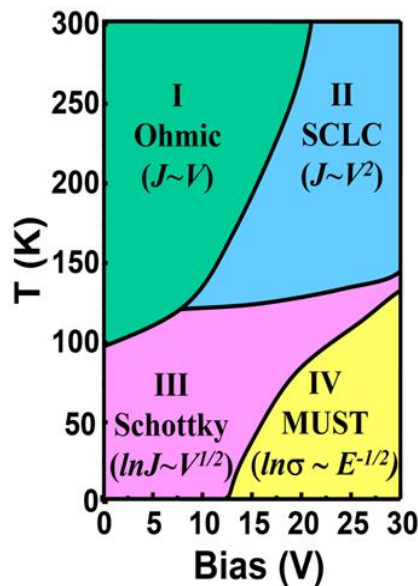| Films on	n_0 (m^{-3})	T_t (K)	N_t (m^{-3})	P_0 (eV^{-1}m^{-3})	μ (cm^{2}V^{-1}s^{-1})
Glass	2.5 x 10^{18}	600	4.5 x 10^{21}	8.7 x 10^{24}	0.095
(0001)Sapphire	9.6 x 10^{18}	236	9.8x10^{20}	1.9 x 10^{22}	0.98

Fig. 2. Charge transport mechanism of CoPc films deposited on LaAlO$_3$ at different temperature and bias range

carrier to the transport level by the application of electric field. The mobility in these films is quite low and is calculated to be 0.095 cm^{2}V^{-1}sec^{-1}which is due to the presence of large number of deep traps created by chemisorbed oxygen. On the other hand, the charge transport in MPc films on sapphire is governed by the shallow traps which yield non-hysteretic *J-V* characteristics throughout the temperature range [9]. A comparison of different parameter for the MPc films deposited on glass and sapphire are presented in table 1 which clearly indicate enhancement of mobility in sapphire substrate over the glass. The enhanced mobility in MPc films on sapphire is due to the nature and decreased number of traps, which is owing to improved ordering in MPc films on sapphire substrate.

As seen in the previous section a highly ordered MPc films are grown along the twin boundary of (001) LaAlO$_3$, the same is manifested in the charge transport measurement along the twin boundary. The measured *J-V*characteristics show no sign of hyterisis with improved mobility of around ~ 7 cm^{2}v^{-1}sec^{-1}. The improved mobility allow us to measure charge transport down to 25 K. Based on the nature of current dependence on bias and temperature, four distinct regions (marked as I to IV) have been identified and a proposed temperature bias phase diagramis presented in figure 2. Broadly, regions I and II belong to the temperature region of 300-100 K, whereas regions III and IV lie in the temperature zone below 100 K. In the high temperature region i.e. regions I and II, the transport is mainly dominated by bulk of the film. The linear variation of current density with voltage indicates that the transport is via Ohmic

Founder's Day Special Issue October 2017

conduction in the region I, where as in region II, i.e. high bias the transport is dominated by trap free SCLC.For temperatures <100K, transport characterises show very different behaviors in the regions III and IV and that is mainly dominated by electrode limited process. In the region III, i. e. at low bias the transport is via Schottky conduction and at high bias (region IV) the transport is governed by multi step tunnelling from electrode to transport level of the semiconductor [10]. Similar to the previous one, CoPc molecule also form ordered film along bi-crystal boundary of (001) $SrTiO_3$and charge transport measurement indicate the same. The mobility is calculated from temperature dependent *J-V* characteristics and found to be ~ 150 $cm^2v^{-1}sec^{-1}$ and the charge conduction down to 30K can be described by Ohmic conduction followed by trap free SCLC at higher voltage [11].
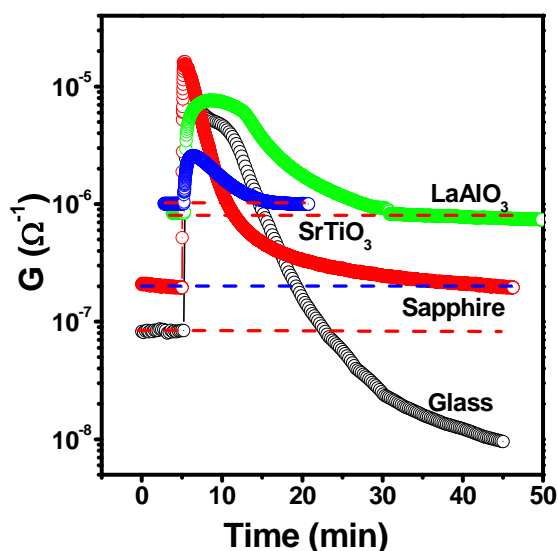

Fig. 3:Typical response of 20 nm CoPc films grown on glass, sapphire, twined (001) $LaAlO_3$ and 36.8° cut bicrystal (001) $SrTiO_3$ for 2 ppm Cl_2 gas.

Gas sensing properties of metal Phthalocyanine thin films:

The efficient gas sensing of any MPc films depends on two processes, (*i*) adsorption of gas molecule on MPc films and consequently charge carrier generation and (*ii*) efficient transport of generated charge carrier to the respected electrodes. The first process requires active sites in the films for the interaction of gas molecules and MPc films. The second process requires high mobility of the films. These two parameters will depend on the morphology of the films and ordering of CoPc molecules. In previous section, we have seen that CoPc films have different morphology and ordering on different substrates. Thus these films have different sensitivity for chlorine gas. The measured response of 20 nm CoPc films grown on different substrates, such as glass, sapphire, twined (001) $LaAlO_3$ and 36.8° cut bicrystal (001) $SrTiO_3$, for 2 ppm Cl_2 gasare shown in figure3 and the calculated sensor parameters are tabulated in the table – 2.The conductivity of the films deposited on glass drifts below initial base conductivity after the exposure of Cl_2 gas. This drift can be explained by the deep traps created by chemisorptions of oxygen by CoPc molecules. Although CoPc films on glass have enough sites to interact with Cl_2 molecule but due to low mobility and drift in the conductivity these films are not suitable for gas sensing application. On the other hand the films deposited on the sapphire do not have these problems, and therefore, they show a reversible response with very high sensitivity and fast response and recovery, which is very essential for the sensor application. The highly ordered CoPc films, grown along twin boundary of (001) $LaAlO_3$ and along bicrystal boundary of (001) $SrTiO_3$ have lower sensitivity for Cl_2 gas as compared to that grown on sapphire. This is due to the ordering of CoPc molecules which reduces the available interaction sites although they have very high mobility.As the CoPc films grown on sapphire substrate have highest sensitivity with very fast response and recovery the chemi-resistive sensors are made and have been demonstrated that these sensors can detect any concentration of hazardous Chlorine ranging from 5 ppb to 2000 ppb at an operating temperature of 180°C (a typical response shown in figure 4). These sensors are found to be very stable but more importantly these sensors can detect as low as 5 ppb of Cl_2 gas with faster response time (18 s), higher base line stability (< 5%) and enhanced response (80%) [12].

Table 2. Comparison of sensitivity of CoPc films (20 nm) grown on different substrate for 2 ppm Cl_2 gas.

Sensors	Sensitivity (S in %)	Response time (s)	Recovery time (s)
Polycrystalline CoPc films on Glass	7.2×10^3	35	510
Polycrystalline CoPc films on Sapphire	9.2×10^3	15	230
Ordered CoPc films on (001) $LaAlO_3$	7.8×10^2	90	1440
Ordered CoPc films on (001) $SrTiO_3$	1.57×10^2	55	480
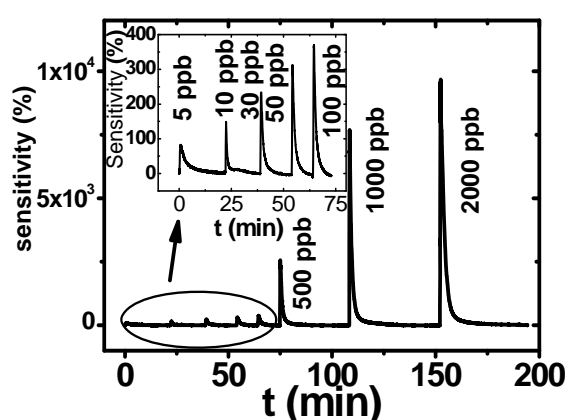
Fig. 4: Response of CoPc sensor with different concentration of chlorine gas.

Conclusions:

We have demonstrated that by choosing appropriate substrate, the mobility can be enhanced (graphically shown in figure 5) from <0.5 $cm^2V^{-1}s^{-1}$ (obtain for amorphous CoPc films on glass) to ~150 $cm^2V^{-1}s^{-1}$ (for highly ordered CoPc films grown along the 38.6° bi-crystal boundary of bicrystal $SrTiO_3$). The electronic charge transports in disordered and highly ordered MPc films have been investigated as a function of bias and temperature (down to 25K). We have generated a new bias-temperature phase-diagram for ordered Pc films on $LaAlO_3$ substrates. The Pc films have also been used for ppb level Cl_2 gas sensing application.
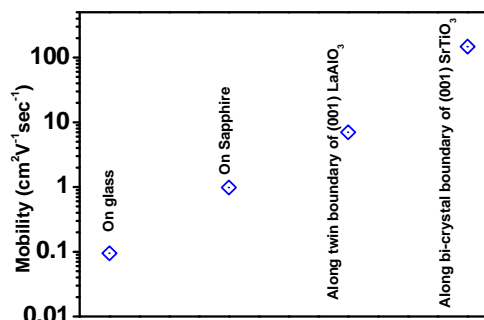

Fig. 5: Mobility values with choice of substrate

Refference:

1. H. Y. Choi, S. H. Kim, J. Jang, Self-organized organic thin-film transistor on plastic, Adv. Mater. 16, 732 (2004).

2. T. Tsutsui, K. Fujita, The shift from hard to soft electronics, Adv. Mater. 14, 949 (2002).

3. C. D. Dimitrakopoulos, P. R. L. Malenfant, Organic thin film transistors for large area electronics, Adv. Mater. 14, 99 (2002).

4. W. D. Howard, O. F. Prache, Microdisplays based upon organic light-emiting diodes, IBM J. Res & Dev. 45, 115 (2001).

5. V. Coropceanu, J. Cornil, D. A. de Silva Filho, Y. Olivier, R. Silbey, J. L. Bredus, Charge transport in organic semiconductors, Chem. Rev. 107, 926 (2007).

6. A.K. Debnath, S. Samanta, A. Singh, D.K. Aswal, S. K. Gupta and J.V. Yakhmi, S.K. Deshpande, A.K. Poswal, C. Sürgers, Growth of iron phthalocyaninenanoweb and nanobrush using molecular beam epitaxy, Physica E, 41(1), 154 (2008).

7. S. Samanta, A. Singh, A.K.Debnath, D.K.Aswal, S.K.Gupta and J.V.Yakhmi, S. Singh, S. Basu, and S.K. Deshpande, Oxygen induced hysteritc current-voltage characteristics of iron-phthallocyanine thin films, J. Appl. Phys 104, 073717(2008).

8. Samanta, A.K.Debnath, A. Singh, D.K.Aswal, S.K.Gupta and J.V.Yakhmi, Temperature dependent current-voltage characteristics of iron-phthalocyainthine films, J. Nanosci. Nanotechnol. 9, 5262 (2009).

9. A. Singh, S. Samanta, A. Kumar, A. K. Debnath, D. K. Aswal, S. K. Gupta, J. V. Yakhmi, Y. Hayakawa, S. K. Deshpande, Role of structural disorder in charge transport properties of cobalt-phthalocyanine thin films grown by molecular-beam epitaxy, Org. electron. 11, 1835 (2010).

10. S. Samanta, D. K. Aswal, A. Singh, A.K. Debnath, M. S. Kumar, Y. Hayakawa, S. K. Gupta and J.V. Yakhmi, Bias and temperature dependent charge transport in high mobility cobalt-phthalocyanine thin films, Appl. Phys. Lett. 96, 013305 (2010).

11. S. Samanta, A. Singh, A. Kumar, A.K. Debnath, D. K. Aswal, S. K. Gupta, J. V. YakhmiImprove charge conduction in cobalt-phthalocyanine thin films grown alonh 36.8° boundary of $SrTiO_3$bicrystals, Appl. Phys. Lett. 98, 1433051(2011).

12. A.K. Debnath, S. Samanta, A. Singh, D.K. Aswal, S. K. Gupta and J.V. Yakhmi, Parts-per-billion level chlorine sensors with fast kinetics using ultrathin cobalt phthalocyanine films, Chem. Phys. Lett. 480, 185-188 (2009).

Ultrafast Structural Dynamics of Charge Transfer Organic Molecules Studied by Femtosecond Pump-probe Spectroscopy

Rajib Ghosh
Radiation & Photochemistry Division

Introduction

Photoinduced charge transfer in chemical systems play important role in photosynthesis, photocatalysis and solar energy harvesting. [1] Thus fundamental understanding of the structure and dynamics of the intramolecular charge transfer (ICT) process in the excited states of donor (D) and acceptor (A) substituted aromatic molecules has been of great interest. Because of the ultrafast nature of the time scale of the charge transfer events, it is imperative to probe the real time dynamics of these processes to discern the microscopic mechanism and governing factors to manipulate towards best possible exploitation of a chemical entity towards artificial light harvesting. Over the past few decades, time resolved spectroscopic tools have been extensively used to address fundamental electronic dynamics with real time mapping of structural changes associated with the photoinduced chemical reactions relevant to natural and artificial light driven chemical reactions. The ICT state often leads to quantitative charge separation by structural reorganization towards mutually twisted conformation of donor and acceptor groups, which makes the ICT process irreversible, a desirable process for efficient solar energy harvesting. The fully charge separated twisted conformation is known as TICT state. [2] Unraveling the factors facilitating TICT relaxation in a charge transfer organic molecule is imperative to design better light harvesting materials. For last few years, we have actively pursued investigations on several charge transfer molecules with a long-standing goal to establish structure-property correlation of TICT dynamics. Time resolved pump-probe transient absorption and fluorescence spectroscopy with femtosecond temporal resolution allowed us to interrogate the charge transfer events and associated structural relaxation in real time. A general scheme of excited state relaxation dynamics of the TICT molecules is shown in Figure 1.
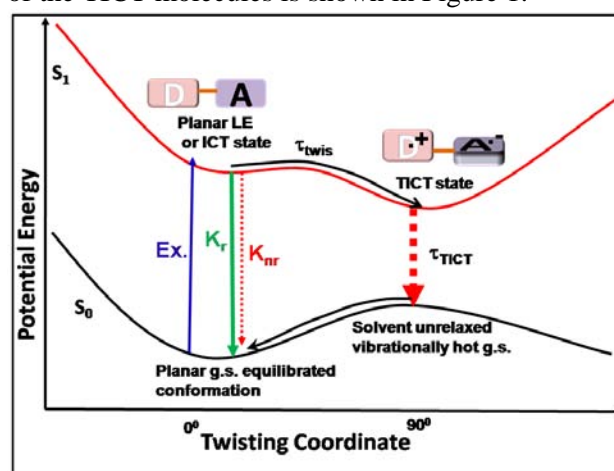

Fig. 1: Schematic of excited state potential energy surface showing LE to TICT relaxation. The barrier along the twisting coordinate depends on the molecular structure and nature of donor and acceptor groups.

Our studies on several model charge transfer molecules have revealed that conjugation length and relative strength of the donor and acceptor groups profoundly influence TICT relaxation. Solvent polarity also significantly influences the kinetics of torsional relaxation. Measurements on structurally constrained molecular systems have helped to identify the reaction coordinates and shape of the excited state potential energy surfaces along the twisting coordinate. These aspects of TICT relaxation is summarized in this article.

Role of donor-acceptor conjugation on TICT dynamics: The role of donor and acceptor conjugation in intramolecular charge transfer (ICT) dynamics has been demonstrated by comparing the photophysical parameters of two isomeric dimethylaminochalcone derivatives, namely DMAC-A and DMAC-B (Figure, 2).[3] While both isomers exhibit strong ICT character in excited state, their photophysical properties (fluorescence yields and the excited state lifetimes) are shown to be remarkably different. A small increase in conjugation length from DMAC-A to DMAC-B results to increase in the fluorescence lifetime from 1.4 ps to 300 ps (Figure 2).
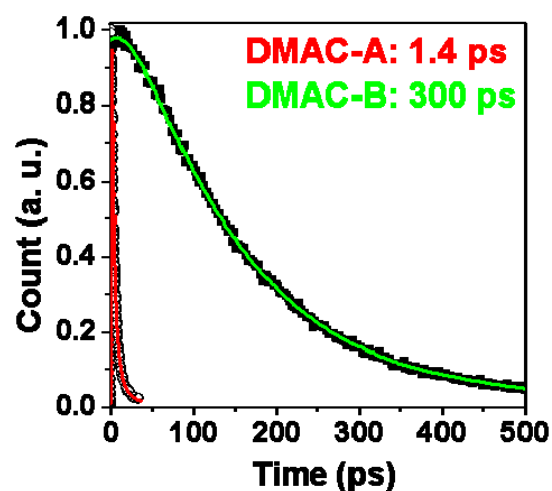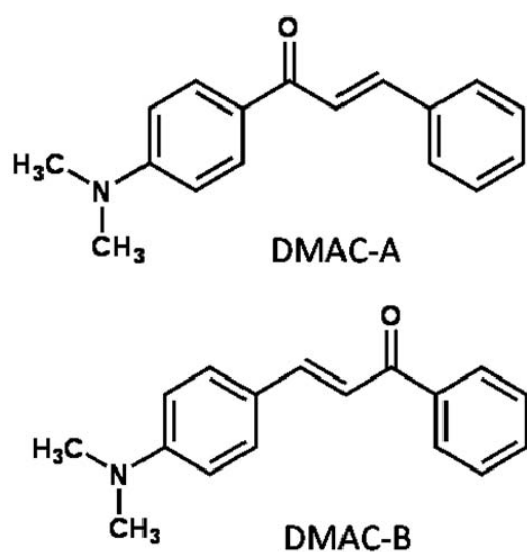

Fig. 2: Molecular structures (left) and excited state deactivation timescale (right) of DMAC-A and DMAC-B.

Femtosecond pump-probe experiment revealed that ultrafast torsional relaxation with a lifetime of 1.4 picoseconds dominates deactivation of the S_1 state of DMAC-A molecule. In DMAC-B, large energy barrier along any torsional path inhibits TICT relaxation and thus planar ICT structure with long lifetime (300 ps) determines the photophysical properties of the S_1 state of the molecule. This difference in behavior of the S_1 states is attributed to the strong coupling
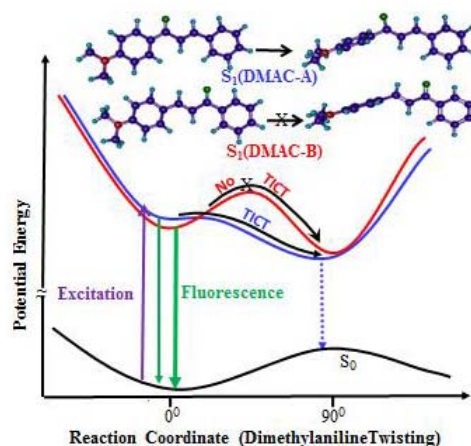

Fig. 3: Schematic potential energy surface (PES) diagrams illustrating the difference in structural relaxation behaviour of DMAC-A (blue) and DMAC-B (red).

between the donor and acceptor groups in DMAC-A, while extended conjugation in DMAC-B renders weak coupling and consequently negligible twisting probability.

The difference in the dynamics of excited state of the two molecules is schematically presented in figure 3. The study highlights the role of conjugation on the TICT relaxation process. Effect of D-A conjugation on the ICT↔TICT relaxation dynamics is found to be a common feature, as exemplified in an another set of charge transfer molecules.[4, 5]

Identification of the torsional coordinate of DMAC-A: In DMAC-A with multiple rotatable single and double bonds, identifying the rotating bond involved in LE to TICT relaxation in the S_1 state potential energy surface (PES) was a difficult task. To experimentally identify the TICT coordinate, a structurally bridged derivative of DMAC-A (abbreviated as c-DMAC, figure 4) was synthesized which locks the dimethylaniline and carbonyl groups in planar conformation. This new compound, c-DMAC exhibits orders of magnitude higher fluorescence yield and lifetime as compared to that of DMAC-A. Based on the comparison of ultrafast transient spectroscopy of DMAC-A with c-DMAC), the reactive coordinate of TICT relaxation has been identified to be the single bond connecting dimethylaniline and carbonyl group.[6] While the ICT character of the two molecules are same, ultrafast deactivation mechanism of the two compounds are quite different due to impeding TICT relaxation in c-DMAC. The results also support the fact that large intramolecular charge transfer occurs without TICT mechanism.

Role of acceptor strength in TICT relaxation: ICT character of a D-A system is known to be dependent on the strength of electron donating and electron withdrawing character of the D and A, respectively. However, their importance
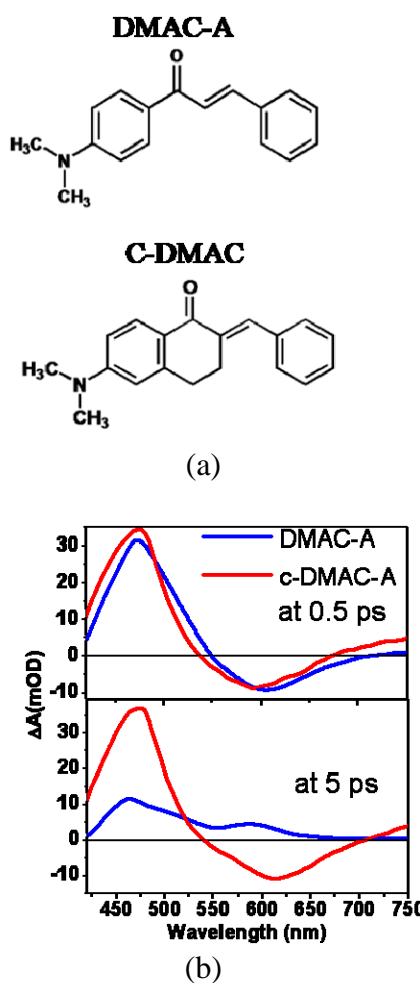

(a)

(b)

Fig. 4 (a) Molecular structures of DMAC-A and c-DMAC. (b) Comparison of femtosecond tranient spectral evolution.

in facilitating TICT relaxation was not known. However, this is of importance for fine tuning of the charge transfer kinetics of a light harvesting system. To address this aspect, employing time resolved spectroscopic experiments, rate of TICT relaxation of a series of dimethylaminochalcone derivatives were measured (Figure 5). It is revealed that TICT relaxation gets systematically faster with increase in the acceptor strength. By varying the charge pulling capacity of the acceptor, the barrier of TICT coordinate in the electronic excited state is possible to fine tune which modulates TICT relaxation rate.[7]
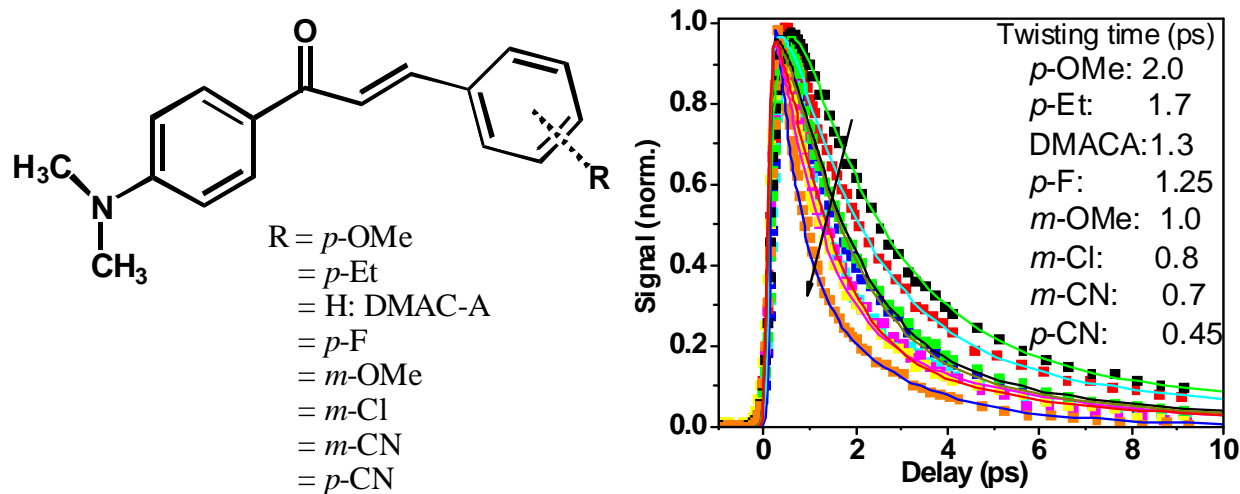
Fig. 5: Structure of substituted DMAC-A derivatives (left) and their excited state deactivation kinetics measured by ultrafast transient fluorescence spectroscopy (right).

The importance of acceptor strength on promoting TICT relaxation of a charge transfer system was further exemplified in a different set of charge transfer system. Comparison of ultrafast dynamics of the excited states of two push-pull biphenyl derivative, namely, 4-N,N-dimethylamino-4'-cyanobiphenyl (DMACBP) and 4-N,N-dimethylamino-4'-nitrobiphenyl (DMANBP) (Figure 6) revealed that stronger electron accepting nitro group promotes ultrafast TICT relaxation (with a lifetime of 400 femtosecond) in DMANBP while relatively weaker electron accepting cyano group does not at all facilitate TICT formation in DMACBP.[8]

Proton transfer coupled TICT dynamics: Intramolecular proton transfer dynamics can significantly perturb the electronic structure of a charge transfer molecule, thereby altering TICT dynamics. Solvent polarity assisted change in the direction of excited state intramolecular proton transfer (ESIPT) has been demonstrated to control TICT dynamics of an asymmetric charge transfer diketone. Depending upon solvent polarity, differential stabilization of the two cis-enol tautomers (Enol-A and Enol-B) of dimethylaminodikeone (DMADK) changes the direction of ESIPT and the coupling for ICT to TICT relaxation.[9] In low polarity solvents, the A*(ICT) state is thermodynamically more stable than that of B*(ICT) state and thus A*(ICT) state governs the properties of the S_1 state of DMADK (Fig. 7).

In low polarity solvents, Enol-B*(LE) state undergoes ultrafast ESIPT reaction to populate Enol-A* state, followed by intramolecular relaxation to populate the A*(ICT) state. In these solvents, TICT relaxation does not occur due to stabilization of planar A*(ICT) state facilitated by extended conjugation between the donor and acceptor units. On the other hand, in high polarity solvents, Enol-B* is stabilized and strong coupling between the donor and acceptor groups facilitate TICT relaxation. Thus in polar solvent, ESIPT is followed by conformational relaxation to TICT state of Enol-B*. Asymmetry in the enol structure and strong electron donating group were two necessary features to demonstrate
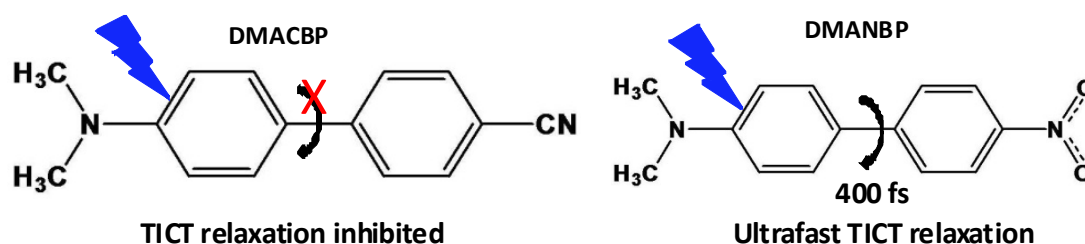
Fig. 6: Molecular structure of cyano and nitro derivative of dimethylaminobiphenyl.
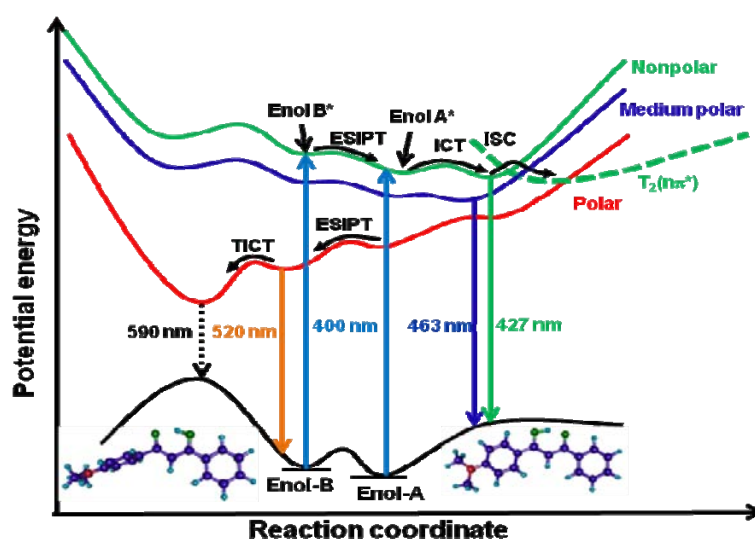

Fig. 7: Simplified potential energy diagram depicting excited state dynamics in the S_1 state of DMADK.

ESIPT directed TICT dynamics in this system; as such dynamical aspects were not exhibited by symmetrical diketone, namely curcumin.[10] The latter was found to exhibit only solvent relaxation dynamics without featuring ESIPT or TICT relaxation.

Conclusion:
In summary, ultrafast spectroscopic measurements were performed to probe the photoinduced structural dynamics associated with the charge transfer organic molecules in real time with femtosecond resolution. Systematic variation of molecular structures of a series of D-A compounds and probing their

ultrafast spectroscopic kinetics led us to understand how conjugation and strength of electron accepting and donating groups modulate the photophysical outcome on account of variation of TICT relaxation. Extending the conjugation length decreases feasibility of TICT driven charge separation. On the other hand, increase in electron donating and accepting ability facilitates TICT relaxation. Solvent polarity and intramolecular proton transfer was also shown to control TICT dynamics in tailored molecular system. The fundamental understanding of the factors controlling torsional relaxation driven charge transfer kinetics and deactivation dynamics

may contribute towards development of efficient photonic and light harvesting materials.

Acknowledgements

References:
1. S. Sasaki, G. P. C. Drummen, G. Konishi, *J. Mater. Chem. C,* 2016, 4, 2731-2743.
2. Z. R. Grabowski, K. Rotkiewicz, W. Rettig, *Chem. Rev.* 2003, 103, 3899-4032.
3. R. Ghosh, D. K. Palit, *J. Phys. Chem. A*, 2015, 119, 11128–11137.
4. R. Ghosh, D. K. Palit, *J. Phys. Chem. A*, 2012, 116, 1993–2005.
5. A. Nandi, R. Ghosh, D. K. Palit, *J. Photochem. Photobiol. A*, 2016, 321, 171-179.
6. R. Ghosh, B. Manna, *Phys. Chem. Chem. Phys*., 2017, DOI: 10.1039/c7cp03461j
7. R. Ghosh, *unpublished work.*
8. R. Ghosh, A. Nandi, D. K. Palit, *Phys. Chem. Chem. Phys*., 2016,18, 7661-7671.
9. R. Ghosh, D. K. Palit, *Photochem. Photobiol. Sci.* 2013, 12, 987-95.
10. R. Ghosh, J. A. Mondal, D. K. Palit. *J. Phys. Chem. B* 2010, 114, 12129–12143.

Development of Process for Fluidized Bed Thermal Denitration of Uranyl Nitrate

Sandip Bhowmick

Chemical Engineering Division

Sandip Bhowmick is the recipient of the DAE Young Scientist Award for the year 2015

Abstract

The direct denitration of uranyl nitrate reduces number of processing steps and avoids handling of ammonia during production of uranium oxide from uranyl nitrate. Hence, experimental investigation has been carried out to explore the direct thermal denitration of uranyl nitrate in an 80 NB laboratory scale fluidized bed reactor. Initially in a series of experiments the operating parameters – bed temperature, u/u_{mf} and feed concentration were varied over a range and optimized for smooth continuous operation. Later this process has been demonstrated in a 150 NB bench scale reactor. The problem related to formation of local agglomerate was completely eradicated by selecting proper operating temperature, particle size and spray nozzle. The product UO_3 obtained from the reactor was successfully reduced to UO_2. However, the only size fractions of less than 53 µm could be successfully fluorinated to 94-96.5% UF_4.

Introduction

In India the oxides of uranium (U_3O_8) is produced after treating the uranyl nitrate pure solution (UNPS) with ammonia (NH_3) and subsequently calcining the resultant ammonium diuranate (ADU). This conventional process includes several steps such as neutralization of the nitrate solution with NH_3, precipitation, filtration, drying, and calcination. On the other hand the direct denitration process offers savings in chemical costs, since it avoids the use of ammonia and permits the recovery of nitric acid. Hence, an economical and efficient way is to decompose the uranyl nitrate solution thermally and obtain the oxides of uranium in a single step. At first the thermal denitration of uranyl nitrate was carried out batch wise in agitated pot calciner[1]. This process gave reactive product which was very fine and not suitable to subsequent powder handling. Afterward a continuous denitration process was developed using stirred trough calciners. However, the excellent heat transfer characteristics and mechanical simplicity of fluidized beds were adequate inspiration for the development of a denitration process based on this technology. Moreover fluidized bed delivers a free-flowing product of acceptable bulk density suitable for subsequent process steps and it is a closed system with no moving parts and thus would minimize the possibility of personal exposure to dust. A number of reports describing the operating experience gained from the pilot scale as well as production scale fluidized bed denitrator are available in literature[2 – 10]. But the sustainability of the production of uranium trioxide (UO_3) in a fluidized bed denitrator depends on the product characteristics, mainly the reactivity of UO_3[11]. The ease of reduction of UO_3 to uranium dioxide (UO_2), and the subsequent ease of hydro-fluorination to uranium tetra-fluoride (UF_4) are a measure of the reactivity of the UO_3.

This report serves two purposes. Firstly, it describes a limited experimental investigation to select the optimum process variables for continuous smooth operation in an 80 NB fluidized bed reactor. The characterizations of the product oxide and reactivity analysis results are also included. Secondly, it shares operating experience gained in scaled up 150 NB fluidized bed reactor.

BARC NEWSLETTER

Founder's Day Special Issue October 2017

Fluidizability of Uranium Oxide Powder

An experimental set up comprising of 80 NB transparent acrylic column has been installed for testing the fluidizability of uranium oxide powder. Initially the uranium oxide powder (mainly U_3O_8) was obtained from Uranium Extraction Division. But this fine powder ($\overline{d_p} = 30\ \mu m$) was not suitable for fluidization operation as rate of entrainment was very high. Grinding sludge was also recieved from uranium oxide pellet production plant at Nuclear Fuel Complex, Hyderabad. This powder was also very fine in size and not appropriate for bubbling fluidization. Due to the nonavailability of desired size of uranium oxide particles, the glass beads ($\overline{d_p} = 385\ \mu m$) were used as intial bed material for feasibility study and understanding the coating mechanism. Glass beads coated with uranium oxide were used for parametric investigation. But the removal of oxide coating from glass beads is a daunting task. Jet grinding system was not tested to remove the coating as this may break the glass beads. Steel bead ($\overline{d_p} = 200\ \mu m$) was used as an alternative starting bed material. The steel bead has very high attrition resistance compared to glass bead. Later considerably bigger size U_3O_8 particles were obtained from Rare Materials Plant, Mysore. The particles were screened and particles having size in between 106 and 500 μm were used as starting bed material.

Reactor System

The equipment used in this work is shown as a simplified diagram of the experimental setup in Figure 1. Initially the experimental investigations were carried out in a laboratory scale reactor. At the later stage a bench scale reactor has been installed to study the effect of scale up on the direct denitration process.

Laboratory Scale Reactor System

The laboratory scale denitration reactor was fabricated from SS 304L (80 NB Schedule 40 pipe). The length of the reactor was 1000 mm. A freeboard section having nearly 4 times the diameter (300 NB schedule 40 pipe) of the main reactor was provided to minimize the entrainment of particles. The reactor was fitted with a perforated plate type distributor. Fluidizing air was passed through a flow meter before entering the plenum chamber of the reactor. The pressure drop across the fluidized bed was monitored by differential pressure transmitter. Purge method of pressure measurement has been adopted to prevent chkoing of pressure probes due to the ingress of particles into the pressure taps. The qualititive information of increase in bed weight and formation of agglomerates can be found out from bed pressure drop. The uranyl nitrate solution was injected as atomized manner into the fluidized bed using an external mix type twin fluid nozzle. The nozzle was fabricated inhouse by inserting a 1/8" tube through ¼" tube. The atomization air was passed through the annulus region between two tubes. The solution was introduced into the nozzle by a peristaltic pump.The reactor was heated by 2.5 kW resistance heater made of 19 gauge nichrome wire. The bed and surface temperatures of reactor were measured by k – type thermocouples. The bed temperature was controlled at desired level using a PID controller. Resistance heaters were also provided on freeboard and filter housings to avoid condensation of water vapor.

On leaving the reactor, the off-gases passed through the sintered metal filters (5 µm), which removed entrained particles from the gas stream. Two filter housings, one in operation and other in standby mode, were installed with blowback arrangement. The particles were dislodged from the filter candle by manual blowback with 6 kg/ cm^2 (g) pulse of dry air. The blowback was operated when the reactor top presser exceeded 0.5 kg/ cm^2 (g). The off-gas then passed through two water scrubbers to recover the NO_x as dilute nitric acid. Two water ring vacuum pumps were installed after water scrubber to operate the off-gas system under atmospheric pressure. This ensures zero leakage of NO_x and fine particles from off-gas system to plant area. After that off-gas was passed through air-water separator, condenser, and demister for complete removal of water. Water from a chiller unit was used as cooling media in the condenser. The off-gas was then reheated before passing it through HEPA filter. The gas is finally released to the stack ensuring adequate dilution to meet the gas emission norms.
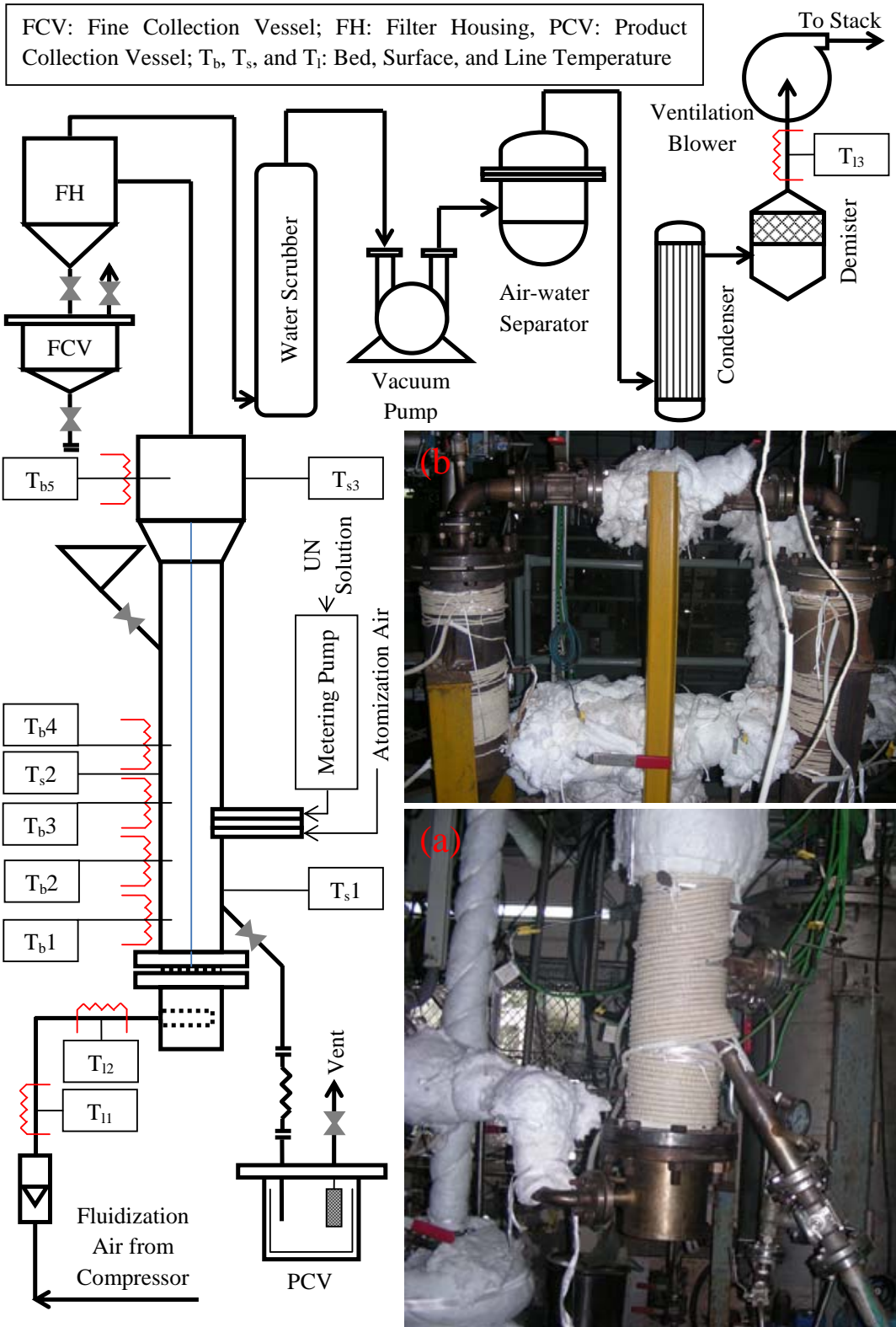
FCV: Fine Collection Vessel; FH: Filter Housing, PCV: Product Collection Vessel; T_b, T_s, and T_l: Bed, Surface, and Line Temperature

Fig. 1: Schematic Sketch of Experimental Setup. (a) Photograph of Denitration Column; (b) Photograph of Filter Housings.

Table 1.   Run Summary (Laboratory Scale Reactor)

Run No.	1	2	3	4	5	6
Concentration (g U /l)	164.5			311	164.5	311
Solution processed (l)	10		20	50	27	20
Feed rate (LPH)	1				2	
Nozzle ALR (volumetric)	780					
$\overline{d}_p$ (µm)	376.67[*]			318.9[#]	106 – 250 (U_3O_8)	
Bed temperature (^{0}C)	325	350	380			
u/u_{mf} at 25 ^{0}C	2.0				2.5	
Nozzle ALR (volumetric)	780					
Agglomeration	Large agglomerate		No agglomerates			
Reactivity analysis	----	----	----	Powder collected from FH successfully converted to UF_4	Powder below 53 µm size successfully converted to UF_4	

[*]Glass bead coated with UO_3; [#]Steel bead coated with UO_3; ALR: Air to Liquid Ratio

Bench Scale Reactor System

The bench scale reactor was fabricated from 150 NB Schedule 40 SS 304L pipe. The length of the reactor was 1550 mm. Two line heaters each of 2 kW were installed on the fluidization air supply line. Product oxide was withdrawn from the reactor through 50 NB pipe to the product collection vessel (PCV). An isolation valve was provided in solid withdrawal line.

An external mix type nozzle (Spraying System (India) Pvt. Ltd.) was used to inject the liquid inside fluidized bed as atomized manner. The solution was introduced into the nozzle by a double diaphragm metering pump. A safety relief valve with set pressure of 6 kg/cm^2 (g) was installed in the liquid line to prevent the leakage from joints due to overpressurization. Four resistance heaters each of 2.5 kW were wound on the outer surface of the bench scale denitration column. The bed and surface temperature was measured at four and two different axial locations respectively. The off-gas system for bench scale reactor was same as laboratory scale reactor and described in the previous section. A fine collection vessel (FCV) was installed below filter housing to collect fine oxide of uranium during continuous operation of bench scale reactor. Filter candles of sintered metal (10 µm) were installed in the vent lines of both FCV and PCV to prevent

escape of fines during transfer of solid and blowback operation.

Experiments in Laboratory Scale Reactor

6 experimental runs were carried out initially to establish the general range of operating conditions and to develop a satisfactory operating procedure. In addition the effect of bed temperature, concentration of uranium in feed solution, and u/u_{mf} was examined. A summary of test runs is presented in the Table 1.

Particle Growth Mechanism

In this study glass beads were used as starting seed material in the fluidized bed reactor. The UO_3 coated spherical glass balls were mounted on cold setting resin. It was polished till half of the UO_3 coating is only remaining. It was then seen under (Make: Olympus, Model: GX-51) inverted optical microscope. The images were taken using Olympus colour view1 camera (Figure 2). In the optical micrograph it can be seen that the UO_3 layer deposited on glass bead is ~20 µm thick. The formation of laminar layer of uranium oxide on glass bead suggests that the atomized liquid droplets deposit on the fluidized solid particles prior to decomposition. This factor is judged to be dominant in particle growth.
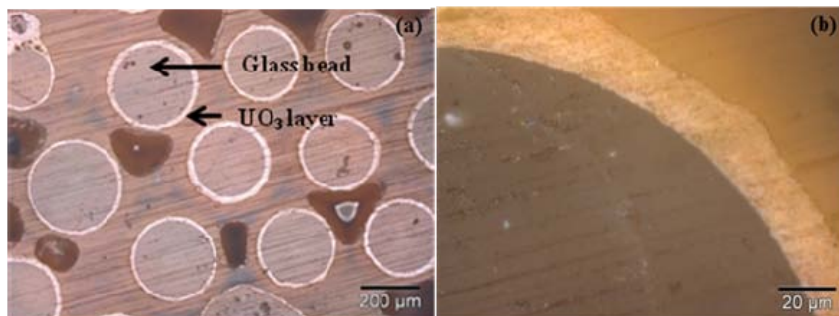
Fig. 2: Optical micrograph of UO$_3$ coated glass beads seen at (a) 100× (b) 1000×

Effect of Operating Temperature

Formation of large agglomerates was observed at both operating temperatures of 325 and 350^{0}C. From the thermo-gravimetric analysis, Pagliai et al. showed that the denitration process of Uranyl Nitrate Hexahydrate (UNH) takes place at 250^{0}C and develops up to 350^{0}C through decomposition of residual nitrate[12]. They measured the force required to break the solid bridges formed between two particles at different temperatures during decomposition of Magnesium Nitrate Hexahydrate (simulant of UNH). They concluded that the adhesiveness developed by completely decomposed material bridges is much weaker with respect to those just partially reacted. In fact, partially reacted material bridges could have enough strength to withstand the disruptive forces developed during fluidization. Certainly the possibility of incomplete decomposition of uranyl nitrate trapped between particles is higher during operation at lower temperature ($\leq$ 350^{0}C). On the other hand high temperature operation (380^{0}C) significantly reduces the formation of agglomerates.

Effect of Feed Concentration

After establishing the optimum operating temperature, the bed temperature was kept constant at 380^{0}C in the subsequent experiments. The production rate of UO$_3$ can be increased by increasing the concentration of feed solution. Initial experiments were conducted with feed solution having concentration in the order of 150 g U/ l. Later it was increased to 300 g U/ l. It was found that the reactor can be operated smoothly with high concentration solution.

Effect of Operating Velocity Ratio (u/ u$_{mf}$)

In this parametric study the U$_3$O$_8$ powder having size in between 106 and 250 μm was used as starting bed material. The powder was taken in an 80 mm diamter acrylic column for fluidizability test. The minimum fluidization velocity (u$_{mf}$) was determined from visual observation and it was in the order of 0.128 m/ s. The operating velocity ratio (u/u$_{mf}$) and solution concentration were varied in the range of 1.4 – 2.5 (corresponding to room temperature) and 150 – 300 g U/ l. It was found that continuous feeding could not be established at a u/u$_{mf}$ $\leq$ 2. This is mainly due to the low wall to bed heat transfer coefficient. At 2.5u$_{mf}$ a steady feeding rate of 2 LPH (300 g U/ l) was achieved. On the basis of the cross sectional area of the bed, production rate for the UO$_3$ was 143 kg/ hr – m^2.

Reactivity Study

For checking the reactivity of the UO$_3$ powder produced in direct denitration process, reduction, and hydro-fluorination was carried out. UO$_2$ was produced by reducing the UO$_3$ with ammonia gas at 750°C. The furnace was first evacuated three times and back flushed with argon; the flow of argon was continued till 750°C and after that flow of ammonia was started. The reduction was done in a static bed set up. UF$_4$ was produced by hydro-fluorination of the UO$_2$ with anhydrous HF at 450°C in a static bed set up[13]. The reduction and hydro-fluorination behaviour of UO$_3$ having mean particle size ranging from 2 to 149.17 μm was studied. The UO$_3$ was segregated into various size fractions viz. less than 53 μm (2.2 & 22.4 μm mean particle size) and 53-106 μm (88.9 μm mean particle size). The UO$_3$ of various size fractions were reduced with ammonia to

produce UO_2. It was observed that UO_3 of all the size fractions could be successfully reduced to UO_2. The UO_2 was then hydro-fluorinated with anhydrous HF. It was observed that the hydro-fluorination characteristics were quite different than that of the reduction characteristics and only size fractions of less than 53 µm (2.2 & 22.4 µm mean particle size) could be successfully fluorinated to 94-96.5% UF_4 which is suitable for metallothermy. The tap density of the fluorinated powder was between 1.39 to 2.48 g/ cm^3.
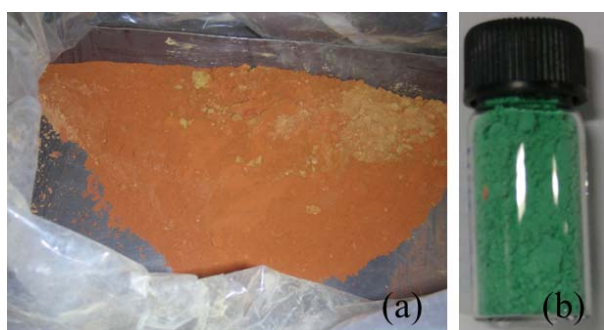
Fig. 3: **(a) Powder received from filter housing. (b) UF_4 produced from fine oxide powder.**

Experiments in Bench Scale Reactor

A summary of test runs conducted in bench scale reactor is presented in the Table 2. Formation of large agglomerate was observed in the first two experimental runs. The cause of the local agglomeration was investigated thoroughly. In Run No.1 the U_3O_8 powder having size in between 106 and 250 µm was used as starting bed material. In a bubbling fluidized bed, the size of gas bubble increases with increase in bed height and bed diameter. Hence, the size of gas bubbles was bigger in bench scale reactor compared to laboratory scale reactor. Consequently, the agitation of particles was significant in the bench scale reactor due to these bigger bubbles. Therefore the rate of particle attrition and entrainment was very high in bench scale reactor. The level of fluidized particles was decreased below the feed nozzle. Thus the spray touched the opposite wall of the reactor and lead to gradual growth of the lump.

In the next experimental run (Run No. 2) bigger size particles was used as starting bed material and continuous operation was establish. At the end of the run again large agglomerate was found in the solid discharged from the reactor. The hollow shape of the agglomerate indicates that it was formed around the feed nozzle. The feed nozzle which was used in the bench scale reactor had a threaded joint at nozzle head. A portion of the solution pushed into the nozzle was leaked from this joint and caused dripping of solution. This dripping phenomena lead to the formation of agglomerates around the nozzle. A permanent joint was made between nozzle head and its body by welding. After this arrangement formation of agglomerate was not observed in subsequent runs.

The product oxide obtained from the bench scale reactor and filter housings were sent to Quality Control Section (QCS) of Uranium Extraction Division (UED) for chemical analysis. The results of chemical analysis for Run No. 2 are presented in Table 3. The value of O/U ratio is approximately 3 and it depicts that the product oxide is uranium trioxide (UO_3).

Figure 4(a) shows the trend of the bed level recorded in Run No. 4. The steady increase in bed level indicates continuous generation of product uranium oxide due to thermal decomposition of uranyl nitrate inside the fluidized bed reactor. The time variation of bed temperature at different axial location is presented in Figure 4(b). The differences in bed temperatures measured at different axial locations are small and it indicates good fluidization inside the reactor.

Fig. 5 shows the inside of the reactor after processing 200 l of solution (Run No. 3) and solid discharged from the reactor into the PCV. After selection of larger size U_3O_8 particles as initial bed materials and modification in the spray nozzle, agglomerates were not observed inside reactor and also in the product oxide.

Table 2: Run Summary (Bench Scale Reactor)

Run No.	1	2	3	4
Concentration (g U /l)	164.5	124.5		311
Solution processed (l)	28	100	200	66
Feed rate (LPH)	2 – 3	2 – 4	2 – 5	
Initial bed inventory (kg)	22	25	27	34
Average particle size (µm)	106 – 250*	250 – 500*	308.45#	343.38$
Bed temperature (^{0}C)	380^{0}C			
Operating velocity ratio at 25^{0}C (u/u$_{mf}$)	2.5			
Nozzle Air to liquid ratio (volumetric)	780			
Powder collected from FH (kg)	11.4	12.0	6.0	9.90
Powder collected from reactor (kg)	16.1	26.34	51.29	49.30
Agglomeration	Large agglomerate		No agglomerates	

* U_3O_8; # Particles from Run 2; $ Particles from Run 3

Table 3: Chemical Analysis of Product Uranium Oxide

Origin	Moisture (%)	% U	NO3$^-$ (ppm)	PSA (µm)	O/U
Reactor	0.01	82.03	445	308.49	3.10
Filter Housing	0.08	82.85	4050	8.14	2.97
Filter Candle	0.53	81.25	3935	6.22	3.10
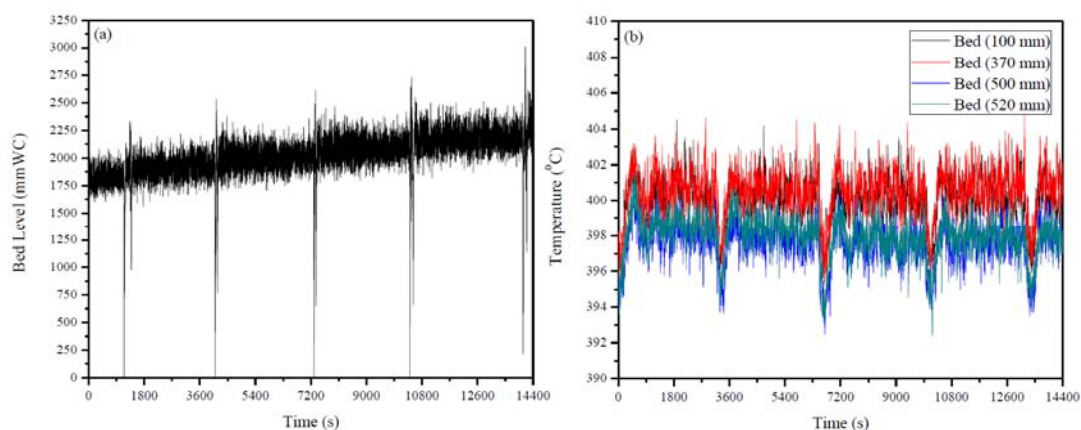
Fig. 4: a) Time variation of bed level in bench scale reactor b) Time variation of bed temperature at different axial locations. The distances are measured from the distributor plate.
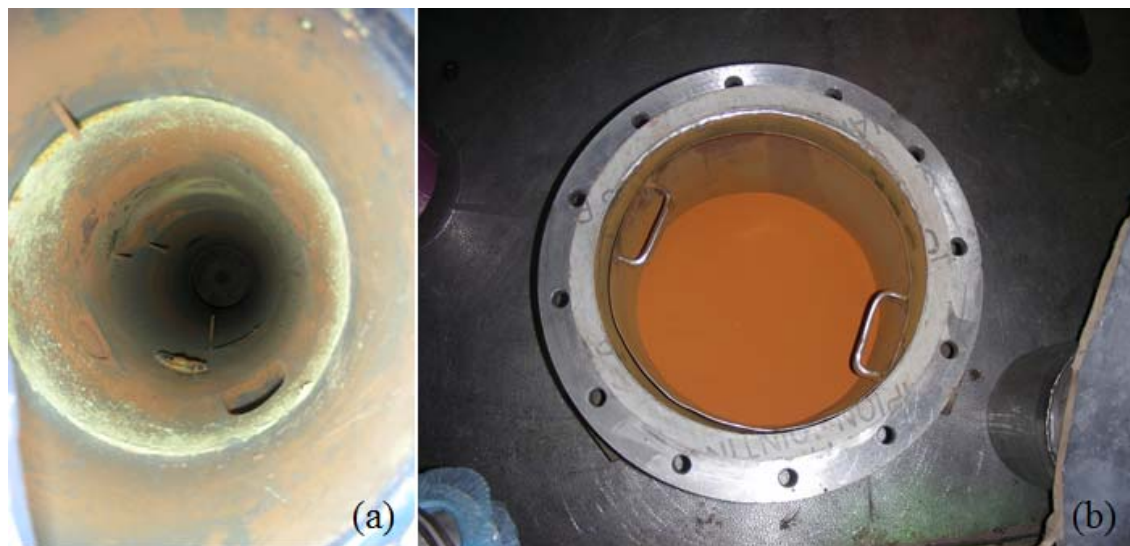
Figure 5. **(a) Inside of bench scale reactor after processing 200 l (124.5 g U/ l) solution (b) Product UO₃ discharged from the reactor to the Product Collection Vessel (PCV).**

Conclusion

A process has been developed for direct denitration of uranyl nitrate based on fluidized bed technology. Initially process feasibility was tested in a laboratory scale reactor. The process parameters were optimized in a series of experiments for continuous smooth operation of the reactor. Later this process has been demonstrated in a bench scale reactor. It was found that the prevention of local agglomerate formation inside the reactor is a challenging task. This problem was completely eradicated by selecting proper operating temperature, particle size and spray nozzle. The product UO_3 obtained from the reactor was successfully reduced to UO_2. However, the only size fractions of less than 53 µm could be successfully fluorinated to 94-96.5%. Hence, in future a fluidized bed denitrator combined with size reduction unit (such as ball mill) can be explored to overcome this hydro-fluorination problem.

Acknowledgement

References

1. Harrington, C.D., Ruehle, A.E. Uranium Production Technology, Princeton, N.J., Van-Nostrand, **1959**.
2. Legler, B.M. Fluidized bed processing in the nuclear fuel cycle, *Chem. Eng. Prog. Symp. Ser.,* 66(105), 167, **1970**.
3. Robinson, S.N., Todd, J.E. Plant Scale Fluid Bed Denitrator, Report MCW 1509, U.S. Atomic Energy Commission, Washington, D.C., **1966**.
4. Jonke, A.A. Report ANL-5363, U.S. Atomic Energy Commission, Washington, D.C., **1954**.
5. Grimmett, E.S. Calcination of Al-Type Reactor Fuel Waste, Report IDO-14416, U.S. Atomic Energy Commission, Washington, D.C., **1957**.
6. Philoon, W.C., Samders, E.F., Trask, W.T. Uranium trioxide in a fluidized bed reactor, *Chem. Eng. Prog.,* 56(4), 106, **1960**.
7. Otero, A.R., Rof, J.S., Lago, E.C. Fluidized bed calcination of uranyl nitrate solutions, in

Proc. Int. Symp. on Fluidization, Drinkenburg, A.A.H., Ed., Netherlands University Press, Amsterdam, 769, **1967**.

8. Otero, A.R., Garcia, V.G. Cake formation in a fluidized bed calciner, *Chem. Eng. Prog. Symp. Ser.,* 66(105), 267, **1970**.

9. Bjorklund, W.J., Offutt, G.F. Fluidized bed denitration of uranyl nitrate, *AIChE Symp. Ser.,* 69 (128), 123, **1973**.

10. Fane, A.G., Charlton, B.G., Alfredson, P.G. Thermal denitration of uranyl nitrate in a fluidized bed reactor; Technical Report AAEC/E284; Australian Atomic Energy Commission: Lucas Heights, Australia, **1974**.

11. Gupta, C. K., Sathiyamoorthy, D. Fluid Bed Technology in Material Processing, CRC Press LLC, **1999**.

12. Pagliai, P., Simons, S.J.R., and Rhodes, D., A novel experimental study of temperature enhanced cohesive interparticle forces, *Powder Technol.*, 174, 71–74, **2007**.

13. Kumar, R., Das, S., Roy, S.B., Srivastava, P.K. Development of (*i*) Static Bed Batch Fluorination Set Up for Preparation of Specific Grade UF4 and *(ii)* Process for Production of Small Ingot of Specific Uranium, BARC Internal Report, **2013**.

AUTHOR INDEX